# Applications of cavitation dynamics in a three fluid system

by

Mark David Esson

A thesis submitted to
The University of Birmingham
for the degree of
Doctor of Philosophy

School of Mathematics
The University of Birmingham
September 2014

# Abstract

In this thesis a numerical method is developed for modelling multiple bubbles with axis-symmetric geometry, in a domain of three fluids separated by two fluid-fluid interfaces. The density ratios across these interfaces can vary allowing simulations of bubble interaction with rigid boundaries, free surfaces and any density ratio values between these two extremes. The inclusion of buoyancy and surface tension into the simulations allow for a wide array of possible models, including investigations into explosion bubbles and biomedical applications. The evolution of the bubble is analysed in various scenarios right through to the toroidal stage of bubble collapse.

The numerical simulations are conducted using the boundary integral method with vortex ring calculations for modelling the bubble transition from the simply connected bubble to the doubly connected toroidal phase. The numerical method is then compared with numerical and experimental data from other work to verify the validity of the model. The results show good agreement with past numerical results for spherical bubble oscillations and rigid boundary collapse.

The verified model is then used to simulate a multitude of scenarios to investigate two bubble interaction with applications to mixing. A range of parameters are investigated and results are given for an optimal mixing approach. The introduction of a curved density interface is explored to determine the effect it has on bubble collapse. The curved interface collapse is then adapted to consider bubble collapse near a cell wall.

# Acknowledgements

I would like to first and foremost show my gratitude to my supervisor Dr. David Leppinen for all the help he has given me, both as an undergraduate and especially now as a postgraduate student. His advice and teachings have been invaluable in developing this thesis and without him would not have been possible.

I am also grateful to the EPSRC for funding me throughout my PhD.

I would also like to thank those within the School of Mathematics, whose friendship and welcomed distractions have kept me entertained and sane over the years. And an extra mention to my housemate, Jonathan Simmons, for getting through PhD life with me.

And finally I would like to thank my family for their support and guidance, with special thanks to my Mom and Nan for ensuring I wasn't homeless and hungry during my writing up.

# Contents

# Chapter 1

# Introduction

## 1.1 Overview of Cavitation Dynamics

The area of bubble dynamics has been well researched for the past hundred years. One of the original driving forces behind the advancement of this subject was to investigate the causes of damage to hydraulic machinery and ship propellers. It was found that the surfaces of these instruments showed signs of rapid erosion with no obvious cause. Since then it has been shown that during the operation of these machines, areas of low pressure are formed within their fluid domains. Cavitation bubbles are then formed when the liquid pressure drops below the corresponding vapour pressure. When in the vicinity of a rigid boundary these newly formed cavities grow and then eventually collapse violently. During this collapse a liquid jet forms through the bubble reaching large velocities which impact greatly on surfaces, leading to erosion over time. The realisation that cavitation can have such a large impact on industrial processes came from extensive research both experimentally and mathematically.

One of the first papers on cavitation came from Rayleigh [50] in which he showed that high pressures can be formed from the collapse of a spherical cavity oscillating under the

Navier-Stokes equations in an infinite, incompressible fluid. He suggested that the cavity contains a small amount of gas which allows the cavity to rebound after a rapid collapse. This theory became the basis for many papers including that of Plesset [46], who adapted the idea of the spherical cavity collapse to consider bubbles in a liquid flow. This led to the construction of the Rayleigh-Plesset equation, which accurately models the growth and collapse of a spherical bubble in a pressure field. The Rayleigh-Plesset equation will appear later in Chapter 3 of this thesis as a comparison. The analysis of the spherical bubble led to work on the collapse of bubbles near boundaries.

A broad review of papers on cavitation, starting with Rayleigh, was written by Benjamin and Ellis [2]. It summarises the cause of cavitation damage in machinery by referencing experimental papers that observe the formation of bubble clouds in the fluids near the affected surfaces. By looking at individual bubble interaction with a rigid boundary, it was found that the bubble took on an axisymmetric shape as it translated towards the surface. The bubble translation towards the rigid boundary is explained by the Bjerknes effect, where the attraction to the surface is caused by the volume changes of the bubble. As the cavity moves through the fluid it no longer remains spherical and flattens on the side in the direction of motion. As the bubble volume decreased the bubble surface would fold inwards from the pole on the opposite side of the bubble to the boundary. This would form a jet through the bubble eventually impacting on the wall at the axis of symmetry. The impacting jet caused greater pressures on the surface than those pressures formed by compression of the bubble, leading to the theory that the damage is caused by the jet. The final chapter of the review [2] presents experiments conducted by Benjamin and Ellis themselves, which showed agreement with previous works. The images show the translation of the bubble toward the boundary, and the jet threading through the axis of the bubble toward the other side forming a toroid. It can be seen that the speed of the jet

depends on the proximity of the bubble to the surface, and for a bubble sufficiently close to the rigid boundary the jet speeds attained can be highly damaging. This experimental observation has been supported since by various works including that of Lauterborn and Bolle [32].

With a concise and accurate experimental representation of bubble collapse near a rigid boundary it was now possible to perform a rigorous comparison with numerical simulations. Plesset and Chapman [47] used a finite difference method to simulate the bubble collapse from a sphere. By solving Bernoulli's equation and surface conditions in terms of the potential, the velocity could be calculated along the bubble surface, as well as displacement and change in velocity, which can then be stepped forward in time using various approximations. The model yielded very detailed bubble collapses for spherical bubbles in the vicinity of, and touching, a rigid wall. The jetting through the axis of the bubble from the far side of the bubble towards the wall can clearly be seen in both cases. The bubble that began away from the wall shows the movement of the bubble centroid towards the rigid surface as observed experimentally. They concluded that the jet velocities simulated would be sufficient enough to cause damage to a rigid structure. This paper was the first fully numerical paper to simulate bubble collapse near a rigid boundary. The accuracy in doing so made it the benchmark of comparison for many papers since, including that of Taib [56].

While cavitation was the driving force behind these experiments, this was not the only bubble property observed. In many of the experiments buoyancy was apparent in the bubble motion, the first experiments of Benjamin and Ellis showed the effect. Though being far from any boundaries, the bubble still exhibited the same jetting as before. This is due to the fluid falling under the effect of gravity, causing the buoyant motion of

the cavity. The movement of the bubble forces a flat side in the direction of travel, as mentioned before. The jet forms during the collapse phase and protrudes through to the top of the bubble. The initial motion of the bubble is attributed to an impulse, which is a concept introduced by Kelvin [31].

Blake et al. [6] describes the Kelvin impulse as the linear momentum of the bubble and is used to determine the bubble motion. They modelled the collapse of a bubble above a rigid boundary and compared the Bjerknes effect with that of buoyancy. To simulate the bubble collapse the boundary integral method is used. In Chapter 2 of this thesis a more comprehensive explanation of the boundary integral method is given and implemented. To solve Laplace's equation in the fluid domain, the velocity potential is given by the solution of the Green's functions. To simulate the rigid boundary, the Green's function is made from a source and an equal source at an image point located on the opposite side of the rigid boundary. These equations are discretised across the surface of the bubble and solved for the time derivative of the velocity potential. This is then advanced forward in time using Euler time steps, to model the surface of the bubble over time. This method is broadly used to model bubble surfaces and has been used by Taib [56], Curtis [17], Pearson et al. [42] and Lee et al. [34].

In the absence of gravity, the simulated bubble collapse showed good comparison with that of the results from Plesset and Chapman [47]. It was also seen that the speed of the jet increased as the stand-off distance of the bubble centroid from the boundary increased. This was due to the bubble having the opportunity to collapse to a smaller size, allowing for higher velocities and pressures. When gravity is included in the simulation there is a contest between buoyancy and the Bjerknes forces. It is seen that for a bubble close to the rigid boundary the Bjerknes forces are the stronger of the two, with the bubble collapsing by producing a jet toward the boundary. As the stand-off distance is increased, the strength of the jet decreases, showing buoyancy taking greater effect. When the stand-off

distance is sufficiently large compared to the buoyancy, the bubble no longer jets towards the boundary but instead jets in the direction of the buoyant motion. By calculating the Kelvin impulse they were able to show that the direction of the jet produced by a collapsing bubble near a rigid boundary changes when the buoyancy or stand-off is altered. It was found that when the product of buoyancy, $\delta$, and stand-off, $\gamma$, is $\delta\gamma > 0.442$ the bubble will migrate away from the boundary, and when $\delta\gamma < 0.442$ it will collapse towards the boundary, thus showing the strength of the Bjerknes forces and the effect buoyancy can have on a collapsing bubble [6].

Though buoyancy can have a relatively small effect on cavitation bubbles, it is a major factor in the movement and collapse of underwater explosion bubbles. There has been a large amount of interest in the mechanics of explosion bubbles due to their use by naval forces in both protecting and destroying ships. When considering torpedoes or underwater mines, it has been found that the damage from the resultant shock is minimal compared to the damage from the collapsing cavity thereafter, agreeing with the cavitation damage of smaller bubbles. Cavitation bubbles differ from explosion bubbles by size, but the same methods can be used to model both. The modelling of underwater explosions led to modelling the interaction of a bubble and a free surface.

In a second paper by Blake et al. [7], the same boundary integral method and Kelvin impulses analysis as before are applied to the collapse of a bubble near a free surface. To simulate the free surface, the initial velocity potential is modified to incorporate a negative image, the surface itself is now able to move with the pressures exerted by the bubble. In the absence of buoyancy forces it is seen that for a large stand-off distance the free surface moves away from the bubble during the growth phase. The free surface falls again during the bubble collapse though at a slower rate nearer the axis of symmetry, leaving a slight hump. The bubble surface nearest the free surface becomes flat during

the collapse, and then forms a jet away from the free surface. It is noted that this jet is much broader than those produced near a rigid boundary. When the stand-off distance is decreased, the bubble moves toward the free surface creating a larger hump on the fluid interface than seen for the larger stand-off distances. As the expansion continues, the top of the bubble enters the base of the free-surface hump. The bubble moves away from the surface during the collapse and a jet is again produced away from the free surface through the bubble, though this time the free surface hump continues to grow along the axis of symmetry in the opposite direction to the bubble jet. This forms a stagnation point between the bubble and the free surface. By looking at the pressure field during the collapse it can be seen that a high pressure forms between the bubble and the free surface on the axis of symmetry.

When a small amount of buoyancy is included there is little change to the growth and collapse of the bubble, there is some slight elongation towards the free surface at maximum volume but during collapse the bubble migrates and jets away from the free surface as before. When the buoyancy is increased, as in the case of explosion bubbles, the bubble migrates towards the free surface during the collapse phase with the jet directed towards it. This shows that buoyancy can affect the direction of bubble migration and the jet direction as observed in the rigid boundary case. When the Kelvin impulse is calculated in the same manner as the rigid boundary case, it can be shown that the direction of jet and bubble migration can change due to the buoyancy, $\delta$, and stand-off distance, $\gamma$, when the null-Kelvin-impulse line $\gamma\delta = 0.442$ is crossed [7]. This shows that in the case of smaller cavitation bubbles, buoyancy plays less of a role, but for underwater explosion bubbles it is a dominant feature.

The numerical models mentioned thus far give good comparison with experimental results for bubble collapse near both rigid boundaries and free surfaces, though none of the models

are able to simulate the bubble after the jet has impacted the other side of the bubble and achieved a toroidal form. The boundary integral method fails at this point as the fluid domain goes from singly connected to doubly connected, causing Laplace's equation to no longer have a unique solution. Various methods have been developed to overcome this problem. The method suggested by Best [3] is to introduce a cut in the flow domain to maintain a simply connected domain. At the point where the jet tip impacts the far side of the bubble, a contour is placed across the toroidal bubble gap. The Green's functions are modified to account for the jump in potential across the cut, the potential jump corresponds to the circulation round the bubble. This method has been tested against experimental data for rigid boundaries by Brujan et al. [10] and was found to give a favourable comparison. One weakness in this approach is the need to continually track the cut as it circulates round the bubble, this can result in the contour becoming complex and unmanageable.

An alternative method by Zhang et al. [62] is to attach a vortex sheet to the bubble. Across the sheet the pressures and normal velocities of the fluid are continuous and the tangential velocities are discontinuous. The sheet is attached to the bubble at a circular line called the triple-point line, which causes a cusp at this point on the bubble. The results from this method show less rotation about the bubble than those of Best, with a pressure ring about the jet as opposed to a singular point.

A different approach to accounting for the circulation caused by the bubble going toroidal is to introduce a vortex ring. As the vortex ring is not attached to the surface of the bubble there is no need to track position through time, also there is no need to create a cusp on the bubble for attachment. The idea was first introduced by Pedley [43] to trace the history of a toroidal bubble after formation. The bubble is threaded by a vortex ring allowing for no interaction with the bubble surface, yet allows for the circulation by the jet impact while keeping the potential unique. Though this proved to be very accurate

in finding the streamlines of the flow field round the toroidal bubble, it did not show the transition from a singly connected bubble to toroidal form. This was achieved by Lundgren and Mansour [39] by modifying the boundary integral method to include the potential formed by the vortex ring. Once the jet impact occurs the vortex ring is then introduced and the circulation is taken to be the difference in potential across the point of impact. This method was then improved by Wang et al. [59] and used to consider the toroidal bubbles formed by cavitation bubbles near a rigid boundary. The results showed good agreement with the dynamic cut approach used by Best [3]. One advantage of the vortex ring is that it can be used in three dimensional simulations without the need of axial symmetry [62]. In this thesis the method of the vortex ring will be adopted and the details can be found in Chapter 2.

The advancement of numerical models has led to a greater understanding in the physical processes in experiments, this allows for cavitation dynamics to be applied to areas that require a greater degree of accuracy. Developments have been made to use the free-surface spikes caused by bubble collapse in printing processes. In a paper by Duocastella et al. [20] an experiment is set-up to produce a laser bubble in a thin film of liquid. The resultant cavity will collapse while producing a jet away from the free surface, as seen in bubble interaction with a free surface. As the bubble jet threads the bubble, the surface hump continues to grow forming a liquid jet on the free surface. This surface jet can now protrude far enough to touch another substrate, effectively printing a droplet of the fluid on to the surface of the substrate. This process is known as laser induced forward transfer and is looked at in more detail in Chapter 3. Due to the small size of the droplets produced, this technique can be used in the printing of nano-particle inks for electrodes in transistors, polymers for chemical sensors and living cells for tissue engineering [21]. As this is a relatively new technique, there are not many numerical simulations of the process.

Another area of cavitation dynamics with little numerical investigation is that of a bubble between two rigid plates. While bubble-rigid boundary interaction has been extensively researched both experimentally and numerically, the addition of another boundary to the fluid domain appears in few papers. In a paper by Ishida et al. [15] the experimental results show a bubble growing between the two plates. The bubble is arranged with two parallel plates directly above and below, equidistant from the bubble centroid. It experiences spherical growth until it reaches near maximum radius when the bubble becomes flat on the top and bottom. During collapse, the sides of the bubble contract forming a 'dumbbell' shape, this continues till the bubble splits into two smaller bubbles along the axis of symmetry. Ishida et al. use a boundary element method to gain good comparison with the experimental results, though a more rigorous numerical model was produced by Choi et al. [16]. In Chapter 3 this problem will be modelled and analysed in more detail with the methods mentioned previously and developed in the next chapter.

## 1.2 Aim

The purpose of this research is to provide more insight into the area of bubble growth and collapse. By looking at the interactions between a bubble and two interfaces of variable density, a numerical analysis of various physical processes can be performed. The numerical simulations will be able to model different industrial applications to aid in understanding the mechanics involved and help refine the overall procedure.

## 1.3 Thesis Synopsis

Chapter 1 has given preface to some of the research involved in cavitation dynamics, showing the original work produced on spherical bubbles and the stimulus for investigating more vigorous bubble collapse. The application of the boundary integral method to bubble

collapse has been introduced, along with various modifications to allow for modelling of the toroidal phase. This outlines some of the numerical methods to be used in latter chapters. Various experiments involving multiple interfaces have been introduced with the aim to model them in later chapters.

The numerics for the boundary integral method are introduced in Chapter 2, and how they are applied to modelling the non-spherical collapse of a bubble. The kinematic and dynamic boundary conditions are derived for the bubble surface and each of the fluid-fluid interfaces. A method for discretising the surface equations is shown allowing for the Green's functions to be solved at nodes placed along the surfaces, these equations are then arranged into matrix notation and solved to give solutions to Laplace's equation. The process of reconstructing the surface using quintic splines is shown in detail, and how the splines are matched to the far field conditions.

In Chapter 3, the numerics outlined in Chapter 2 are used to produce simulations which are compared with results using the Rayleigh-Plesset equation and other proven numerical results from some of the papers mentioned in Chapter 1, this will give sufficient data to gauge the accuracy of the model. The model will then be used to simulate experimental results along with those of the laser induced forward transfer experiment and the bubble between two plates. Once the model has been verified through comparisons with other work, the model will then be used for original work.

The content of Chapter 4 will utilise the model to better understand the mixing of two fluid using bubbles. Previous applications for the mixing of fluids and microfluids will be introduced and discussed. The model is then used to simulate the mixing of two fluids using two bubbles either side of a density interface. The strength and inception time of the second bubble is varied to see the effect on the interface and the surrounding fluid domain. These results are then interpreted to give a description of how the fluids can be mixed effectively. Additionally, the dynamics of the bubble collapses will be

applied to a simplified ideal gas law to better understand the temperatures achieved within the bubbles, and thus whether these temperatures could be used to aid in the chemical reactions of the fluids being mixed. The densities of the fluids will be varied to consider a wider range of fluids being mixed and to see the most efficient way to mix two fluids.

In Chapter 5 the geometry of the interface is altered to consider the collapse of a bubble against a curved boundary. The simulations incorporating the new geometries will be compared to results obtained by Tomita et al. [58] to better understand bubble interaction near a curved rigid boundary, both convex and concave. The simulations will then be extended beyond the scope of the paper to identify more extreme curvatures and the effects of buoyancy. The interface shape will then be varied to consider other geometries. A dome shape will be introduced with surface tension and small density ratios to approximate a biological cell. The interaction between bubble, cell and rigid boundary will be simulated to give understanding to the use of bubble collapse in cell injection.

In Chapter 6, the effectiveness of the numerical method developed in Chapter 2 will be discussed by referring to the accuracy of the results obtained in Chapter 3. Once the model has been verified as a very useful tool for simulating bubble collapse, the results of the industrial and biological processes modelled in Chapters 4 and 5 will be summarised. Areas for further research will then be introduced and briefly discussed.

# Chapter 2

# Problem Outline and Numerical Method for Modelling Bubble Collapse in a Three Fluid System

The work in this thesis is a direct extension of the work by Curtis [17] which is originally based on the numerical methods found in work by Taib [56]. These previous works have modelled bubble interaction with a single fluid-fluid interface. In this thesis, a second interface is included to separate the fluid domain into three fluids. By considering the growth and collapse of bubbles near two fluid-fluid interfaces, the modelling capabilities of previous works to be applied to a much wider array of scenarios.

## 2.1 Problem Outline

The model geometry for bubbles in a three fluid system can be seen in Figure 2.1, in the works mentioned previously interface B was not used. The inclusion of the third fluid has a great impact on cavitation bubbles located in fluid 1 due to the close proximity to both fluid-fluid interfaces.

The all three fluids start having zero velocity, with gravity the only external force acting

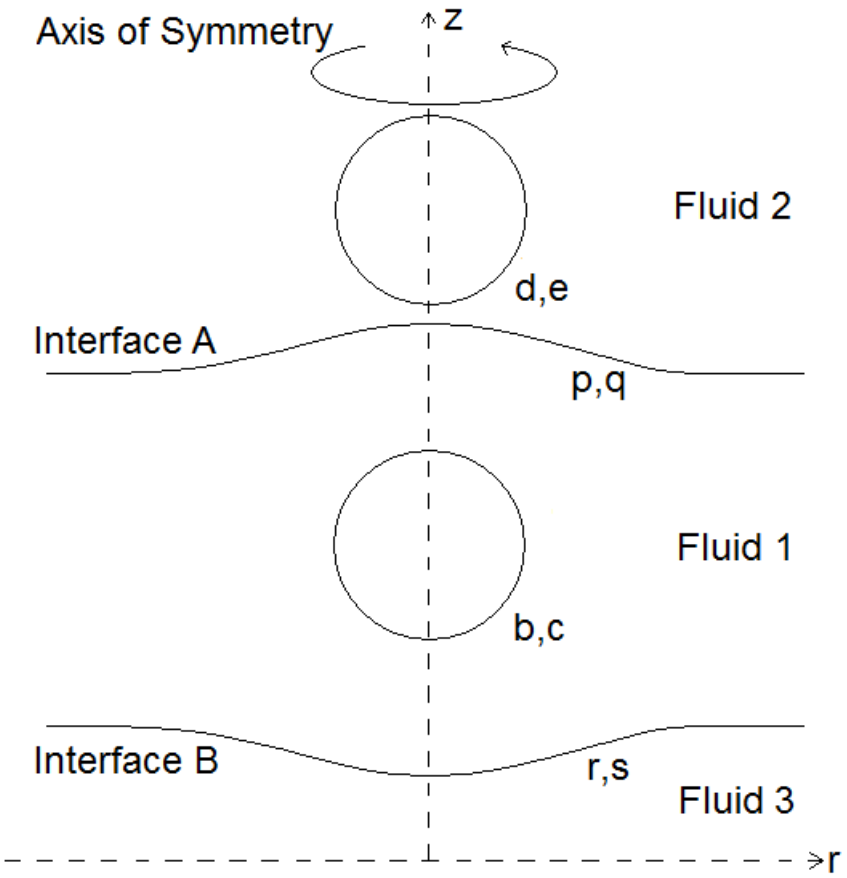


Figure 2.1: Model geometry for the three fluid system

on the system. Each fluid is assumed to be incompressible, irrotational and inviscid, allowing for the calculations to be written in terms of the velocity potential $\mathbf{u}_i = \nabla\phi_i$ in fluids $i = 1, 2, 3$. The physical examples considered in this thesis can all be represented by the axisymmetric geometry shown in figure 2.1, though the methods used in this chapter can also be modified for non-aligned cases [62]. Each bubble is initially introduced into the fluid domain along the axis of symmetry as a spherical cavity with radius equal to the minimum radius of a high pressure bubble. The axisymmetric geometry in this model is used for both the singly and doubly connected stages of the bubble collapse, allowing the dimension of the problem to be reduced by one.

To account for the incompressibility of the fluids, the equation for continuity of mass is

given by $\nabla \cdot \mathbf{u}_i = 0$. Writing this in terms of velocity potentials gives Laplace's equation,

$$\nabla \cdot \mathbf{u}_i = \nabla \cdot \nabla \phi_i = \nabla^2 \phi_i = 0, \tag{2.1.1}$$

in each fluid $i = 1, 2, 3$. As the fluids tend to infinity the boundary conditions are given as,

$$\begin{aligned} \mathbf{u}_i &\rightarrow 0, \\ p &\rightarrow p_\infty(t), \end{aligned} \tag{2.1.2}$$

where $p$ is pressure and $p_\infty$ is the far field pressure. The far field pressure is represented as a time dependent function to allow for the inclusion of acoustic forcing [17]. The next step is to set the boundary conditions on the bubble surfaces and fluid-fluid interfaces.

## 2.2 Boundary Conditions

### Kinematic Boundary Conditions

The kinematic boundary condition specifies that a particle that starts on any surface will remain on that surface. Therefore, the velocity of the particle must equal the normal velocity of the surface. Particles located on any bubble surface have velocity equal to the normal velocity of the exterior fluid, for example the velocity of a particle on the surface of a bubble in fluid 1 is,

$$\frac{d\mathbf{b}}{dt} = \mathbf{u}_1(\mathbf{b}),$$

with a similar expression for bubbles in fluid 2. Across both fluid-fluid interfaces the normal velocities must remain continuous to prevent any voids forming in the fluid. Therefore the conditions,

$$\mathbf{u}_1 \cdot \mathbf{n}_2 = \mathbf{u}_2 \cdot \mathbf{n}_2, \quad \mathbf{u}_1 \cdot \mathbf{n}_3 = \mathbf{u}_3 \cdot \mathbf{n}_3, \tag{2.2.1}$$

hold across interface $A$ and interface $B$, respectively. The earlier assumption of the model being inviscid leads to a difference in the tangential velocity of the fluid across the interfaces, so any particle on an interface will move with the average velocity of the fluids either side of the interface,

$$\frac{d\mathbf{p}}{dt} = \frac{\mathbf{u}_1(\mathbf{p}) + \mathbf{u}_2(\mathbf{p})}{2}, \quad \frac{d\mathbf{r}}{dt} = \frac{\mathbf{u}_1(\mathbf{r}) + \mathbf{u}_3(\mathbf{r})}{2}. \tag{2.2.2}$$

This holds mathematically as the Green's integral formula only uses the normal velocities of the particles on the interfaces to find the velocity potentials, allowing for discrepancies in the tangential velocities. To simplify the boundary conditions, notation for the velocity potentials is introduced

$$\begin{aligned} \phi_A(\mathbf{p}) &= \phi_1(\mathbf{p}) + \phi_2(\mathbf{p}), \quad \phi_B(\mathbf{r}) = \phi_1(\mathbf{r}) + \phi_3(\mathbf{r}) \\ \mu_A(\mathbf{p}) &= \phi_1(\mathbf{p}) - \phi_2(\mathbf{p}), \quad \mu_B(\mathbf{r}) = \phi_1(\mathbf{r}) - \phi_3(\mathbf{r}), \end{aligned} \tag{2.2.3}$$

This allows the kinematic conditions to be written as

$$\frac{d\mathbf{p}}{dt} = \frac{\nabla\phi_A(\mathbf{p})}{2} = \mathbf{u}_{av1}, \quad \frac{d\mathbf{r}}{dt} = \frac{\nabla\phi_B(\mathbf{r})}{2} = \mathbf{u}_{av2}, \tag{2.2.4}$$

on interface $A$ and interface $B$, respectively.

## Dynamic Boundary Conditions

Throughout the three fluids, the pressure is related to the velocity potentials by Bernoulli's equation

$$\frac{\partial \phi_i}{\partial t} + \frac{1}{2}|\mathbf{u}_i|^2 = -\frac{p}{\rho_i} - g\,(z - z_0) + \frac{p_\infty}{\rho_i}. \tag{2.2.5}$$

Here the subscript $i = 1, 2, 3$ denotes which fluid the equation is describing, $p_\infty$ is the far field pressure, $\rho_i$ is fluid density and $g$ is the gravitational constant. The constant $z_0$ is a reference coordinate for the points on a surface. In the case of the bubble surfaces, $z_0$ is taken as the initial centroid, the hypothetical point where the bubble was generated. For the fluid-fluid interfaces $z_0$ is taken as the initial starting point on the $z$-axis of each point on the interface, for example on interface $A$, $z_0 = 0$. The pressure term, $p$, is used to account for the pressure jump that occurs across the interface due to surface tension interaction. For bubble surfaces the fluid pressure is related to the internal pressure of the bubble through Young-Laplace's equation [9]

$$p_{bubble} = p_{fluid} + \sigma \nabla \cdot \mathbf{n}, \tag{2.2.6}$$

where $\sigma$ is the surface tension of the bubble. All the bubbles in this thesis are assumed to be ideal and adiabatic, allowing for the bubble pressure to be represented as

$$p_{bubble} = p_v + p_0 \left(\frac{R_0}{R}\right)^{3\gamma}, \tag{2.2.7}$$

where $p_v$ is the vapour pressure at the surface of the bubble, $p_0$ is the internal pressure of the bubble when it is at the initial minimum radius $R_0$, $R\,(t)$ is the bubble radius at time $t$ and $\gamma$ is the ratio of specific heats. Equations (2.2.6) and (2.2.7) are substituted into Bernoulli's equation (2.2.5). All terms are non-dimensionalised with respect to the maximum radius the bubble would reach in an infinite fluid as described by the Rayleigh-Plesset equation. The density of fluid 1, $\rho_1$, is used to non-dimensionalise the equations, giving density ratios $\rho_A = \frac{\rho_2}{\rho_1}$ and $\rho_B = \frac{\rho_3}{\rho_1}$. So for a bubble in fluid 1 the equation on the surface is given by

$$\frac{\partial \phi_1(\mathbf{b})}{\partial t} + \frac{1}{2}|\mathbf{u}_1(\mathbf{b})|^2 = 1 - \varepsilon\left(\frac{R_0}{R}\right)^{3\gamma} - \delta(z - z_0) + \sigma_{b1}\nabla \cdot \mathbf{n}_{b1}, \tag{2.2.8}$$

and similarly in fluid 2,

$$\frac{\partial \phi_2(\mathbf{d})}{\partial t} + \frac{1}{2}|\mathbf{u}_2(\mathbf{d})|^2 = \frac{1}{\rho_A}\left(1 - \varepsilon\left(\frac{R_0}{R}\right)^{3\gamma} + \sigma_{b2}\nabla \cdot \mathbf{n}_{b2}\right) - \delta(z - z_0). \tag{2.2.9}$$

Here $\delta$ represents the buoyancy parameter given by

$$\delta = \frac{\rho_1 g R_{max}}{\Delta_p}, \tag{2.2.10}$$

where $R_{max}$ is the maximum bubble radius and $\Delta_p = p_{\inf} - p_v$ is the difference between the pressure at infinity and the vapour pressure of the bubble. Introducing the substantial derivative

$$\frac{D}{Dt} = \frac{\partial}{\partial t} + \mathbf{u} \cdot \nabla,$$

gives the Lagrangian evolution of the potentials on the bubble surface as

$$\begin{aligned}
\frac{D\phi_1(\mathbf{b})}{Dt} &= \frac{1}{2}|\mathbf{u}_1(\mathbf{b})|^2 + 1 - \varepsilon\left(\frac{R_0}{R}\right)^{3\gamma} - \delta(z - h_1) + \sigma_{b1}\nabla \cdot \mathbf{n}_{b1}, \\
\frac{D\phi_2(\mathbf{d})}{Dt} &= \frac{1}{2}|\mathbf{u}_2(\mathbf{d})|^2 + \frac{1}{\rho_A}\left(1 - \varepsilon\left(\frac{R_0}{R}\right)^{3\gamma} + \sigma_{b2}\nabla \cdot \mathbf{n}_{b2}\right) - \delta(z - h_2).
\end{aligned} \tag{2.2.11}$$

At the fluid-fluid interfaces Young-Laplace's equation is used to show the relationship between the fluids on either side of the interface,

$$p_1 = p_2 - \widehat{\sigma}_{I_A} \nabla \cdot \mathbf{n}_1, \tag{2.2.12}$$

$$p_1 = p_3 - \widehat{\sigma}_{I_B} \nabla \cdot \mathbf{n}_1, \tag{2.2.13}$$

where $\widehat{\sigma}_{I_A}$ and $\widehat{\sigma}_{I_B}$ are the interfacial tension of interfaces $A$ and $B$ respectively. Rearranging Bernoulli's equation (2.2.5) for pressure and substituting into (2.2.12) the above gives

$$\rho_1 \left( \frac{\partial \phi_1 (\mathbf{x}_0)}{\partial t} + \frac{1}{2} |\mathbf{u}_1 (\mathbf{x}_0)|^2 + gz \right) = \rho_2 \left( \frac{\partial \phi_2 (\mathbf{x}_0)}{\partial t} + \frac{1}{2} |\mathbf{u}_2 (\mathbf{x}_0)|^2 + gz \right) - \widehat{\sigma}_{I_A} \nabla \cdot \mathbf{n}_1. \tag{2.2.14}$$

Rearranging and non-dimensionalising as before gives

$$\left( \frac{\partial \phi_1 (\mathbf{x}_0)}{\partial t} + \frac{1}{2} |\mathbf{u}_1 (\mathbf{x}_0)|^2 \right) - \rho_A \left( \frac{\partial \phi_2 (\mathbf{x}_0)}{\partial t} + \frac{1}{2} |\mathbf{u}_2 (\mathbf{x}_0)|^2 \right) = \delta z (1 + \rho_A) + \sigma_{I_A} \nabla \cdot \mathbf{n}_2. \tag{2.2.15}$$

Using the substantial derivative and the notation introduced in (2.2.3) gives

$$\frac{D}{Dt} (\phi_A (1 - \rho_A) + \mu_A (1 + \rho_A)) = (1 - \rho_A) (\mathbf{u}_1 \cdot \mathbf{u}_2) - 2\delta z (1 + \rho_A) - 2\sigma_{I_A} \nabla \cdot \mathbf{n}_2. \tag{2.2.16}$$

Similarly for fluid-fluid interface $B$

$$\frac{D}{Dt} (\phi_B (1 - \rho_B) + \mu_B (1 + \rho_B)) = (1 - \rho_B) (\mathbf{u}_1 \cdot \mathbf{u}_3) - 2\delta z (1 + \rho_B) - 2\sigma_{I_B} \nabla \cdot \mathbf{n}_3. \tag{2.2.17}$$

The dimensionless parameters in equations (2.2.11), (2.2.16) and (2.2.17) are the buoyancy parameter $\delta$, the strength parameter $\varepsilon$, the ratio of specific heats $\gamma$, the bubble stand-off distances $h_i$, and the surface tension of the fluid-fluid interfaces and the bubble surfaces $\sigma_I$ and $\sigma_b$ respectively. They are given by

$$\delta = \frac{gR_{max}\rho_1}{\Delta_p},\ \rho_A = \frac{\rho_2}{\rho_1},\ \rho_B = \frac{\rho_3}{\rho_1},\ \sigma_{bi} = \frac{\overline{\sigma_{bi}}}{\Delta_p R_{max}},\ \sigma_I = \frac{\widehat{\sigma_I}}{\Delta_p R_{max}},\ \varepsilon = \frac{p_0}{\Delta_p}\ h_i = \frac{h_{dim}}{R_{max}}. \tag{2.2.18}$$

## 2.3 Overview of the Numerical Method

To solve this problem, a boundary integral approach is used, with the previous kinematic and dynamic boundary conditions, to reduce the problem from three dimensions over the three fluid volumes, to a one dimensional problem over the axisymmetric surfaces. As mentioned in the Chapter 1 the boundary integral method has been widely used and accepted as a very useful tool for modelling bubble collapse [17, 34, 42, 56].

The boundary integral method is derived through discretising an integral equation which is mathematically equivalent to an original governing partial differential equation. The reformulation of the PDE consists of an integral equation defined on the boundary of the domain and one which relates the boundary solution to the solution at points in the domain. In the case of this problem, the PDE to be solved is the Laplace's equation, $\nabla^2\phi$, and the integral equation is given by Green's integral formula (2.4.1). This discretised form of the Green's integral formula is used to give approximations for the unknown potentials and normal velocities from various known values.

With these potentials and normal velocities obtained from the boundary integral method, the kinematic and dynamic boundary conditions, given by ordinary differential equations, can then be explicitly advanced forward in time to provide the boundary locations and

velocity potentials needed to repeatedly apply this algorithm. For the bubble and interface surfaces between the collocation points, quintic splines are incorporated to give the location and functional behaviour along these sections.

The general overview of this method is as follows:

1. Derive Green's integral formula from Laplace's equation.
2. Rewrite Green's integral formula in terms of an axissymetric coordinate system.
3. Discretise the rewritten Green's integral formula.
4. Find the unknown potentials and normal velocities.
5. Use the boundary conditions to advance advance forward in time.
6. Interpolate the collocation points with quintic splines.

This can then be repeated until the simulation has completed.

The rest of this Chapter will detail points 2-4 to show how the boundary integral method has been used, and provide the equations for the quintic splines and far field approximations. The end section of this chapter will show how this method is changed to incorporate toroidal bubbles.

## 2.4 Green's Integral Formula

The solution to Laplace's equation is given by the Green's integral formula [18] applied to a simply connected domain, $\Omega$, in terms of the velocity potential normal velocity on the boundary of the domain, $\partial\Omega$, given by,

$$c\left(\mathbf{x}_0\right)\phi\left(\mathbf{x}_0\right) = \int_{\partial\Omega}\left(\frac{\partial\phi}{\partial n}\left(\mathbf{x}\right)G\left(\mathbf{x},\mathbf{x}_0\right) - \phi\left(\mathbf{x}\right)\frac{\partial G}{\partial n}\left(\mathbf{x},\mathbf{x}_0\right)\right)dS. \tag{2.4.1}$$

Here $\mathbf{n}$ is the unit normal vector which points out of the fluid domain, $\mathbf{x}_0 \in \Omega$ is the point where the potential is to be determined and $\mathbf{x} \in \partial\Omega$ represents the points along the

surface. As shown in Figure 2.1, the points on the surface of a bubble in fluid 1 are $\mathbf{x} = \mathbf{c}$ and the nodes related to the surface are written as $\mathbf{x}_0 = \mathbf{b}$, similarly for bubbles in fluid 2 $\mathbf{x} = \mathbf{e}$ and $\mathbf{x}_0 = \mathbf{d}$. For points on interface $A$ it is given that $\mathbf{x}_0 = \mathbf{p}$ and $\mathbf{x} = \mathbf{q}$, while on interface $B$, $\mathbf{x}_0 = \mathbf{r}$ and $\mathbf{x} = \mathbf{s}$. The coefficients $c(\mathbf{x}_0)$ are the solid angles subtended from the surface geometry at the nodes, and must be calculated at each collocation point. However, when the surface has continuous first and second derivatives, $\partial\Omega$ is considered sufficiently smooth enough for the coefficient $c(\mathbf{x}_0)$ to be given by,

$$c(\mathbf{x}_0) = \begin{cases} 4\pi & \mathbf{x}_0 \in \Omega \setminus \partial\Omega, \\ 2\pi & \mathbf{x}_0 \in \partial\Omega. \end{cases} \tag{2.4.2}$$

The function $G(\mathbf{x}, \mathbf{x}_0)$ in (2.4.1), comes from the free space Green's function in two dimensions, with the factor $4\pi$ included in the coefficients to give,

$$G(\mathbf{x}, \mathbf{x}_0) = \cdot \frac{1}{|\mathbf{x} - \mathbf{x}_0|}. \tag{2.4.3}$$

The Green's function is written in cylindrical polar coordinates with $\mathbf{x}_0 = (r_0, \theta_0, z_0)$ and $\mathbf{x} = (r, \theta, z)$, as the geometry is axisymmetric $\theta_0$ is taken to be zero. This gives

$$\begin{aligned} G(\mathbf{x}, \mathbf{x}_0) = \frac{1}{|\mathbf{x} - \mathbf{x}_0|} &= \frac{1}{\sqrt{(r\cos(\theta) - r_0)^2 + (r\sin(\theta))^2 + (z - z_0)^2}} \\ &= \frac{1}{\sqrt{r^2 + r_0^2 + 2rr_0 - 2rr_0(\cos(\theta) + 1) + (z - z_0)^2}} \\ &= \frac{1}{\sqrt{(r + r_0)^2 + (z - z_0)^2 - 4rr_0\cos^2\left(\frac{\theta}{2}\right)}}. \end{aligned} \tag{2.4.4}$$

The surfaces $\partial\Omega$ are parametrised by the arc length variable $\xi$ and angle $\theta$ so $\mathbf{x}_0 = (r(\xi), \theta, z(\xi))$. The unit normal can be expressed as

$$\mathbf{n} = \frac{1}{\sqrt{z'^2 + r'^2}} \left(z', 0, -r'\right), \tag{2.4.5}$$

where $'$ represents differentiation with respect to $\xi$. Differentiation of (2.4.4) gives

$$\nabla \frac{1}{|\mathbf{x} - \mathbf{x}_0|} = \frac{-\left(r + r_0 - 2r_0 \cos^2\left(\frac{\theta}{2}\right), 0, (z - z_0)\right)}{\left((r + r_0)^2 + (z - z_0)^2 - 4rr_0 \cos^2\left(\frac{\theta}{2}\right)\right)^{\frac{3}{2}}}. \tag{2.4.6}$$

Multiplying by $\mathbf{n}$ in (2.4.5) gives the derivative of the free space Green's function with respect to the normal vector,

$$\frac{\partial G\left(\mathbf{x}, \mathbf{x}_0\right)}{\partial n} = \frac{r'\left(z - z_0\right) - z'\left((r + r_0) - 2r_0 \cos^2\left(\frac{\theta}{2}\right)\right)}{\sqrt{z'^2 + r'^2}\left((r + r_0)^2 + (z - z_0)^2 - 4rr_0 \cos^2\left(\frac{\theta}{2}\right)\right)^{\frac{3}{2}}}. \tag{2.4.7}$$

The Green's integral formula (2.4.1) can now be simplified using the arc length, $L$, given by

$$L = \int_0^{\xi_{end}} \sqrt{\left(\frac{dr}{d\xi}\right)^2 + \left(\frac{dz}{d\xi}\right)^2}\, d\xi, \tag{2.4.8}$$

into integrals over $\xi$ and complete elliptic integrals of the first and second kind over $\theta$. Therefore, integrals of the form

$$\int_{\partial\Omega} \frac{1}{|\mathbf{x} - \mathbf{x}_0|} \chi\left(\mathbf{x}\right) dS, \tag{2.4.9}$$

where $\chi\left(\mathbf{x}\right) = \chi\left(\xi\right)$ is a known function parametrised by $\xi$, can be given by

$$\begin{aligned}\int_{\partial\Omega}\frac{1}{|\mathbf{x}-\mathbf{x}_0|}\chi(\mathbf{x})\,dS &= \int_{\partial\Omega}\frac{1}{\sqrt{(r+r_0)^2+(z-z_0)^2-4rr_0\cos^2\left(\frac{\theta}{2}\right)}}\chi dS\\ &= \int_0^L r\chi\sqrt{r'^2+z'^2}\int_0^{2\pi}\frac{d\theta d\xi}{\sqrt{(r+r_0)^2+(z-z_0)^2-4rr_0\cos^2\left(\frac{\theta}{2}\right)}}\\ &= \int_0^L\frac{r\sqrt{r'^2+z'^2}}{\left[(r+r_0)^2+(z-z_0)^2\right]^{\frac{1}{2}}}\chi\int_0^{2\pi}\frac{d\theta}{\left(1-\frac{4rr_0\cos^2\left(\frac{\theta}{2}\right)}{(r+r_0)^2+(z-z_0)^2}\right)^{\frac{1}{2}}}d\xi,\end{aligned} \tag{2.4.10}$$

where $r=r(\xi)$, $z=z(\xi)$ and $\chi=\chi(\xi)$. Letting the elliptic parameter be

$$m^2=\frac{4rr_0}{(r+r_0)^2+(z-z_0)^2},$$

expression (2.4.10) becomes

$$\int_{\partial\Omega}G(\mathbf{x},\mathbf{x}_0)\,\chi(\mathbf{x})\,dS=\int_0^L\frac{m}{2}\sqrt{\frac{r\left(r'^2+z'^2\right)}{r_0}}\chi\int_0^{2\pi}\frac{d\theta d\xi}{\left(1-m^2\cos^2\left(\frac{\theta}{2}\right)\right)^{\frac{1}{2}}}. \tag{2.4.11}$$

Putting $\theta=\pi-2\psi$ allows the integral can now be written as

$$\begin{aligned}\int_{\partial\Omega}G(\mathbf{x},\mathbf{x}_0)\,\chi(\mathbf{x})\,dS &= \int_0^L\frac{m}{2}\sqrt{\frac{r\left(r'^2+z'^2\right)}{r_0}}\chi\int_{-\frac{\pi}{2}}^{\frac{\pi}{2}}\frac{2d\psi d\xi}{\left(1-m^2\sin^2(\psi)\right)^{\frac{1}{2}}}\\ &= \int_0^L\frac{m}{2}\sqrt{\frac{r\left(r'^2+z'^2\right)}{r_0}}\chi\int_0^{\frac{\pi}{2}}\frac{4d\psi d\xi}{\left(1-m^2\sin^2(\psi)\right)^{\frac{1}{2}}}\\ &= 2\int_0^L\chi(\xi)\,m\sqrt{\frac{r\left(r'^2+z'^2\right)}{r_0}}K(m)\,d\xi,\end{aligned} \tag{2.4.12}$$

where $K(m)$ is the complete elliptic integral of the first kind [14]. Similarly to above, an expression can be found for

$$\int_{\partial\Omega} \chi(\mathbf{x}) \frac{\partial}{\partial n}\left(\frac{1}{|\mathbf{x}-\mathbf{x}_0|}\right) dS.$$

Expression (2.4.7) is used to give $\int_{\partial\Omega} \chi(\mathbf{x}) \frac{\partial G}{\partial n}(\mathbf{x},\mathbf{x}_0)\, dS$ as

$$\begin{aligned}
&= \int_0^L r\sqrt{r'^2+z'^2} \int_0^{2\pi} \frac{r'(z-z_0) - z'(r+r_0) + 2z'r_0\cos^2\left(\frac{\theta}{2}\right)}{\sqrt{z'^2+r'^2}\left((r+r_0)^2+(z-z_0)^2-4rr_0\cos^2\left(\frac{\theta}{2}\right)\right)^{\frac{3}{2}}} d\theta d\xi \\
&= \int_0^L \frac{r}{\left((r+r_0)^2+(z-z_0)^2\right)^{\frac{3}{2}}} \int_0^{2\pi} \frac{r'(z-z_0) - z'(r+r_0) + 2z'r_0\cos^2\left(\frac{\theta}{2}\right)}{\left(1-\frac{4rr_0\cos^2\left(\frac{\theta}{2}\right)}{(r+r_0)^2+(z-z_0)^2}\right)^{\frac{3}{2}}} d\theta d\xi \\
&= \int_0^L \frac{m^3 r}{(4rr_0)^{\frac{3}{2}}} \int_0^{2\pi} \frac{r'(z-z_0) - z'(r+r_0) + 2z'r_0\cos^2\left(\frac{\theta}{2}\right)}{\left(1-m^2\cos^2\left(\frac{\theta}{2}\right)\right)^{\frac{3}{2}}} d\theta d\xi \\
&= \int_0^L \frac{m^3 r\left(r'(z-z_0) - z'(r+r_0)\right)}{(4rr_0)^{\frac{3}{2}}} \int_0^{2\pi} \frac{1}{\left(1-m^2\cos^2\left(\frac{\theta}{2}\right)\right)^{\frac{3}{2}}} d\theta d\xi \\
&\quad - \int_0^L \frac{2mrr_0z'}{(4rr_0)^{\frac{3}{2}}} \int_0^{2\pi} \frac{-1+1-m^2\cos^2\left(\frac{\theta}{2}\right)}{\left(1-m^2\cos^2\left(\frac{\theta}{2}\right)\right)^{\frac{3}{2}}} d\theta d\xi \\
&= \int_0^L \left(\frac{m^3 r\left(r'(z-z_0) - z'(r+r_0)\right)}{(4rr_0)^{\frac{3}{2}}} + \frac{2mrr_0z'}{(4rr_0)^{\frac{3}{2}}}\right) \int_0^{2\pi} \frac{1}{\left(1-m^2\cos^2\left(\frac{\theta}{2}\right)\right)^{\frac{3}{2}}} d\theta d\xi \\
&\quad - \int_0^L \frac{2mrr_0z'}{(4rr_0)^{\frac{3}{2}}} \int_0^{2\pi} \frac{1}{\left(1-m^2\cos^2\left(\frac{\theta}{2}\right)\right)^{\frac{1}{2}}} d\theta d\xi \\
&= \int_0^L \frac{m}{(4rr_0)^{\frac{1}{2}}} \left(\left(\frac{m^2}{r_0}\left(r'(z-z_0) - z'(r+r_0)\right) + 2z'\right)\frac{E(m)}{1-m^2} - 2z'K(m)\right) d\xi,
\end{aligned} \tag{2.4.13}$$

where $E(m)$ is the complete elliptic integral of the second kind [14].

## 2.5 Discretisation

The next step in the boundary integral method is to discretise equations (2.4.12) and (2.4.13) in terms of the sections of arc length between each node. The parameter $\chi(\xi)$, as before, represents a function parametrised by $\xi$; for example the velocity potential or the

derivative of the velocity potential. The unknown $\chi$ is approximated by a linear function on $\xi \in [\xi_i, \xi_{i+1}]$ between nodes $i$ and $i+1$, given by

$$\chi(\xi) = \chi_i \left( \frac{\xi_{i+1} - \xi}{\Delta_i} \right) + \chi_{i+1} \left( \frac{\xi - \xi_i}{\Delta_i} \right), \tag{2.5.1}$$

where $\Delta_i = (\xi_{i+1} - \xi_i)$. This expression for $\chi(\xi)$ can now be substituted into equation (2.4.12) to give the following expression for each node at $\xi = \xi_j$,

$$\int_{\partial\Omega} G\chi_j dS = 2\sum_{k=1}^{n-1} \int_{\xi_k}^{\xi_{k+1}} \left( \chi_k \left( \frac{\xi_{k+1} - \xi}{\Delta_k} \right) + \chi_{k+1} \left( \frac{\xi - \xi_k}{\Delta_k} \right) \right) m_{k,j} \sqrt{\frac{r_k \left( r_k'^2 + z_k'^2 \right)}{r_j}} K(m_{k,j})\, d\xi.$$

Here the discrete nodal values are given by $r_j = r(\xi_j)$, $z_j = z(\xi_j)$, and the continuous $k^{th}$ spline segments are $r_k = r_k(\xi)$, $z_k = z_k(\xi)$. The elliptic parameter along the $k^{th}$ segment with respect to the $j^{th}$ node can now be written as,

$$(m_{k,j})^2 = \frac{4 r_k(\xi)\, r_j}{\left( r_k(\xi) + r_j \right)^2 + \left( z_k(\xi) - z_j \right)^2}.$$

For continuity in axisymmetric coordinates, any function at the nodes along the axis of symmetry must have either a local minimum or maximum, giving $\frac{\partial \chi}{\partial \xi} = 0$. As $\chi$ is written as a linear interpolate, the nodes adjacent to those on the axis of symmetry must have the same functional values. This allows for quadratic interpolation to be used at these nodes,

$$\chi(\xi \in [0, \xi_2]) \approx \chi_1 \left( 1 - \frac{\xi^2}{\Delta_1^2} \right) + \chi_2 \left( \frac{\xi^2}{\Delta_1^2} \right),$$

$$\chi(\xi \in [\xi_{N-1}, \xi_N]) \approx \chi_{N-1} \left( \frac{(\xi_N - \xi)^2}{\Delta_{N-1}^2} \right) + \chi_N \left( 1 - \frac{(\xi_N - \xi)^2}{\Delta_{N-1}^2} \right). \tag{2.5.2}$$

A system of linear equations can now be constructed using all the nodes at $\xi_j$, $j = 1...n$,

giving the coefficient matrix $G_{j,k}$ as,

$$\begin{aligned}
G_{j,1} &= 2\int_0^{\xi_2}\left(1-\frac{\xi^2}{\xi_2^2}\right)m_{1,j}\sqrt{\frac{r_1\left(r_1'^2+z_1'^2\right)}{r_j}}K\left(m_{1,j}\right)d\xi,\\
G_{j,2} &= 2\int_0^{\xi_2}\left(\frac{\xi^2}{\xi_2^2}\right)m_{1,j}\sqrt{\frac{r_1\left(r_1'^2+z_1'^2\right)}{r_j}}K\left(m_{1,j}\right)d\xi\\
&\quad +2\int_{\xi_2}^{\xi_3}\left(\frac{\xi^3-\xi}{\Delta_2}\right)m_{2,j}\sqrt{\frac{r_2\left(r_2'^2+z_2'^2\right)}{r_j}}K\left(m_{2,j}\right)d\xi,\\
G_{j,k} &= 2\int_{\xi_{k-1}}^{\xi_k}\left(\frac{\xi-\xi_{k-1}}{\Delta_{k-1}}\right)m_{k-1,j}\sqrt{\frac{r_{k-1}\left(r_{k-1}'^2+z_{k-1}'^2\right)}{r_j}}K\left(m_{k-1,j}\right)d\xi\\
&\quad +2\int_{\xi_k}^{\xi_{k+1}}\left(\frac{\xi^{k+1}-\xi}{\Delta_k}\right)m_{k,j}\sqrt{\frac{r_k\left(r_k'^2+z_k'^2\right)}{r_j}}K\left(m_{k,j}\right)d\xi,\\
G_{j,n-1} &= 2\int_{\xi_{n-2}}^{\xi_{n-1}}\left(\frac{\xi-\xi_{n-2}}{\Delta_{n-2}}\right)m_{n-2,j}\sqrt{\frac{r_{n-2}\left(r_{n-2}'^2+z_{n-2}'^2\right)}{r_j}}K\left(m_{n-2,j}\right)d\xi\\
&\quad +2\int_{\xi_{n-1}}^{\xi_n}\left(\frac{\left(\xi^n-\xi\right)^2}{\Delta_{n-1}^2}\right)m_{n-1,j}\sqrt{\frac{r_{n-1}\left(r_{n-1}'^2+z_{n-1}'^2\right)}{r_j}}K\left(m_{n-1,j}\right)d\xi,\\
G_{j,n} &= 2\int_{\xi_{n-1}}^{\xi_n}\left(1-\frac{\left(\xi_n-\xi\right)^2}{\Delta_{n-1}^2}\right)m_{n-1,j}\sqrt{\frac{r_{n-1}\left(r_{n-1}'^2+z_{n-1}'^2\right)}{r_j}}K\left(m_{n-1,j}\right)d\xi.
\end{aligned} \tag{2.5.3}$$

Similarly, equations of the type seen in (2.4.13) can be approximated linearly with regards to the attached potentials. Although, the spline approximations can be used if $\chi$ is known a priori, when using $n$ nodes located at $\xi_j$ a vector can be made with the following type

$$\begin{aligned}
\int_{\partial\Omega}\frac{\partial G}{\partial n}\chi_j dS = \sum_{k=1}^{n-1}\Bigg(&\int_{\xi_k}^{\xi_{k+1}}\frac{m_{k,j}\chi_k}{\left(r_k r_j\right)^{\frac{1}{2}}}\left(z_k'+\frac{m_{k,j}^2\left[z_k'\left(r_k-r_j\right)-r_k'\left(z_k-z_j\right)\right]}{2r_j}\right)\frac{E\left(m_{k,j}\right)}{1-m_{k,j}^2}d\xi\\
&-\int_{\xi_k}^{\xi_{k+1}}\frac{z_k' m_{k,j}\chi_k}{\left(r_k r_j\right)^{\frac{1}{2}}}K\left(m_{k,j}\right)d\xi\Bigg).
\end{aligned} \tag{2.5.4}$$

## 2.6 Compiling the Equations in Matrix Form

The Green's integral formula from equation (2.4.1) now needs to be put in the context of the three fluid system shown in the model geometry 2.1. As before, the nodes $\mathbf{x}_0, \mathbf{x}$ on the bubble surface in fluid 1 are represented by $\mathbf{b}, \mathbf{c}$, on the bubble surface in fluid 2 by $\mathbf{d}, \mathbf{e}$, on interface $A$ by $\mathbf{p}, \mathbf{q}$, and interface $B$ by $\mathbf{r}, \mathbf{s}$. When considering the velocity potential at a node $\mathbf{b}$ on the surface of a bubble in fluid 1, the boundary of the fluid domain $\partial\Omega$ consists of the nodes that are along interface $A$, $\partial I_A$, the nodes along the second interface $B$, $\partial I_B$ and the other nodes on the bubble surface, $\partial B$. If there are $NB > 1$ bubbles in fluid 1, the nodes along each $k$th bubble must be includes, $\partial B_k$. Therefore, the Green's integral formula gives the expression

$$\begin{aligned} 2\pi\phi_1(\mathbf{b}) = & \int_{\partial I_A} \left( G(\mathbf{b},\mathbf{q}) \frac{\partial \phi_1}{\partial n_1}(\mathbf{q}) - \frac{\partial G}{\partial n_1}(\mathbf{b},\mathbf{q}) \phi_1(\mathbf{q}) \right) dS(\mathbf{q}) \\ + & \int_{\partial I_B} \left( G(\mathbf{b},\mathbf{s}) \frac{\partial \phi_1}{\partial n_1}(\mathbf{s}) - \frac{\partial G}{\partial n_1}(\mathbf{b},\mathbf{s}) \phi_1(\mathbf{s}) \right) dS(\mathbf{s}) \\ + & \sum_{k=1}^{NB} \int_{\partial B_k} \left( G(\mathbf{b},\mathbf{c}) \frac{\partial \phi_1}{\partial n_1}(\mathbf{c}) - \frac{\partial G}{\partial n_1}(\mathbf{b},\mathbf{c}) \phi_1(\mathbf{b}) \right) dS(\mathbf{c}). \end{aligned} \quad (2.6.1)$$

Once the equation has been discretised, the surfaces of the $NB$ bubbles can be represented in one integral over a single bubble surface $B_i$ in each fluid layer $i$. Thus, removing the need for a summation sign in the above expression. Equation (2.6.1) can be further simplified by considering the normal velocity balance at the fluid-fluid interfaces,

$$\frac{\partial \phi_1}{\partial n_2} = \frac{\partial \phi_2}{\partial n_2}, \quad \frac{\partial \phi_1}{\partial n_3} = \frac{\partial \phi_3}{\partial n_3}. \quad (2.6.2)$$

The fluid potentials can be rewritten using the notation from equation (2.2.3) and introducing,

$$
\begin{aligned}
F_A(\mathbf{p}) &= \phi_A(\mathbf{p})(1-\rho_A) + \mu_A(\mathbf{p})(1+\rho_A) \\
F_B(\mathbf{r}) &= \phi_B(\mathbf{r})(1-\rho_B) + \mu_B(\mathbf{r})(1+\rho_B),
\end{aligned}
$$

giving the expressions

$$
\begin{aligned}
\phi_1 &= \phi_A \frac{\rho_A}{1+\rho_A} + F_A \frac{1}{2(1+\rho_A)} = \phi_B \frac{\rho_B}{1+\rho_B} + F_B \frac{1}{2(1+\rho_B)}, \\
\phi_2 &= \phi_A \frac{1}{1+\rho_A} - F_A \frac{1}{2(1+\rho_A)}, \\
\phi_3 &= \phi_B \frac{1}{1+\rho_B} - F_B \frac{1}{2(1+\rho_B)}.
\end{aligned}
$$

Equation (2.6.1) can now be written as

$$
\begin{aligned}
2\pi\phi_1(\mathbf{b}) &= \int_{\partial B_1} \left( G(\mathbf{b},\mathbf{c}) \frac{\partial \phi_1}{\partial n_1}(\mathbf{c}) - \frac{\partial G}{\partial n_1}(\mathbf{b},\mathbf{c}) \phi_1(\mathbf{c}) \right) dS(\mathbf{c}) \\
&+ \int_{\partial I_A} \left( -G(\mathbf{b},\mathbf{q}) \frac{\partial \phi_2}{\partial n_2}(\mathbf{q}) + \frac{\partial G}{\partial n_2}(\mathbf{b},\mathbf{q}) \left( \phi_A(\mathbf{q}) \frac{\rho_A}{1+\rho_A} + F_A(\mathbf{q}) \frac{1}{2(1+\rho_A)} \right) \right) dS(\mathbf{q}) \\
&+ \int_{\partial I_B} \left( -G(\mathbf{b},\mathbf{s}) \frac{\partial \phi_3}{\partial n_3}(\mathbf{s}) + \frac{\partial G}{\partial n_3}(\mathbf{b},\mathbf{s}) \left( \phi_B(\mathbf{s}) \frac{\rho_B}{1+\rho_B} + F_B(\mathbf{s}) \frac{1}{2(1+\rho_B)} \right) \right) dS(\mathbf{s}).
\end{aligned}
$$

A similar expression is given for the potential in fluid 2, except there is no integral for the second fluid-fluid interface as the domain of fluid 2 is not bordered by $I_B$,

$$
\begin{aligned}
2\pi\phi_1(\mathbf{d}) &= \int_{\partial B_2} \left( G(\mathbf{d},\mathbf{e}) \frac{\partial \phi_2}{\partial n_2}(\mathbf{e}) - \frac{\partial G}{\partial n_2}(\mathbf{d},\mathbf{e}) \phi_2(\mathbf{e}) \right) dS(\mathbf{e}) \\
&+ \int_{\partial I_A} \left( G(\mathbf{d},\mathbf{q}) \frac{\partial \phi_2}{\partial n_2}(\mathbf{q}) - \frac{\partial G}{\partial n_2}(\mathbf{d},\mathbf{q}) \left( \phi_A(\mathbf{q}) \frac{1}{1+\rho_A} - F_A(\mathbf{q}) \frac{1}{2(1+\rho_A)} \right) \right) dS(\mathbf{q}).
\end{aligned}
$$

On fluid-fluid interface $A$ between fluids 1 and 2 two expressions are given,

$$\begin{aligned}
2\pi\phi_A(\mathbf{p}) &= \int_{\partial B_1}\left(G(\mathbf{p},\mathbf{c})\frac{\partial\phi_1}{\partial n_1}(\mathbf{c})-\frac{\partial G}{\partial n_1}(\mathbf{p},\mathbf{c})\phi_1(\mathbf{c})\right)dS(\mathbf{c})\\
&+ \int_{\partial B_2}\left(G(\mathbf{p},\mathbf{e})\frac{\partial\phi_2}{\partial n_2}(\mathbf{e})-\frac{\partial G}{\partial n_2}(\mathbf{p},\mathbf{e})\phi_2(\mathbf{e})\right)dS(\mathbf{e})\\
&- \int_{\partial I_A}\left(\frac{\partial G}{\partial n_2}(\mathbf{p},\mathbf{q})\left(-F_A(\mathbf{q})\frac{1}{1+\rho_A}+\phi_A(\mathbf{q})\frac{1-\rho_A}{1+\rho_A}\right)\right)dS(\mathbf{q})\\
&+ \int_{\partial I_B}\left(-G(\mathbf{p},\mathbf{s})\frac{\partial\phi_3}{\partial n_3}(\mathbf{s})+\frac{\partial G}{\partial n_3}(\mathbf{p},\mathbf{s})\left(\phi_B(\mathbf{s})\frac{\rho_B}{1+\rho_B}+F_B(\mathbf{s})\frac{1}{2(1+\rho_B)}\right)\right)dS(\mathbf{s}),
\end{aligned}$$

$$\begin{aligned}
2\pi\left(\frac{F_A(\mathbf{p})}{1+\rho_A}-\phi_A(\mathbf{p})\frac{1-\rho_A}{1+\rho_A}\right) &= \int_{\partial B_1}\left(G(\mathbf{p},\mathbf{c})\frac{\partial\phi_1}{\partial n_1}(\mathbf{c})-\frac{\partial G}{\partial n_1}(\mathbf{p},\mathbf{c})\phi_1(\mathbf{c})\right)dS(\mathbf{c})\\
&- \int_{\partial B_2}\left(G(\mathbf{p},\mathbf{e})\frac{\partial\phi_2}{\partial n_2}(\mathbf{e})-\frac{\partial G}{\partial n_2}(\mathbf{p},\mathbf{e})\phi_2(\mathbf{e})\right)dS(\mathbf{e})\\
&+ \int_{\partial I_A}\left(-2G(\mathbf{p},\mathbf{q})\frac{\partial\phi_2}{\partial n_2}(\mathbf{q})+\frac{\partial G}{\partial n_2}(\mathbf{p},\mathbf{q})\phi_A\right)dS(\mathbf{q})\\
+\int_{\partial I_B}\left(-G(\mathbf{p},\mathbf{s})\frac{\partial\phi_3}{\partial n_3}(\mathbf{s})+\frac{\partial G}{\partial n_3}(\mathbf{p},\mathbf{s})\left(\phi_B(\mathbf{s})\frac{\rho_B}{1+\rho_B}+F_B(\mathbf{s})\frac{1}{2(1+\rho_B)}\right)\right)dS(\mathbf{s}).
\end{aligned}$$

Similarly on fluid-fluid interface $B$ the two equations are

$$\begin{aligned}
2\pi\phi_B(\mathbf{r}) = &\int_{\partial B_1}\left(G(\mathbf{r},\mathbf{c})\frac{\partial\phi_1}{\partial n_1}(\mathbf{c})-\frac{\partial G}{\partial n_1}(\mathbf{r},\mathbf{c})\phi_1(\mathbf{c})\right)dS(\mathbf{c})\\
&+ \int_{\partial I_A}\left(-G(\mathbf{r},\mathbf{q})\frac{\partial\phi_2}{\partial n_2}(\mathbf{q})+\frac{\partial G}{\partial n_2}(\mathbf{r},\mathbf{q})\left(\phi_A(\mathbf{q})\frac{\rho_A}{1+\rho_A}+F_A(\mathbf{q})\frac{1}{2(1+\rho_A)}\right)\right)dS(\mathbf{q})\\
&- \int_{\partial I_B}\left(\frac{\partial G}{\partial n_3}(\mathbf{r},\mathbf{s})\left(-F_B(\mathbf{s})\frac{1}{1+\rho_B}+\phi_B(\mathbf{s})\frac{1-\rho_B}{1+\rho_B}\right)\right)dS(\mathbf{s}),
\end{aligned}$$

$$2\pi\left(\frac{F_B(\mathbf{r})}{1+\rho_B}-\phi_B(\mathbf{r})\frac{1-\rho_B}{1+\rho_B}\right)=\int_{\partial B_1}\left(G(\mathbf{r},\mathbf{c})\frac{\partial\phi_1}{\partial n_1}(\mathbf{c})-\frac{\partial G}{\partial n_1}(\mathbf{r},\mathbf{c})\phi_1(\mathbf{c})\right)dS(\mathbf{c})$$
$$+\int_{\partial I_A}\left(-G(\mathbf{r},\mathbf{q})\frac{\partial\phi_2}{\partial n_2}(\mathbf{q})+\frac{\partial G}{\partial n_2}(\mathbf{r},\mathbf{q})\left(\phi_A(\mathbf{q})\frac{\rho_A}{1+\rho_A}+F_A(\mathbf{q})\frac{1}{2(1+\rho_A)}\right)\right)dS(\mathbf{q})$$
$$+\int_{\partial I_B}\left(-2G(\mathbf{r},\mathbf{s})\frac{\partial\phi_3}{\partial n_3}(\mathbf{s})+\frac{\partial G}{\partial n_3}(\mathbf{r},\mathbf{s})\phi_B\right)dS(\mathbf{s}).$$

These equations are now discretised using,

$$\int_{\partial\Omega}G(\mathbf{x},\mathbf{x}_0)\frac{\partial\phi}{\partial n_i}(\mathbf{x})\,dS(\mathbf{x})\approx G_{x_0,x}\frac{\partial\boldsymbol{\phi}(\mathbf{x}_0)}{\partial n_i},\tag{2.6.3}$$
$$\int_{\partial\Omega}\phi(\mathbf{x})\frac{\partial G(\mathbf{x},\mathbf{x}_0)}{\partial n_i}dS(\mathbf{x})\approx DG_{x_0,x}\boldsymbol{\phi}(\mathbf{x}_0),\tag{2.6.4}$$

where $G$ and $DG$ are the coefficient matrices that account for the interpolation of the known and unknown functions along the surfaces. The discrete values of the potentials and normal potential derivatives at the node $\mathbf{x}_0$ are in vectors $\boldsymbol{\phi}$ and $\frac{\partial\boldsymbol{\phi}(\mathbf{x}_0)}{\partial n_i}$ respectively. This can now be written as a matrix of equations for the unknown potentials and their normal derivatives in terms of the known variables.

$$
\begin{bmatrix}
G_{bc} & 0 & -G_{bq} & -G_{bs} & \frac{\rho_A}{1+\rho_A}DG_{bq} & \frac{\rho_B}{1+\rho_B}DG_{bs} \\
0 & G_{de} & G_{dq} & 0 & \frac{-1}{1+\rho_A}DG_{dq} & 0 \\
G_{pc} & G_{pe} & 0 & -G_{ps} & \frac{\rho_A-1}{\rho_A+1}DG_{pq} - 2\pi I_{pq} & \frac{\rho_B}{1+\rho_B}DG_{ps} \\
G_{pc} & -G_{pe} & -2G_{pq} & -G_{ps} & DG_{pq} + 2\pi\frac{1-\rho_A}{1+\rho_A}I_{pq} & \frac{\rho_B}{1+\rho_B}DG_{ps} \\
G_{rc} & 0 & -G_{rq} & 0 & \frac{\rho_A}{1+\rho_A}DG_{rq} & \frac{\rho_B-1}{\rho_B+1}DG_{rs} - 2\pi I_{rs} \\
G_{rc} & 0 & -G_{rq} & -2G_{rs} & \frac{\rho_A}{1+\rho_A}DG_{rq} & DG_{rs} + 2\pi\frac{1-\rho_B}{1+\rho_B}I_{rs}
\end{bmatrix}
\begin{bmatrix}
\frac{\partial\phi_1(\mathbf{c})}{\partial n_1} \\
\frac{\partial\phi_2(\mathbf{e})}{\partial n_2} \\
\frac{\partial\phi_2(\mathbf{q})}{\partial n_2} \\
\frac{\partial\phi_3(\mathbf{s})}{\partial n_3} \\
\phi_A(\mathbf{q}) \\
\phi_B(\mathbf{s})
\end{bmatrix}
$$

$$
= \begin{bmatrix}
2\pi I_{bc} + DG_{bc} & 0 & \frac{-1}{2+2\rho_A}DG_{bq} & \frac{1}{2+2\rho_B}DG_{bs} \\
0 & 2\pi I_{de} + DG_{de} & \frac{-1}{2+2\rho_A}DG_{dq} & 0 \\
DG_{pc} & DG_{pe} & \frac{-1}{1+\rho_A}DG_{pq} & \frac{-1}{2+2\rho_B}DG_{ps} \\
DG_{pc} & -DG_{pe} & 2\pi\frac{1}{1+\rho_A}I_{pq} & \frac{-1}{2+2\rho_B}DG_{ps} \\
DG_{rc} & 0 & \frac{-1}{2+2\rho_A}DG_{rq} & \frac{-1}{1+\rho_B}DG_{rs} \\
DG_{rc} & 0 & \frac{-1}{2+2\rho_A}DG_{rq} & 2\pi\frac{1}{1+\rho_B}I_{rs}
\end{bmatrix}
\begin{bmatrix}
\phi_1(\mathbf{c}) \\
\phi_2(\mathbf{e}) \\
F_A(\mathbf{q}) \\
F_B(\mathbf{s})
\end{bmatrix}. \tag{2.6.5}
$$

Both sides of equation (2.6.5) have dimension $(N_{b1} + N_{b2} + 2N_{pA} + 2N_{pB}, 1)$, where $N_{bi}$ are the number of nodes on the surface of bubbles in fluid $i$, and $N_{pA}$ and $N_{pB}$ and the number of nodes on interfaces $I_A$ and $I_B$ respectively. This system of equations can now be solved to find the vector of unknown variables, which is the second term on the left hand side. With these variables known it is now possible to calculate the components of the kinematic and dynamic boundary conditions. By incorporating a time step $dt$ and using $\mathbf{u} = \nabla\phi = \frac{d\mathbf{x}}{dt}$, the surfaces can be advanced forward in time with a fourth order Runge-Kutta method.

## 2.7 Quintic Spline Interpolation

The previous equations tell us the positions of the nodes along the surfaces, along with the velocity potential and the normal derivative at these points. But to model the surfaces completely this information also needs to be known along the surface between these collocation points, this is achieved by incorporating polynomial spline interpolation. Spline interpolation fits a polynomial of degree $\widehat{n}$ between two adjacent nodes to approximate the surface section, using the function values and their derivatives to find the polynomial's coefficients. By assuming continuity along the surface, linear equations are established to link the unknown $\widehat{n}-1$ derivatives at the $n$ nodes. In the work by Taib [56] linear and quadratic splines are used for interpolating the surface, allowing for accurate results and remaining relatively computationally cheap.

In this thesis quintic splines will be used, as the increase in computational time is out weighed by the gain in accuracy. The increase in the polynomial degree will mean additional coefficients of the polynomial will need to be determined. However, a more accurate representation of the splined surface is achieved at both fist and second derivative. This ensures there is less noise formed on the bubble surface, which becomes a large problem surface tension or external pressure fields are included in the model [18]. As mentioned in section 2.2, this accuracy to second derivative allows for the surfaces to be sufficiently smooth enough to give values for the collocation coefficients $c(\mathbf{x}_0)$ in equation (2.4.2). For each spline segment six polynomial coefficients need to be determined, so the quintic polynomial is

$$q_i(\xi) = \sum_{k=0}^{5} a_{i,k}\xi^k, \quad i = 1, ...n-1. \tag{2.7.1}$$

The second derivative of the quintic spline behaves as a cubic and is labelled $q_i''(\xi_i) = N_i$ at the nodes. Differentiating twice more gives the fourth derivative which is a linear

polynomial, using a similar label as before, $q_i^{iv}(\xi_i) = M_i$ at the nodes, the interpolation of the fourth derivative can be written as

$$q_i^{iv}(\xi) = \frac{M_i(\xi_{i+1} - \xi) + M_{i+1}(\xi - \xi_i)}{\xi_{i+1} - \xi_i}. \tag{2.7.2}$$

Integrating (2.7.2) twice with respect to $\xi$ gives an equation for the interpolation of the second derivative in terms of the fourth derivatives at the collocation points,

$$q_i''(\xi) = \frac{M_i(\xi_{i+1} - \xi)^3 + M_{i+1}(\xi - \xi_i)^3}{6(\xi_{i+1} - \xi_i)} + A_i(\xi - \xi_i) + B_i(\xi_{i+1} - \xi). \tag{2.7.3}$$

Equating this equation at $\xi = \xi_i$ with the second derivative at the nodes, $N_i$, gives an expression for $B_i$. Using $\Delta_i = (\xi_{i+1} - \xi_i)$ it is written as

$$N_i = \frac{M_i\Delta_i^2}{6} + B_i\Delta_i \implies B_i = \frac{6N_i - M_i\Delta_i^2}{6\Delta_i}. \tag{2.7.4}$$

Similarly at $\xi = \xi_{i+1}$ using $N_{i+1}$, an expression for $A_i$ is given as

$$A_i = \frac{6N_{i+1} - M_{i+1}\Delta_i^2}{6\Delta_i}. \tag{2.7.5}$$

Substituting in these expressions for coefficients $A_i$ and $B_i$ into equation (2.7.3) and integrating twice gives the equation for the $i$th quintic spline as

$$\begin{aligned} q_i(\xi) &= \frac{M_i(\xi_{i+1} - \xi)^5 + M_{i+1}(\xi - \xi_i)^5}{120(\xi_{i+1} - \xi_i)} + \left(\frac{6N_{i+1} - M_{i+1}\Delta_i^2}{36\Delta_i}\right)(\xi - \xi_i)^3 \\ &+ \left(\frac{6N_i - M_i\Delta_i^2}{36\Delta_i}\right)(\xi_{i+1} - \xi)^3 + C_i(\xi - \xi_i) + D_i(\xi_{i+1} - \xi). \end{aligned}$$

Continuity of the functions and their second and fourth derivatives allows the $6n$ polynomial coefficients to be found from $3n$ variables, with $n$ of these variables coming from the

known discrete function values $q_i(\xi_i) = Q_i$. Using this discrete function value along with the known value from the adjacent node, $q_i(\xi_{i+1}) = Q_{i+1}$, coefficients $C_i$ and $D_i$ can be expressed as

$$D_i = \frac{Q_i}{\Delta_i} + \frac{7M_i\Delta_i^3}{360} - \frac{N_i\Delta_i}{6}$$
$$C_i = \frac{Q_{i+1}}{\Delta_i} + \frac{7M_{i+1}\Delta_i^3}{360} - \frac{N_{i+1}\Delta_i}{6}$$

Substituting these into the equation for the quintic spline segment above gives

$$\begin{aligned} q_i(\xi) &= \frac{M_i(\xi_{i+1}-\xi)^5 + M_{i+1}(\xi-\xi_i)^5}{120(\xi_{i+1}-\xi_i)} + \left(\frac{6N_{i+1} - M_{i+1}\Delta_i^2}{36\Delta_i}\right)(\xi-\xi_i)^3 \\ &+ \left(\frac{6N_i - M_i\Delta_i^2}{36\Delta_i}\right)(\xi_{i+1}-\xi)^3 \\ &+ \left(\frac{Q_{i+1}}{\Delta_i} + \frac{7M_{i+1}\Delta_i^3}{360} - \frac{N_{i+1}\Delta_i}{6}\right)(\xi-\xi_i) + \left(\frac{Q_i}{\Delta_i} + \frac{7M_i\Delta_i^3}{360} - \frac{N_i\Delta_i}{6}\right)(\xi_{i+1}-\xi). \end{aligned}$$

Equating the coefficients of this equation to those in equation (2.7.1) gives

$$
\begin{aligned}
a_{i,5} &= \frac{M_{i+1}-M_i}{120\Delta_i} \\
a_{i,4} &= \frac{M_i\xi_{i+1}-M_{i+1}\xi_i}{24\Delta_i} \\
a_{i,3} &= \frac{M_{i+1}\xi_i^2-M_i\xi_{i+1}^2}{12\Delta_i}+\frac{6\left(N_{i+1}-N_i\right)+\Delta_i^2\left(M_i-M_{i+1}\right)}{36\Delta_i} \\
a_{i,2} &= \frac{M_i\xi_{i+1}^3-M_{i+1}\xi_i^3}{12\Delta_i}+\frac{\xi_{i+1}\left(6N_i-M_i\Delta_i^2\right)-\xi_i\left(6N_{i+1}-M_{i+1}\Delta_i^2\right)}{12\Delta_i} \\
a_{i,1} &= \frac{M_{i+1}\xi_i^4-M_i\xi_{i+1}^4}{24\Delta_i}+\frac{\xi_i^2\left(6N_{i+1}-M_{i+1}\Delta_i^2\right)-\xi_{i+1}^2\left(6N_i-M_i\Delta_i^2\right)}{12\Delta_i} \\
&+ \left(\frac{Q_{i+1}}{\Delta_i}+\frac{7M_{i+1}\Delta_i^3}{360}-\frac{N_{i+1}\Delta_i}{6}\right)-\left(\frac{Q_i}{\Delta_i}+\frac{7M_i\Delta_i^3}{360}-\frac{N_i\Delta_i}{6}\right) \\
a_{i,0} &= \frac{M_i\xi_i^5-M_{i+1}\xi_{i+1}^5}{120\Delta_i}+\frac{\xi_{i+1}^3\left(6N_i-M_i\Delta_i^2\right)-\xi_i^3\left(6N_{i+1}-M_{i+1}\Delta_i^2\right)}{12\Delta_i} \\
&- \xi_i\left(\frac{Q_{i+1}}{\Delta_i}+\frac{7M_{i+1}\Delta_i^3}{360}-\frac{N_{i+1}\Delta_i}{6}\right)+\xi_{i+1}\left(\frac{Q_i}{\Delta_i}+\frac{7M_i\Delta_i^3}{360}-\frac{N_i\Delta_i}{6}\right).
\end{aligned}
\tag{2.7.6}
$$

The problem of determining the $6n$ polynomial coefficients has now been reduced to finding the $2n$ unknowns $N_i$ and $M_i$ with $i = 1, ..., n$. Continuity of the first and third derivative provides $2n - 4$ equations for these unknowns, the final four unknowns are established at nodes 1 and $n$. Differentiating (2.7.1) three times, and equating adjacent spline segments at node $i$ yields

$$
60a_{i,5}\xi_i^2+24a_{i,4}\xi_i+6a_{i,3}=60a_{i-1,5}\xi_i^2+24a_{i-1,4}\xi_i+6a_{i-1,3}, \quad i=2,...,n-1. \tag{2.7.7}
$$

Substituting in the expressions for the polynomial coefficients from (2.7.6) and rearranging gives half the equations that need to be solved for the unknown derivatives,

$$0 = M_i \frac{\Delta_i + \Delta_{i-1}}{3} + \frac{M_{i+1}\Delta_i}{6} + \frac{M_{i-1}\Delta_{i-1}}{6} + N_i \left( \frac{1}{\Delta_{i-1}} + \frac{1}{\Delta_i} \right) - \frac{N_{i-1}}{\Delta_{i-1}} - \frac{N_{i+1}}{\Delta_i}.$$

Similarly, continuity of the first derivative of (2.7.1) at nodes $i = 2..n-1$ gives

$$5a_{i,5}\xi_i^4 + 4a_{i,4}\xi_i^3 + 3a_{i,3}\xi_i^2 + 2a_{i,2}\xi_i + a_{i,1} = 5a_{i-1,5}\xi_i^4 + 4a_{i-1,4}\xi_i^3 + 3a_{i-1,3}\xi_i^2 + 2a_{i-1,2}\xi_i + a_{i-1,1}.$$

Substituting in the expressions in (2.7.6) gives the remaining simultaneous equations

$$\begin{aligned} \frac{Q_{i+1} - Q_i}{\Delta_i} + \frac{Q_{i-1} - Q_i}{\Delta_{i-1}} = &-M_i \frac{\Delta_i^3 + \Delta_{i-1}^3}{45} - \frac{7M_{i+1}\Delta_i^3}{360} - \frac{7M_{i-1}\Delta_{i-1}^3}{360} \\ &+N_i \frac{\Delta_i + \Delta_{i-1}}{3} + \frac{N_{i+1}\Delta_i}{6} + \frac{N_{i-1}\Delta_{i-1}}{6}. \end{aligned}$$

These equations can be written in matrix form $\mathbf{Ax} = \mathbf{b}$ where $\mathbf{A}$ is a sparse banded matrix with a bandwidth of 6, this system of equations can then be solved using the Thomas algorithm. On the axis of symmetry the first and third derivatives of the velocity potential and normal velocities must be zero due to the axisymmetric nature of the model. When the bubble becomes toroidal the surface spline becomes a closed curve, therefore the first node is also the last node making all derivatives continuous at the end of the loop, giving $2n$ unknowns with $2n$ equations.

## 2.8 Far Field Approximations

For the boundary integral method, it is assumed that the two fluid-fluid interfaces extend to infinity, though only a finite number of collocation points can be used. Therefore in the far field it is assumed that the velocity potentials $\phi_1$, $\phi_2$ and $\phi_3$ decay approximately as $O\left(\frac{1}{|\mathbf{r}_0|}\right)$, where $\mathbf{r}_0$ is the distance from the bubbles being modelled. Thus $F_A$, $F_B$, $\phi_A$, $\phi_B$,

$\mu_A$ and $\mu_B$ all decay in the same way. This allows for a least squares approximation to be taken for the surfaces as they extend to infinity. An additional node $N_{pA+1}$ is introduced on interface $I_A$ with a fixed position in $r$, an approximation is taken at this point for the values of $F_A$, $\phi_A$, $\frac{\partial \phi_2}{\partial n_2}$ and $z$, with similar approximations for node $N_{pB+1}$ on interface $I_B$. For brevity, the notation $N_{p+1}$ will be used to represent the additional node for the following equations, which will be applied to each fluid-fluid interface independently. The functions are assumed to be of the form $\chi \approx a + \frac{b}{R} + \frac{c}{R^3}$, where $R = \sqrt{r^2 + (z - z_c)}$ and $(0, z_c)$ is the location of the bubble centroid. For multiple bubbles the linear approximation is taken for each bubble then averaged over the number of bubbles. The term $a$ in the linear approximation allows for the functions to tend to a constant, as opposed to 0, which is applicable for finding an expression for $z$ on interface $B$. Also, when the density ratio across both interfaces is relatively high the movement of the interfaces becomes more restricted causing a greater radial flow in the $r$-direction, therefore the velocity potentials and linear combinations of the potentials will no longer tend to 0 as $R$ tends to infinity. This becomes more apparent when considering the extreme of a bubble between two infinite rigid plates, $\rho_A = \rho_B = \infty$, as shown by Leighton [35] and Ishida et al. [15].

The least squares fit is employed through $\alpha$ surface nodes to find unknown coefficients $a$, $b$ and $c$ to minimise,

$$\sum_{k=N_p-\alpha}^{N_p} \left( \chi\left(R_k\right) - \left( a + \frac{b}{R_k} + \frac{c}{R_k^3} \right) \right)^2 . \tag{2.8.1}$$

To minimise this expression, equation (2.8.1) is differentiated with respect to each unknown to give the following system of equations,

$$
\begin{aligned}
0 &= \sum_{k=N_p-\alpha}^{N_p} \left( a + \frac{b}{R_k} + \frac{c}{R_k^3} - \chi_k \right), \\
0 &= \sum_{k=N_p-\alpha}^{N_p} \left( \frac{a}{R_k} + \frac{b}{R_k^2} + \frac{c}{R_k^4} - \frac{\chi_k}{R_k} \right), \\
0 &= \sum_{k=N_p-\alpha}^{N_p} \left( \frac{a}{R_k^3} + \frac{b}{R_k^4} + \frac{c}{R_k^6} - \frac{\chi_k}{R_k^3} \right).
\end{aligned}
$$

Which can be written in matrix notation as,

$$
\begin{bmatrix}
\alpha + 1 & \sum_{k=N_p-\alpha}^{N_p} \frac{1}{R_k} & \sum_{k=N_p-\alpha}^{N_p} \frac{1}{R_k^3} \\
\sum_{k=N_p-\alpha}^{N_p} \frac{1}{R_k} & \sum_{k=N_p-\alpha}^{N_p} \frac{1}{R_k^2} & \sum_{k=N_p-\alpha}^{N_p} \frac{1}{R_k^4} \\
\sum_{k=N_p-\alpha}^{N_p} \frac{1}{R_k^3} & \sum_{k=N_p-\alpha}^{N_p} \frac{1}{R_k^4} & \sum_{k=N_p-\alpha}^{N_p} \frac{1}{R_k^6}
\end{bmatrix}
\begin{bmatrix} a \\ b \\ c \end{bmatrix}
=
\begin{bmatrix}
\sum_{k=N_p-\alpha}^{N_p} \chi_k \\
\sum_{k=N_p-\alpha}^{N_p} \frac{\chi_k}{R_k} \\
\sum_{k=N_p-\alpha}^{N_p} \frac{\chi_k}{R_k^3}
\end{bmatrix}. \tag{2.8.2}
$$

This can now be solved to find the vector of unknown coefficients, which can be substituted into equation (2.8.1) along with $\chi = z$ to give the $z$-coordinate at node $N_{p+1}$,

$$
z_{N_{p+1}} = a + \frac{b}{\sqrt{r_{N_{p+1}}^2 + \left(z_{N_{p+1}} - z_c\right)^2}} + \frac{c}{\left(r_{N_{p+1}}^2 + \left(z_{N_{p+1}} - z_c\right)^2\right)^{\frac{3}{2}}}. \tag{2.8.3}
$$

As $z_{N_{p+1}}$ is a function of $r_{N_{p+1}}$ and itself a solution can be found iteratively. The remaining approximated functions can now be found by substituting the known value of $z_{N_{p+1}}$ into (2.8.2), then substituting the coefficients $a$, $b$, and $c$ into equation (2.8.1).

To find an expression for the surface beyond the node $N_{p+1}$ the first and second derivatives of $z$ and $r$ must be found and parametrised with respect to $\xi$. Differentiating equation

(2.8.3) gives the following expression for $z_r$,

$$\frac{dz}{dr} = -r\left(\frac{a}{R^3} + \frac{3b}{R^5}\right)\left(1 + (z - z_c)\left(\frac{a}{R^3} + \frac{3b}{R^5}\right)\right)^{-1}. \tag{2.8.4}$$

Applying the quotient rule now gives,

$$z_{rr} = \frac{vu_r - uv_r}{v^2}, \tag{2.8.5}$$

where

$$\begin{aligned}
u &= -r\left(\frac{a}{R^3} + \frac{3b}{R^5}\right), \\
v &= 1 + (z - z_c)\left(\frac{a}{R^3} + \frac{3b}{R^5}\right), \\
u_r &= -\left(\frac{a}{R^3} + \frac{3b}{R^5}\right) + (r + z_r(z - z_c))\left(\frac{3a}{R^5} + \frac{15b}{R^7}\right), \\
v_r &= z_r\left(\frac{a}{R^3} + \frac{3b}{R^5}\right) - (r + z_r(z - z_c))\left(\frac{3a}{R^5} + \frac{15b}{R^7}\right).
\end{aligned}$$

To determine the derivatives for the spline at $N_{p+1}$ the chain rule is applied to parametrise the equations in terms of $\xi$. By assuming the arc length with respect to $\xi$ satisfies $\sqrt{r_\xi^2 + z_\xi^2} = 1$ and writing the first derivative of $z$ as,

$$\frac{dz}{d\xi} = \frac{dz}{dr}\frac{dr}{d\xi}, \tag{2.8.6}$$

it can be shown that,

$$1 = \frac{dr}{d\xi}^2\left(\frac{dz}{dr} + 1\right) \quad \Rightarrow \quad \frac{dr}{d\xi} = \frac{1}{\sqrt{1 + \frac{dz}{dr}^2}}. \tag{2.8.7}$$

To find an expression for the second derivative equation (2.8.6) is differentiated to give,

$$\begin{aligned}\frac{d^2z}{d\xi^2} &= \frac{d}{d\xi}\left(\frac{dr}{d\xi}\frac{dz}{dr}\right) \\ &= \frac{dr}{d\xi}\frac{d}{dr}\left(\frac{dr}{d\xi}\frac{dz}{dr}\right) \\ &= \left(\frac{dr}{d\xi}\right)^2\frac{d^2z}{dr^2} + \frac{dr}{d\xi}\frac{dz}{dr}\frac{d}{dr}\left(\frac{dr}{d\xi}\right) \\ &= \left(\frac{dr}{d\xi}\right)^2\frac{d^2z}{dr^2} + \frac{dz}{dr}\left(\frac{d^2r}{d\xi^2}\right). \end{aligned} \tag{2.8.8}$$

The second derivative of $r$ is found by differentiating equation (2.8.7) with respect to $\xi$,

$$\frac{d^2r}{d\xi^2} = -\frac{\frac{dz}{d\xi}\frac{d^2z}{d\xi^2}}{\frac{dr}{d\xi}}. \tag{2.8.9}$$

Substitution of (2.8.9) into (2.8.8) gives,

$$\frac{d^2z}{d\xi^2} = \left(\frac{dr}{d\xi}\right)^2\frac{d^2z}{dr^2} - \frac{\frac{dz}{dr}\frac{dz}{d\xi}\frac{d^2z}{d\xi^2}}{\frac{dr}{d\xi}} \;\Rightarrow\; \frac{d^2z}{d\xi^2} = \frac{\frac{dr}{d\xi}\frac{d^2z}{dr^2}}{\frac{dr}{d\xi} + \frac{dz}{d\xi}\frac{dz}{dr}}. \tag{2.8.10}$$

Finally substituting the above into (2.8.9) gives the second derivative of $r$ as,

$$\frac{d^2r}{d\xi^2} = -\frac{\frac{dz}{d\xi}\frac{d^2z}{dr^2}}{\frac{dr}{d\xi} + \frac{dz}{d\xi}\frac{dz}{dr}}. \tag{2.8.11}$$

The far field can now be splined accurately with the discretised nodes $1, ..., N_p$ by the addition of node $N_{p+1}$.

## 2.9 Equations for the Toroidal Bubble

During the collapse phase of a bubble near an interface, it is not uncommon for a liquid jet to be formed about the axis. The jet is caused by pressure forming on one side of the bubble, forcing fluid toward the bubble centroid. When the jet tip reaches the opposite side the bubble is threaded and becomes toroidal, causing the fluid domain to go from

being simply connected to doubly connected and equation (2.4.1) to no longer have a unique solution. There are numerical techniques to overcome this problem mentioned previously, here the vortex ring model is implemented in the same manner as Wang et al. [59] and Zhang et al. [62].

### 2.9.1 Vortex Ring Calculations

To introduce the vortex ring into the model the potential velocity $\phi$ in the fluid is decomposed into two components: the ring potential created by the circulation generated from the threading of the bubble ring, $\psi_{vr}$, and the continuous remnant potential from the bubble surface, $\psi$,

$$\phi\left(r,z,t\right)=\psi_{vr}\left(r,s\right)+\psi\left(r,z,t\right). \tag{2.9.1}$$

The strength of the vortex ring comes from the circulation of the flow $\Gamma$ which is equal to the jump in potential across the contacting nodes at the time of impact. In axisymmetric coordinates this is given by the difference in velocity potential at the two nodes on the bubble surface that lie on the axis of symmetry,

$$\Gamma=\phi_N-\phi_1. \tag{2.9.2}$$

To change the bubble from being simply connected to the toroidal form after impact these two nodes, $\phi_1$ and $\phi_N$, are removed. The bubble surface is now found by interpolating through nodes $2,...,N-1$, as seen in figure 2.2. The nodes 2 and $N-1$ need to be sufficiently close to minimise the loss in bubble volume and potential energy during this evolution.

The ring is considered to be a circle with its centre at the axis of symmetry. The position of the ring is deemed to be unimportant as long as it is located within the toroidal bubble, though it is required that the ring does not come too close to the bubble surface

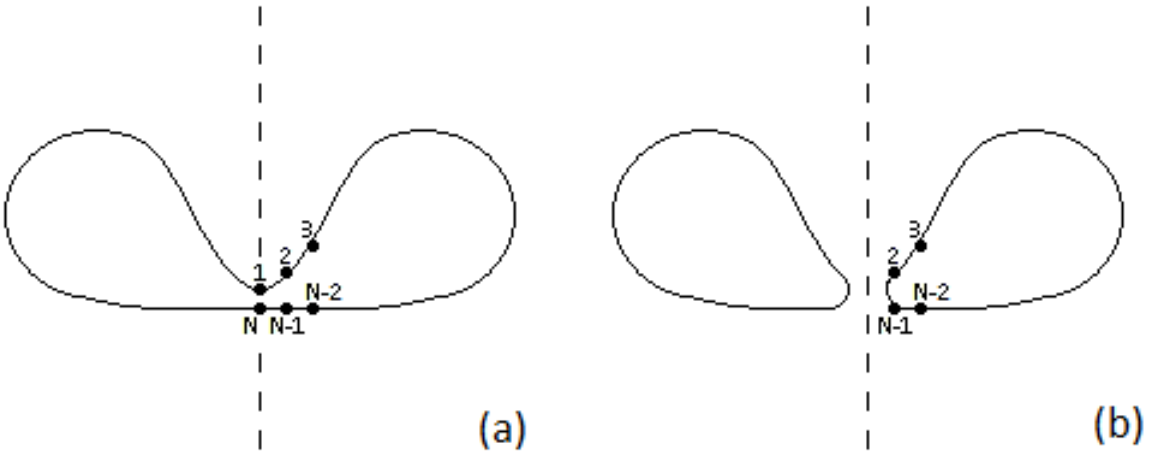


Figure 2.2: Removal of nodes to evolve the bubble from (a) before jet impact to (b) toroidal form.

to maintain stability.

To find the ring potential $\psi_{vr}$ on the bubble surface the Biot-Savart law [62, 59] is incorporated to calculate the velocity field at $\mathbf{x}_0 = (r_0, 0, z_0)$ formed by the vortex ring at $\mathbf{x}_{vr} = (r_{vr}, \theta, z_{vr})$,

$$\begin{aligned}
\frac{4\pi}{\Gamma}\mathbf{v}_{vr}\left(\mathbf{x}_0\right) &= \oint_{vr} d\mathbf{x}_{vr} \times \frac{\left(\mathbf{x}_0 - \mathbf{x}_{vr}\right)}{\left|\mathbf{x}_0 - \mathbf{x}_{vr}\right|^3} \\
&= \int_0^{2\pi} \frac{r_{vr}\mathbf{e}_r \times \left(r_0\cos\theta - r_{vr}, \theta, \left(z_0 - z_{vr}\right)\right)}{\left(\left(r_0 + r_{vr}\right)^2 + \left(z_0 - z_{vr}\right)^2 - 4r_0 r_{vr}\cos^2\left(\frac{\theta}{2}\right)\right)^{\frac{3}{2}}} \\
&= \int_0^{2\pi} \frac{r_{vr}\left(z_0 - z_{vr}\right)\mathbf{e}_r + r_{vr}\left(r_{vr} - r_0\cos\left(\theta\right)\right)\mathbf{e}_z}{R^3\left(1 - m^2\cos^2\left(\frac{\theta}{2}\right)\right)^{\frac{3}{2}}}.
\end{aligned} \tag{2.9.3}$$

Where $\mathbf{e}_r$ and $\mathbf{e}_z$ are unit vectors of cylindrical polar coordinates, $R^2 = \left(r_0 + r_{vr}\right)^2 + \left(z_0 - z_{vr}\right)^2$, and $m^2 = 4r_0 r_{vr} R^{-2}$. As before these integrals can be simplified using elliptic integrals of the first and second kind, $K\left(m\right)$ and $E\left(m\right)$ respectively, giving

$$\int_0^{2\pi} \frac{1}{\left(1-m^2\cos^2\left(\frac{\theta}{2}\right)\right)^{\frac{3}{2}}} d\theta = 4\frac{E(m)}{1-m^2}, \tag{2.9.4}$$

and

$$\begin{aligned}
\int_0^{2\pi} \frac{\cos(\theta)}{\left(1-m^2\cos^2\left(\frac{\theta}{2}\right)\right)^{\frac{3}{2}}} d\theta &= \int_0^{2pi} \frac{2\cos^2\left(\frac{\theta}{2}\right)-1}{\left(1-m^2\cos^2\left(\frac{\theta}{2}\right)\right)^{\frac{3}{2}}} d\theta \\
&= -\frac{2}{m^2}\int_0^{2\pi} \frac{\left(1-m^2\cos^2\left(\frac{\theta}{2}\right)\right)+\left(-1+\frac{1}{2}m^2\right)}{\left(1-m^2\cos^2\left(\frac{\theta}{2}\right)\right)^{\frac{3}{2}}} \\
&= \frac{1}{m^2}\left[-8K(m)+\left(8-4m^2\right)\frac{E(m)}{1-m^2}\right].
\end{aligned} \tag{2.9.5}$$

With no velocity in the $\theta$-direction the velocity field of the vortex ring can be written as $\mathbf{v}_{vr} = u_{vr}\mathbf{e}_r + w_{vr}\mathbf{e}_z$, where

$$u_{vr} = \frac{\Gamma r_{vr}(z-z_{vr})}{\pi R^3 m^2}\left(\left(2-m^2\right)\frac{E(m)}{1-m^2} - 2K(m)\right), \tag{2.9.6}$$

$$w_{vr} = \frac{\Gamma r_{vr}}{\pi R^3}\left(r_{vr}\frac{E(m)}{1-m^2} - \frac{r_0}{m^2}\left(\left(2-m^2\right)\frac{E(m)}{1-m^2} - 2K(m)\right)\right). \tag{2.9.7}$$

The solid angle formula can now be used to find the vortex potential $\psi_{vr}$ on most of the surfaces in the same manner as Zhang et al [62]

$$\psi_{vr}(\mathbf{x}) = \frac{\Gamma}{4\pi}\int_{S_c} \frac{\partial G(\mathbf{x},\mathbf{x}_{S_c})}{\partial n} dS(\mathbf{x}_{S_c}). \tag{2.9.8}$$

The surface of discontinuity $S_c$, which extends over the vortex ring, is taken to be a disc of radius $r_{vr}$ in the plane $z_{vr}$, given as $S_c = \{(r,\theta,z_{vr})\,|0 \leqslant r \leqslant r_{vr}, 0 \leqslant \theta < 2\pi\}$. So at the point $\mathbf{x}_0$,

$$\begin{aligned}
\psi_{vr}\left(\mathbf{x}_0\right) &= \frac{\Gamma}{4\pi}\int\limits_{S_c}\frac{\partial G\left(\mathbf{x}_0,\mathbf{x}_{S_c}\right)}{\partial n}dS\left(\mathbf{x}_{S_c}\right), \\
&= \frac{\Gamma}{4\pi}\int\limits_0^r r\int\limits_0^{2\pi}\frac{\partial}{\partial z}\frac{1}{\left|\mathbf{x}_{vr}-\mathbf{x}_0\right|}d\theta dr, \\
&= -\frac{\left(z_{vr}-z_0\right)\Gamma}{\pi}\int\limits_0^{r_{vr}}\frac{r}{R^3}\frac{E\left(m\right)}{\left(1-m^2\right)}dr. \qquad (2.9.9)
\end{aligned}$$

The vortex potential on the discontinuity forming across the disk $S_c$ can be calculated by using the properties of equation 2.9.9. The method by Curtis [17] exploits the existence of a point $r_{ex}=r_k\left(\xi_{ex}\right)$ on the side of the torus furthest from the axis, which has potential $\psi_{vr}\left(r_{ex},z_{vr}\right)$ equal to zero. Here $\xi_{ex}$ is the root of $z_k\left(\xi\right)-z_{vr}=0$, on the segment $k$ of the bubble toroid surface. A node is introduced at $\left(r_{ex},z_{vr}\right)$ temporarily, and the other nodes are reordered so $\left(r_{ex},z_{vr}\right)$ is the first node, and the potentials at $j>1$ can now be found by,

$$\psi_{vr}\left(r_j,z_j\right)=\int\limits_{\xi(j-1)}^{\xi(j)}\left(u_{vr}r'+w_{vr}z'\right)\sqrt{r'^2+z'^2}d\xi-\psi_{vr}\left(r_{j-1},z_{j-1}\right). \qquad (2.9.10)$$

A jump in potential now occurs at $\left(r_{ex},z_{vr}\right)$, so the circulation $\Gamma$ is subtracted from the potential of all nodes where $z_j>z_{vr}$, effectively mapping the jump in potential to the point $\left(r_{s_c},z_{vr}\right)$ where the discontinuity surface and the torus intersect.

Now the vortex potential is known, the remnant potential can be found for nodes $2,...,N-1$ by,

$$\psi\left(r_j,z_j\right)=\phi\left(r_j,z_j\right)-\psi_{vr}\left(r_j,z_j\right). \qquad (2.9.11)$$

On the fluid-fluid interfaces, the notation $F_A=\phi_A\left(1-\rho_A\right)+\mu\left(1+\rho_A\right)=2\phi_1-2\rho_A\phi_2$

is decomposed to give the new surface potentials,

$$\begin{aligned}
\psi_A &= \psi_1 + \psi_2 = \phi_1 + \phi_2 - \psi_{vr_1} - \psi_{vr_2}, \\
\psi_B &= \psi_1 + \psi_3 = \phi_1 + \phi_3 - \psi_{vr_1}, \\
\overline{\mu}_A &= \psi_1 - \psi_2 = \phi_1 - \phi_2 - \psi_{vr_1} + \psi_{vr_2}, \\
\overline{\mu}_B &= \psi_1 - \psi_3 = \phi_1 - \phi_3 - \psi_{vr_1}, \\
\overline{F}_A &= \psi_A (1 - \rho_A) + \overline{\mu}_A (1 + \rho_A) - 2\psi_{vr_1} + 2\rho_A \psi_{vr_2} \\
\overline{F}_B &= \psi_B (1 - \rho_B) + \overline{\mu}_B (1 + \rho_B) - 2\psi_{vr_1}
\end{aligned} \tag{2.9.12}$$

### 2.9.2 Boundary Conditions

The introduction of the vortex potential does not affect the far field conditions and the decomposed potentials still satisfy Laplace's equation. The inclusion of the vortex ring has to be shown in the boundary conditions on the bubble surfaces and the fluid-fluid interfaces.

As vortex ring potentials $\psi_{vr}$ are constant in time, the time derivatives on the surfaces remain the same,

$$\frac{\partial \phi}{\partial t} = \frac{\partial \psi}{\partial t}.$$

Therefore the substantial derivative on the bubble surfaces is given by,

$$\frac{D\phi_i}{Dt} = \frac{\partial \psi_i}{\partial t} + \mathbf{u}_i (\nabla \psi_i) + \mathbf{u}_i \cdot \mathbf{v}_{vr_i} \Rightarrow \frac{D\psi_i}{Dt} = \frac{D\phi_i}{Dt} - \mathbf{u}_i \cdot \mathbf{v}_{vr_i}. \tag{2.9.13}$$

The dynamic boundary conditions can now be found by substituting this into equations (2.2.8),

$$\frac{D\psi_1}{Dt} = \frac{|\nabla\psi_1|^2}{2} - \frac{|\overline{v}_{vr_1}|^2}{2} + 1 - \varepsilon\left(\frac{V_0}{V}\right)^{\gamma} + \sigma_{b1}\nabla\cdot\mathbf{n}_{b1} - \delta\left(z - z_0\right),$$
$$\frac{D\psi_2}{Dt} = \frac{|\nabla\psi_2|^2}{2} - \frac{|\overline{v}_{vr_2}|^2}{2} + \frac{1}{\rho_A}\left(1 - \varepsilon\left(\frac{V_0}{V}\right)^{\gamma} + \sigma_{b2}\nabla\cdot\mathbf{n}_{b1}\right) - \delta\left(z - z_0\right). \quad (2.9.14)$$

Similarly on the fluid-fluid interfaces,

$$\begin{aligned}\frac{D\overline{F}_A}{Dt} &= \left(1-\rho_A\right)\left(\mathbf{u}_1\cdot\mathbf{u}_2\right) - 2\mathbf{u}_{av_1}\cdot\left(\mathbf{v}_{vr_1} - \rho_A\mathbf{v}_{vr_2}\right) + 2\sigma_A\nabla\cdot\mathbf{n}_2 - 2\left(1+\rho_A\right)\delta z,\\ \frac{D\overline{F}_B}{Dt} &= \left(1-\rho_B\right)\left(\mathbf{u}_1\cdot\mathbf{u}_3\right) - 2\mathbf{u}_{av_2}\cdot\mathbf{v}_{vr_1} + 2\sigma_B\nabla\cdot\mathbf{n}_3 - 2\left(1+\rho_B\right)\delta z. \quad (2.9.15)\end{aligned}$$

### 2.9.3 Boundary Integral Equations

When previously deriving the equations for the boundary integral method, the balance of the normal velocities at the fluid-fluid interfaces in equation (2.6.2) is used to simplify the Green's equations. These equations do not hold for the decomposed potentials, instead the normal derivatives across the fluid-fluid interfaces are written as,

$$\frac{\partial\psi_1\left(\mathbf{p}\right)}{\partial n_2} = \frac{\partial\psi_2\left(\mathbf{p}\right)}{\partial n_2} + vr_{2_{n_2}}\left(\mathbf{p}\right) - vr_{1_{n_2}}\left(\mathbf{p}\right), \quad \frac{\partial\psi_1\left(\mathbf{r}\right)}{\partial n_3} = \frac{\partial\psi_3\left(\mathbf{p}\right)}{\partial n_3} - vr_{1_{n_3}}\left(\mathbf{p}\right),$$

where $vr_{i_{n_2}}$ is the normal scalar component of $\mathbf{v}_{vr_i}$ in fluid layer $i$ with respect to $\mathbf{n}_2$, similarly for $vr_{1_{n_3}}$. As before, the normals in the Green's equations are pointing out of fluid 2 on interface $A$ and out of fluid 3 on interface B. The sums of the potentials are given by $\psi_A = \psi_1 + \psi_2$ and $\psi_B = \psi_1 + \psi_3$. Therefore the decomposed potential in fluid 1 is given by,

$$
\begin{aligned}
2\pi\psi_1(\mathbf{b}) = & \int\limits_{\partial B_1} \left[ G(\mathbf{b},\mathbf{c}) \frac{\partial \psi_1(\mathbf{c})}{\partial n_1} - \psi(c) \frac{\partial G(\mathbf{b},\mathbf{c})}{\partial n1} \right] dS(c) \\
& - \int\limits_{\partial I_A} G(\mathbf{b},\mathbf{q}) \left( \frac{\partial \psi_2(\mathbf{q})}{\partial n_2} + vr_{2_{n_2}}(\mathbf{q}) - vr_{1_{n_2}}(\mathbf{q}) \right) dS(\mathbf{q}) \\
& + \int\limits_{\partial I_A} \frac{\partial G(\mathbf{b},\mathbf{q})}{\partial n_2} \left( \psi_A(\mathbf{q}) \frac{\rho_A}{1+\rho_A} + \overline{F}_A(\mathbf{q}) \frac{1}{2(1+\rho_A)} \right) dS(\mathbf{q}) \\
& + \int\limits_{\partial I_B} G(\mathbf{b},\mathbf{s}) \left( \frac{\partial \psi_3(\mathbf{s})}{\partial n_3} - vr_{1_{n_3}}(\mathbf{s}) \right) dS(\mathbf{s}) \\
& - \int\limits_{\partial I_B} \frac{\partial G(\mathbf{b},\mathbf{s})}{\partial n_3} \left( \psi_B(\mathbf{s}) \frac{\rho_B}{1+\rho_B} + \overline{F}_B(\mathbf{s}) \frac{1}{2(1+\rho_B)} \right) dS(\mathbf{s}) .
\end{aligned}
$$

In fluid 2 the decomposed potential is

$$
\begin{aligned}
2\pi\psi_2(\mathbf{d}) = & \int\limits_{\partial B_2} \left[ G(\mathbf{d},\mathbf{e}) \frac{\partial \psi_2(\mathbf{e})}{\partial n_2} - \psi(e) \frac{\partial G(\mathbf{d},\mathbf{e})}{\partial n2} \right] dS(e) \\
& + \int\limits_{\partial I_A} \left( G(\mathbf{d},\mathbf{q}) \frac{\partial \psi_2(\mathbf{q})}{\partial n_2} - \frac{\partial G(\mathbf{d},\mathbf{q})}{\partial n_2} \left( \psi_A(\mathbf{q}) \frac{1}{1+\rho_A} - \overline{F}_A(\mathbf{q}) \frac{1}{2(1+\rho_A)} \right) \right) dS(\mathbf{q}) .
\end{aligned}
$$

On fluid-fluid interface $A$ the two equations are given by,

$$
\begin{aligned}
2\pi\psi_A(\mathbf{p}) = & \int\limits_{\partial B_1}\left[G(\mathbf{p},\mathbf{c})\frac{\partial\psi_1(\mathbf{c})}{\partial n_1}-\psi(\mathbf{c})\frac{\partial G(\mathbf{p},\mathbf{c})}{\partial n1}\right]dS(\mathbf{c})\\
& + \int\limits_{\partial B_2}\left[G(\mathbf{p},\mathbf{e})\frac{\partial\psi_2(\mathbf{e})}{\partial n_2}-\psi(\mathbf{e})\frac{\partial G(\mathbf{p},\mathbf{e})}{\partial n2}\right]dS(\mathbf{e})\\
& - \int\limits_{\partial I_A} G(\mathbf{p},\mathbf{q})\left(vr_{2_{n_2}}(\mathbf{q})-vr_{1_{n_2}}(\mathbf{q})\right)dS(\mathbf{q})\\
& + \int\limits_{\partial I_A}\frac{\partial G(\mathbf{p},\mathbf{q})}{\partial n_2}\left(\overline{F}_A(\mathbf{q})\frac{1}{(1+\rho_A)}-\psi_A(\mathbf{q})\frac{1-\rho_A}{1+\rho_A}\right)dS(\mathbf{q})\\
& + \int\limits_{\partial I_B} G(\mathbf{p},\mathbf{s})\left(\frac{\partial\psi_3(\mathbf{s})}{\partial n_3}-vr_{1_{n_3}}(\mathbf{s})\right)dS(\mathbf{s})\\
& - \int\limits_{\partial I_B}\frac{\partial G(\mathbf{p},\mathbf{s})}{\partial n_3}\left(\psi_B(\mathbf{s})\frac{\rho_B}{1+\rho_B}+\overline{F}_B(\mathbf{s})\frac{1}{2(1+\rho_B)}\right)dS(\mathbf{s}),
\end{aligned}
$$

and

$$
\begin{aligned}
2\pi\left(\frac{\overline{F}_A(\mathbf{p})}{1+\rho_A}+\psi_A(\mathbf{p})\frac{\rho_A-1}{\rho_A+1}\right) = & \int\limits_{\partial B_1}\left[G(\mathbf{p},\mathbf{c})\frac{\partial\psi_1(\mathbf{c})}{\partial n_1}-\psi(\mathbf{c})\frac{\partial G(\mathbf{p},\mathbf{c})}{\partial n1}\right]dS(\mathbf{c})\\
& - \int\limits_{\partial B_2}\left[G(\mathbf{p},\mathbf{e})\frac{\partial\psi_2(\mathbf{e})}{\partial n_2}-\psi(\mathbf{e})\frac{\partial G(\mathbf{p},\mathbf{e})}{\partial n2}\right]dS(\mathbf{e})\\
& - \int\limits_{\partial I_A} G(\mathbf{p},\mathbf{q})\left(2\frac{\partial\psi_2(\mathbf{q})}{\partial n_2}+vr_{2_{n_2}}(\mathbf{q})-vr_{1_{n_2}}(\mathbf{q})\right)dS(\mathbf{q})\\
& + \int\limits_{\partial I_A}\frac{\partial G(\mathbf{b},\mathbf{q})}{\partial n_2}\psi_A(\mathbf{q})\,dS(\mathbf{q})\\
& + \int\limits_{\partial I_B} G(\mathbf{p},\mathbf{s})\left(\frac{\partial\psi_3(\mathbf{s})}{\partial n_3}-vr_{1_{n_3}}(\mathbf{s})\right)dS(\mathbf{s})\\
& - \int\limits_{\partial I_B}\frac{\partial G(\mathbf{p},\mathbf{s})}{\partial n_3}\left(\psi_B(\mathbf{s})\frac{\rho_B}{1+\rho_B}+\overline{F}_B(\mathbf{s})\frac{1}{2(1+\rho_B)}\right)dS(\mathbf{s}).
\end{aligned}
$$

Similarly on fluid-fluid interface B,

$$
\begin{aligned}
2\pi\psi_B(\mathbf{r}) = & \int_{\partial B_1}\left[G(\mathbf{r},\mathbf{c})\frac{\partial\psi_1(\mathbf{c})}{\partial n_1}-\psi(\mathbf{c})\frac{\partial G(\mathbf{r},\mathbf{c})}{\partial n1}\right]dS(\mathbf{c}) \\
& + \int_{\partial I_A} G(\mathbf{r},\mathbf{q})\left(\frac{\partial\psi_2}{\partial n_2}(q)+vr_{2_{n_2}}(\mathbf{q})-vr_{1_{n_2}}(\mathbf{q})\right)dS(\mathbf{q}) \\
& - \int_{\partial I_A}\frac{\partial G(\mathbf{r},\mathbf{q})}{\partial n_2}\left(\psi_A(\mathbf{q})\frac{\rho_A}{1+\rho_A}+\overline{F}_A(\mathbf{q})\frac{1}{2(1+\rho_A)}\right)dS(\mathbf{q}) \\
& + \int_{I_B} G(\mathbf{r},\mathbf{s})\,vr_{1_{n_3}}dS(\mathbf{s}) \\
& + \int_{\partial I_B}\frac{\partial G(\mathbf{r},\mathbf{s})}{\partial n_3}\left(\overline{F}_B(\mathbf{s})\frac{1}{(1+\rho_B)}-\psi_B(\mathbf{s})\frac{1-\rho_B}{1+\rho_B}\right)dS(\mathbf{s}),
\end{aligned}
$$

and

$$
\begin{aligned}
2\pi\left(\frac{\overline{F}_B(\mathbf{r})}{1+\rho_B}+\psi_B(\mathbf{r})\frac{\rho_B-1}{\rho_B+1}\right) = & \int_{\partial B_1}\left[G(\mathbf{r},\mathbf{c})\frac{\partial\psi_1(\mathbf{c})}{\partial n_1}-\psi(\mathbf{c})\frac{\partial G(\mathbf{r},\mathbf{c})}{\partial n1}\right]dS(\mathbf{c}) \\
& + \int_{\partial I_A} G(\mathbf{r},\mathbf{q})\left(\frac{\partial\psi_2}{\partial n_2}(q)+vr_{2_{n_2}}(\mathbf{q})-vr_{1_{n_2}}(\mathbf{q})\right)dS(\mathbf{q}) \\
& - \int_{\partial I_A}\frac{\partial G(\mathbf{r},\mathbf{q})}{\partial n_2}\left(\psi_A(\mathbf{q})\frac{\rho_A}{1+\rho_A}+\overline{F}_A(\mathbf{q})\frac{1}{2(1+\rho_A)}\right)dS(\mathbf{q}) \\
& - \int_{I_B} G(\mathbf{r},\mathbf{s})\left(2\frac{\partial\psi_3(\mathbf{s})}{\partial n_3}-vr_{1_{n_3}}\right)dS(\mathbf{s}) \\
& + \int_{\partial I_B}\frac{\partial G(\mathbf{r},\mathbf{s})}{\partial n_3}\left(\psi_B(\mathbf{s})\frac{\rho_B}{1+\rho_B}+\overline{F}_B(\mathbf{s})\frac{1}{2(1+\rho_B)}\right)dS(\mathbf{s}).
\end{aligned}
$$

These equations can now be discretised in the same manner as before and written in matrix form,

$$
\begin{bmatrix}
G_{bc} & 0 & -G_{bq} & -G_{bs} & \frac{\rho_A}{1+\rho_A}DG_{bq} & \frac{\rho_B}{1+\rho_B}DG_{bs} \\
0 & G_{de} & G_{dq} & 0 & \frac{-1}{1+\rho_A}DG_{dq} & 0 \\
G_{pc} & G_{pe} & 0 & -G_{ps} & \frac{\rho_A-1}{\rho_A+1}DG_{pq} - 2\pi I_{pq} & \frac{\rho_B}{1+\rho_B}DG_{ps} \\
G_{pc} & -G_{pe} & -2G_{pq} & -G_{ps} & DG_{pq} + 2\pi\frac{1-\rho_A}{1+\rho_A}I_{pq} & \frac{\rho_B}{1+\rho_B}DG_{ps} \\
G_{rc} & 0 & -G_{rq} & 0 & \frac{\rho_A}{1+\rho_A}DG_{rq} & \frac{\rho_B-1}{\rho_B+1}DG_{rs} - 2\pi I_{rs} \\
G_{rc} & 0 & -G_{rq} & -2G_{rs} & \frac{\rho_A}{1+\rho_A}DG_{rq} & DG_{rs} + 2\pi\frac{1-\rho_B}{1+\rho_B}I_{rs}
\end{bmatrix}
\begin{bmatrix}
\frac{\partial\psi_1(\mathbf{c})}{\partial n_1} \\
\frac{\partial\psi_2(\mathbf{e})}{\partial n_2} \\
\frac{\partial\psi_2(\mathbf{q})}{\partial n_2} \\
\frac{\partial\psi_3(\mathbf{s})}{\partial n_3} \\
\psi_A(\mathbf{q}) \\
\psi_B(\mathbf{s})
\end{bmatrix}
$$

$$
= \begin{bmatrix}
2\pi I_{bc} + DG_{bc} & 0 & \frac{-1}{2+2\rho_A}DG_{bq} & \frac{1}{2+2\rho_B}DG_{bs} & G_{bq} & G_{bs} \\
0 & 2\pi I_{de} + DG_{de} & \frac{-1}{2+2\rho_A}DG_{dq} & 0 & 0 & 0 \\
DG_{pc} & DG_{pe} & \frac{-1}{1+\rho_A}DG_{pq} & \frac{-1}{2+2\rho_B}DG_{ps} & G_{pq} & G_{ps} \\
DG_{pc} & -DG_{pe} & 2\pi\frac{1}{1+\rho_A}I_{pq} & \frac{-1}{2+2\rho_B}DG_{ps} & G_{pq} & G_{ps} \\
DG_{rc} & 0 & \frac{-1}{2+2\rho_A}DG_{rq} & \frac{-1}{1+\rho_B}DG_{rs} & -G_{rq} & -G_{rs} \\
DG_{rc} & 0 & \frac{-1}{2+2\rho_A}DG_{rq} & 2\pi\frac{1}{1+\rho_B}I_{rs} & -G_{rq} & -G_{rs}
\end{bmatrix}
\begin{bmatrix}
\psi_1(\mathbf{c}) \\
\psi_2(\mathbf{e}) \\
F_A(\mathbf{q}) \\
F_B(\mathbf{s}) \\
vr_{2_{n_2}} - vr_{1_{n_2}} \\
vr_{1_{n_3}}
\end{bmatrix}. \tag{2.9.16}
$$

This system of equations can now be solved to find the vector on the left-hand-side of the equation as before, allowing the toroidal bubble to be stepped forward in time in the same manner as before.

## 2.10 Chapter Summary

In this chapter the numerics for modelling the interaction of bubbles with two density interfaces have been presented. The boundary integral method has been adapted to model the growth and collapse of bubbles in a three fluid system, and the appropriate kinematic and dynamic boundary conditions have been chosen. By interpolating the discrete surfaces with quintic splines an accurate representation of the bubble surface can be obtained. Finally, the equations for a vortex ring are introduced to model the toroidal stage of

bubble collapse. In Chapter 3 the model developed will be tested through comparisons with the Rayleigh-Plesset equation, the numerical results of Pearson [42] and experimental results from various papers [4, 20, 15].

# Chapter 3

# Comparisons and Results

The validity of the Boundary Integral Method shown in Chapter 2 now has to be verified. Using well established results from previous works, comparisons can be made to gauge the accuracy of the simulations. For simplicity, gravity and surface tension have been neglected in the following examples, the bubbles considered are small enough for these parameters to be considered negligible. The first comparison will be made with the Rayleigh-Plesset equation.

## 3.1 Comparison with the Rayleigh-Plesset Equation

The Rayleigh-Plesset equation is a time dependent second order ordinary differential equation which models the radius of a spherically symmetric bubble in a Newtonian, infinite and incompressible fluid. The growth and collapse of a spherical bubble is a simple yet fundamental form of bubble movement, therefore showing the capability of the boundary integral method in modelling this effect is fundamental. The equation can be derived from first principles using the properties of the fluid and the bubble, the derivation by Brennen [9] is shown in the appendix. The non-dimensional form of the Rayleigh-Plesset equation is given by

$$R\ddot{R} + \frac{3}{2}\left(\dot{R}\right)^2 = \varepsilon\left(\frac{R_0}{R}\right)^{3\gamma} - 1 - \frac{2\sigma}{R}, \tag{3.1.1}$$

where $\varepsilon$ is the strength parameter, $\gamma$ is the ratio of specific heats and $\sigma$ is surface tension. This equation can be solved easily using a MATLAB ODE solver with a given set of initial conditions for $R$ and $\dot{R}$. The boundary integral method can be used to simulate a spherical bubble by removing the interfaces to see the bubble oscillating under the influence of the pressure difference. Figure 3.1 shows plots of the radius of an oscillating spherical bubble with varying strengths starting from minimum radius. Both the Rayleigh-Plesset equation, RPE, and the boundary integral method, BIM, are solved using a fourth order Runge-Kutta method. It is easy to see there is excellent agreement for two oscillations with a small amount of divergence towards the end of the second oscillation, which is expected due to the small discrepancies that occur when recreating the bubble surface using splines. After this point the boundary integral method still maintains a close approximation to the Rayleigh-Plesset equation.

In the derivation of the Rayleigh-Plesset equation the velocity field in the fluid around a spherical bubble is also derived and given by,

$$u_r\left(r,t\right) = \frac{R^2\dot{R}}{r^2}, \tag{3.1.2}$$

where dot, $\dot{}$ , denotes differentiation with respect to time. By placing points where the interfaces would originate in the boundary integral method, it is now possible to show the movement of the interfaces from the results of the Rayleigh-Plesset equation using the above equation. Figure 3.2 shows the growth of a spherical bubble in the vicinity of two fluid interfaces with density ratios $\rho_A = \rho_B = 1$, this effectively gives fluids 1, 2 and 3 the same density and therefore the bubble is in an infinite fluid. The interfaces are therefore showing how the fluid around the bubble moves during the growth phase.

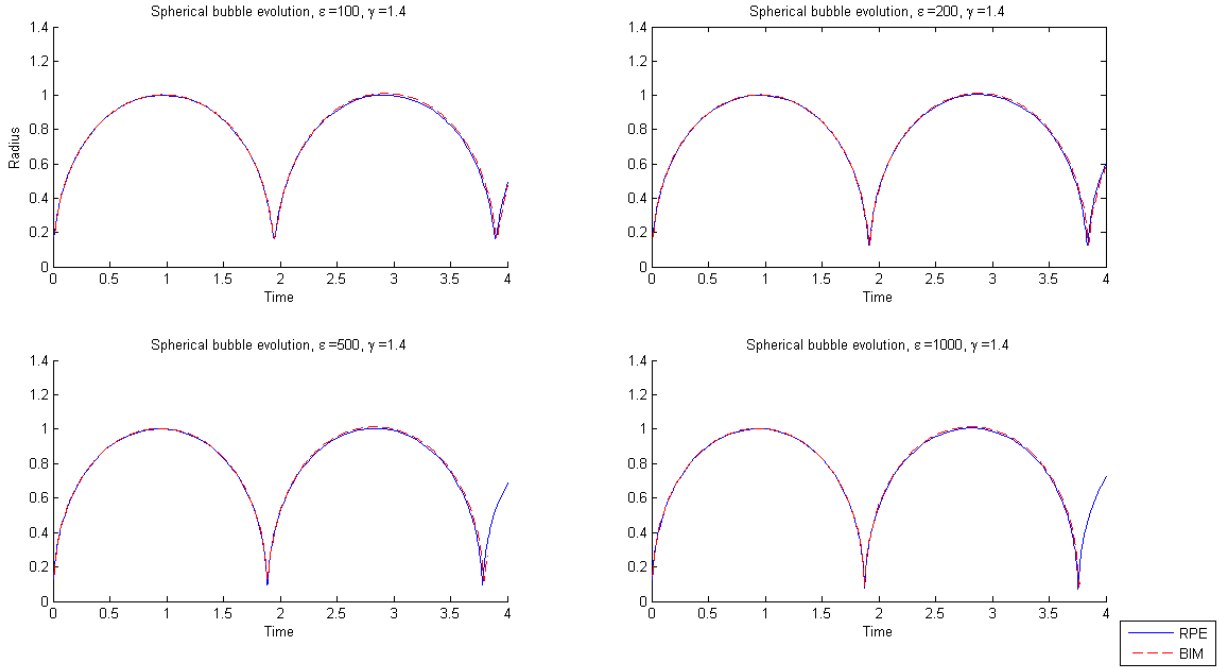


Figure 3.1: Comparison between the Rayleigh-Plesset equation and the boundary integral method when plotting the radius of a spherical bubble. Good agreement can be seen for strength parameters $\varepsilon = 100$, $\varepsilon = 200$, $\varepsilon = 500$, $\varepsilon = 1000$.

The left-hand side of the plot is produced from the results of the ODE solver for the Rayleigh-Plesset equation and equation (3.1.2), the right-hand side is produced from the results of the boundary integral method. Both simulations appear identical to the naked eye, suggesting the boundary integral method is very accurate when modelling both the bubble and the interfaces.

Comparing the boundary integral method with the ordinary differential equation has shown that the numerics described in Chapter 2 give an accurate representation of an oscillating spherical bubble. The next step is to vary the density ratios across a fluid-fluid interface to look at more complex bubble collapse.

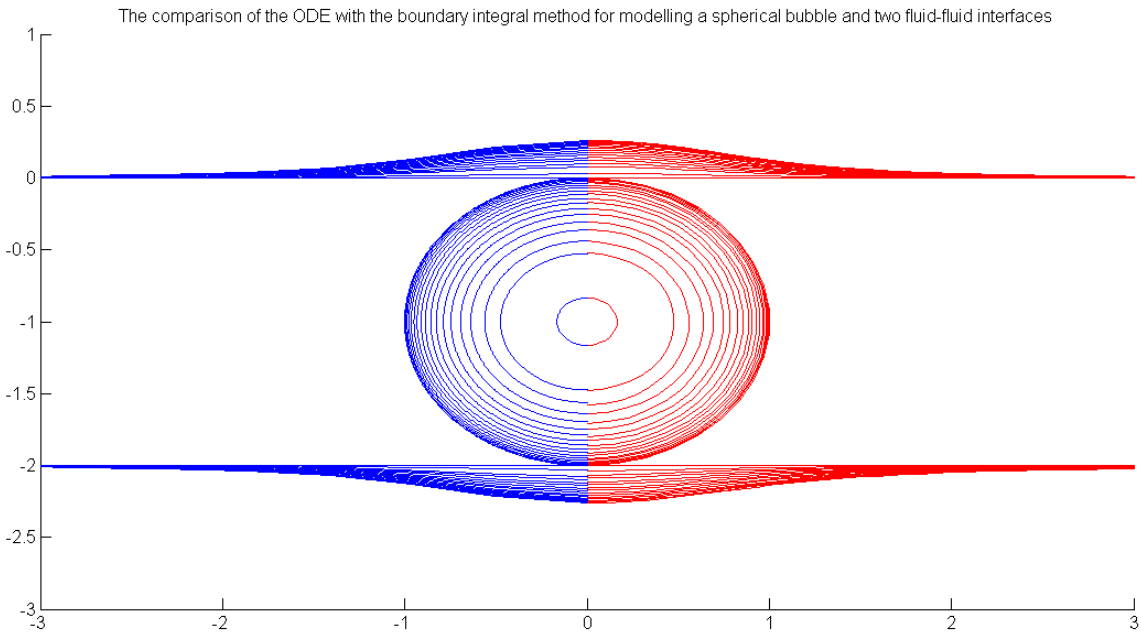


Figure 3.2: Comparison between the Rayleigh-Plesset equation (blue) and the boundary integral method (red) when plotting the radius of a spherical bubble with the evolution of two fluid-fluid interfaces. The bubble and interface evolution appear the same when generated by the ODE and by the BIM.

## 3.2 Rigid Boundary Bubble Collapse Comparisons

The boundary integral method can be used to model bubble interaction with a rigid boundary by setting one of the density ratios across the respective interface to infinity. In previous models, rigid boundaries have been represented using the method of images, where a bubble of equal strength and size is introduced to the fluid domain to mirror the original bubble across the location of the rigid boundary [6]. This method was effective, though required altering the Green's function in equation (2.4.3) to include the image bubble. In the results that follow interface $B$ is chosen to be the rigid boundary by setting $\rho_B = \infty$. Unfortunately it is not possible to perform the calculations from Chapter 2 with $\rho_B = \infty$, this problem can be circumvented by simply setting the density interface to a very high number. To simulate a rigid boundary in the following results the density ratio across interface $B$ is $\rho_B = 10000$, the density ratio across interface $A$ is chosen to

be $\rho_A = 1$ and therefore has no impact on the evolution of the bubble but will give a representation of the fluid motion near the bubble as in the spherical bubble case above. As mentioned in Chapter 1, the work of Plesset and Chapman [47] is highly cited and their model is thought to give an accurate representation of bubble collapse near a rigid boundary, and has since been used as a comparison to verify the accuracy of more recent models. Therefore it seemed appropriate to use the boundary integral method in this thesis to recreate some of their results. Figure 3.3 shows the results of Plesset and Chapman modelling the collapse of a bubble near a rigid wall using a finite difference method. The bubble has an initial stand-off distance of $h = 1.5$ and is initiated at its maximum radius as a spherical bubble, the shape of the bubble is shown at various times throughout its evolution on a single plot. This is then simulated by the boundary integral method to compare the results.

The two results compare very well showing the same bubble shapes during the collapse. In the results for the boundary integral method a plot of the toroidal bubble is also included, Plesset and Chapman's model did not have the ability to advance the bubble into the toroidal stage. Interface $A$ is seen at the top of the boundary integral method plot, the interface moves downwards as time progresses showing that fluid is drawn down by the bubble as it collapses towards the rigid boundary. The results of the numerical methods of this thesis match very well those of Plesset and Chapman, it is now necessary to see if the boundary integral method compares with experimental data as well.

In experiments performed by Philipp and Lauterborn [44] lasers are used to generate bubbles in the vicinity of rigid boundaries to investigate cavitation erosion. By varying stand-off distance and the orientation of the camera they have produced a plethora of detailed results showing the collapse of the bubble. Figure 3.4 shows the collapse of a bubble that was initiated at a stand-off distance of $h = 0.9$. The top of the bubble can

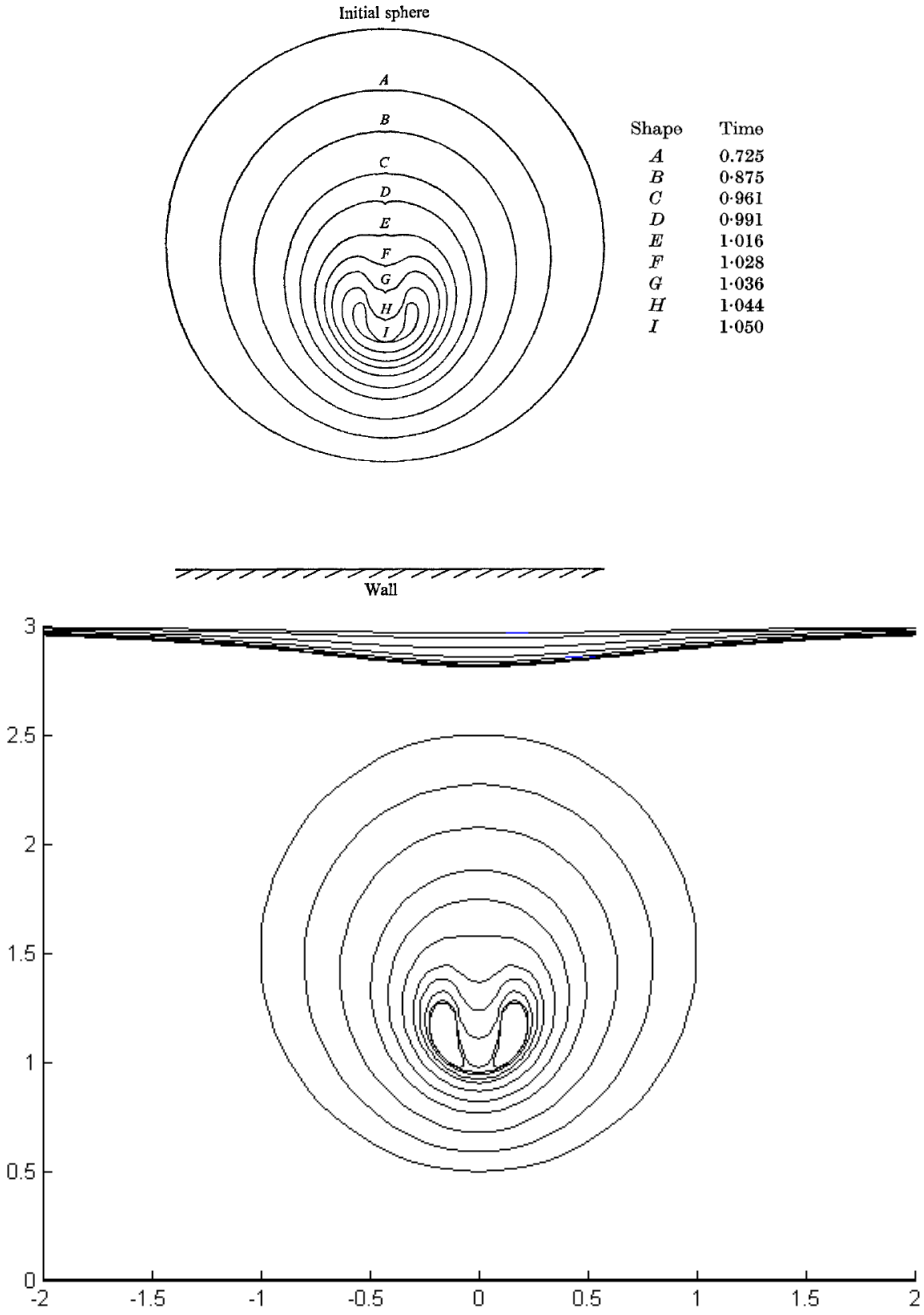


Figure 3.3: Plesset and Chapman's results (top) for a spherical bubble with $h = 1.5$ collapsing towards a rigid boundary modelled using a finite difference method. Result from the Boundary integral method (bottom) showing the same bubble collapse with $\rho_A = 1$ and $\rho_B = 10000$, and an additional image for the toroidal stage.

be seen moving towards the boundary, eventually forming a jet through the bubble which impacts on the surface in the final frame. Each time frame is separated by $17.7\mu s$, which corresponds to a non-dimensional time of approximately $t = 0.13$. Below that are the results of the boundary integral method of the same stand-off distance, the density ratios across interfaces $A$ and $B$ are $\rho_A = 1$ and $\rho_B = 10000$ respectively.

The experimental and the numerical results show good agreement throughout the collapse, none of the images above show the toroidal stage of the bubbles evolution as the experimental results become too convoluted to make any useful comparisons. The numerical results however continue past the jet impact to the formation of the toroidal bubble, allowing for the jet to impact on the rigid boundary. Figure 3.5 shows the high non-dimensional velocities and pressures achieved by the jet impacting on the rigid boundary. This is consistent with previous accounts of cavitation damage by Benjamin and Ellis [2]. Comparisons of the boundary integral method against the numerical results of Plesset and Chapman and the experimental results of Philipp and Lauterborn suggest the numerical methods in this thesis are accurate in representing bubble collapse near a rigid boundary.

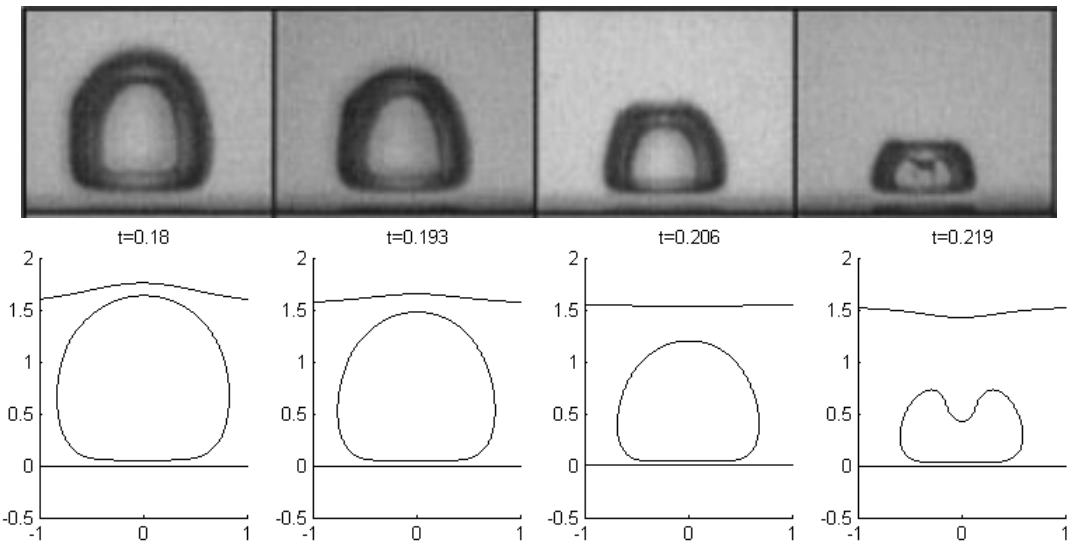


Figure 3.4: Experimental results (top) and numerical results (bottom) of a bubble collapsing against a rigid boundary with $h = 0.9$, $\rho_A = 1$ and $\rho_B = 10000$.

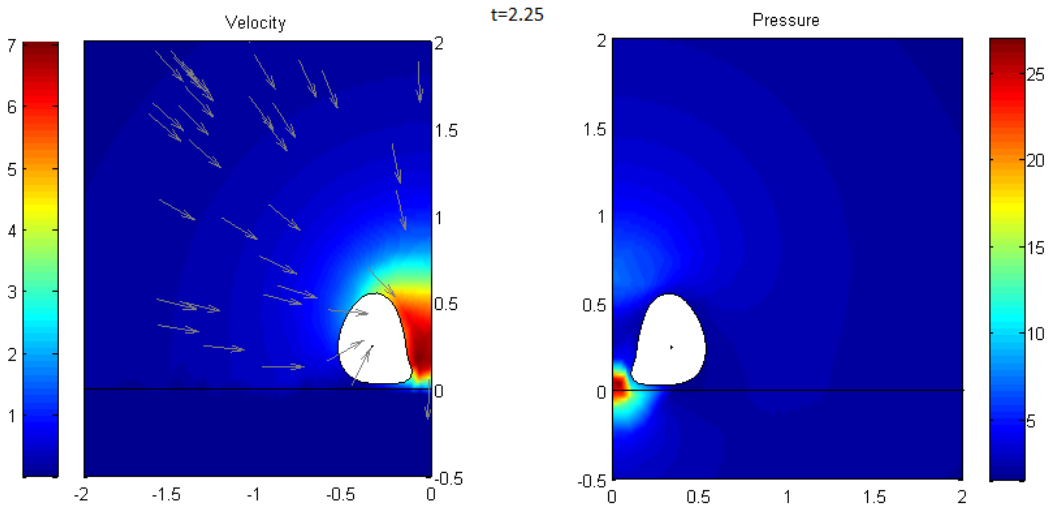


Figure 3.5: Velocity and Pressure plots from the numerical results of a bubble collapsing against a rigid boundary with $h = 0.9$, $\rho_A = 1$ and $\rho_B = 10000$.

The method will now be verified for modelling bubble interactions with a free surface.

## 3.3 Free Surface Bubble Collapse Comparison

Extensive research of free surface collapse has been completed by Blake and Gibson [4, 7, 5], in both numerical and experimental areas. The comparisons here will be with the experimental results as any numerical results have already been verified against the same experiments within the papers mentioned. To create the free surface next to a fluid layer with the numerical method is effectively the same as having a fluid-fluid interface with a density ratio of zero, so setting $\rho_A = 0$ lets fluid 1 have no density compared to fluid 2. Figure 3.6 shows the collapse of a bubble near a free surface with a stand-off $h = 0.56$, below are the numerical results for the same stand-off distance.

As the bubble expands it deforms the free surface as it pushes fluid outwards from the bubble centroid, during its growth the bubble becomes elongated towards the surface. When the bubble begins to collapse the free surface continues to move upwards forming a surface jet as described in Chapter 1. The bubble then begins to produce a jet directed

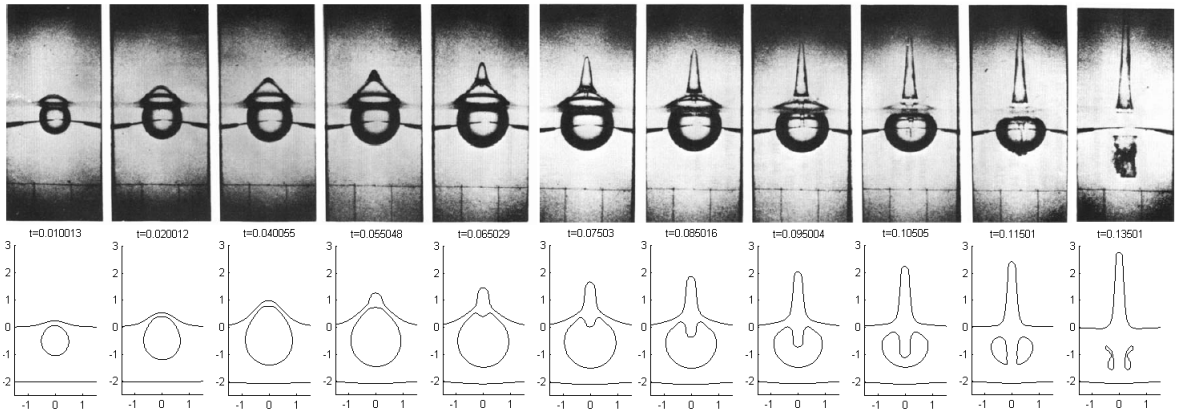


Figure 3.6: Experimental results of Blake and Gibson compared with the numerical results for a bubble near a free surface with stand-off distance $h = 0.56$ and density ratios $\rho_A = 0$ and $\rho_B = 1$

from the surface through to the opposite side of the bubble, as this jet propagates and threads the bubble the surface continues to move in the other direction. This is due to the high pressures formed between the bubble and the free surface, as seen in figure 3.7. The point of high pressure pushes fluid down through the bubble and up into the free surface, forming the faster jet through the bubble and the slower jet into fluid 2.

Once the bubble enters toroidal stage of its collapse the surface jet appears to slow as it reaches a maximum height. The numerical results produced by the boundary integral method show excellent comparison with the experiment and are therefore a good method for modelling free surface interactions with a bubble.

The applications so far have required one or both density ratios to be equal to one across the interfaces, effectively only using the interaction between two fluids. As the numerics have been developed for a three fluid system this method has not been fully explored. In the following comparisons neither density ratio will be equal to one and therefore utilise both interfaces in the modelling the evolution of a bubble.

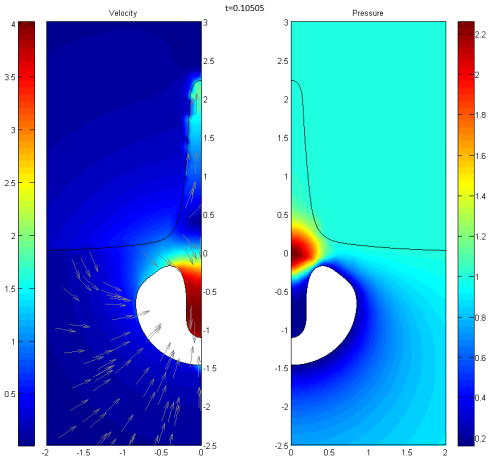


Figure 3.7: Velocity and pressure plots from the numerical results for a bubble near a free surface with stand-off distance $h = 0.56$ and density ratios $\rho_A = 0$ and $\rho_B = 1$

## 3.4 Bubble Collapse Between Two Plates

Interaction between a bubble and a rigid boundary has been extensively researched in previous papers and Section 3.3, but the addition of a second interface can drastically change the collapse. Experiments of bubbles between plates have been conducted by Ishida et al. [15] and Choi and Chahine [16], the results of Ishida et al. are shown here. Figure 3.8 shows the results of a bubble initiated equidistant from two plates with a stand-off distance of $h = 1.1$, therefore the gap between the two plates is slightly larger than the maximum radius of the bubble.

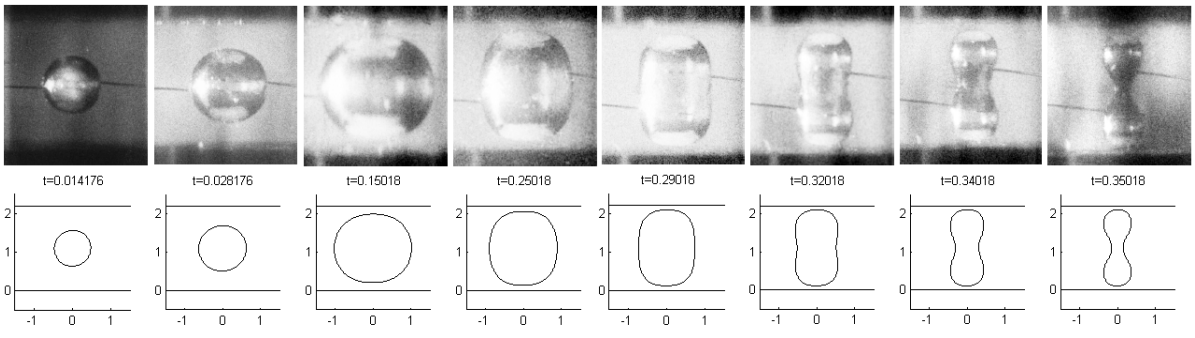


Figure 3.8: Collapse of a bubble between two plates with a distance of 2.2 between them and a stand-off distance of $h = 1.1$ from both plates, for the numerical results the density ratios across both interfaces are $\rho_A = \rho_B = 10000$.

The bubble remains fairly spherical during its growth, as it reaches maximum radius the top and bottom start to flatten and the bubble becomes "squashed". The collapse phase of the bubble evolution is completely different to that of a bubble near a single rigid wall. The bubble experiences the same attraction to each rigid boundary, causing the bubble centroid to remain equidistant to the two plates. Therefore the bubble tries to migrate towards both boundaries, causing it to collapse in from the sides at the point of highest curvature. The bubble forms a "dumbbell" shape which can be seen in the last frame, after this point the bubble splits into two equally sized bubbles along the axis of symmetry. The numerical results show all the same features seen in the experimental results, the most notable comparison is the "dumbbell" shape appearing in both the experimental and numerical results. These results also agree with Kucera and Blake [30], who used the method of images to yield similar results for bubble collapse between two rigid boundaries.

The same paper shows another experiment by Ishida et al. with the same set-up except the bubble is offset, positioning it closer to one plate than the other. Figure 3.9 has the same 2.2 gap between the plates except the bubble now has a stand-off distance of $h = 0.8$ from one of the plates.

The experimental and numerical results compare very well here, both show a fairly spherical growth with the top of the bubble gradually being flattened along the upper plate. When the bubble reaches maximum radius it is no longer spherical, with the top side flat against the boundary and the rest of the bubble slightly elongated towards the bottom. During the collapse the sides come inwards as in the previous experiment, except as most of the bubble is towards the upper boundary only the bottom part comes in from the sides. This forms a "bullet" shape pointing downwards, as the collapse continues the bottom of the bubble forms a tip and becomes more conical towards the top of the bubble. In frame 9 the experiment and the numerics differ slightly, in the experimental

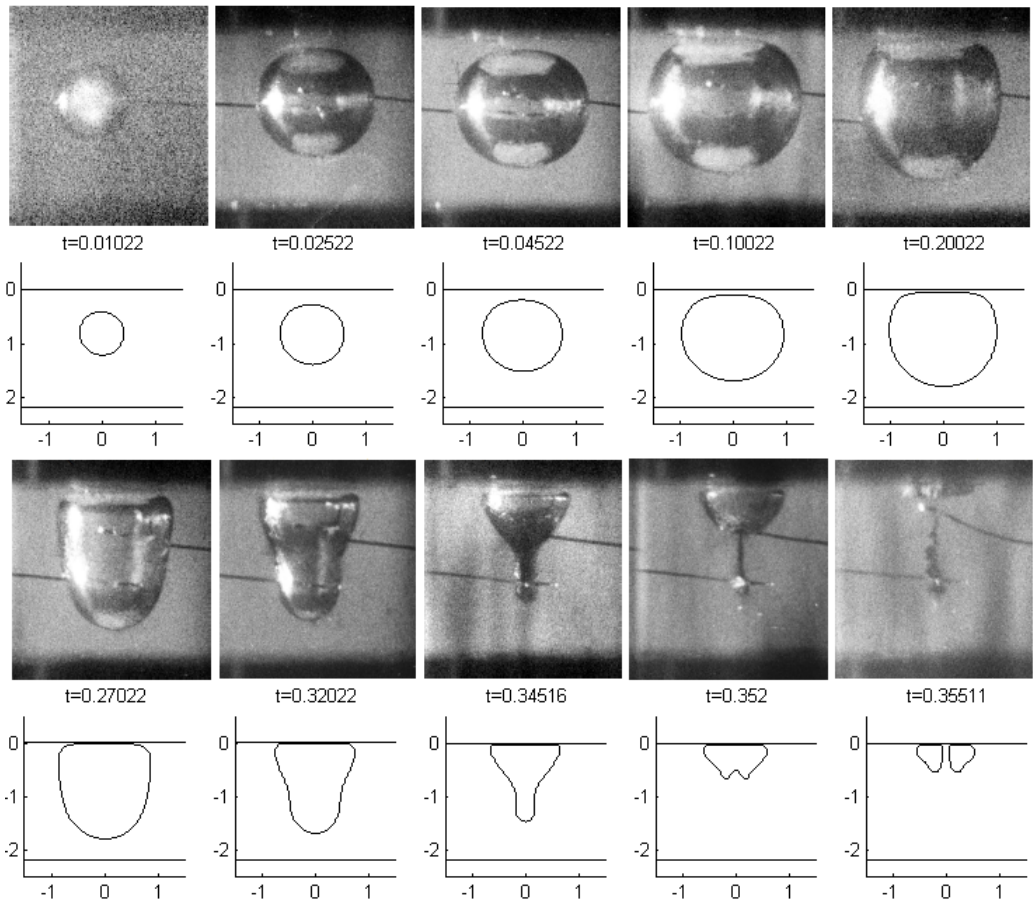


Figure 3.9: Collapse of a bubble between two plates with a distance of 2.2 between them and a stand-off distance of $h = 0.8$ from interface $A$ and 1.4 from interface $B$, for the numerical results the density ratios across both interfaces are $\rho_A = \rho_B = 10000$.

results the bubble separates into two bubbles with the lower bubble being much smaller. The numerical results show the bubble remaining intact and forming only the top bubble in the experimental results. Though the smaller bubble is not shown, the numerics still model the collapse of the top bubble very well. The last few frames of both the experiment and the numerics show the top bubble becoming toroidal with a jet formed towards the upper boundary. The numerics model the experimental results very well throughout the majority of the bubble evolution, with a slight discrepancy in the form of a smaller bubble pinching off, though good agreement is still shown with the remaining bubble.

## 3.5 Modelling Laser Induced Forward Transfer

The use of bubbles in printing techniques was mentioned briefly in Chapter 1, laser induced forward transfer is a method of transferring a droplet of a fluid onto the surface of another substrate. This method of printing removes the issue of nozzle clogging seen in ink-jet printing and allows for smaller droplets to be produced. This allows for more precise and detailed prints, as well as the option to print biological fluids on to the substrate. The experiment performed by Duocastella et al. [20] uses a laser pulse to generate a bubble in a thin liquid film, the resulting surface jet due to the bubble collapse is the mechanism observed in the results shown in Figure 3.10. The initial surface deformation observed in frames 1 and 2 are due to the initial growth of bubble, in frame 3 a surface jet begins to emerge from this raised surface signalling the start of the collapse phase of the bubble. This surface jet then extends far from the fluid surface at great speeds producing a very thin line. The tip of the jet can then touch another substrate to transfer a droplet of the fluid.

This can be modelled by the numerical method by considering a bubble near both a free surface and a rigid boundary, therefore the density ratios across interfaces $A$ and $B$ will be $\rho_A = 0$ and $\rho_B = 10000$ respectively. Figure 3.11 shows the numerical results of the

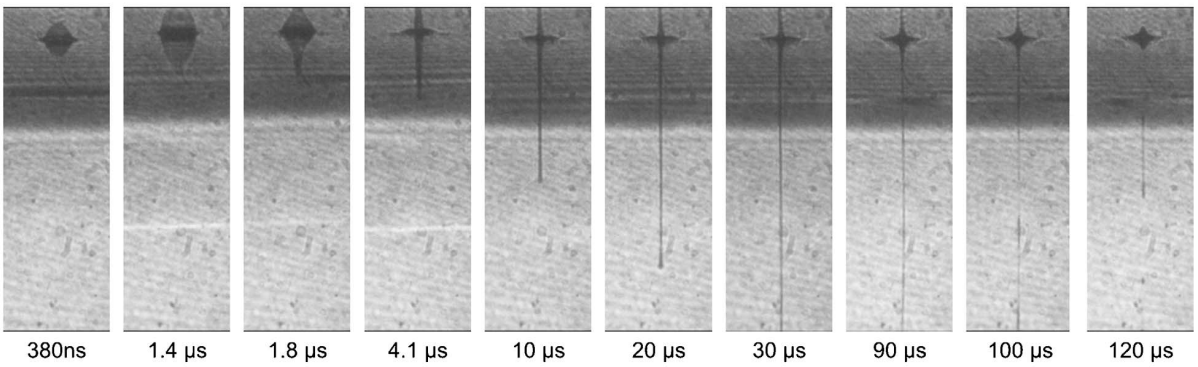


Figure 3.10: Images from an experiment performed by Duocatella et al. [20] showing the process of laser induced forward transfer.

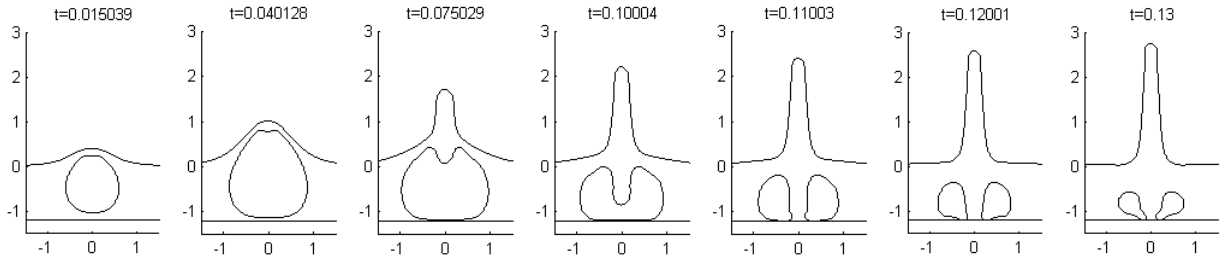


Figure 3.11: Numerical results modelling laser induced forward transfer for a bubble sith stand-off distance $h = 0.56$ and density ratios $\rho_A = 0$ and $\rho_B = 10000$

collapse, as you can see there is a close comparison with the experimental results for the first seven frames.

Unfortunately the bubble comes in contact with the rigid boundary in the last frame, this terminates the model as to avoid interference between surfaces. For the first few frames there is clear agreement between experimental and numerical results, advancing the numerics further will have to be included as further work.

## 3.6 Chapter Summary

The numerical model outlined in Chapter 2 has been compared with past numerical and experimental results. For a single bubble in an infinite fluid the boundary integral method compared very well with the Rayleigh-Plesset equation. The radius of the bubble remained the same as the RPE throughout the growth and collapse phase, with little divergence during the rebound. The fluid-fluid interfaces set to $\rho_A = \rho_B = 1$ also matched with the predicted fluid domain from the growth of a RPE bubble.

The introduction of a rigid boundary saw the bubble collapse with a jet forming on the far side of the bubble, and threading through to form a toroidal bubble directed towards the wall. This is the expected result corroborated by both numerical and experimental results obtained by Plesset and Chapman [47]. The large velocities and pressures observed also show how bubble collapse near a rigid wall can be responsible for known cavitation

damage.

With a change in density ratio of one interface to $\rho = 0$ the collapse of a bubble near a free surface was modelled. Both the bubble jet and the fluid jet observed were comparable with experimental data. With both jets being explained by the high pressures that form between the bubble and the free surface.

Both fluid-fluid interfaces were utilised to see the evolution of a bubble between two rigid plates. The bubble grew to the size of the cavity and formed the characteristic "dumbbell" shape during the collapse. When the bubble is initiated closer one interface than the other, the collapse continued to agree with experimental data.

Finally the laser induced forward transfer experiment was modelled with a high thin surface jet produced. Although the bubble collapse is not present in the experimental results, the high surface jets produced were in agreement.

Therefore the numerical model has been tested in a range of scenarios with enough success when compared with past results to conclude, the boundary integral method introduced in Chapter 2 is an accurate method in modelling bubble collapse in a three fluid system.

# Chapter 4

# Mixing with Bubbles

Many chemical processes require an interaction between two fluids, either to form a solution or to produce a chemical reaction. In both cases the process is greatly aided by mixing the two fluids, as solutions are produced quicker and chemical reaction rates are increased due to the increase in surface area between the reactants. Large quantities of fluids can be mixed simply by stirring to agitate the fluids, but in some cases the amount of fluids to be mixed are too small for this method to be effective.

The concept of Lab on a Chip (LOC) devices has been introduced in the last 20 years. A LOC device will be a microfluidic device equipped with a range of apparatus, for example 'microfabricated fluidic channels, heaters, temperature sensors and fluorescence sensors' [11], which analyse properties of fluids. Various aspects of the analysis process will require the mixing of two fluids on a micro-scale within the chip. One method of promoting mixing within a fluid is to stretch and fold the fluid on itself multiple times, the mathematics involved with this mixing has been looked at by Ottino and Wiggins [60] [40]. The physical process can be created by flowing the fluid across a ridged wall or through an angularly rotating partitioned pipe; both of which promote Bernoulli mixing of the fluid. A similar approach was adopted by Garstecki et al. [25] [26], with the fluid flowing

through channels designed to mix. The difference here being instead of using ridges along the channel to promote mixing, the channel now branches and recombines at several junctures. Bubbles are also introduced into the flow to aid the process. These 'gaseous slugs' travelling within the branched channels cause temporal variations in the pressure distribution which leads to stretching and folding of the fluids to be mixed. The natural oscillation of a bubble is another property that can be used for mixing. When an acoustic field is applied across a fluid which contains a bubble, the frequency of the sound field and the natural frequency of the bubble can resonate causing the bubble to undergo various size and shape oscillations [22]. These oscillations can then excite the fluid around the bubble causing mixing. This method has been used by Liu et al [37] where multiple bubbles are placed in a reaction chamber which, when introduced to a sound field, generate steady circular flows resulting in rapid mixing.

It has been shown in Chapter 3 that laser induced cavitation bubbles collapse when in the vicinity of rigid boundaries, this collapse is rapid and causes disruption to the surrounding fluid. It is shown by Hellman et al. [29], that this disruption in the fluid can also promote mixing in small channels. Using a laser pulse a bubble can be inserted in a channel containing two fluid streams running parallel to each other. The growth of the bubble begins to agitate the fluid within the channel, and the collapse stage disrupts the laminar flow of two fluid streams.

In this Chapter, the idea of using bubble collapse for mixing purposes is explored by simulating a similar process to that used in Hellman et al. By placing various bubbles in a fluid domain containing two fluids that are to be mixed, the amount of mixing can be observed to find how bubble properties can enhance this process. The properties to be looked at will be the strength of the bubble and the initial inception time of the bubble.

## 4.1 Quantifying Mixing

To begin with, the model geometry has to be set so these parameters can be accurately tested. At initial time $t = 0$ both fluids are at rest separated by a fluid-fluid interface at $z = 0$. Two bubbles of equal initial radii will be placed within the fluid domain, either side of the interface. Through multiple simulations of varying the distance between two bubbles, it was seen a distance of 2 bubble radii showed the most bubble-bubble interaction. If the bubbles were any closer, the bubble surfaces would cause the interfaces to overlap and end the simulation. If the separation distance was greater than 2 bubble radii the Bjerknes forces between them became too weak to show any significant interaction. Hence both bubbles will be 1 bubble radius away from the initial interface, as shown in Figure 4.1.

To be able to make mixing comparisons between the different parameter values for bubble strength and inception time, mixing has to be quantified. To do this two different values within the simulation will be considered.

Firstly, the vertical distance one fluid is injected into the other will be analysed. For example, when two fluids begin with a horizontal interface at $z = 0$, and by the end of the bubble interaction if fluid 1 is now past the initial interface into the domain of fluid 2, it can be said that mixing has occurred.

And secondly, the volume of fluid displaced from the initial fluid domain into the other can be measured. This has a similar idea to measuring the vertical distance, but can differentiate between a small amount of fluid going far into the other domain or a large amount of fluid only moving slightly past the initial interface. This will be calculated using the trapezoidal rule on the space between the deformed interface and $z = 0$.

The case of two fluids of equal density is to be looked at; giving the density ratio across

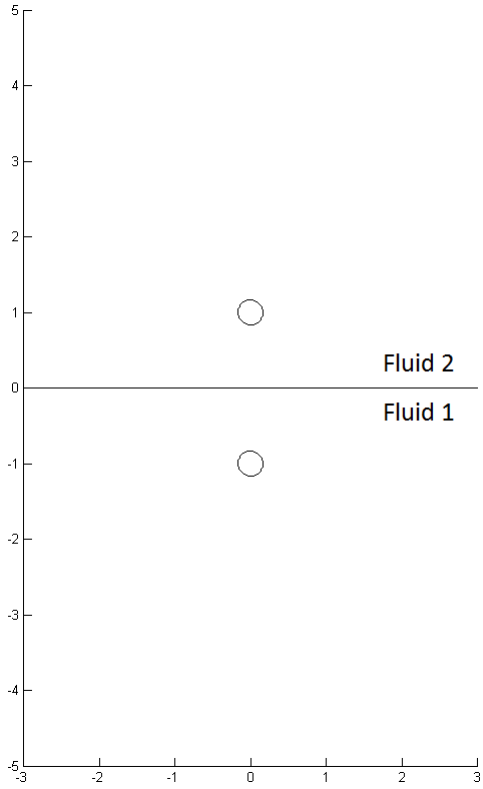


Figure 4.1: The initial placement of two bubbles in two different fluids, separated by an interface at $z = 0$

the interface as $\rho_A = 1$. The surface tension of both bubbles and the interface is assumed to be $\sigma_{b_1} = \sigma_{b_2} = \sigma_I = 0$. Both bubbles are adiabatic with ratios of specific heats of $\gamma = 1.4$ in each case.

## 4.2 Bubble Strength Comparison

The first variable to consider is the strength of the bubbles. The strength of bubble 1 in fluid 1 is fixed at $\varepsilon = 100$, the strength of the second bubble is varied for comparison. To begin with, the second bubble has $\varepsilon = 50$; half the strength of bubble 1.

Figure 4.2 shows the bubble collapse at given intervals. Both bubbles grow spherically

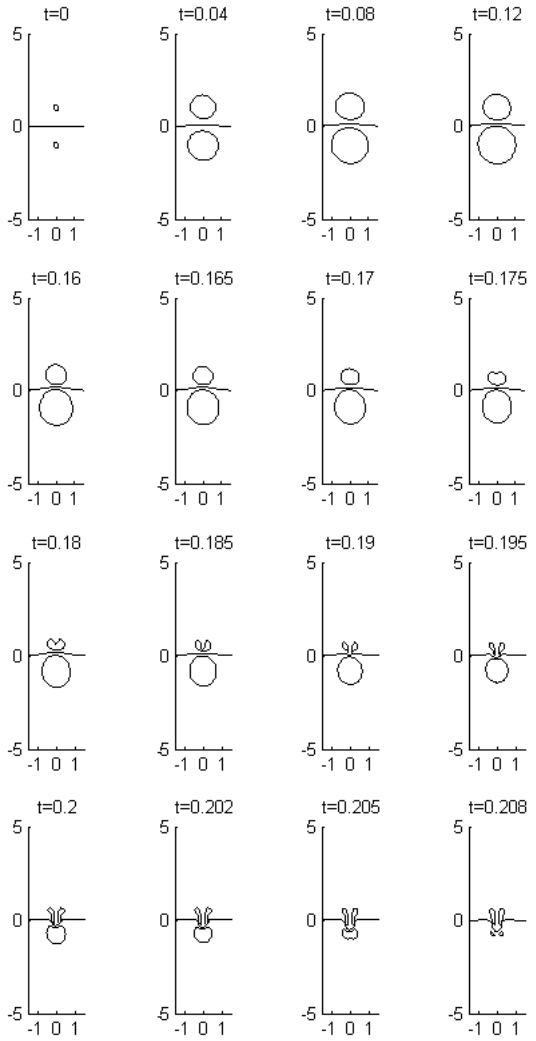


Figure 4.2: Numerical results modelling the collapse of two bubbles in two fluids of equal density. The top bubble has a strength of $\varepsilon = 50$ while the lower bubble has strength $\varepsilon = 100$.

at the start, the greater strength of bubble 1 can be seen by comparing the radii of the bubbles at maximum volume. The force from bubble 1 pushes the interface upwards; which in-turn causes the bottom of bubble 2 to flatten slightly, this will promote a small amount of mixing of the fluids. As the weaker of the two bubbles, bubble 2 has a greater attraction to bubble 1 during the collapse stage. The jet forms from the top of bubble 2 at $t = 0.175$, and penetrates the bottom with speed. This jet continues into the toroidal

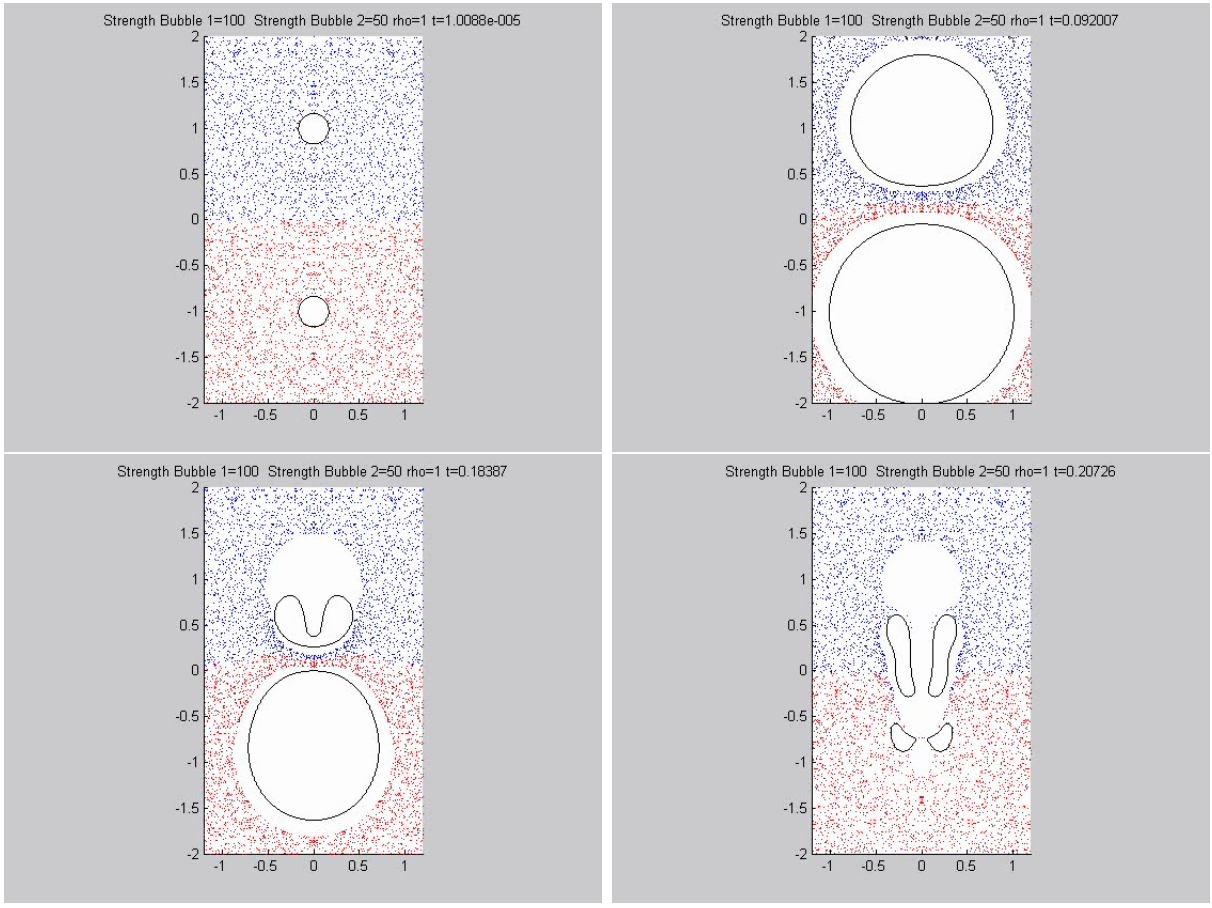


Figure 4.3: Numerical results modelling the motion of the fluid surrounding two bubbles of different strength. The top bubble has a strength of $\varepsilon = 50$ while the lower bubble has strength $\varepsilon = 100$.

stage pushing the interface down, along with bubble 1. At $t = 0.195$, fluid 2 has been injected into fluid 1, with the fluid jet still travelling with high velocity. The simulation ends as the bubble surfaces and interface become extremely close, though before termination it can be seen that bubble 1 is collapsing towards bubble 2. This will reduce the speed of the jet, though it can be assumed fluid 2 would continue further into fluid 1. Due to the limitations of the model any quantities for mixing will only be taken before termination, without speculation about the fluid jet after this point. It can be seen in the final frame the tip of the jet is 0.62 bubble radii into fluid 1 with a volume of 0.14.

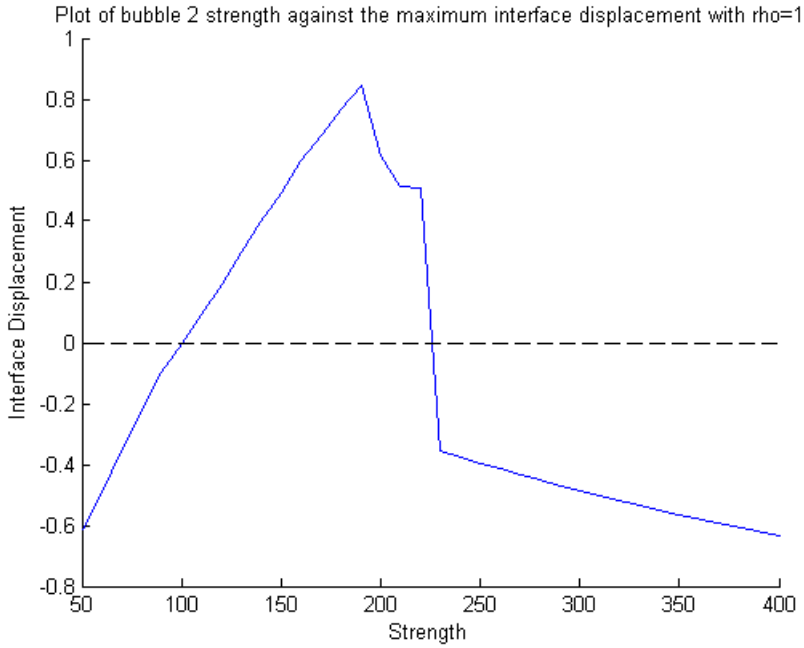


Figure 4.4: Plot of the maximum interface displacement against the strength of bubble 2 with $\rho = 1$.

To understand the fluid motion better during the collapse, the interface is removed in Figure 4.3. Points have been placed in the fluid domain, where red and blue represent fluids 1 and 2 respectively. The motion of the points are found using the Greens function in Equation 2.4.1 with $c(\mathbf{x}_0) = 4\pi$, and stepped forward in time as before. The initial placement of the points are random with the colour difference set either side of the interface from the start of the simulation. As expected, the points nearest the bubble surfaces are pushed away rapidly during the expansion. Many red points are pushed above the line $z = 0$, but the main aspect to notice is towards the end of the collapse. In the final frames the blue particles are pushed far into fluid 1, to the surface of bubble 1. This figure shows the mixing potential of two fluids well, though it is easier to measure the mixing values mentioned above using the interface representation.

The strength of the second bubble is increased by 10 and the simulation is ran again. For

each run the maximum indent and volume transfer are taken. Figure 4.4 shows the plot of the strength of bubble 2 against the maximum vertical interface displacement during the simulation. Negative values show when the maximum displacement moves the interface into fluid 1, with positive values for the interface moving into fluid 2. When determining the maximum displacement the absolute values were taken to find the point when the interface was furthest from $z = 0$, on either side.

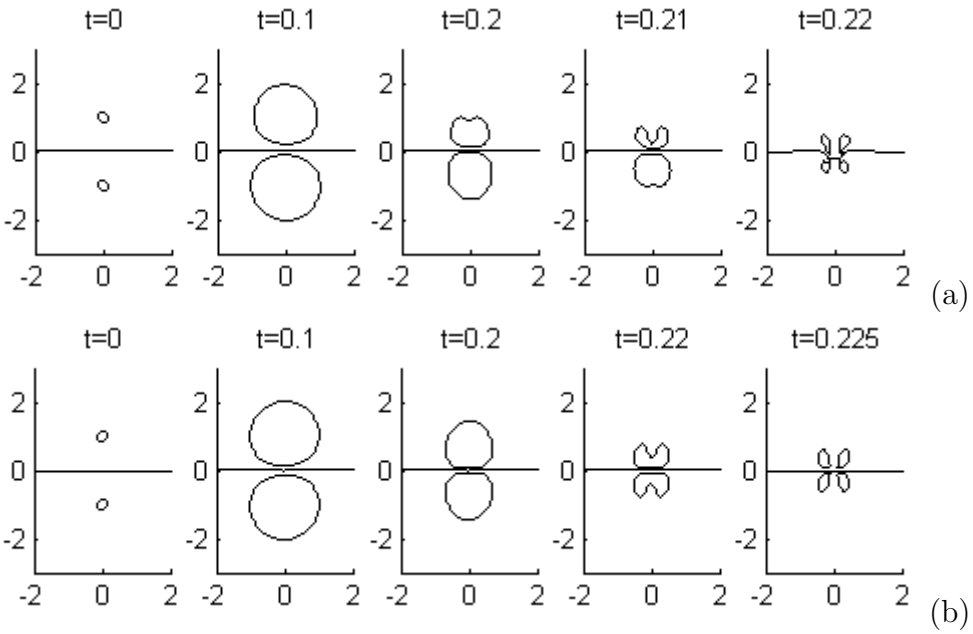


Figure 4.5: Numerical results modelling the collapse of two bubbles in two fluids of equal density. The lower bubble has strength $\varepsilon = 100$ while the top bubble has strength (a) $\varepsilon = 80$ and (b) $\varepsilon = 100$.

The plot shows that while the strength of bubble 2 is less than bubble one, the interface is jetted into fluid 1. This is to be expected as a weaker bubble will feel a greater attraction towards a stronger bubble, as seen for bubble 2 strengths $\varepsilon = 50$ and $\varepsilon = 80$ in figures 4.2 and 4.5(a) respectively. As the strength of bubble 2 tends towards $\varepsilon = 100$, a linear trend appears showing correlation between increase in strength and increase in maximum interface displacement with a gradient of 0.0025.

Figure 4.5(b) shows when the two bubbles have equal strength of $\varepsilon = 100$ the interface remains at $z = 0$ due to the bubbles collapsing towards each other with the same attractive forces, similar to a singular bubble collapsing near a rigid wall.

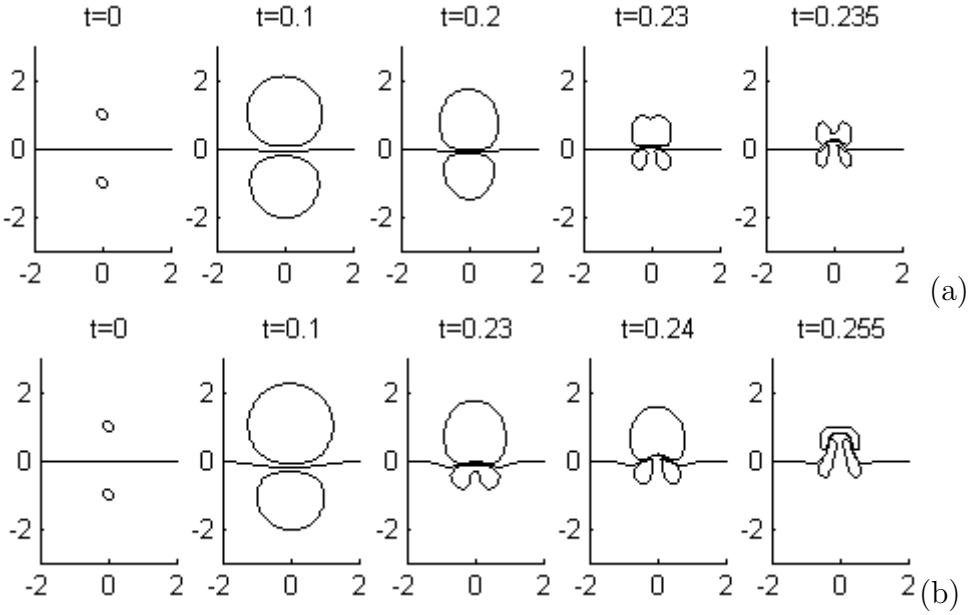


Figure 4.6: Numerical results modelling the collapse of two bubbles in two fluids of equal density. The lower bubble has strength $\varepsilon = 100$ while the top bubble has strength (a) $\varepsilon = 130$ and (b) $\varepsilon = 190$.

When the strength is above $\varepsilon = 100$ bubble 2 becomes the stronger of the two bubbles and exhibits a greater attraction through Bjerknes forces, causing the interface to now move into fluid 2, as seen for $\varepsilon = 130$ and $\varepsilon = 190$ in figure 4.6. The linear trend seen for the strengths below 100 continues. Increasing the strength increases the maximum interface displacement, with fluid 1 now moving into fluid 2. The gradient remains similar at 0.0020, giving further correlation between the variables.

It can be seen from the plot that the trend of maximum displacement drops when strength gets to $\varepsilon = 190$. This drop is due to the limitations of the model. Figure 4.7 shows when

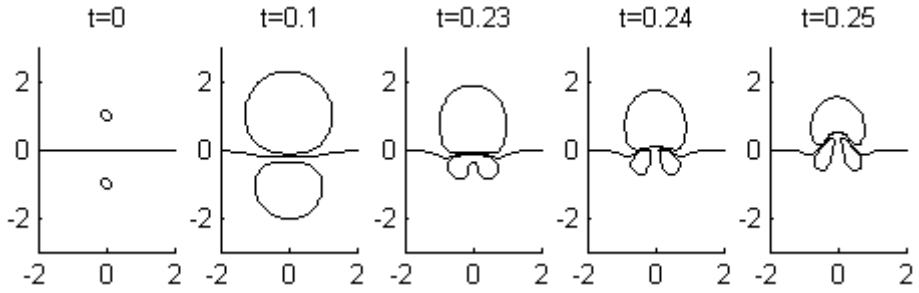


Figure 4.7: Numerical results modelling the collapse of two bubbles in two fluids of equal density. The lower bubble has a strength of $\varepsilon = 100$ while the top bubble has strength $\varepsilon = 210$.

the bubble surface comes too close to the fluid-fluid interface the simulation terminates. Therefore the maximum radius output in the graph does not account for the continued evolution of the bubble jet after this surface interaction. As the strength of bubble 2 increases the interface is forced to touch bubble surface sooner in the simulation, causing an apparent drop in the maximum displacement of the interface.

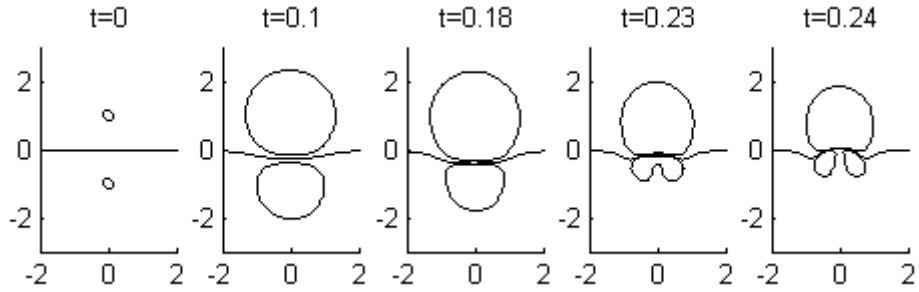


Figure 4.8: Numerical results modelling the collapse of two bubbles in two fluids of equal density. The lower bubble has a strength of $\varepsilon = 100$ while the top bubble has strength $\varepsilon = 230$.

For strengths higher than $\varepsilon = 230$ the maximum displacement is in fluid 1 and begins to climb steadily again with a gradient of $-0.0004$. Figure 4.8 shows the key features of the bubbles collapse. The much stronger second bubble grows rapidly and comes very close to the fluid-fluid interface, giving the maximum interface displacement just before $t = 0.18$. Bubble 1 then begins to collapse forming a jet, which has been the cause of the maximum

interface displacements shown for lower strengths of bubble 2. The jet is not able to push the interface back in this case due to the bubble surfaces and interface becoming too close, as seen in the last plot. This terminates the simulation, giving the maximum interface displacement in fluid 1. This interface displacement occurs earlier in the simulation than the previous maximums, as shown by the plot of bubble strength against the time the maximum interface displacement occurs. Therefore this indicates that the trend for above $\varepsilon = 230$ is not caused by the bubble jet as before, but by the initial expansion of bubble 2.

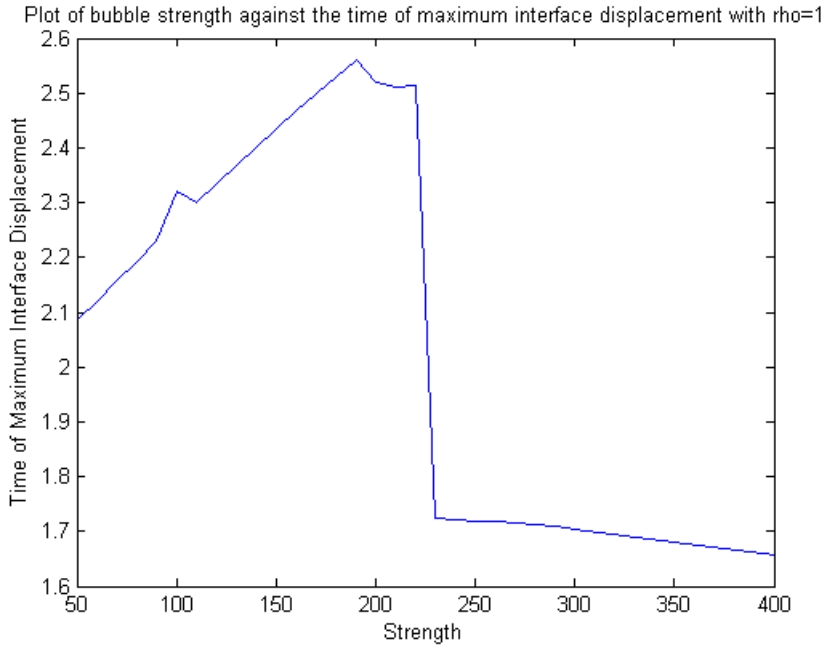


Figure 4.9: Plot of the time of the maximum interface displacement against the strength of bubble 2 with $\rho = 1$.

In a paper by Gonzalez-Avila et al. [28] experiments were carried out to produce microjets by generating a bubble in a fluid near a tapered hole. The expanding and collapsing bubble forced fluid through the hole, generating a fast microjet on the other side. They found two jets were produced though the hole by one bubble; the first being much slower than the second. This first jet was generated by the initial spherical expansion of the

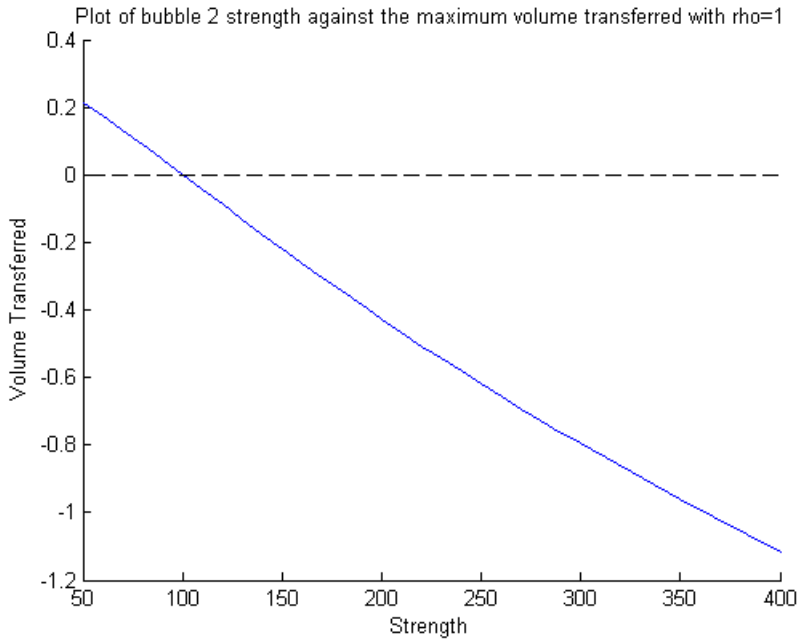


Figure 4.10: Plot of the maximum amount of volume transferred against the strength of bubble 2 with $\rho = 1$.

bubble, the second was produced by the bubble collapsing and forming a jet through the bubble. This is similar to the maximum interface displacements shown in figure 4.4. For smaller strength the entire growth and collapse of the bubble can be simulated, so the maximum displacement shown corresponds to the jet formed by the collapsing bubble. As the strength increases past $\varepsilon = 190$ the simulation is unable to complete, therefore the maximum interface displacements shown are those caused by a jetting bubble part way though the process. As the strength increases further past $\varepsilon = 220$ the jetting stage of the collapse is not achieved, therefore the maximum displacement shown comes from the expansion of the stronger bubble, which increase with the strength of bubble 2. This is represented by a drop in the time of maximum interface displacement, shown in figure 4.9. The time drop shows the change from the displacement being caused by the jet, which occurs later in the bubble evolution, to the displacement being caused by the expansion of the bubble, which occurs earlier in the bubble evolution. Hence the greatest interface

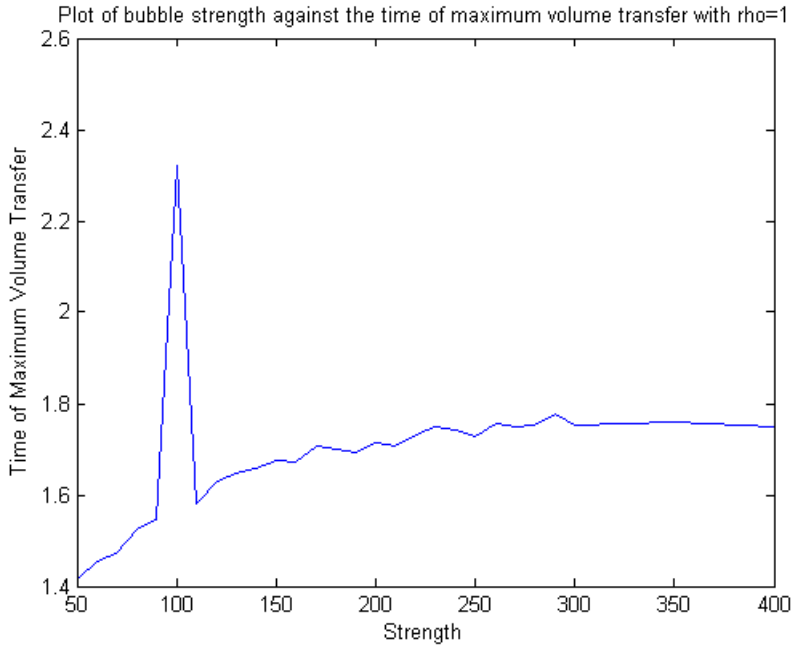


Figure 4.11: Plot of the time of the maximum volume transfer against the strength of bubble 2 with $\rho = 1$

displacement comes from the jetting stage of the bubble lifetime, which increases with the strength of bubble 2.

When considering the maximum amount of volume transferred across the initial resting interface of $z = 0$ during the bubbles interaction, a clearer correlation is given when increasing the strength of bubble 2. Figure 4.10 shows the maximum volume of either fluid 1 or 2 transferred across the line $z = 0$ plotted against the strength of bubble 2, with negative values to show when the maximum volume transferred in fluid 1. For strengths less than $\varepsilon = 100$ the values shown correspond to the maximum volume of fluid 1 moved into fluid 2, and for strengths greater than $\varepsilon = 100$ the maximum volume of fluid 2 moved into fluid 1. This occurs due to the stronger of the two bubbles having a greater impact on the overall motion of the fluid.

A plot of the time of the maximum volume transfer reveals the maximum is achieved early

in the evolution of the bubbles. Figure 4.11 shows the times all come before the jetting stage of the bubble, typically after time $t = 2.0$. The only time that does not follow this rule is at $\varepsilon = 100$, this is due to the bubbles of equal strength producing no volume transfer except for negligible changes that can occur at any time during the lifespans of the bubbles. Therefore the maximum volume transfer can be attributed to the amount of fluid moved during the expansion phase of the bubble evolution, similar to the interface movement caused by the growth of the spherical bubble shown in 3.1. This agrees with the positive correlation shown in figure 4.10, as the increase in strength of bubble 2 will give a faster growth rate, which will move a larger volume of fluid away from the initial point of inception of the bubble.

Therefore, to maximise the distance a fluid is displaced into another, a bubble with strength around $\varepsilon = 190$ should be used. However, to maximise the volume of fluid transferred, a bubble of strength $\varepsilon \geqslant 400$ should be used.

## 4.3 Inception Time Comparison

Two bubbles of equal strength are inserted into the fluid domains out of phase, therefore the second bubble is introduced into the simulation part way through the growth of the first bubble. The interactions of two out-of-phase bubbles can produce interesting collapses. Figure 4.12(a) shows the growth of a single bubble with a second bubble introduced at time=1.0. The growth of bubble 1 is spherical, equal to the growth of a Rayleigh-Plesset bubble. When the second bubble is introduced, bubble 1 has finished the growth phase of its evolution. As a bubble grows the pressure inside the bubble decreases until it is less than the fluid pressure around it, this causes the radial velocity of the bubble to decrease to 0 and eventually collapse. Therefore a bubble earlier in the growth phase has a greater outward velocity and has a greater influence on the fluid domain. As bubble

2 grows it pushes the fluid initially displaced by bubble 1 back into fluid 1 and beyond, causing the surface of bubble 1 nearest the interface to flatten then concave at $t = 0.12$. This causes a jet to form in bubble 1 moving away from bubble 2 at $t = 0.14$, whereas two bubbles of equal strength usually collapse towards each other due to attraction from their Bjerknes forces.

As bubble 1 collapses, fluid is drawn in from the surrounding area. This causes the interface to move towards bubble 1, along with the surface of bubble 2 nearest bubble 1 at $t = 0.16$. Bubble 2 then collapses from this point of high curvature forming a jet away from bubble 1 at $t = 0.18$. This reversal of jet direction for the two bubbles is called the "catapult effect" [23]. The pulling of bubble 2 towards bubble 1 resembles the drawing back of a catapult elastic, with the jet of bubble 2 in the opposite direction similar to the release of the elastic of a catapult. Figure 4.12(b) shows the experimental images collected by Fong et al. [23] for two spark bubbles set up to show the catapult effect. The computer model matches the collapse of both bubble 1 and 2. By adding an interface to the model, as in figure 4.1, the mixing application of the catapulting bubble can be quantified.

A range of inception times are considered from two bubbles started at $t = 0$, to bubble 2 being introduced at $t = 3$. Figure 4.13 shows the plot of the inception time of bubble 2 against the maximum indent of the interface at $r = 0$. For inception time $t = 0$ this is again the equivalent of a bubble collapse near a rigid wall, hence giving no interface movement. When the second bubble is started at $t = 0.1$, just after the inception of the first, the maximum interface displacement occurs when fluid 1 is ejected into fluid 2, as shown in figure 4.14. This is due to bubble 1 jetting towards bubble 2, as the bubbles are only out of phase by a small amount, bubble 1 is attracted to bubble 2 by Bjerknes forces. However the jet from bubble 1 does cause bubble 2 to jet away from bubble 1, giving half of the catapult effect.

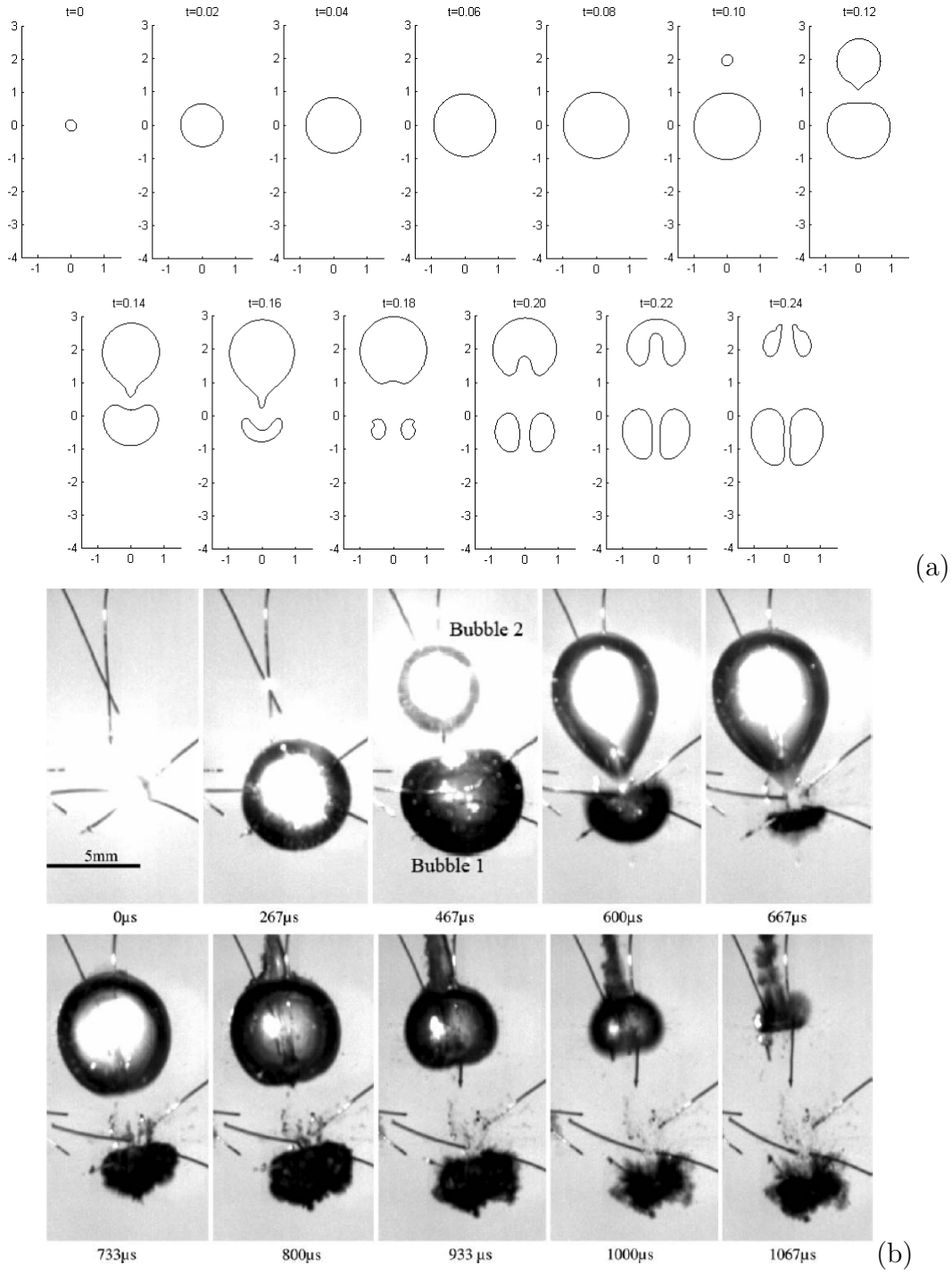


Figure 4.12: (a) Numerical results modelling the collapse of two bubbles out of phase. Bubble 1 starts at $t = 0$ with bubble 2 starting at $t = 1.0$.
(b) Experimental results showing the collapse of two spark-generated bubbles out of phase. Bubble 1 starts at $t = 0\mu s$ with bubble 2 starting at $t = 467\mu s$.

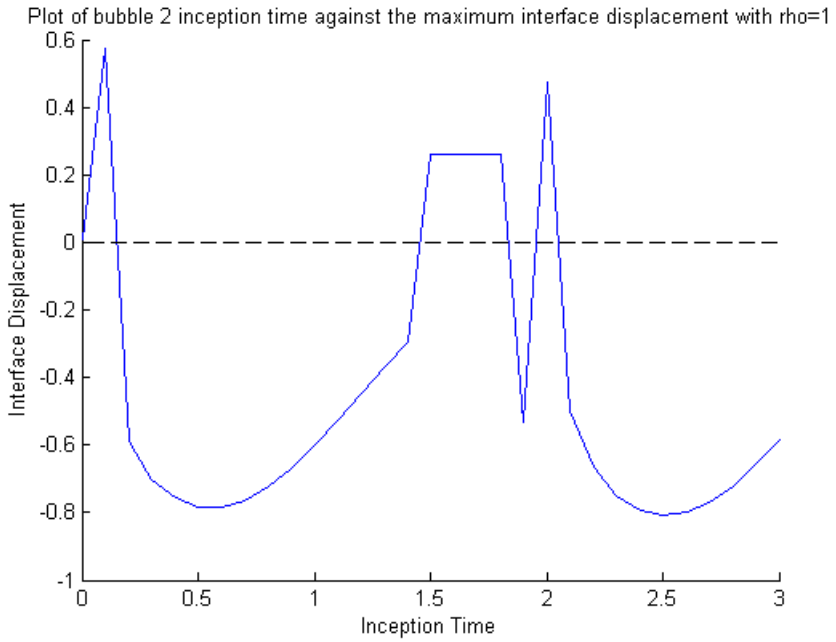


Figure 4.13: Plot of the maximum interface displacement against the inception time of bubble 2 with $\rho = 1$

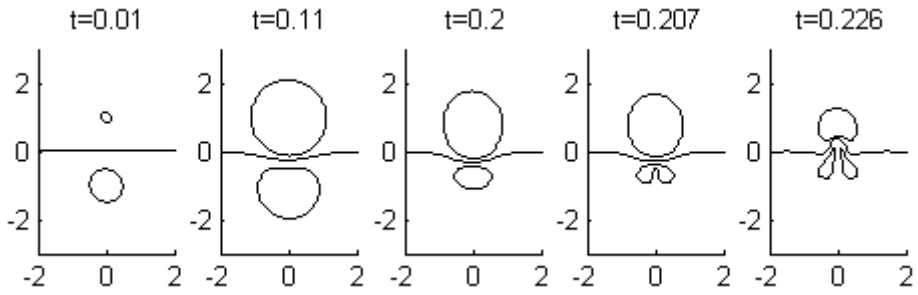


Figure 4.14: Numerical results modelling the collapse of two bubbles in two fluids of equal density. The top bubble has an inception time of $t = 0.1$ while the lower bubble is incepted at time $t = 0$.

When the inception time is increased to 0.2 the catapult effect takes over and the jet from bubble 1 moves away from bubble 2, causing the maximum interface displacement to occur in fluid 1, as seen in figure 4.15(a). After $t = 0.2$, the maximum indent begins to increase with the inception time of bubble 2, until the bubble inception approaches

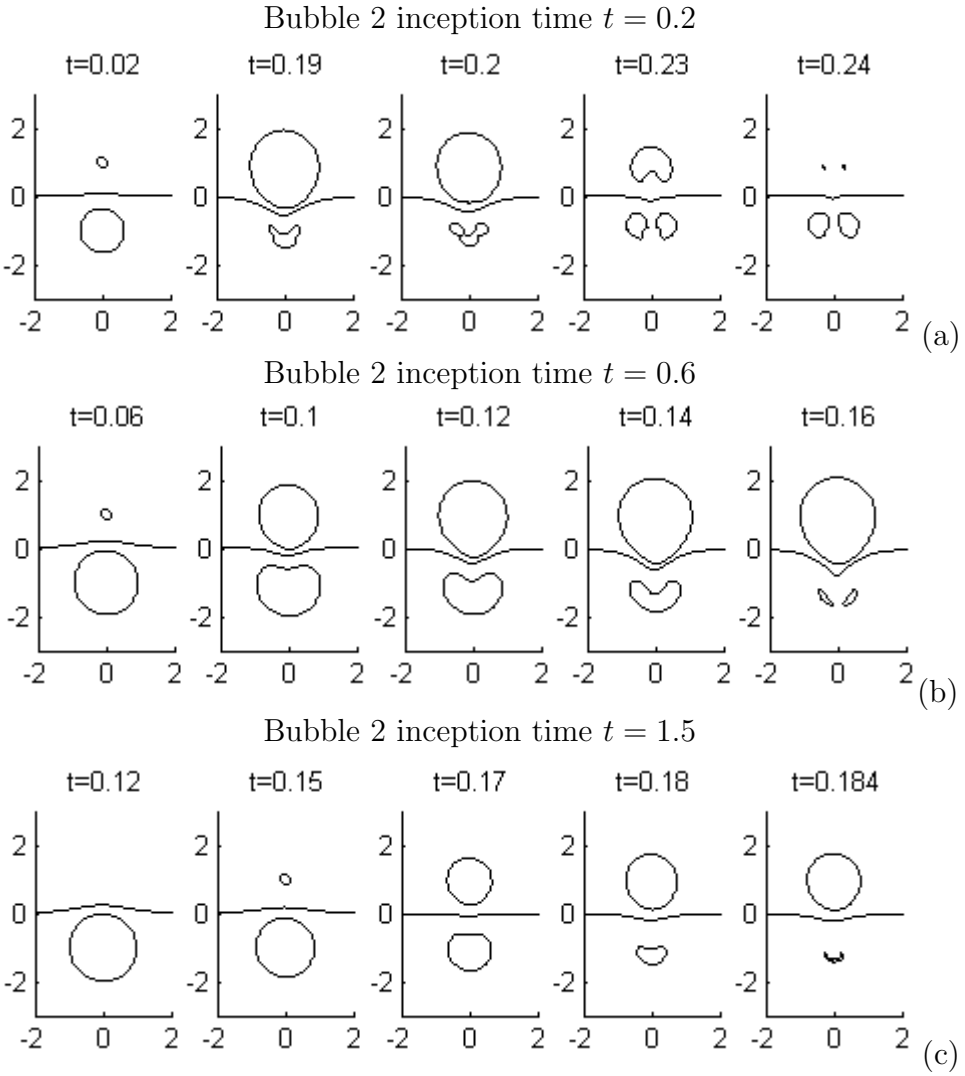


Figure 4.15: Numerical results modelling the collapse of two bubbles in two fluids of equal density. In each case the lower bubble is incepted at time $t = 0$ while the top bubble has an inception time of (a) $t = 0.2$, (b) $t = 0.6$ and (c) $t = 1.5$.

$t = 0.6$. At this time bubble 1 is near maximum radius with a radial velocity approaching zero, shown in the first frame of figure 4.15(b). As bubble 2 expands the surface nearest the interface is the closest to bubble 1 compared to the other inception times. This allows the collapse of bubble 1 to draw bubble 2 closer to the center of bubble 1, which is shown by the maximum displacement of the interface in frame five. For inception times greater than $t = 0.6$, bubble 1 has already begun to collapse when bubble 2 is incepted. Therefore

bubble 2 is not as close to the surface of bubble 1 during the collapse and is not drawn in as far. Causing the maximum displacement to decrease until time $t = 1.5$. For inception times $t = 1.5 - 1.8$ bubble 2 is introduced during the middle of the collapse of bubble 1 as seen in figure 4.15(c). The expansion of bubble 2 forces a rapid collapse of bubble 1, causing the simulation to terminate before any jetting can occur. The maximum interface displacement is given by the expansion of bubble 1 only, hence only a small displacement into fluid 2.

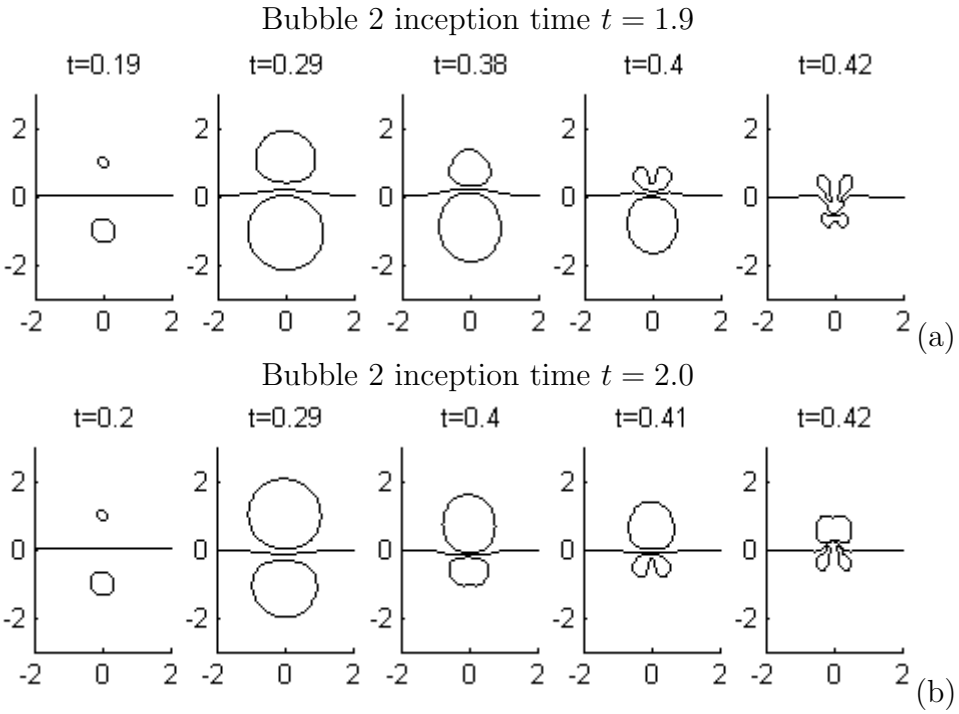


Figure 4.16: Numerical results modelling the collapse of two bubbles in two fluids of equal density. In each case the lower bubble is incepted at time $t = 0$ while the top bubble has an inception time of (a) $t = 1.9$ and (b) $t = 2.0$.

At inception time $t = 1.9$ bubble 1 has almost collapsed to a minimum radius. The expansion of bubble 2 does not force a rapid collapse and the resultant termination of the simulation in this case. Instead the bubbles are out of phase enough to give the same collapse as $t = 0.1$, although in the opposite direction. Hence figure 4.16(a) shows a

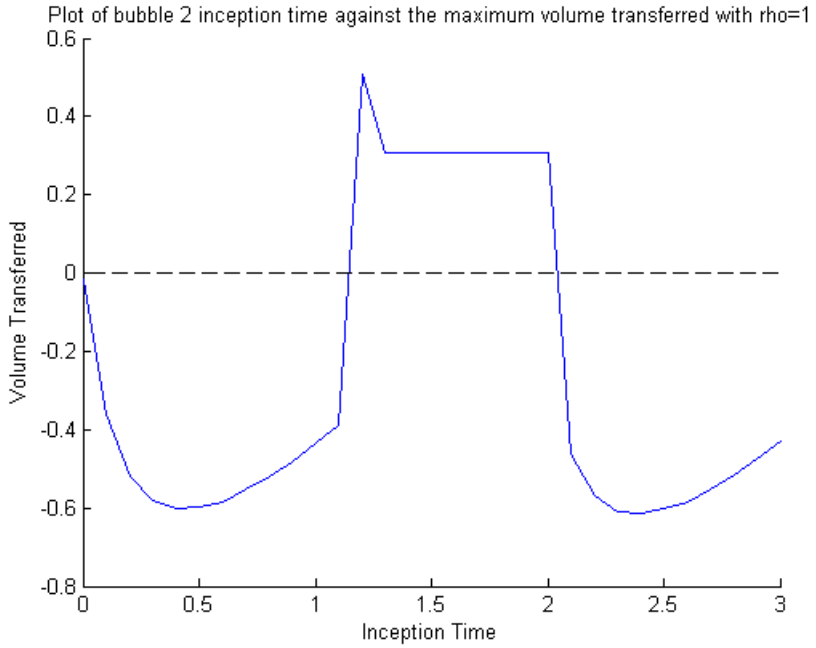


Figure 4.17: Plot of the maximum volume transfer against the inception time of bubble 2 with $\rho = 1$

maximum interface displacement into fluid 1.

Figure 4.16(b) shows that at $t = 2$, bubble 1 has completed one growth and collapse cycle and has begun to grow once more, giving a similar collapse for $t = 0.1$ see previously. Therefore the simulations for times $t = 1.8 - 3.0$ are effectively the same simulations for times $t = 0.0 - 1.0$, as a single bubble in the absence of buoyancy and any other dense fluids will repeat a self-similar life cycle, shown by the plot of a Rayleigh-Plesset bubble in figure 3.1.

A similar pattern appears when considering the maximum volume transferred during the collapse. Figure 4.17 shows the plot of inception time of bubble 2 against the maximum volume transferred, and a repeated pattern is found corresponding to the rebound of bubble 1. However the peak of the graph occurs at $t = 0.4$, less than the peak for maximum interface displacement at $t = 0.6$. As noted in figure 4.12(a), bubble 1 initially moves

fluid 1 into fluid 2 during the expansion phase. When bubble 2 is introduced that fluid is than pushed back into fluid 1 along with more of fluid 2. This bulk of fluid 2 being pushed into fluid 1 gives the maximum volume transferred. When bubble 2 is incepted at $t = 0.4$ bubble 1 has not fully expanded and therefore not pushed much of fluid 1 into fluid 2. Hence the expansion of bubble 2 only pushes fluid 2 into fluid 1 and does not need to push fluid 1 back to the initial position, allowing a greater volume of fluid 2 to be transferred into fluid 1. After $t = 0.4$ bubble 1 is near its maximum radius and has hence pushed a large amount of fluid 1 into fluid 2. The growth of bubble 2 now has to move fluid 1 and fluid 2 beyond $z = 0$ to achieve maximum volume transfer. This can be seen in the plot by a decrease in maximum volume transferred. For inception times $t = 1.2 - 2.0$ the maximum volume transferred comes from the growth of bubble 1 only, similar to the change in maximum interface displacement mentioned previously. After inception time $t = 2.0$ the life cycle of bubble 1 has restarted and the plot repeats.

Therefore, to maximise the distance a fluid is displaced into another, a second bubble with inception time around $t = 0.6$ should be used. However, to maximise the volume of fluid transferred, the inception time of the second bubble should be $t = 0.4$.

## 4.4 Velocity, Pressure and Temperature Analysis

As discussed in this chapter, mixing is an important mechanism which can be used to promote reactions between two different chemical solutions. Though some chemical reactions need more than physical contact with reactants in order to elicit a response. Many reactions require the input of temperature to achieve a particular activation energy to initiate a chemical process. These are called endothermic reactions. Before a mixture has gained enough energy to surpass the required activation energy, the two reactants can sit idle together, with no chemical interaction. Once the activation energy is reached, only

then will the conditions be right to facilitate a response. However, when mixing some fluids, an increase in temperature may want to be avoided.

In some cases the reaction of a substance to an increase in temperature can be violent and sudden. For example, any combustible fluid similar to alcohols, alkenes or other liquid hydrocarbons, can be ignited by rises in temperature. This causes for them to be stored in a control environment and handled carefully during experiments. If the uses of these type of volatile fluids involved interaction with cavitation bubbles, the investigation into the temperatures caused by bubble collapse becomes of great significance. Understanding how to avoid or instigate combustion of a fluid through cavitation dynamics can be beneficial in chemical applications. Other fluids may not react to changes in temperature as violently as an explosive reaction, however a temperature rise can still have a dramatic impact on the substances inside. When considering biological applications, proteins, cells or other biological materials may be suspended in a fluid intended to be mixed with another. Rises in temperature can cause proteins to denature and alter their intended function, rendering them useless, counter-productive or even harmful. Being able to predict whether the mixing process can cause high enough temperatures to cause damage to biological fluids can avoid many failed experiments and possible harm. This gives the motivation to want to find what temperatures can be caused from the collapse of cavitation bubbles.

Various papers have been written on using bubble dynamics to transform the kinetic energy of bubble collapse into other forms of energy. When a single cavitation bubble is introduced into an acoustic cavitation field, the bubble undergoes forced oscillations. With the right frequency and amplitude of the acoustic waves the bubble can achieve much larger radii than its natural maximum radius. This causes very rapid collapse re-

sulting in high pressures and temperatures within the bubble, and can even produce light through sonoluminescence [24] [38]. This allows for chemical reactions to be driven by sound through the process of sonochemistry [53] where extremely high temperatures can be "generated within an otherwise cold liquid" [54]. Sonochemistry can be seen in many different fluids and therefore has a wide array of applications. Storey and Suslick [51] [52] have examined argon and water vapour bubbles within a body of water to see what effect the water vapour within the bubble has on the temperatures achieved. While Oxley et al. [41] have achieved high temperatures in ionic liquids through similar applications of ultrasound to bubbles within the fluid, leading to decomposition of the ionic liquids. The examples considered so far involve the collapse of acoustically driven spherical bubbles, though it has been found, by Calvisi et al. [13], that nonspherical collapse can "achieve similar peak temperatures". Though an acoustic field is needed to supply the bubble with sufficient energy to produce the high temperatures seen in sonoluminescence and sonochemistry, an increase in pressure and temperature can still occur by the collapse of a bubble without external interference. It has been seen in figure 3.5 that high pressures can be achieved by the collapse of a bubble near a rigid boundary, which in turn will produce and increase in temperature. Quinto-Su et al. [49] found that moderate temperature increases can occur when a bubble collapse in a microfluidic gap or when in the vicinity of a single rigid boundary. Yuan and Prosperetti [61] found siginificant inrease in temperature can be found within the tip of a jet formed by a collapsing bubble near a rigid wall. It has been seen in this chapter that collapses similar to the rigid boundary case occur from the interactions between two bubbles separated by a fluid-fluid interface, therefore similar pressure and temperature analysis can be implemented.

The velocities in the fluid domain are obtained from the velocity potentials computed numerically at each time step, and the pressures are found by way of Bernoulli's equation,

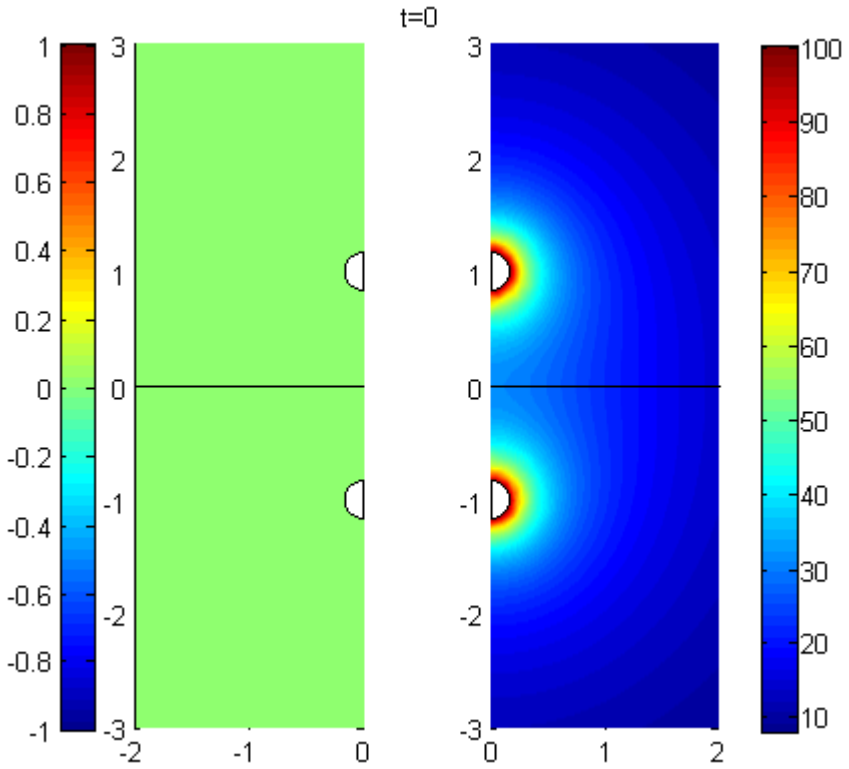


Figure 4.18: Plot of the velocities and pressures for two bubbles at $t = 0$.

as before. The temperatures within the bubble can be found by substituting the pressures obtained into the ideal gas law,

$$T = \frac{pV}{Rn}, \tag{4.4.1}$$

where $T$ is temperature, $p$ is bubble pressure, $V$ is bubble volume, $R$ is the universal gas constant and $n$ is the number of moles of substance within the bubble. To give an indication to the scale of temperatures obtained in bubble collapse, the average pressure on the bubble surface will be multiplied by the bubble volume at that time. More accurate values can be obtained once the composition of the bubbles contents have been established. Hence, temperature will be considered using the equation, $T = pV$, with moles and the universal gas constant neglected.

The greatest pressures are usually found when the bubble is nearest its minimum volume, which occurs either when the bubble is first generated or at the end of its collapse. As mentioned in section 4.2, when the strength of bubble 2 exceeds $\varepsilon = 200$, the simulation terminates before either bubble collapses. Hence the greatest pressures during these simulations are found at $t = 0$, when the simulations are first run. Both bubbles are incepted with equal bubble radius and with an initial surface velocity potential of $\phi = 0$, giving the velocity and pressure profiles shown in figure 4.18. The average pressure inside both bubbles is $p = 100.1$ with a volume of $V = 0.01883$. Therefore for every simulation the initial temperature of both bubbles is given as $T = 1.886$, which will be referred to as $T_0$. This value for temperature will be used as a comparison for other temperature values observed during the bubbles lifetimes.

The faster the collapse of a bubble, the greater the pressures inside the bubble will become. For simulations with a calmer collapse, the greatest temperature readings will be found at $t = 0$, therefore only simulations where the temperatures exceed $T_0 = 1.886$ will be analysed. When the strength of bubble 2 is set as $\varepsilon = 50$ both bubbles become toroidal near the end of the collapse as seen in figure 4.2. At this stage the pressures within bubble 1 reach $p = 227.6$ at a volume of $V = 0.01047$ giving a temperature value of $T = 2.384$. Figure 4.19 shows the velocities and pressures at the end of the simulation. Bubble 1 has fully collapsed yielding high pressures in the fluid domain. Upon the surface of the bubble the pressures are high enough to give a spike in temperature greater than $T_0$.

When the strength of bubble 2 is $\varepsilon = 60$ the bubble collapse is not violent enough to have any pressure readings higher than when the bubbles are first initiated, as seen in figure 4.18. Increasing the strength of bubble 2 to $\varepsilon = 70$ gives lower overall pressures within the fluid domain, which is shown in figure 4.20(a). The greatest pressure occurs on the

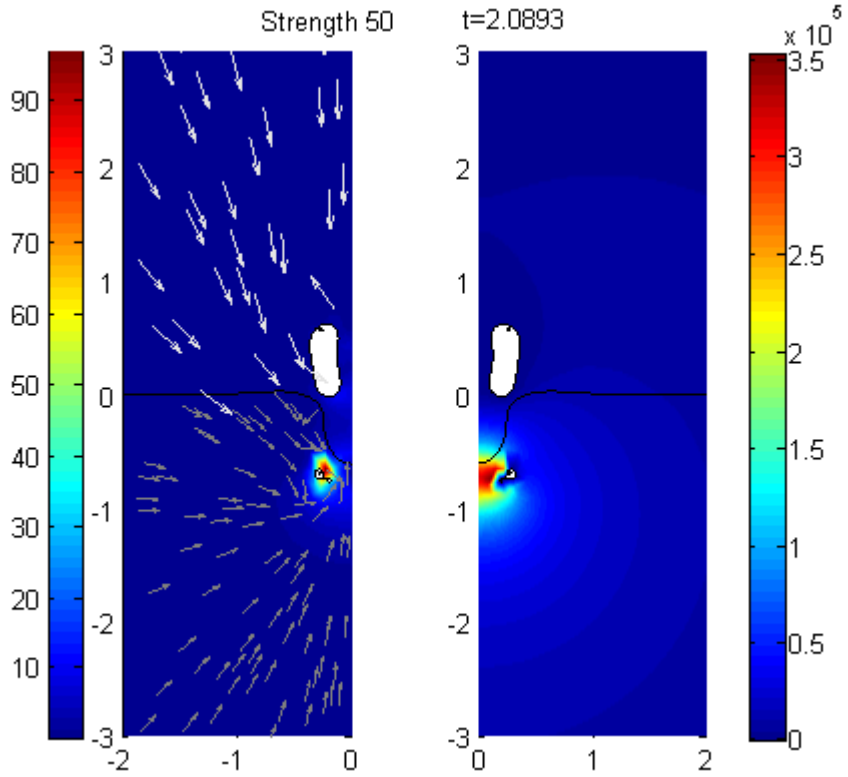


Figure 4.19: Plot of the velocities and pressures for two bubbles near the end of the simulation at $t = 2.0884$. Where bubble 1 has a strength of $\varepsilon = 100$ and bubble 2 has strength $\varepsilon = 50$.

interface with values around $p = 750$, however on the surface of bubble 1 the pressures reach $p = 311.7$. The volume of the bubble at this time is $V = 0.00837$. This increase in maximum pressure from $\varepsilon = 50$ is enough to counter the decrease in bubble volume to yield an increase in bubble temperature to $T = 2.609$.

Further increase of the strength of bubble 2 to $\varepsilon = 80$ gives the maximum bubble surface pressure seen for any of the strength simulations considered in section 4.2. Figure 4.20(b) shows the bubble collapse at the end of the simulation. This time the pressures seen in the fluid domain are greater than those seen for $\varepsilon = 70$, yet less than those seen for $\varepsilon = 50$. Upon the surface of bubble 1 the pressure reaches $p = 807.9$, much greater than the two previous simulations, with a smaller bubble volume of $V = 0.00424$. This give a temperature value of $T = 3.424$, almost double the initial bubble temperature $T_0$.

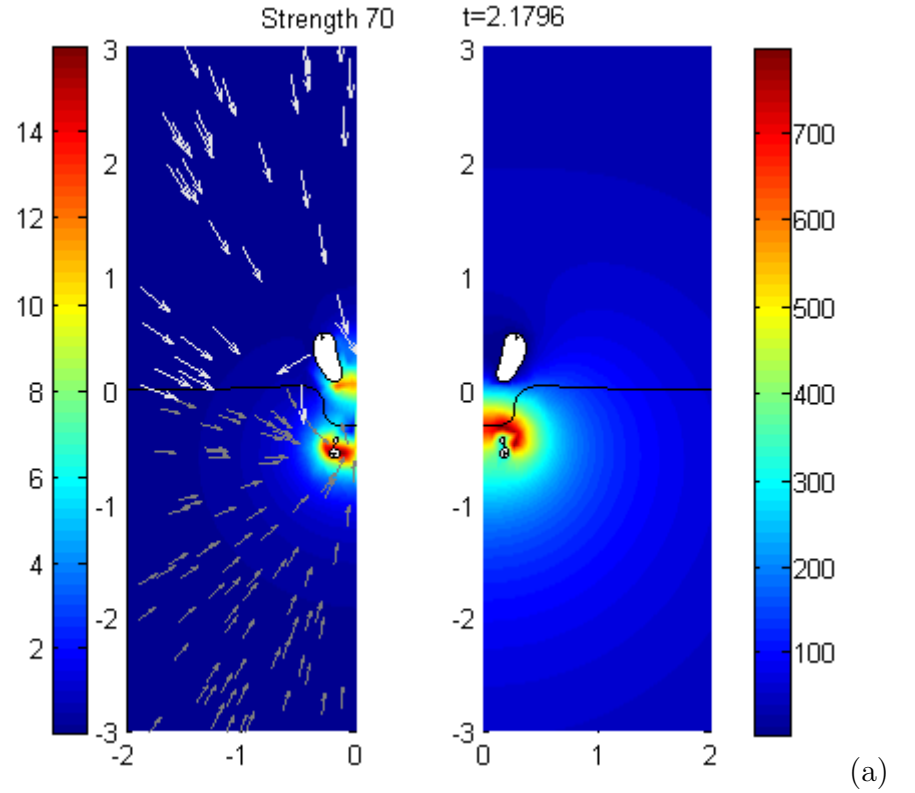


Figure 4.20: Plot of the velocities and pressures for two bubbles near the end of the simulation. Where bubble 1 has a strength of $\varepsilon = 100$ and bubble 2 has strength (a) $\varepsilon = 70$ at time $t = 2.1796$ and (b) $\varepsilon = 80$ at time $t = 2.2224$.

This temperature value agrees with Szeri et al. [55] who, while considering single bubble collapse near a rigid wall, found temperature increases between three and five times the initial temperature depending on bubble stand-off distance. Simulations for greater strengths of bubble 2 give much lower bubble temperatures, with the only two other maximum temperatures greater than $T_0$ being found at $\varepsilon = 100$ and $\varepsilon = 110$ with bubble 1 temperatures of $T = 2.035$ and 1.921 respectively. Although for greater strengths of bubble 2 the simulations terminate before any notable bubble collapse, a spike in temperature will be seen in similar experiments when the bubble collapses to minimum radius, due to the inevitable increase in bubble pressure. Unfortunately the modelling method used in this thesis does not propagate far enough to tell whether this spike will be lesser or greater than the initial $T_0$. From the simulations observed, an increase in temperature can usually be found when the strength of bubble 2 is sufficiently low enough to allow for a complete collapse of bubble 1.

Temperature spikes are also found when delaying the inception of bubble 2. Introducing bubble 2 at $t = 0.1$ causes bubble 1 to collapse and jet into fluid 2 as seen in figure 4.14. This jet then causes bubble 2 to collapse toroidally, as seen in figure 4.21. The collapse then produces a pressure of $p = 132.7$ at a volume of $V = 0.2592$, giving an internal temperature of $T = 2.044$. This is a small increase on the initial temperature of bubble 1, $T_0 = 1.886$. However, the maximum temperature of bubble 1 does not exceed $T_0$ as the simulation terminates before the complete collapse of bubble 1. Therefore, increases in temperature can be caused within the fluid domain even by a slight delay of $t = 0.1$ to the inception time of bubble 2.

Further increasing the inception time gives a dramatic increase in pressure on the surface of the bubble. Figure 4.22 shows the velocity and pressure plots for inception times of

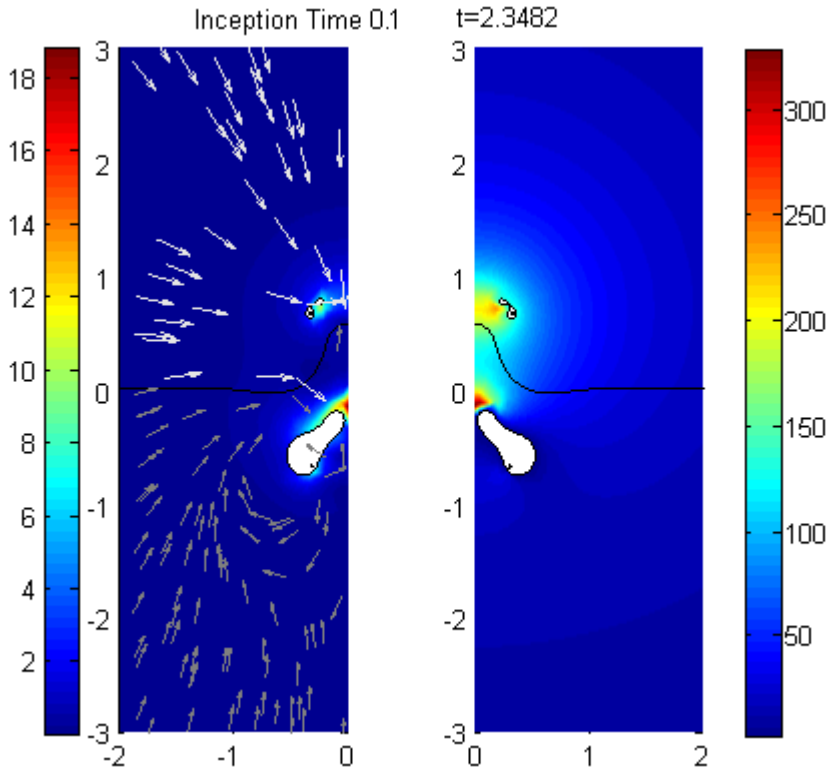


Figure 4.21: Plot of the velocities and pressures for two bubbles near the end of the simulation at $t = 2.3482$. Where bubble 1 has a inception time $t = 0$ and bubble 2 has inception time $t = 0.1$.

bubble 2 $t = 0.2$ and $t = 0.3$. When bubble 2 is incepted at $t = 0.2$ the collapse yields much higher pressures of around 4500 within the fluid domain compared to $t = 0.1$, with pressures on the surface of bubble 2 reaching $p = 638.6$. While bubble 2 seen in figure 4.22(a) is still very small, it has a greater volume of $V = 0.8936$ than that seen for $t = 0.1$. This gives a much larger increase in maximum temperature of $T = 3.202$, simply by delaying the inception of bubble 2 another 0.1 dimensionless time units. Delaying a further 0.1 to $t = 0.3$, as in figure 4.22(b), sees a large drop in the overall pressures seen in the fluid domain to a maximum of around 700. However, the pressure on the surface of bubble 2 has only dropped marginally to $p = 603.9$, while the volume has increased to $V = 1.279$. Though this increase in volume is proportionally smaller than the drop in pressure giving a large, yet lesser, bubble temperature of $T = 3.151$.

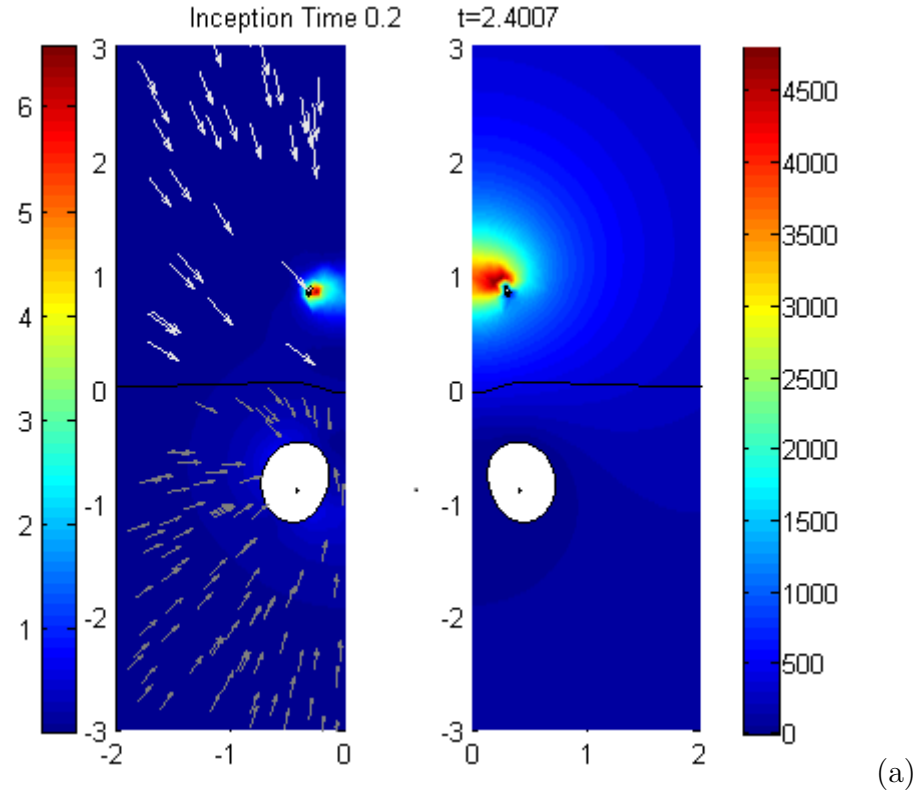


(a)

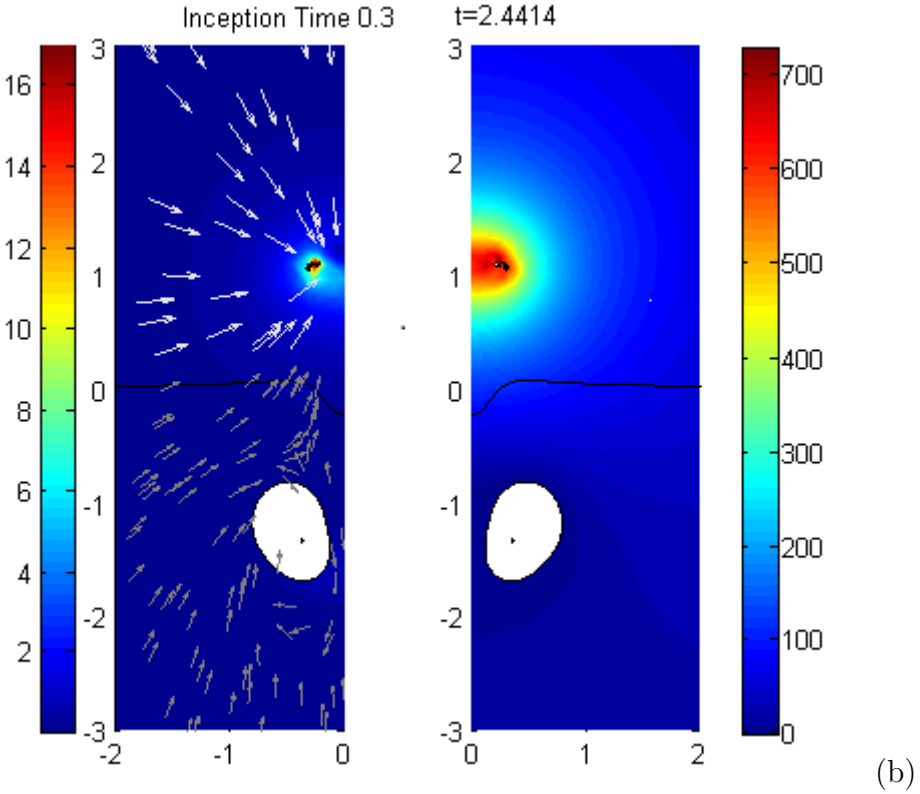


(b)

Figure 4.22: Plot of the velocities and pressures for two bubbles near the end of the simulation. Where bubble 1 has a inception time $t = 0$ and bubble 2 has inception time (a) $t = 0.2$ and (b) $t = 0.3$.

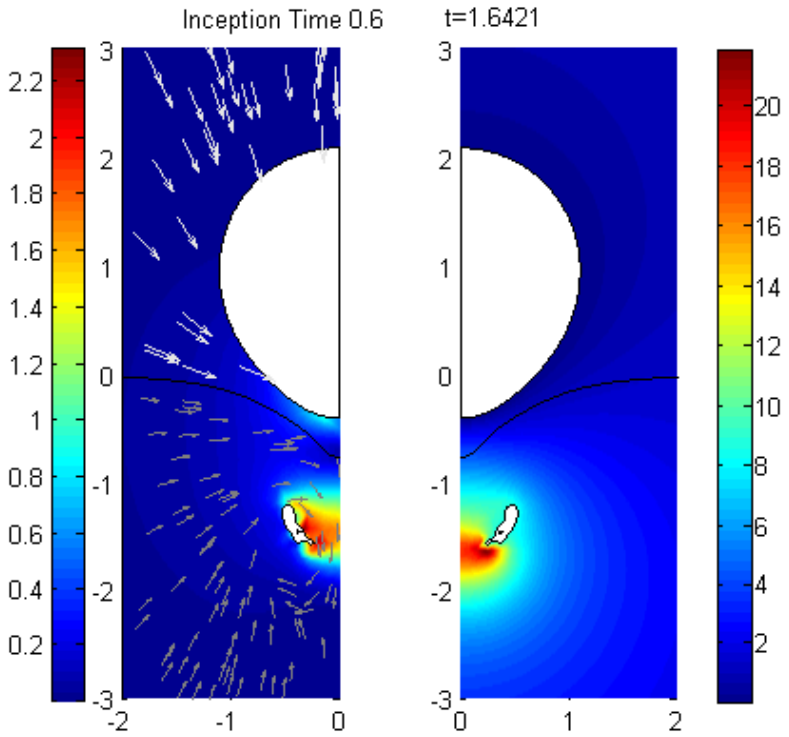


Figure 4.23: Plot of the velocities and pressures for two bubbles near the end of the simulation at $t = 1.642$. Where bubble 1 has a inception time $t = 0$ and bubble 2 has inception time $t = 0.6$.

Further increasing the inception time of bubble 2 does not see the maximum temperatures increase past the initial $T_0$. This is due to bubble 2 being incepted nearer the maximum radius of bubble 1, causing a slow collapse of bubble 1 as seen for $t = 0.6$ in figure 4.15(b). This gives small velocities and low surface pressure on bubble 1 of $p = 9.646$ during the collapse shown in figure 4.23. This collapse causes a temperature of $T = 0.9664$ within the bubble, which is almost half of the initial temperature of $T_0 = 1.886$. When the inception time is increased further to $t = 1.0$ the catapult effect occurs, allowing for bubble 1 to rebound and bubble 2 to collapse slowly. Figure 4.24(a) shows the velocity and pressure plots of the bubbles when bubble 1 has collapsed to minimum volume moments before it begins to rebound, as noted by the velocity direction away from bubble 1. The pressures

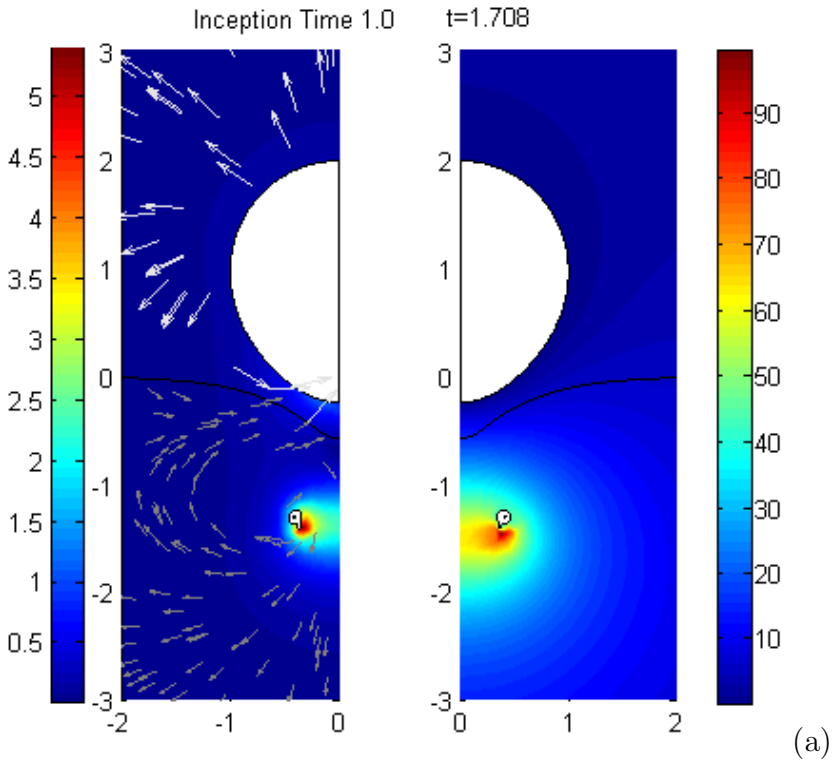


Figure 4.24: Plot of the velocities and pressures for two bubbles near the end of the simulation. Where bubble 1 has a inception time $t = 0$ and bubble 2 has inception time $t = 1.0$ seen at (a) $t = 1.708$ and (b) $t = 2.437$.

on the surface of bubble 1 are $p = 43.14$ with a volume of $V = 0.0344$, giving a bubble temperature of $T = 1.4825$ before the rebound. The next bubble collapse occurs for bubble 2 at $t = 2.437$, as seen in figure 4.24(b). The velocities are slightly lower than those seen for the rebound of bubble 1, with much lower pressures in the fluid domain. On the surface of bubble 2 the pressures are $p = 5.570$ with a volume of $V = 0.148$, giving a temperature of $T = 0.8260$. The temperatures achieved for the collapses of bubbles 1 and 2 are not greater than the initial value of $T_0$, and therefore are of little significance.

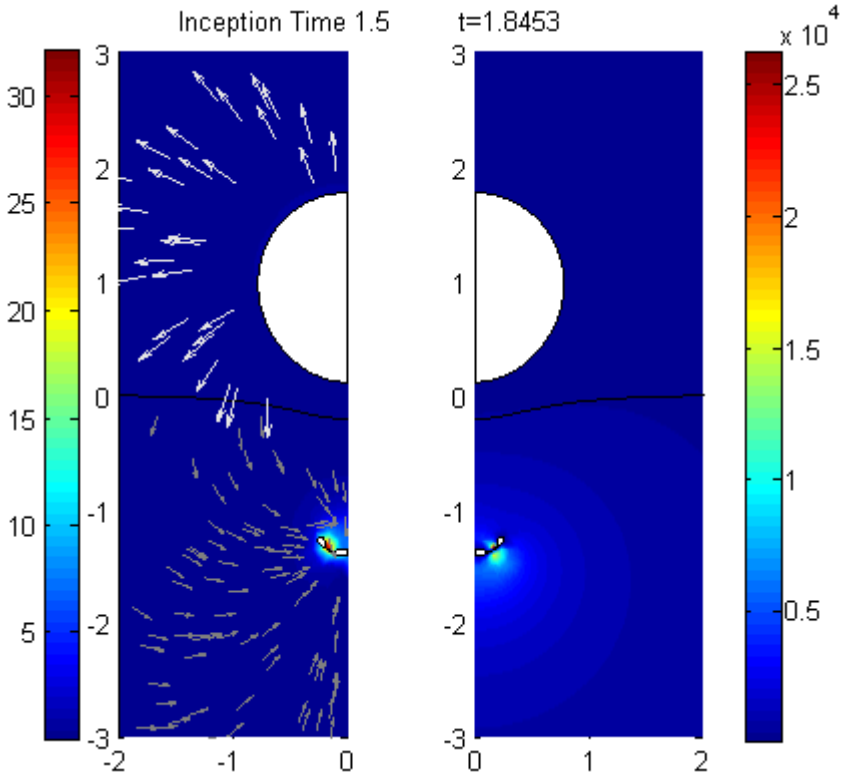


Figure 4.25: Plot of the velocities and pressures for two bubbles near the end of the simulation at $t = 1.8453$. Where bubble 1 has a inception time $t = 0$ and bubble 2 has inception time $t = 1.5$.

The next peaks in temperature above $T_0$ occur when the inception time of bubble 2 is $t = 1.2 - 1.9$, where the introduction of bubble 2 causes rapid collapse of bubble 1. This fast collapse increases the temperature within bubble 1 to reach a maximum of $T = 2.754$

for inception time $t = 1.2$, with similar a result for inception time $t = 1.5$ as seen in figure 4.15(c). Once the expansion of bubble 2 has forced an early collapse of bubble 1, the velocities and pressures within the fluid domain become large, shown in figure 4.25. The pressure on the surface of the bubble reaches $p = 350.9$ with a volume of $V = 0.0077$ giving the temperature $T = 2.698$, similar to the temperature found for $t = 1.2$. These peaks continue for $t = 1.9$ where the temperature reaches the similar value of $T = 2.648$. As mentioned in section 4.3, past inception time $t = 2.0$ bubble 1 has completed one full cycle and begins to expand again. Therefore similar temperature spikes occur, reaching temperatures of $T = 2.993$ and $T = 3.166$ for inception times $t = 2.1$ and $t = 2.3$ respectively. These values are comparable with those obtained for $t = 0.2$ and $t = 0.3$. Therefore adjusting the inception times of two bubbles can yield an increase in the temperature of the fluid.

To aid in the chemical reaction of two fluids, temperatures can be raised to increase the reactivity of the substances and achieve the necessary activation energies. By using bubbles of different strength or by offsetting their inception times, two bubbles can collapse with enough velocity to create high enough pressures, to produce spikes in the temperature of the bubble. Thus producing a higher overall temperature within the fluid domain.

## 4.5 A Comparison of Both Bubble Strength and Inception Time

A series of simulations were run for strengths of bubble 2 ranging from $\varepsilon = 50 - 290$ in increments of 10 and inception times of bubble 2 ranging from $t = 0.0 - 1.0$ in increments of 0.1. It is unnecessary to consider inception times beyond $t = 1.0$ due to the repeating nature of the spherical bubble shown in figures 4.13 and 4.17.

Figure 4.26 shows the plot of the strength of bubble 2 against the maximum interface

displacement for inception times $t = 0.0 - 0.1$. Inception time $t = 0.0$ was discussed previously and can be seen on the plot. It shows the drop in maximum interface displacement and a change in direction of the displacement at strength $\varepsilon = 220$, which is caused when the strength of bubble 2 becomes too great and the rapid collapse of bubble 1 forces the simulation to end. However, when the inception time is increased to $t = 0.1$ the drop occurs at the lower strength of $\varepsilon = 130$. As bubble 1 expands its radial velocity decreases, when bubble 2 is introduced at $t = 0.1$ bubble 1 has begun to decelerate. This allows bubble 2 to force bubble 1 to collapse earlier than if both bubbles were incepted at $t = 0$, causing the change in maximum interface displacement at $\varepsilon = 140$.

Greater inception times force the collapse of bubble 1 even earlier, giving no maximum interface displacement from the jetting of the bubbles. This is shown on the plot by an increasing maximum interface displacement into fluid 1 as strength increases. However, this increase appears to level out at an interface displacement of $z = 1$ bubble radii.
As inception time increases to $t = 0.6$, the maximum interface displacement also increases with strength and tends to $z = 1$ faster, shown in 4.26(a). When inception time is more than $t = 0.6$ the maximum interface displacement begins to decrease, as seen in figure 4.26(b). This is due to $t = 0.6$ being the optimum time for the catapult effect to have greatest impact. This is also seen in figure 4.27, where for all strengths, the maximum bubble radius is achieved at inception time $t = 0.6$.

When considering the maximum volume transferred, optimal mixing occurs for different parameters. Figure 4.28 shows the plot of the inception time of bubble 2 against the maximum volume of fluid transferred across the initial interface for strengths $\varepsilon = 50 - 290$. It can be seen that the maximum volume transfer occurs at $t = 0.6$ for the smaller strengths, as seen for strength $\varepsilon = 100$ in figure 4.17. Increasing the strength sees the

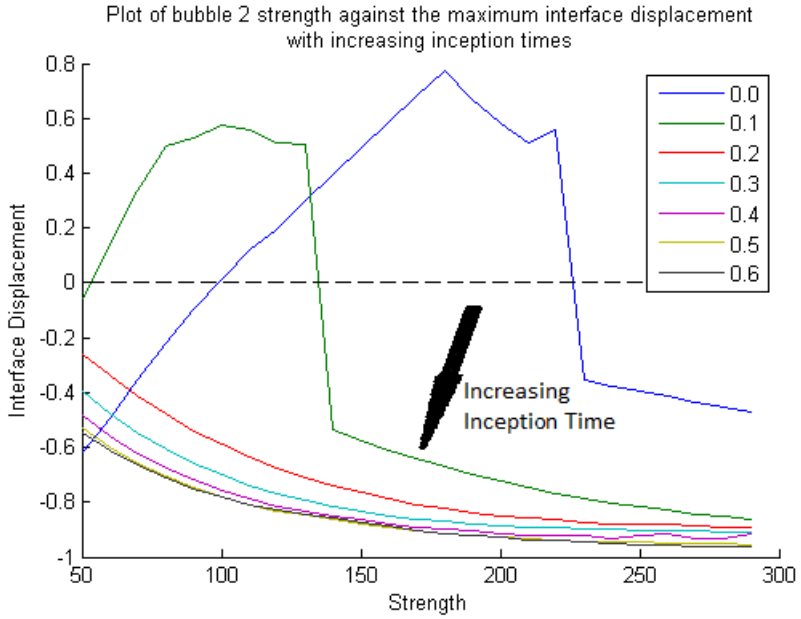


(a)

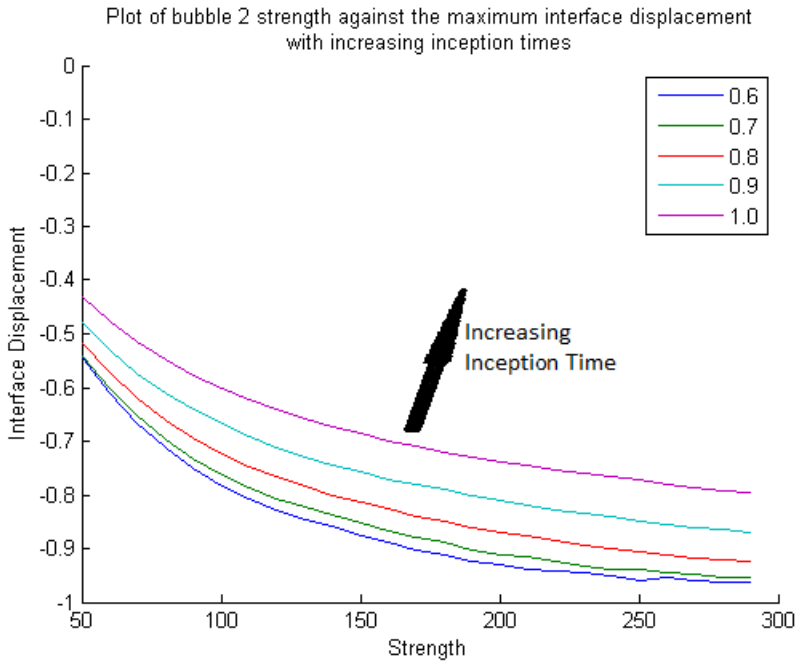


(b)

Figure 4.26: Plots of the time of the maximum interface displacement against the strength of bubble 2 for (a) inception times $t = 0 - 0.6$ and (b) inception times $t = 0.6 - 1$.

maximum volume transfer occurring at decreasing inception times from $t = 0.6$ to $t = 0.1$. For the higher strengths the maximum volume transferred occurs at inception time $t = 0.1$, corresponding to the conditions for bubble 2 to expand with little opposition from bubble

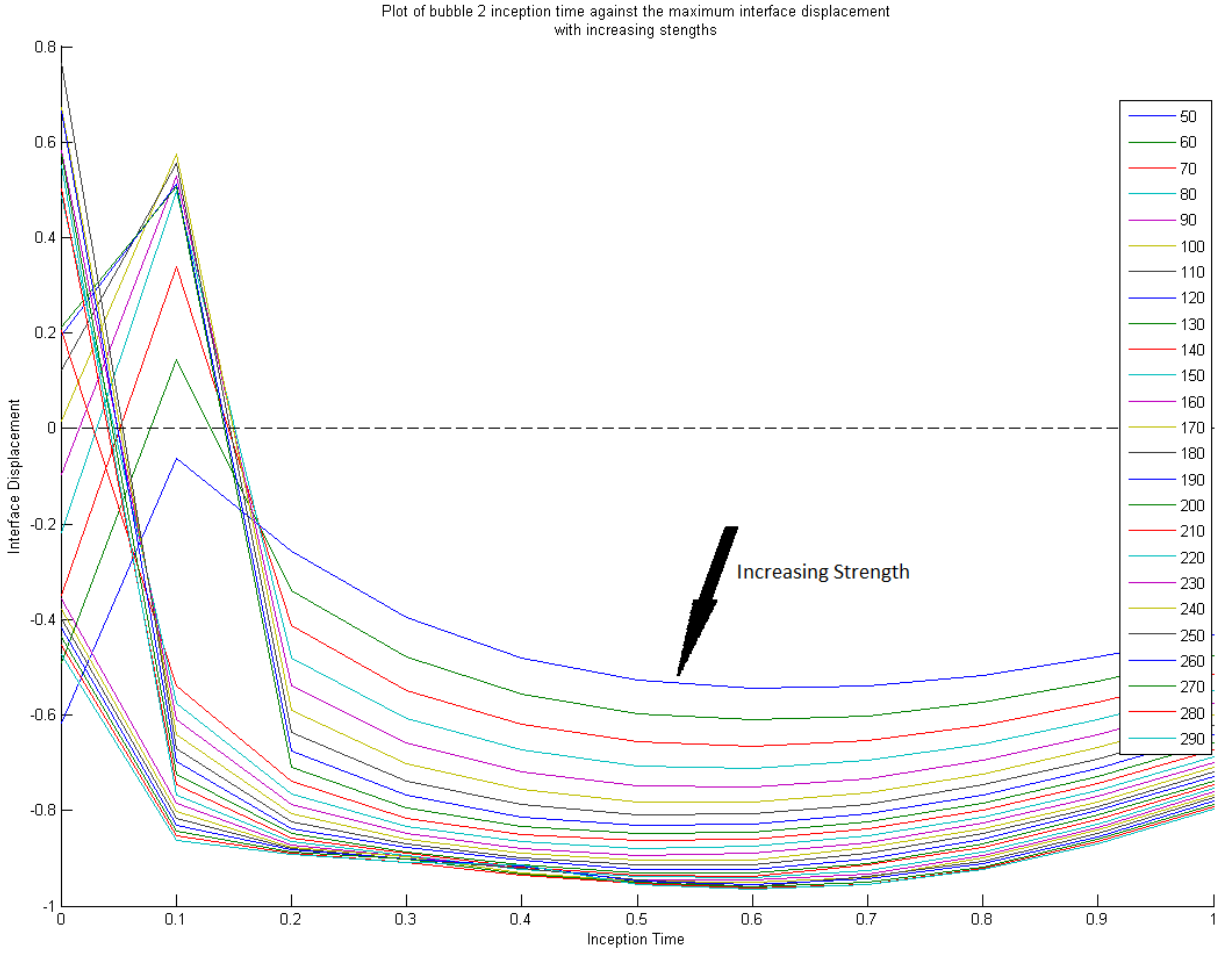


Figure 4.27: Plot of the time of the maximum interface displacement against the inception time of bubble 2 for strengths 50 to 290.

1. For inception time $t = 0.0$, bubble 1 is still in the rapid expansion phase at the beginning of its lifespan, allowing it to counter the amount the interface is deformed by bubble 2. For inception times greater than $t = 0.1$, bubble 1 has grown to a large enough size to push the interface into fluid 2. Thus increasing the amount bubble 2 has to push the interface back into fluid 1, giving a lower maximum volume transferred. This naturally increases with inception time as bubble 1 can push more of fluid 1 into fluid 2, without the intervention of bubble 2. The maximum volume transferred also increases with strength as the maximum volume is given when bubble 2 pushes fluid 2 into fluid 1. Therefore increasing the strength of bubble 2 will move more fluid.

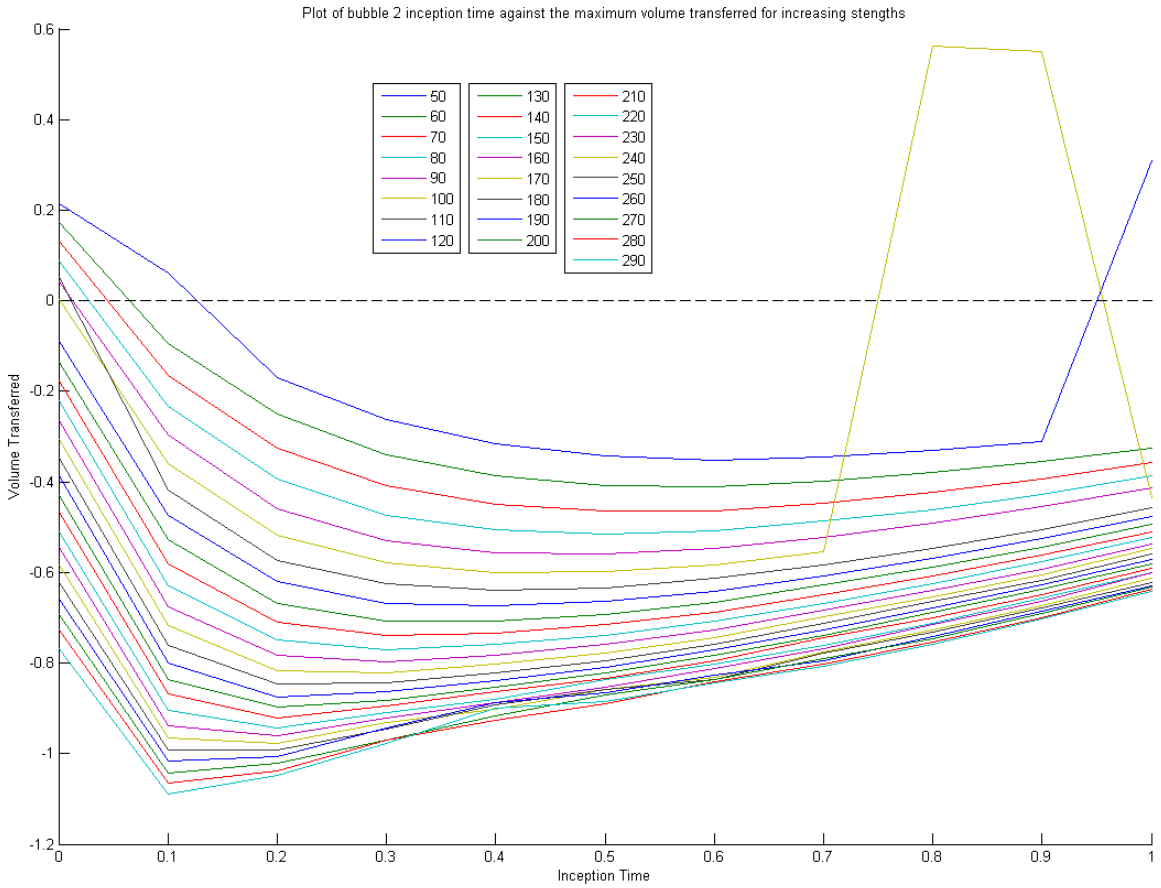


Figure 4.28: Plot of the time of the maximum interface displacement against the inception time of bubble 2 for strengths 50 to 290.

The exception to the trend appears for strengths $\varepsilon = 100$ at inception times $t = 0.8, 0.9$. The equal strength of the bubbles and the inception of bubble 2 near the maximum radius of bubble 1 allows for the rebound of bubble 1 after the jetting stage of its collapse. This rebound pushes fluid 1 back into fluid 2 to register as the maximum volume transferred. The change in pattern for strength $\varepsilon = 50$ at inception time $t = 1.0$ is due to the amount of fluid 2 transferred becoming low enough to be comparable to the amount of fluid 1 transferred.

Therefore, to maximise the distance a fluid is displaced into another, the second bubble should be incepted at $t = 0.6$ with a strength of around $\varepsilon = 290$. However, to maximise

the volume of fluid transferred, the strength of the second bubble will again be $\varepsilon = 290$, though it should be incepted at $t = 0.1$.

## 4.6 Mixing Fluids of Different Densities

The two fluids considered thus far have been of equal density, giving a density ratio across the interface of $\rho = 1$. Though experimentally it is unlikely to have two different fluids with the same densities. The wide range of applications of mixing in mobile labs and Lab on a Chip devices could involve the mixing of dense fluids, for example blood or glycerol, with less dense fluids, for example alcohol or white spirit. To fully explore the method of two bubble interaction of the purpose of mixing, different density ratios must be considered.

### 4.6.1 Different Densities, Different Strengths

To ensure that the effect of density ratio is fully investigated the range of density ratios $\rho =$ 0.4, 0.6, 0.8, 0.909, 1.0, 1.1, 1.5, 2.0, 3.0 are used. This will allow for any commonalities or patterns in the results to be compared, despite some of the extreme values having little or no physical representation. As before, the strength of the second bubble is varied and multiple scenarios are modelled. Figure 4.29 shows the plot of the strength of bubble two against the maximum interface displacement for various density ratios.

For $\rho = 0.4$ the plot is very simple, the maximum interface displacement occurs when fluid 1 is pushed into fluid 2. This is due to fluid 1 being the denser fluid for this density ratio, therefore as bubble 1 expands the interface is pushed upwards with little resistance from the less dense fluid 2. This can be seen in figure 4.30(a) for bubble 2 strength $\varepsilon = 50$. As the strength of bubble two increases, the maximum interface displacement decreases slightly. Figure 4.30(b) shows that the stronger bubble 2 becomes the more it resists the

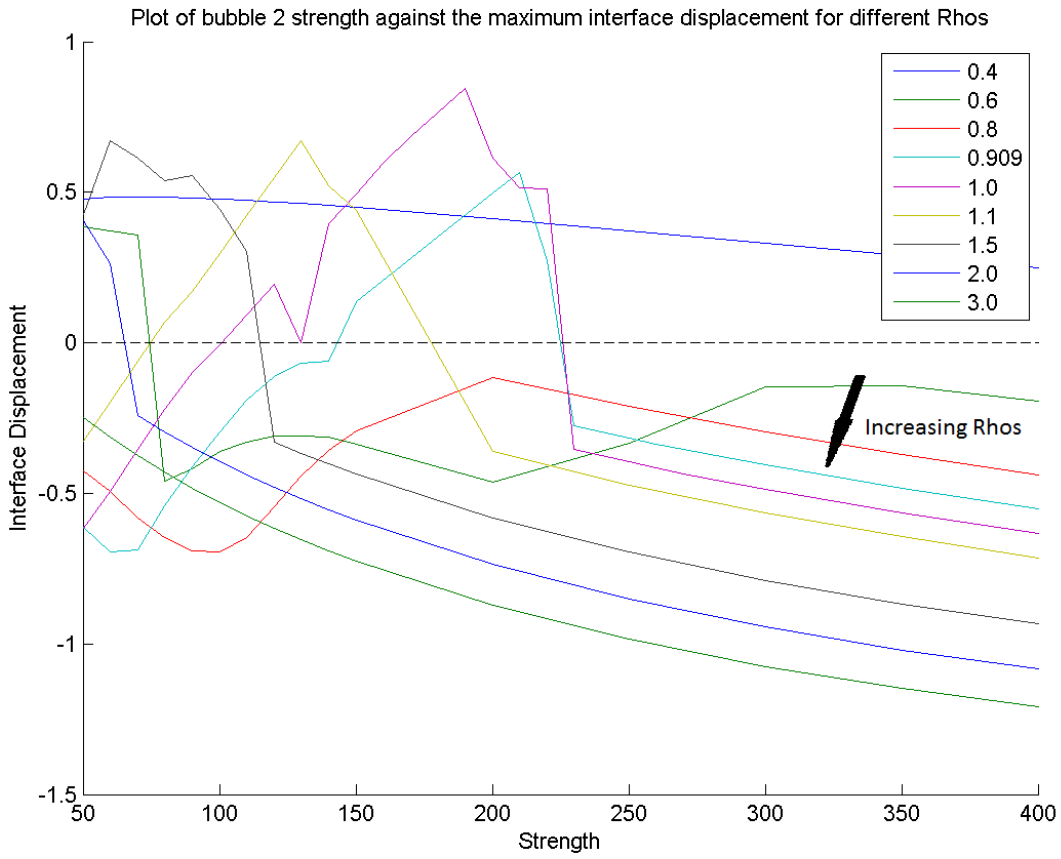


Figure 4.29: Plot of the maximum interface displacement against the strength of bubble 2 for densities $\rho = 0.4$ to 3.0.

expansion of bubble 1 in the denser fluid, causing the gradual decline seen on the plot. The rapid and generally unhindered expansion of bubble 1 causes the simulations to end before the collapse stage of either bubble has an effect on the interface. Though it can be seen that bubble 2 is in the process of jetting towards fluid 1 and bubble 1, due to the Bjerknes forces between a bubble towards a denser fluid and another bubble. The jet produced by bubble 2 is unlikely to resist the expansion of bubble 1 beyond the simulations run time. This gives reason to believe that the plot aptly shows that the most amount of

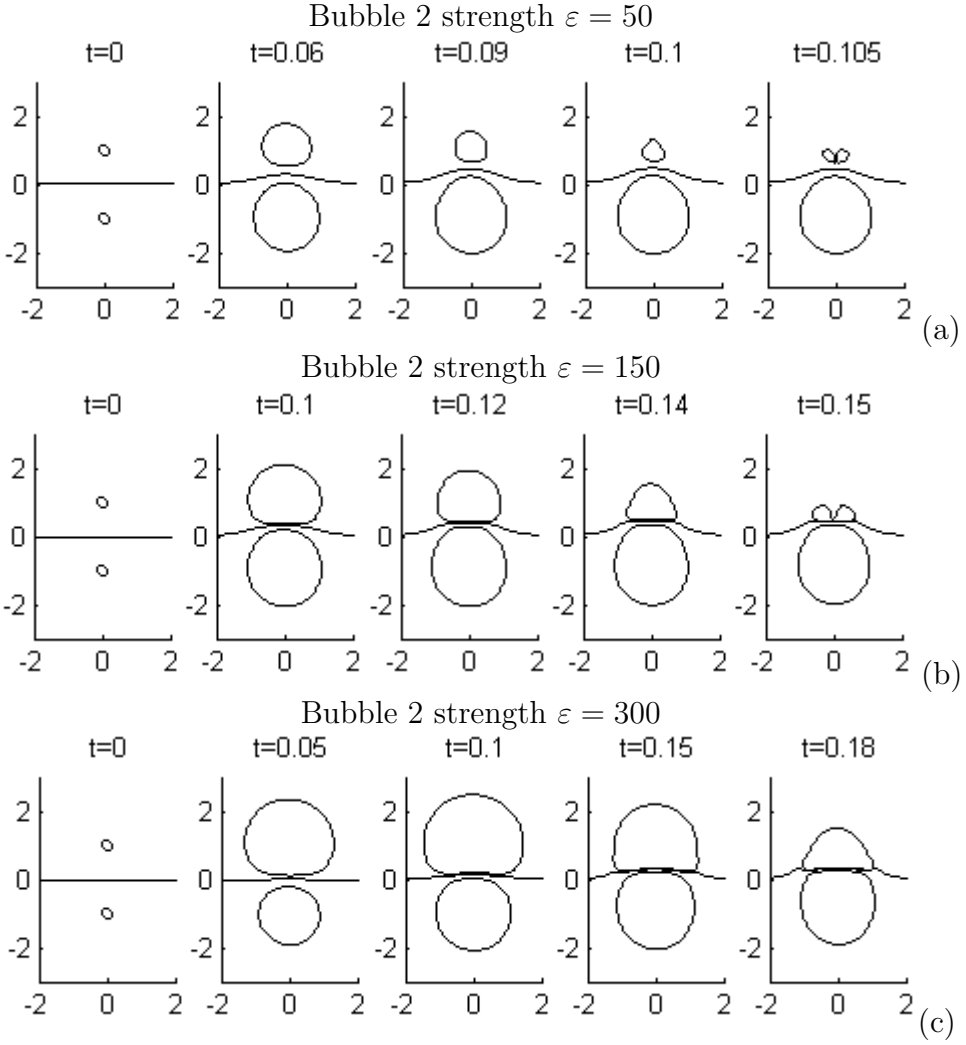


Figure 4.30: Numerical results modelling the collapse of two bubbles in two fluids with density ratio $\rho = 0.4$. In each case the lower bubble has strength $\varepsilon = 100$ while the top bubble has strength (a) $\varepsilon = 50$, (b) $\varepsilon = 150$ and (c) $\varepsilon = 300$.

mixing will occur from the expansion stage of bubble 1 when fluid 1 is injected into fluid 2, for a density ratio of $\rho = 0.4$.

Increasing the density ratio to $\rho = 0.6$ changes the plot drastically. When the strength of bubble 2 is $\varepsilon = 50 - 70$, less than bubble 1, the maximum density interface occurs in fluid 2. Figure 4.31(a) shows the plots when the strength of bubble 2 is $\varepsilon = 50$. This is similar to the collapse of the bubbles seen for density ratio $\rho = 0.4$ mentioned previously, the

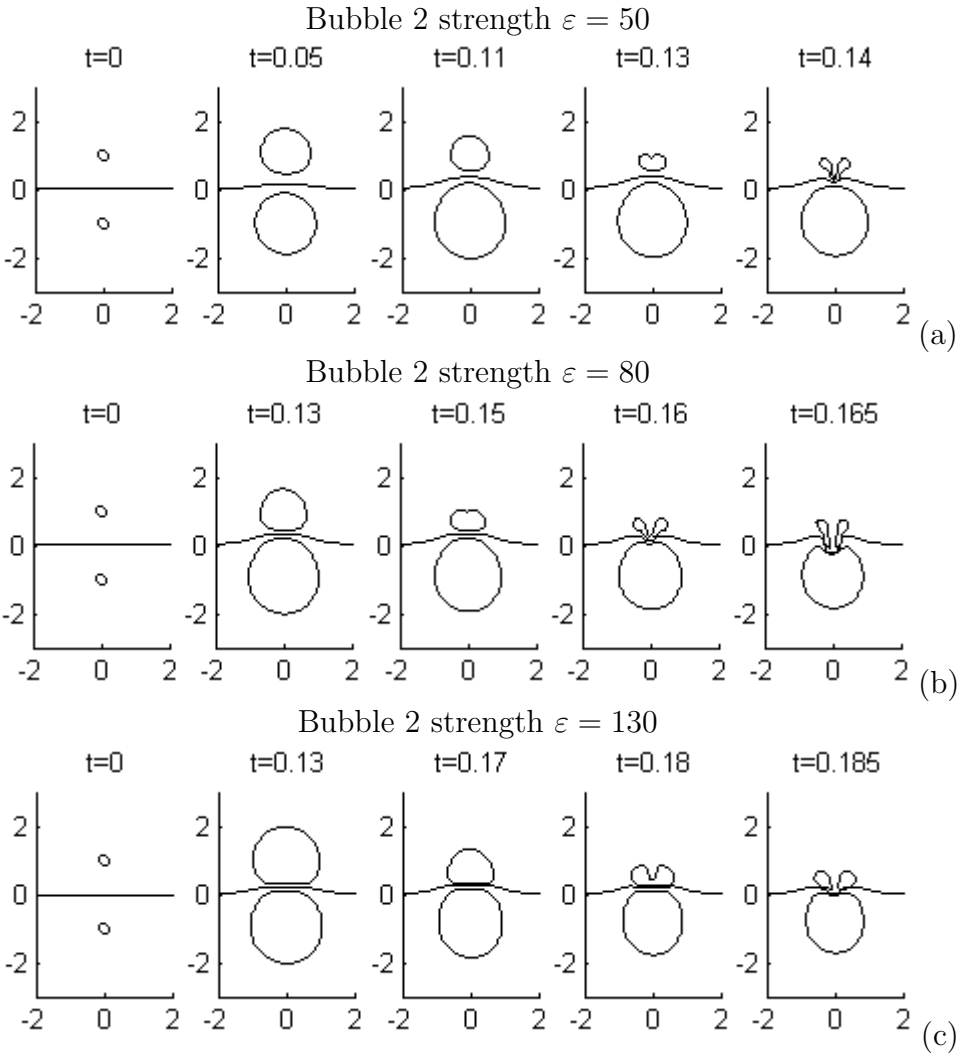


Figure 4.31: Numerical results modelling the collapse of two bubbles in two fluids with density ratio $\rho = 0.6$. In each case the lower bubble has strength $\varepsilon = 100$ while the top bubble has strength (a) $\varepsilon = 50$, (b) $\varepsilon = 80$ and (c) $\varepsilon = 130$.

expansion of bubble 1 pushes fluid 1 into fluid 2, with little hindrance from the weaker bubble 2 or the less dense fluid 2. As the strength of bubble 2 is increased past $\varepsilon = 80$, as in figure 4.31(b), the growth of bubble 1 is lessened by the expansion of bubble 2. Fluid 2 is then pushed into fluid 1 by the impact of the fluid jet formed by bubble 2 during its collapse phase. The simulation ends when the jet pushes the interface onto the surface of bubble 1. In the physical world, this jet of fluid 2 would continue further into fluid 1 through bubble 1. In figure 4.31(c), as the strength of bubble 2 approaches $\varepsilon = 130$ the maximum interface displacement decreases, this is due to the attraction of bubble 1 to bubble 2 through Bjerknes forces overcoming the repulsion of bubble 1 from a less dense fluid. This brings bubble 1 closer to the interface, hence the fluid jet from the collapse of bubble 2 causes the interface and the surface of bubble 1 to touch sooner, which terminates the simulation earlier compared to the lesser strengths of bubble 2.

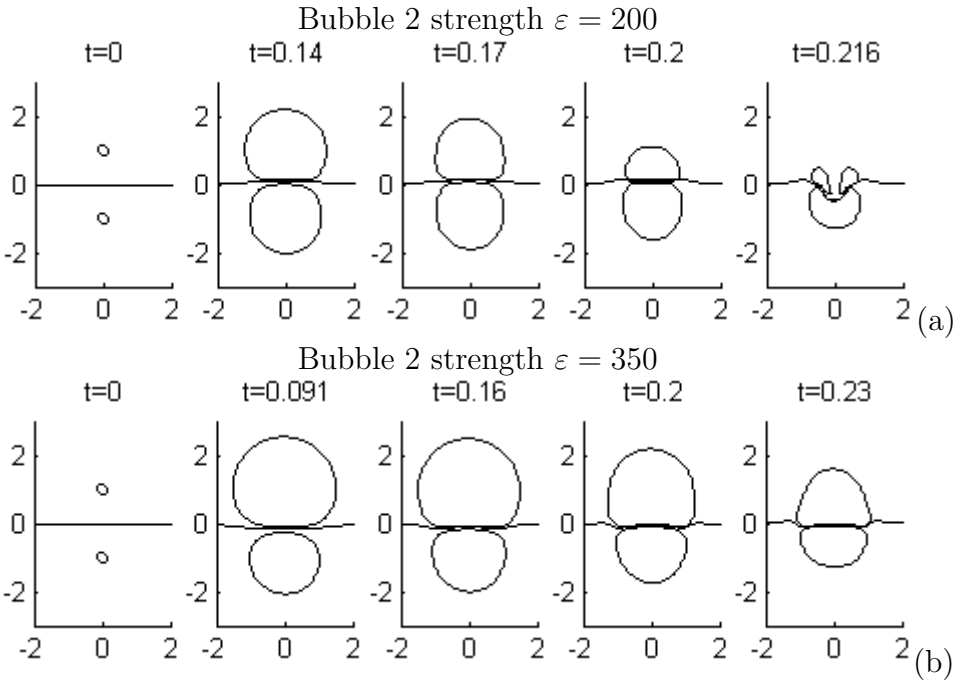


Figure 4.32: Numerical results modelling the collapse of two bubbles in two fluids with density ratio $\rho = 0.6$. In each case the lower bubble has strength $\varepsilon = 100$ while the top bubble has strength (a) $\varepsilon = 200$ and (b) $\varepsilon = 350$.

When the strength of bubble 2 increases further to $\varepsilon = 200$, there is an increase in the maximum interface displacement. Figure 4.32(a) shows that this is caused by the expansion stage of fluid 2 pushing more fluid outwards as its strength increases. This decreases the maximum size bubble 1 achieves enough to increase the time it takes the interface and the surface of bubble 1 touch, which as before terminates the simulation. Therefore allowing the fluid jet to progress further into fluid 1. When the strength of bubble 2 is increased again to $\varepsilon = 350$ the maximum interface displacement decreases once more, this time due to bubble 2 expanding faster and interacting with the interface. Beyond $\varepsilon = 350$ the maximum interface displacement is only caused by the growth of bubble 2, with no bubble jetting occurring before termination as seen in figure 4.32(b).

The simulations created with density ratio $\rho = 0.8$ are similar to those for $\rho = 0.6$, except for small strengths of bubble 2, where the maximum interface displacement occurs in fluid 2. As the density of fluid 2 is greater than previously, bubble 1 does not achieve as great a maximum radius as before. This stops the maximum interface displacement being the result of the expansion of bubble 1, as the case for $\rho = 0.6$ with strengths $\varepsilon = 50 - 70$. The rest of $\rho = 0.8$ shows the same trend with an initial decrease in maximum interface displacement in fluid 1 (around $\varepsilon = 100$ in figure 4.33(a)) then a rise (around $\varepsilon = 200$ in figure 4.33(b)) due to displacement caused by the growth stage of bubble 2, as seen for $\rho = 0.6$. The difference being that each strength for $\rho = 0.8$ has a greater maximum displacement and the trend occurs for lower strengths of bubble 2. With bubble 2 being incepted in a denser fluid than before, it has less resistance from fluid 1 and can therefore penetrate further, accounting for the increase in interface displacement from $\rho = 0.6$ to 0.8. The shift in the trend to lower strengths of bubble 2 is caused by the change in Bjerknes forces. The increase in density ratio creates a greater attraction for bubble 1 to fluid 2, therefore bubble 1 will remain closer to the interface and therefore the termination

seen for $\rho = 0.6$ will occur for lower strengths of bubble 2. For large strengths of bubble 2, greater than $\varepsilon = 200$, the plot shows an increase in maximum interface displacement into fluid 1 with strength. This increase is consistent with the fluid displaced by the expansion of bubble 2, as seen in figure 4.33(c).

Increasing the density ratio continues to increase the maximum interface displacement into fluid 1, and also continues to shift the previous trend to lower strengths. However,

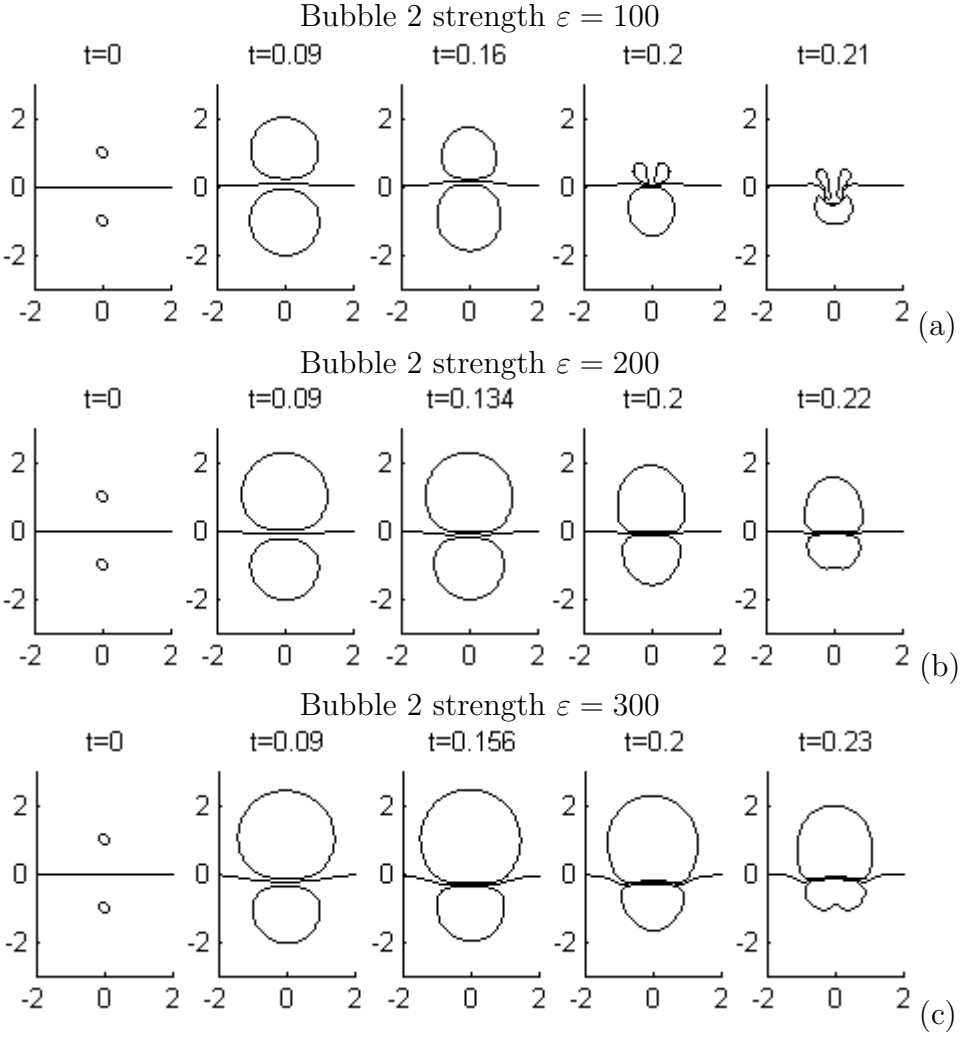


Figure 4.33: Numerical results modelling the collapse of two bubbles in two fluids with density ratio $\rho = 0.8$. In each case the lower bubble has strength $\varepsilon = 100$ while the top bubble has strength (a) $\varepsilon = 100$, (b) $\varepsilon = 200$ and (c) $\varepsilon = 300$.

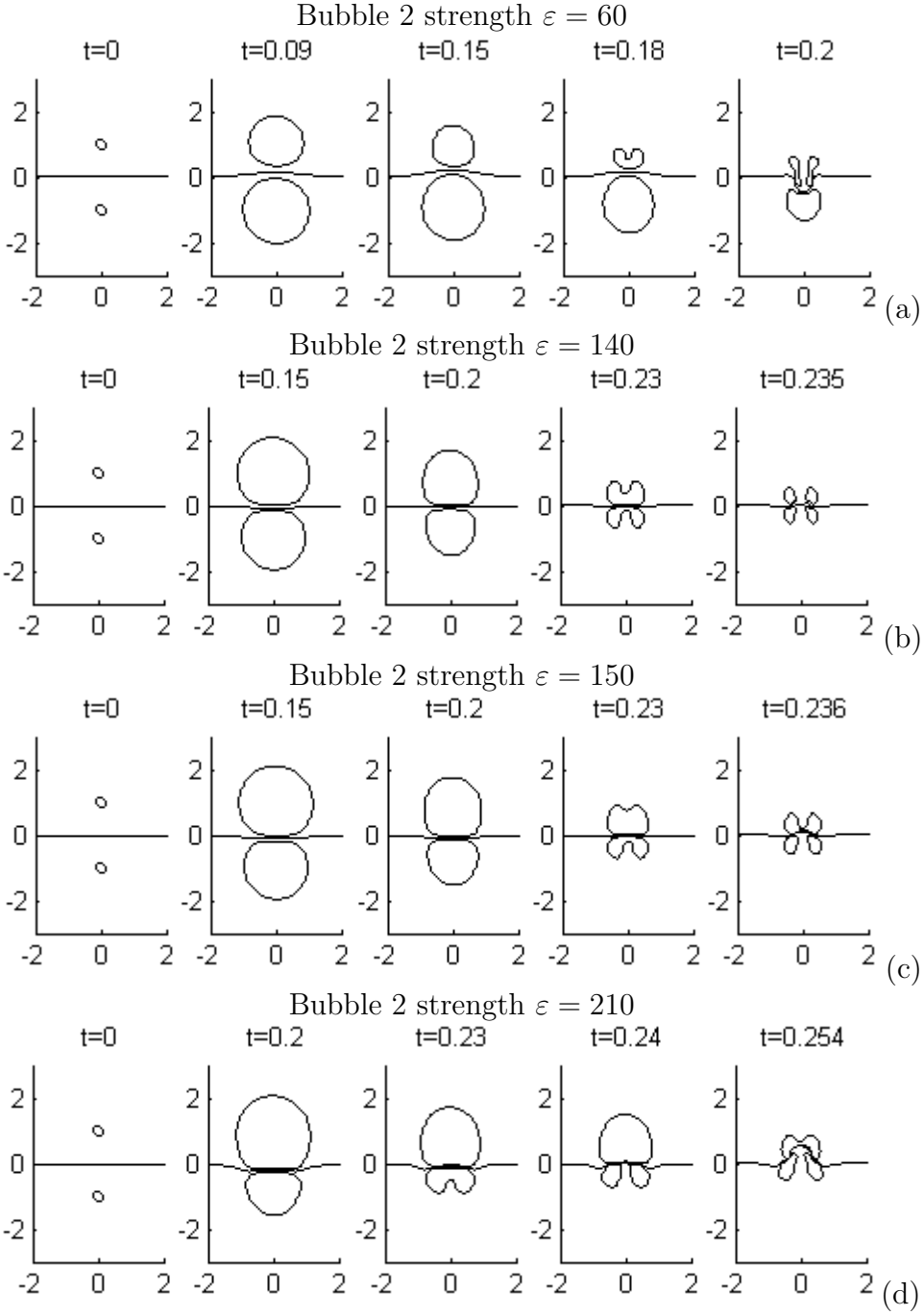


Figure 4.34: Numerical results modelling the collapse of two bubbles in two fluids with density ratio $\rho = 0.909$. In each case the lower bubble has strength $\varepsilon = 100$ while the top bubble has strength (a) $\varepsilon = 60$, (b) $\varepsilon = 140$, (c) $\varepsilon = 150$ and (d) $\varepsilon = 210$.

after the drop in maximum interface in fluid 1, the maximum now occurs in fluid 2. For density ratio $\rho = 0.909$ the interface displacement decreases from a trough at bubble 2

strength $\varepsilon = 60$ to $\varepsilon = 140$, at which point the maximum interface displacement changes to occur in fluid 1 at $\varepsilon = 150$ (shown in figure 4.34(a), (b) and (c) respectively). As the density ratio gives both fluids near equal density, the interaction between the two bubbles now becomes the main driving force in the mixing process. The increase in strength of bubble 2 exhibits a greater attraction on bubble 1, causing bubble 1 to collapse towards bubble 2 before the collapse of bubble 2. This is shown in the plot by the interface moving into fluid 2. Increasing the strength of bubble 2 increases this attraction, giving a greater maximum interface displacement into fluid 2 until it reaches 0.56 bubble radii at strength $\varepsilon = 210$ in the last frame of figure 4.34(d). As the strength of bubble 2 increases, its rate of expansion becomes rapid enough for the surface of bubble 2 to touch the interface before the impact of the jet from bubble 1. Thus terminating the simulation, which is shown by the decrease in maximum interface displacement in fluid 2 at strength $\varepsilon = 220$. For greater strengths the interface displacement is once again in fluid 1, caused by the expansion of bubble 2. As the density ratio increases to $\rho = 1$ and beyond, the peak in maximum interface displacement in fluid 2 continues to occur for lower strengths, consistent with the shifting trend mentioned previously.

When the density ratio is increased beyond $\rho = 1$, making fluid 2 the denser fluid, more of the maximum interface displacements for each density appear in fluid 1. As mentioned previously, these displacements are caused by the growth stage of bubble 2. Increasing the density increases the attraction of bubble 1 to fluid 2 through Bjerknes forces, causing bubble 1 to collapse towards the interface before the collapse of bubble 2. The jet produced by bubble 1 pushes the interface onto the surface of bubble 2 and terminates the simulation. Thus only maximum interface displacement from the growth stage of bubble 2 is recorded. For greater strengths of bubble 2, the jet of bubble 1 becomes weaker due to the faster expansion of bubble 2. In some cases, for example $\rho = 2$ with $\varepsilon \geqslant 250$ or

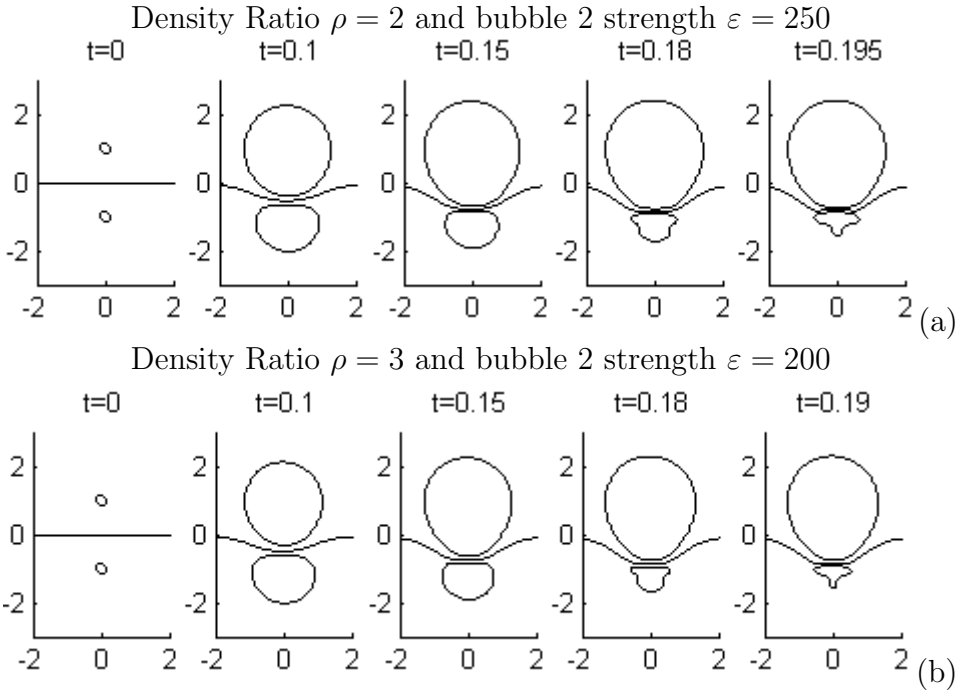


Figure 4.35: Numerical results modelling the collapse of two bubbles in two fluids with (a) density ratio $\rho = 2$ and $\varepsilon = 250$, and (b) density ratio $\rho = 3$ and $\varepsilon = 200$.

$\rho = 3$ with $\varepsilon \geqslant 200$, the expansion of bubble 2 is strong enough to negate the jet from bubble 1 completely, causing bubble 1 to collapse in from the sides as seen in figure 4.35.

As the maximum interface displacements are only caused by the growth stage of bubble 2, the plots show a steady increase in interface displacement with the strength of bubble 2. This can be seen for all densities for large strengths of bubble 2. As the density of fluid 2 increases so does the maximum interface displacement of fluid 2 into fluid 1, noted by the arrow on the plot for increasing densities. This becomes more evident when looking at the plot of maximum volume transferred against the strength of bubble 2 for various density ratios. Figure 4.36 shows the plot of maximum volume transferred against the strength of bubble 2 for various density ratios. It has already been mentioned previously for $\rho = 1$ in Section 4.2 that the maximum volume transferred often comes from the growth stage of the stronger bubble, which can also be seen here for the other density ratios. There

are some variations for densities around $\rho = 1$ at lower bubble strengths which can be attributed to the jetting process, though the trend sees an increase in volume transferred for increasing strengths of bubble 2 along with an overall increase in all values for an increase in density ratio.

By checking density ratios above and below $\rho = 1$ for equal densities, a more effective approach can be made for mixing two fluids of different densities. As the density ratio is given by $\rho = \rho_2/\rho 1$, where $\rho_1$ and $\rho_2$ are the densities of fluids 1 and 2 respectively, the density ratio $\rho = 0.4$ gives fluid 2 as 0.4 times less dense than fluid 1. Inversely, a

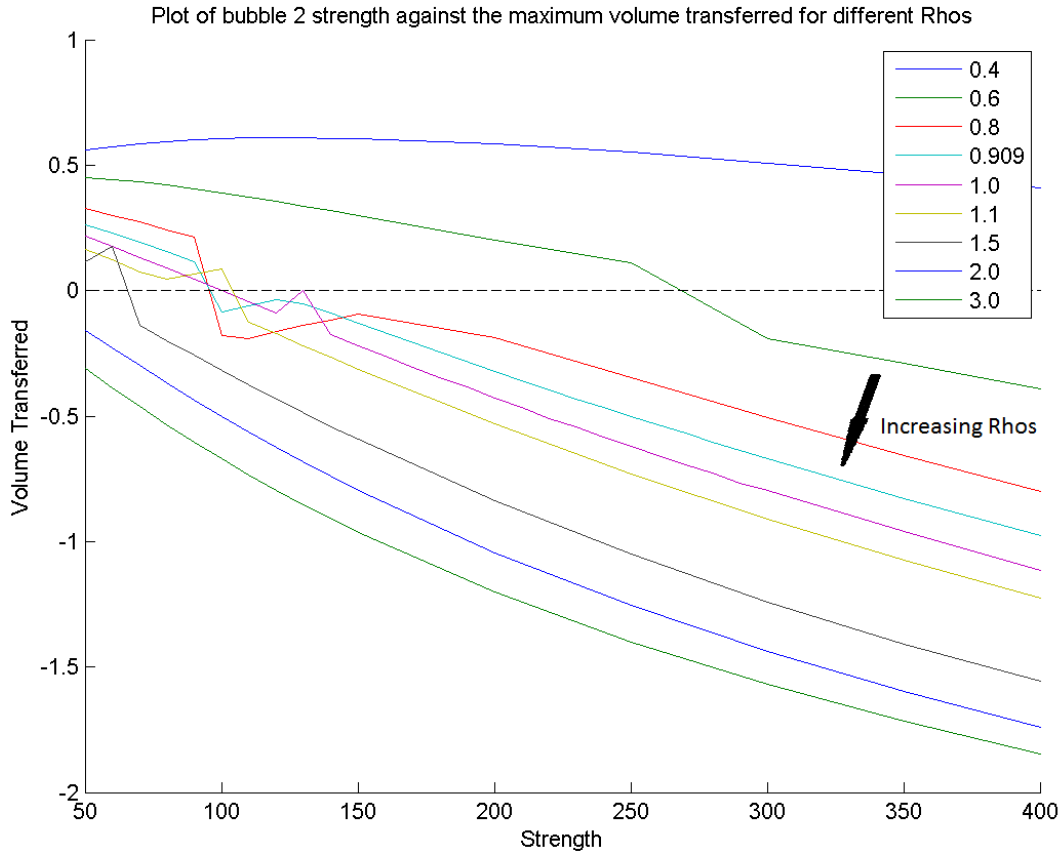


Figure 4.36: Plot of the maximum volume transferred against the strength of bubble 2 for densities $\rho = 0.4$ to 3.0.

density ratio of $\rho = 2.5$ will give fluid 1 as 0.4 times less dense than fluid 2. By comparing the magnitude of the amount of volume transferred for $\rho = 0.4$ with $\rho = 2$, it can be seen from the plots that introducing the stronger bubble into the denser fluid will promote the most amount of mixing. This statement mainly applies to the mixing in both plots caused by the growth phase of the stronger bubble. Though it can be seen by comparing the peaks of $\rho = 0.909$ and $\rho = 1.1$ (as $1/1.1 = 0.909$) in figure 4.29, that the greater maximum interface displacement occurs for $\rho = 1.1$, giving backing to the notion that the stronger bubble in the denser fluid gives the greater amount of mixing.

| Density Ratio $\rho$ | Maximum Displacement | | | Maximum Volume Transfer | | |
|---|---|---|---|---|---|---|
| | Strength $\varepsilon$ | Displacement | Into Fluid | Strength $\varepsilon$ | Volume | Into Fluid |
| 0.4 | 70 | 0.4856 | Fluid 2 | 120 | 0.6093 | Fluid 2 |
| 0.6 | 200 | 0.4641 | Fluid 1 | 50 | 0.4495 | Fluid 2 |
| 0.8 | 100 | 0.6946 | Fluid 1 | 400 | 0.7989 | Fluid 1 |
| 0.909 | 60 | 0.6929 | Fluid 1 | 400 | 0.9756 | Fluid 1 |
| 1.0 | 190 | 0.8452 | Fluid 2 | 400 | 1.1160 | Fluid 1 |
| 1.1 | 400 | 0.7132 | Fluid 1 | 400 | 1.2270 | Fluid 1 |
| 1.5 | 400 | 0.9335 | Fluid 1 | 400 | 1.5590 | Fluid 1 |
| 2.0 | 400 | 1.0830 | Fluid 1 | 400 | 1.7400 | Fluid 1 |
| 3.0 | 400 | 1.2090 | Fluid 1 | 400 | 1.8480 | Fluid 1 |

Table 4.1: Table showing the strengths needed to produce the maximum displacements and maximum volume transfers for each density ratio considered.

Therefore, the introduction of different density ratios can have a varied effect on the maximum interface displacement and maximum volume transferred. Table 4.1 shows the strengths of bubble 2 needed to achieve maximum displacement and maximum volume transfer for each density ratio, as seen in figures 4.29 and 4.36.

### 4.6.2 Different Densities, Different Inception Times

The same density ratios are used to consider their effect on mixing with out-of-phase bubbles. Figure 4.37 shows the plots of the maximum interface displacement against the inception time of bubble 2 for the selection of density ratios. For clarity, the plots have

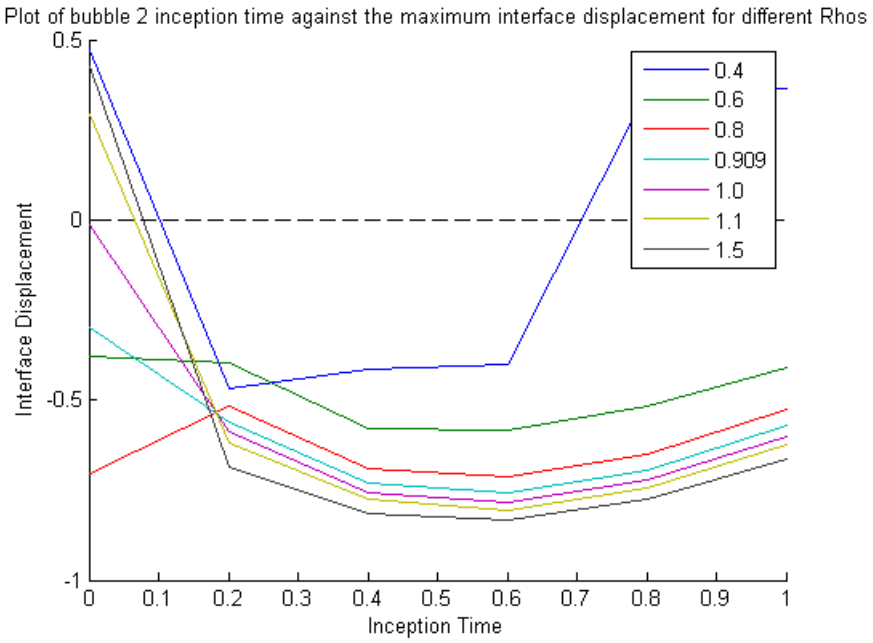


(a)

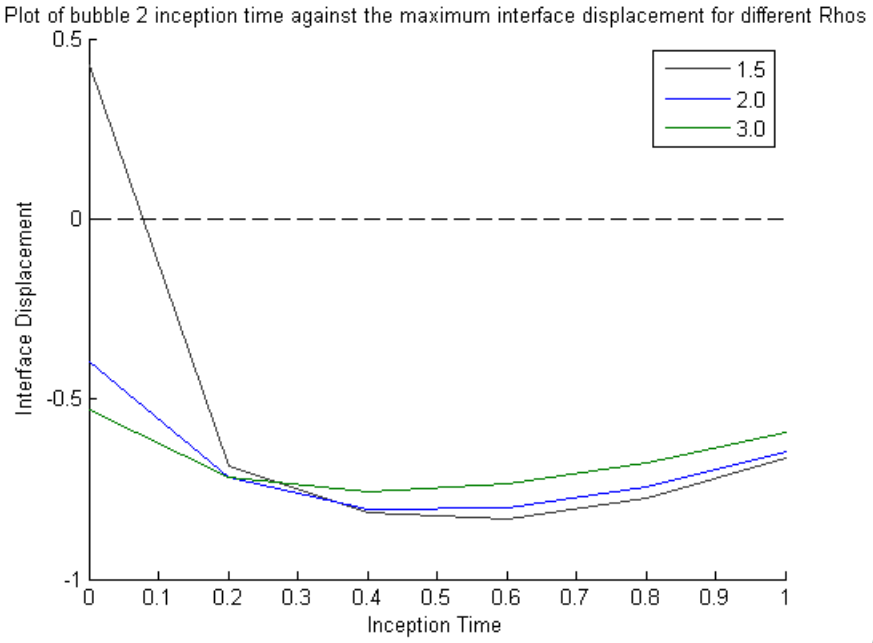


(b)

Figure 4.37: Plot of the maximum interface displacement against the inception time of bubble 2 for densities (a) $\rho = 0.4$ to 1.5 and (b) $\rho = 1.5$ to 3.0.

been spilt to show the density ratios for $\rho = 0.4 - 1.5$ and $\rho = 1.5 - 3$.

When both bubbles are initiated at the same time, the maximum interface displacement is caused by the attraction of the bubbles to one another and the fluid domains. For in-

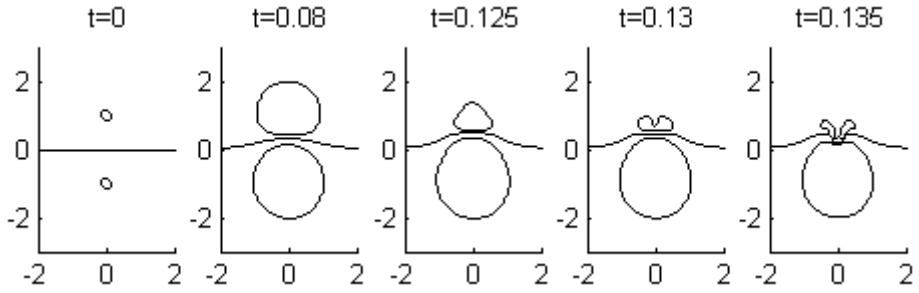


Figure 4.38: Numerical results modelling the collapse of two bubbles in two fluids with density ratio $\rho = 0.4$. Both bubbles are incepted at time $t = 0$.

ception time $t = 0$ and density ratio $\rho = 0.4$, the interface displacement is 0.4779 bubble radii into fluid 2. This is due to the growth phase of bubble 1 being unhindered by the less dense fluid, it can freely push the interface into fluid 2 with little interference, as seen in figure 4.38. Bubble 2 has little effect on the growth of bubble 1, though bubble 2 has an attraction to bubble 1 and the denser fluid 1 which causes it to jet towards the fluid-fluid interface. The jet pushes the interface onto the surface of bubble 1.

Increasing the density ratio to $\rho = 0.6$ drastically changes the maximum interface displacement for $t = 0$. The increase in density of fluid 2 stifles the growth of bubble 1 more than when $\rho = 0.4$, this gives a smaller interface displacement into fluid 2. Bubble 2 still has an attraction to bubble 1 and the denser fluid and produces a similar jet towards the fluid-fluid interface as before. This jet however pushes the interface further into fluid 1 as the interface had not protruded into fluid 2 as much, due to the hindered growth phase of bubble 1. This additional displacement into fluid 1 is enough for the maximum interface displacement to be given as $-0.378$ into fluid 1. Increasing the density ratio to $\rho = 0.8$ emphasises this effect further. The increase in density of fluid 2 causes less growth of bubble 1, which in turn moves the interface less into fluid 2. Finally the jet formed by bubble 2 forces the interface deeper into fluid 1 giving an even greater maximum interface displacement of $-0.7033$ into fluid 1.

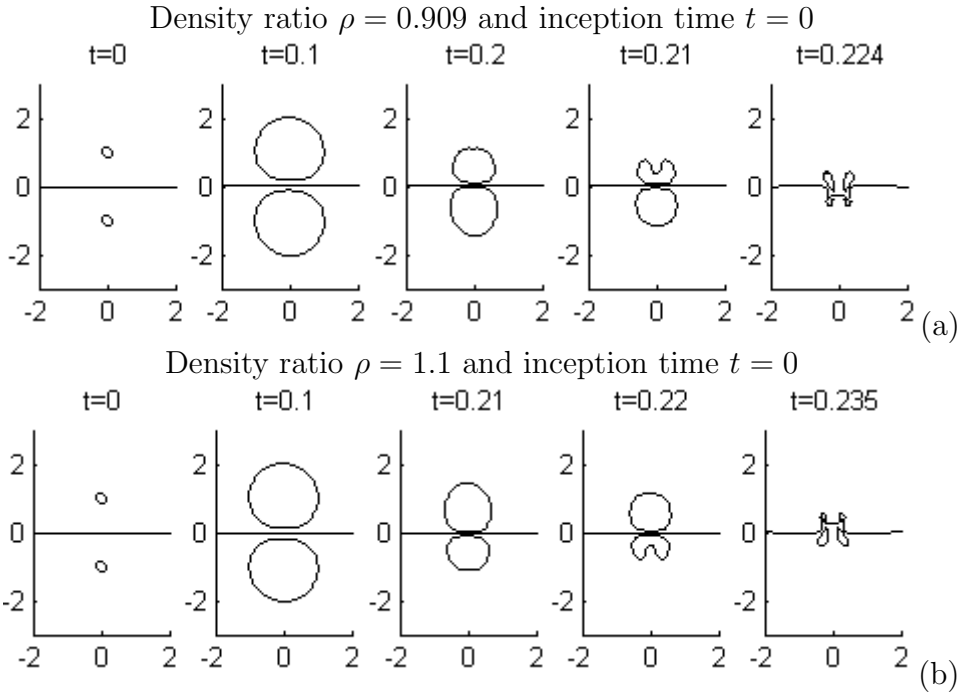


Figure 4.39: Numerical results modelling the collapse of two bubbles in two fluids with density ratio (a) $\rho = 0.909$ and (b) $\rho = 1.1$. Both bubbles are incepted at time $t = 0$.

One would expect to see this trend continue as the density ratio is increased to $\rho = 0.909$, however the maximum interface displacement is $-0.2956$ into fluid 1, much smaller than that for $\rho = 0.8$. As the fluids are almost at equal density, the main Bjerknes force attractions occur between the bubbles. Therefore the bubbles have a very similar growth stage of their evolution, with the only differences occurring during their collapses, as seen in figure 4.39(a). The small additional attraction of bubble 2 to fluid 1 causes it to jet first, pushing the interface into fluid 1 less than the lower density ratios. Increasing the density ratio to $\rho = 1$, for two fluids of equal density, there is no change to the interface. This is expected as the two bubbles are of the same strength and produce the same push and attraction on each other. This effectively simulates the collapse of a bubble near a rigid boundary, as mentioned previously.

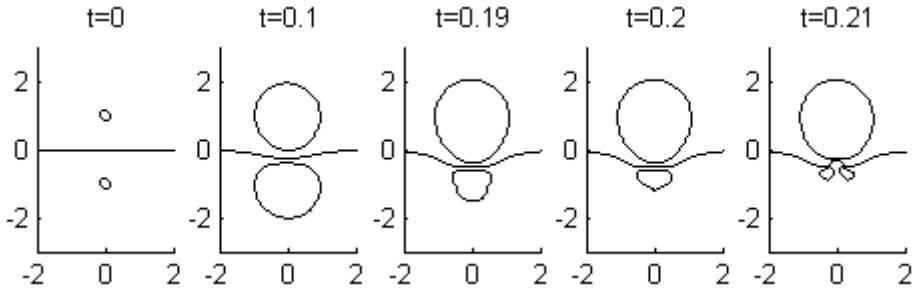


Figure 4.40: Numerical results modelling the collapse of two bubbles in two fluids with density ratio $\rho = 3$. Both bubbles are incepted at time $t = 0$.

Once the density ratio is greater than $\rho = 1$ the effect is reversed, bubble 1 now has an attraction to bubble 2 and fluid 2. Therefore bubble 1 jets towards the fluid-fluid interface, forcing the interface into fluid 2. As $\rho = 1.1$ effectively switches the fluid densities of fluids 1 and 2 from $\rho = 0.909$, the maximum interface displacements are given as 0.2965 and $-0.2965$ respectively, with a mirrored collapse shown in figure 4.39(b). Increasing the density ratio beyond $\rho = 1.1$ to $\rho = 1.5$ sees the maximum interface displacement increase into fluid 2 as expected. The increase in density of fluid 2 increase the attraction of bubble 1 to the interface, pushing the fluid-fluid interface further into fluid 2.

Figure 4.37(b) shows the plots for density ratios $\rho = 1.5$ to 3, it can be seen for bubble 2 inception time $t = 0$ that the maximum interface displacement is now in fluid 1. This is similar to the change in interface displacement seen for the lower density ratios and $\rho = 0.4$ at inception time $t = 0$, only this time the densities and displacement directions are reversed. The growth of bubble 2 pushes the interface into fluid 1 giving the maximum interface displacement as $-0.3935$ for $\rho = 2$, the jet caused by the collapse of bubble 1 towards the interface is not enough to create a large displacement in fluid 2. This interface displacement into fluid 1 is increased with the ratio density to $-0.5296$ for $\rho = 3$, as seen in frame 3 of figure 4.40, due to the reduction in resistance to the growth of bubble 2 from the comparably less dense fluid 1.

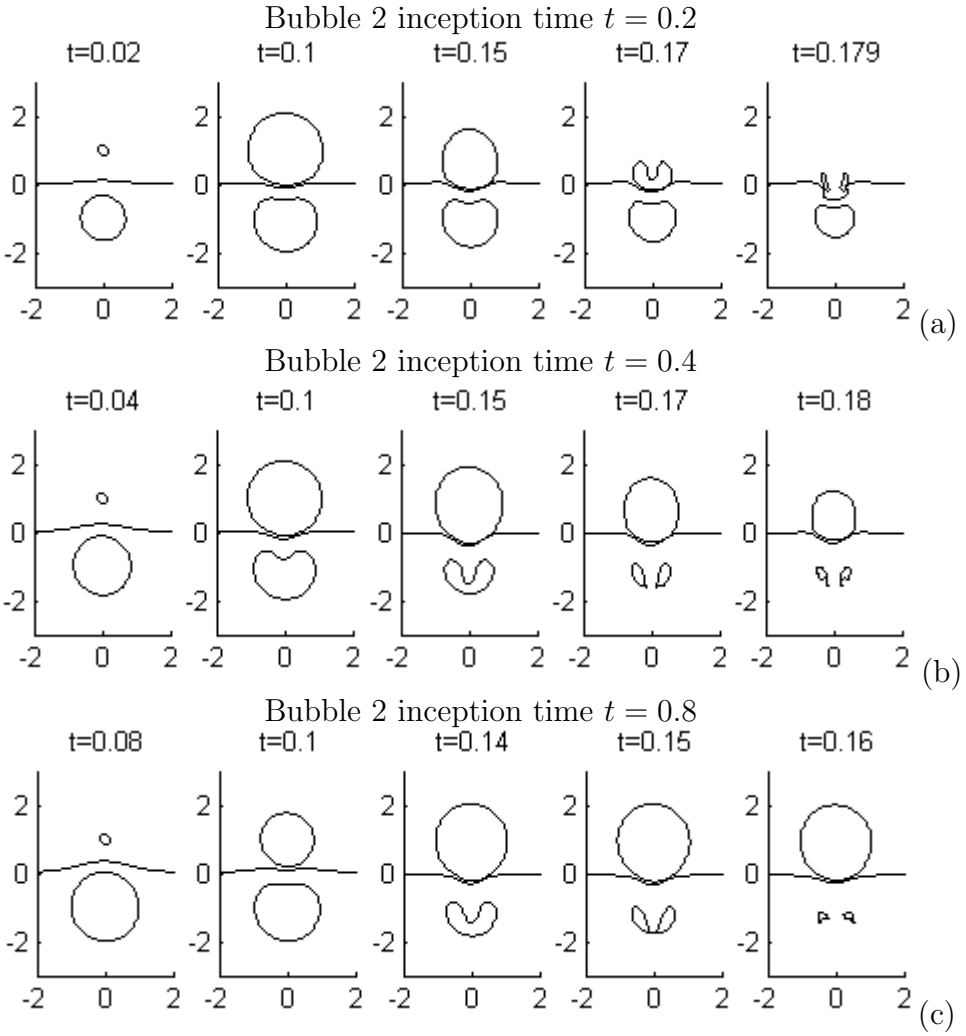


Figure 4.41: Numerical results modelling the collapse of two bubbles in two fluids with density ratio $\rho = 0.4$. In each case the lower bubble has inception time $t = 0$ while the top bubble has inception time (a) $t = 0.2$, (b) $t = 0.4$ and (c) $t = 0.8$.

The introduction of the time delay to the inception of bubble 2 alters the trend of maximum interface displacement seen for time $t = 0$ in figure 4.37. Each density ratio follows a similar relationship between interface displacement and inception time of bubble 2, except for $\rho = 0.4$. When bubble 2 is incepted at $t = 0.2$ with a density ratio of $\rho = 0.4$, the maximum interface displacement is $-0.4678$ in fluid 1. Figure 4.41(a) shows the expansion of bubble 2 interrupts the expansion of bubble 1, decreasing the amount the interface is displaced into fluid 2. This in turn allows bubble 2 to force the interface further into

fluid 1, resulting in bubble 2 collapsing towards bubble 1 and the denser fluid 1. When the inception time is increased to $t = 0.4$ the maximum interface displacement decreases to $-0.4125$. This is due to the expansion of bubble 2 meeting bubble 1 as it decelerates radially when it nears the end of its expansion phase, thus forcing bubble 1 into an earlier collapse. It can be seen in figure 4.41(b) the collapse of bubble 1 ends the simulation before bubble 2 forms a jet to push the interface downwards, as seen for inception time $t = 0.2$. Hence the decrease in maximum interface displacement. This is also the case when bubble 2 is incepted at $t = 0.6$, except bubble 2 is introduced when bubble 1 is at maximum radius. Therefore bubble 2 has to push the fluid-fluid interface further back out of fluid 2, giving a slight decrease in maximum interface displacement (of $-0.4003$) from $t = 0.4$. There is a significant change in the maximum interface displacement for density ratio $\rho = 0.4$ when the inception time of bubble 2 is increased to $t = 0.8$ and beyond. At this point, the later bubble 2 is introduced into fluid the further the interface can move into fluid 2 due to the expansion of bubble 1. This increase in displacement into fluid 2 is enough to eclipse the displacement into fluid 1 caused by the growth of bubble 2, shown in figure 4.41(c). Hence giving the maximum interface displacements of inception times $t = 0.8$ and 1.0 as $z = 0.3608$ and $z = 0.3639$ respectively.

As mentioned previously, for greater densities a trend appears as the inception time of bubble 2 increases from $t = 0.2$. For ratio density $\rho = 0.6$, the maximum interface displacement is $z = -0.3974$, which is less than the same inception time for density interface $\rho = 0.4$. This is due to the decrease in attraction between bubble 2 and the comparably less dense fluid 1. For $\rho = 0.4$, bubble 2 collapses earlier due to the increase in Bjerknes forces and the subsequent jet causes the maximum interface displacement. Where as for density ratio $\rho = 0.6$, the jet of bubble 2 occurs later in its evolution and does not impact the interface before the simulation terminates. Hence the maximum interface displace-

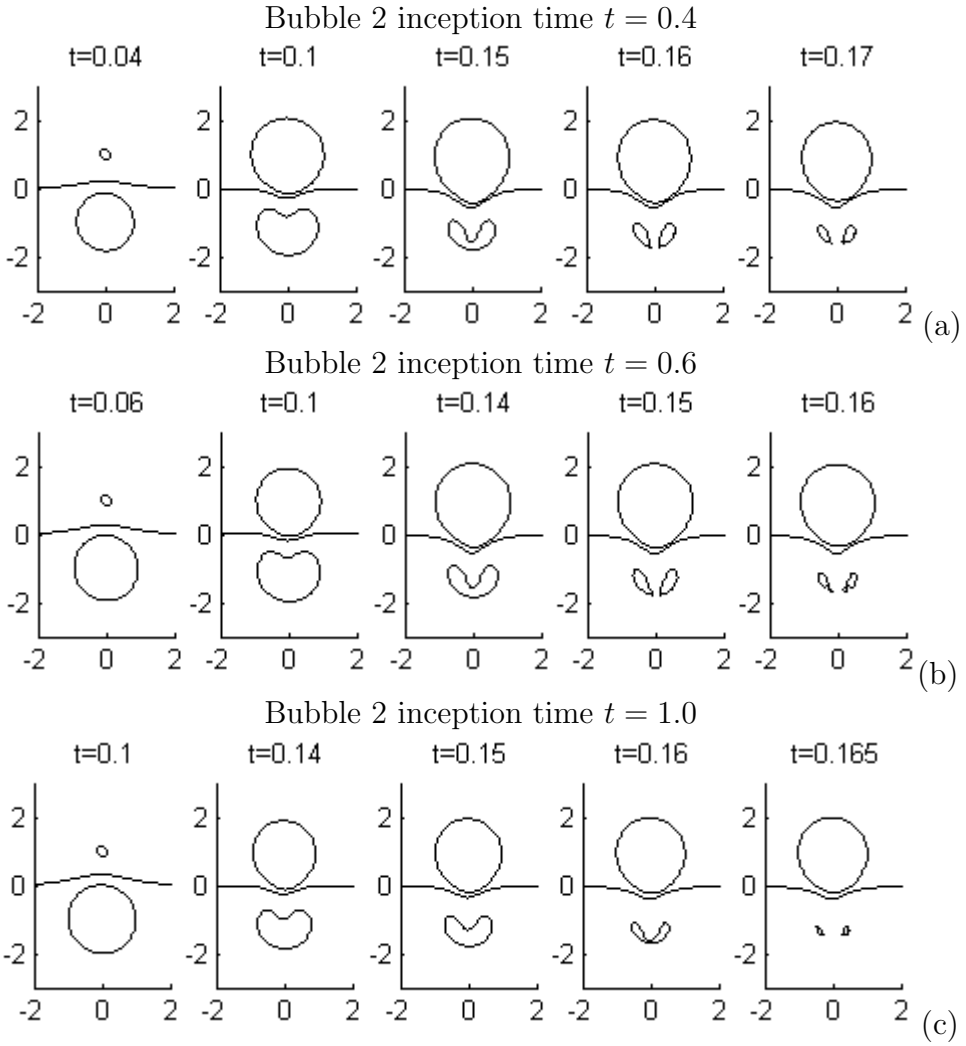


Figure 4.42: Numerical results modelling the collapse of two bubbles in two fluids with density ratio $\rho = 0.6$. In each case the lower bubble has inception time $t = 0$ while the top bubble has inception time (a) $t = 0.4$, (b) $t = 0.6$ and (c) $t = 1.0$.

ment is caused by the growth phase of bubble 2, giving a smaller displacement than that for $\rho = 0.4$. As the inception time is increased to $t = 0.4$ for density ratio $\rho = 0.6$, bubble 2 is incepted when bubble 1 is radially decelerating, as seen in figure 4.42(a). Therefore the outward motion from the newly expanding bubble 2 is greater than that of bubble at this time, causing the fluid-fluid interface to move into fluid 1 away from bubble 2. This gives a maximum interface displacement of $-0.58$, which is an increase on the displacement for inception time $t = 0.2$. Figure 4.42(b) shows when the inception time is $t = 0.6$, bubble

1 is closer to its maximum radius and therefore moving slower than it was at $t = 0.2$. This again allows the growth of fluid 2 to be the more dominant force in the fluid domain, pushing the interface into fluid 1 to give a maximum interface displacement of $z = -0.582$. This is a much smaller increase in interface displacement compared to the increase from inception time $t = 0.2$ to 0.4 as bubble 1 has had more time to expand unhindered by the introduction of the second bubble. This gives more time for the fluid-fluid interface to move further into fluid 2. Therefore when the second bubble is incepted it needs to push the interface a greater distance back to the initial position $z = 0$ and beyond into fluid 1. This becomes more apparent as the inception time of bubble 2 increases. The maximum interface displacement begins to decrease because bubble 1 has more time to push the interface into fluid 2. As bubble 1 is near maximum volume for $t = 0.6 - 1$ the increase in inception time does little to increase the interface displacement as it did for inception times $t = 0.2$ to 0.6. Hence, for later inception times, the increase in movement into fluid 2 by the expansion of bubble 1 outweighs the greater effect of bubble 2 due the decelerated bubble 1 seen in figure 4.42(c). Therefore, for density ratio $\rho = 0.6$ the greatest maximum interface displacement is given by incepting the second bubble at time $t = 0.6$.

This curve repeats as the density ratio is increased to $\rho = 1.5$, though the overall trend in maximum interface displacement moves further into fluid 1. As mentioned previously, the interface displacement at this point is caused by the growth stage of bubble 2. Therefore, increasing the density ratio effectively decreases the density of fluid 1 by comparison. Hence the fluid displaced by the expansion of bubble 2 can move further into fluid 1, pushing the interface to achieve increasingly greater maximum interface displacements with increasingly greater density ratios. However, as the density ratio approaches $\rho = 1.5$ the amount the curves are translated down by, begins to decrease. For density ratios

greater than $\rho = 1.5$, the curve begins to decrease giving smaller maximum interface displacements. This is due to the increase in attraction between bubble 1 to the second fluid. As the density ratio increased past $\rho = 1$ fluid 2 became the denser fluid, which initially allowed the expansion of bubble 2 to move the interface easily due to fluid 1 being comparably less dense. But as fluid 2 became much denser it causes a stronger attraction on bubble 1, which begins to migrate towards the fluid-fluid interface during its growth phase. Once bubble 2 is incepted bubble 1 has a closer proximity than for lower density ratios. Therefore the expansion of bubble 2 must push the interface and the surface of bubble 1 back into fluid 1, thus decreasing the maximum interface displacement.

The same trend appears when considering the amount of volume transferred past the initial fluid-fluid interface position of $z = 0$. It has been mentioned previously that the maximum volume transferred is usually caused by the growth phase of a bubble. As the maximum interface displacement for all density ratios with inception times greater $t = 0.2$ are caused by the expansion of bubble 2 (with exception to $\rho = 0.4$ and inception times $t = 0.2$, 0.8 and 1.0), the plot of maximum volume transferred against bubble 2 inception time shows the same trend, which can be seen in figure 4.43. The main difference being that the maximum volume transferred occurs at inception time $t = 0.6$ for smaller density ratios, and moves to $t = 0.2$ as the density ratio is increased. This shift to a lower inception time is similar to that seen for maximum volume transferred against inception times for increasing strength in figure 4.28. Previously this shift was caused by the increase in strength of the second bubble having a greater influence over the fluid-fluid interface, and hence achieving maximum volume transferred when incepted while bubble 1 is small and has had little effect on the interface. Now however, the decrease in density of fluid 1 gives less resistance to the expanding second bubble, and therefore has more influence over the movement of the interface. Hence it can also achieve maximum volume transferred when

incepted during the early expansion of bubble 1, at $t = 0.2$.

The curves converge as the density ratio approaches $\rho = 3.0$, it can be assumed that for greater density ratios the trend will decrease as seen for maximum interface displacement. Further increasing the density ratio will see the trend to decrease until very little movement of the interface is observed, which is consistent with a rigid boundary being simulated with large density ratios of $\rho \geqslant 10000$. Once again the values for density ratio $\rho = 0.4$ differs from the trend of the other density ratios due to less dense fluid 2 being the more pliable fluid. Though it is consistent with idea that the maximum volume transferred is caused by the growth of a bubble, except in this case it is the expansion of

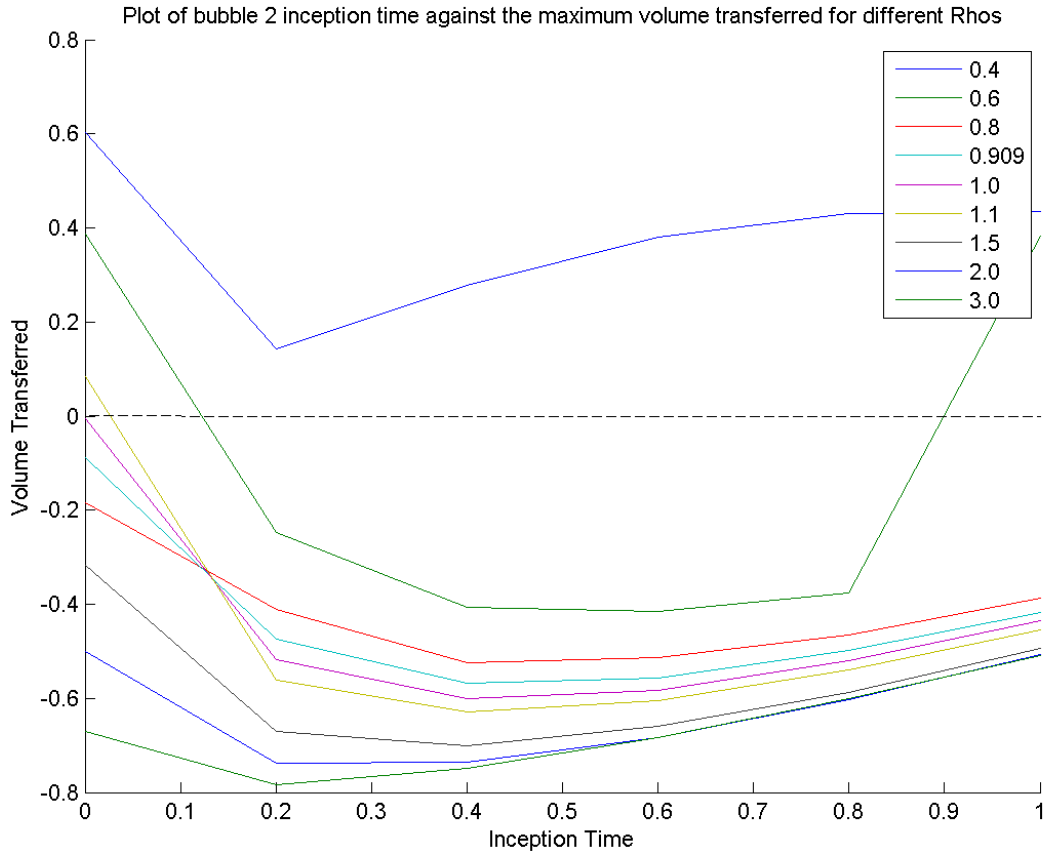


Figure 4.43: Plot of the maximum volume transferred against the inception time of bubble 2 for densities $\rho = 0.4$ to 3.0.

bubble 1 that transfers fluid 1 into fluid 2.

By considering the maximum interface displacement and the maximum volume transferred for different inception times of bubble 2, it can be seen that the most effective approach to mixing two fluids of different densities is to delay the inception of the bubble in the denser fluid by $t = 0.6$, around the maximum radius of bubble 1. Though for optimising volume transfer of one fluid to another, an earlier inception time (toward $t = 0.2$) should be considered for increasingly large differences in fluid densities.

| Density Ratio $\rho$ | Maximum Displacement | | | Maximum Volume Transfer | | |
|---|---|---|---|---|---|---|
| | Inception Time $t$ | Displacement | Into Fluid | Inception Time $t$ | Volume | Into Fluid |
| 0.4 | 0.0 | 0.4779 | Fluid 2 | 0.0 | 0.6036 | Fluid 2 |
| 0.6 | 0.6 | 0.5852 | Fluid 1 | 0.6 | 0.4157 | Fluid 1 |
| 0.8 | 0.6 | 0.7145 | Fluid 1 | 0.4 | 0.7989 | Fluid 1 |
| 0.909 | 0.6 | 0.7572 | Fluid 1 | 0.4 | 0.5686 | Fluid 1 |
| 1.0 | 0.6 | 0.7847 | Fluid 1 | 0.4 | 0.6012 | Fluid 1 |
| 1.1 | 0.6 | 0.8045 | Fluid 1 | 0.4 | 0.6297 | Fluid 1 |
| 1.5 | 0.6 | 0.8312 | Fluid 1 | 0.4 | 0.7006 | Fluid 1 |
| 2.0 | 0.4 | 0.8073 | Fluid 1 | 0.2 | 0.7376 | Fluid 1 |
| 3.0 | 0.4 | 0.7576 | Fluid 1 | 0.2 | 0.7833 | Fluid 1 |

Table 4.2: Table showing the strengths needed to produce the maximum displacements and maximum volume transfers for each density ratio considered.

Therefore, the introduction of different density ratios can have a varied effect on the maximum interface displacement and maximum volume transferred. Table 4.2 shows the inception times of bubble 2 needed to achieve maximum displacement and maximum volume transfer for each density ratio, as seen in figures 4.37 and 4.43.

## 4.7 Chapter Summary

The simulations run and data collected in this chapter have shown that two fluids can be mixed from the interaction of two bubbles. By using either different strengths or different inception times, the fluid-fluid interface separating two fluids can be manipulated to deposit one fluid within another. The jet, formed during the collapse of the weaker of the two bubbles, gives the greatest penetration of the fluid containing the weaker bubble into

the fluid containing the stronger bubble. Which is due to the greater attraction through the Bjerknes forces of the weakest bubble to the strongest. Increasing the difference in the strength of the two bubbles increases the maximum interface displacement, until the growth of the stronger bubble impacts on the interface and weaker bubble. This can be further aided by the introduction of a phase difference between the bubbles. By incepting the second bubble when the first bubble is near its maximum radius, creates a catapult effect between the two bubbles which increases the maximum interface displacement.

The growth phase of the stronger bubble gives the greatest volume transferred across the initial interface. The greater the strength of the stronger bubble the faster it grows, this gives a greater volume of fluid moved away from the centre of the bubble. Hence, positive correlation between the strength of the second bubble and the maximum volume transferred. Choosing the inception time of the second bubble near the maximum radius of the first bubble also increases the amount of volume transferred for lesser strengths. As the strength of the second bubble increases, the inception time needs to decrease to give the maximum volume transferred.

A general assessment of the bubbles dynamics showed that significant changes in the temperature of the bubbles can be found when a bubble collapses to a small volume with high velocity and pressure. By allowing the bubble strength to be low enough to allow the simulation to run to bubble collapse, allows for temperature jumps twice the initial inception temperature of the bubble. Giving reinforcement to the idea that both mixing and chemical activation energies can be achieved by the same process. Additionally similar temperature increases can be observed by offsetting the inception of the second bubble to allow for a forced collapse of either bubble.

When considering two fluids of different density the same techniques can be applied. For fluids with large density ratios mixing becomes more ineffective, which is to be expected. To optimise the mixing process of fluids with more comparable densities, the stronger of

the two bubbles should be placed within the denser fluid. Similarly, when applying a time delay to the inception of one of the bubbles, the latter bubble should be placed with the denser fluid for a greater effect.

To summarise, the maximum interface displacement can be increased by using a stronger second bubble incepted near the maximum radius of the first bubble. Whereas the maximum volume transferred can be increased by using a strong bubble incepted just after the inception of the first bubble. For fluids of different densities, the stronger latter bubble should be in the denser fluid.

# Chapter 5

# Bubble Interaction with a Curved Boundary

The importance of rigid boundary collapse has been mentioned in this thesis and throughout cavitation dynamics. It was the driving force behind the first mathematical and experimental papers in the area, due to its applications to the damage of propellers and hydraulic machinery. As shown in figure 3.3, the collapse of a bubble near a flat rigid boundary produces a jet through the bubble directed towards the boundary. With sufficient strength and proximity, this jet can cause the observed damage to the rigid boundary. However, altering the geometry of the rigid boundary can cause the bubble to react differently during its evolution, leading to a change in the jet impact and boundary damage.

## 5.1 Experimental Comparisons with a Curved Rigid Boundary

Tomita et al. [58] carried out experiments of laser induced cavitation bubbles near concave and convex boundaries. These experiments were then modelled using a combination of the boundary integral method and image theory to gain better understanding into bubble

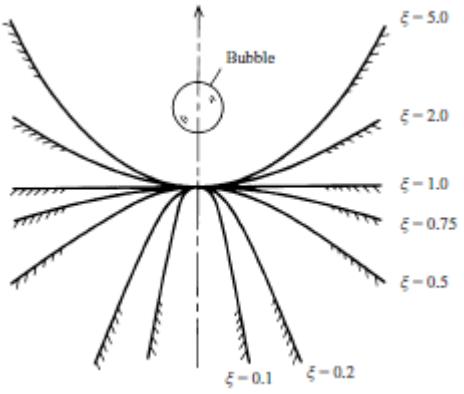


Figure 5.1: Image showing the curvature of the rigid boundary associated with varying values of $\xi$.

collapse near a curved wall. The shape of the axisymmetric curved wall is obtained from the image theory and introducing the surface parameter $\xi$. The Cartesisan coordinates for the surface of the rigid boundary are given by,

$$\begin{aligned} f(x,y,z) &= \left\{x^2+y^2+(h-z)^2\right\}^{1/2}\left[\xi^2(z+\xi h)+\left(1-\xi^2\right)\left\{x^2+y^2+(z+\xi h)^2\right\}^{1/2}\right] \\ &\quad -(h-z)\left\{x^2+y^2+(z+\xi h)^2\right\}^{1/2} \\ &= 0. \end{aligned} \tag{5.1.1}$$

where $h$ is the stand-off distance. Figure 5.1 shows the shape of the boundary for various values of $\xi$. For $\xi < 1$ the rigid boundary becomes convex and flattens as $\xi \to 1$, giving a flat interface for $\xi = 1$. For values of $\xi$ greater than 1 the rigid boundary becomes concave. Tomita et al. then set the Green's function as $G(\mathbf{x}_0, \mathbf{x}) = 1/|\mathbf{x}_0 - \mathbf{x}| + |\text{image}|$, to incorporate the bubbles image in the curved interface into the model.

To model these curved interface interactions using the method outlined in Chapter 2, the nodes on the interface are aligned using equation (5.1.1) with $y = 0$. For the density interface to be infinite, the curve $f(x, 0, z)$ is only applied for $x \leqslant 3$. Then quintic

splines are used for $3 < x < 4$ to match the curve to the line $z = 0$ for $x \geqslant 4$, with the previous far field approximations implemented. As the value of $\xi$ changes so does the depth or height of the concave or convex surface respectively. For extreme values of $\xi$ the difference between the bottom and the top of the curved boundary can be several bubble radii. Therefore the axes are then adjusted to position the centre of the curve at the origin $(x, z) = 0$ for the modelled images shown henceforth. The density ratio across the interface is set to $\rho_A = 10000$ to simulate a rigid boundary. The stand-off distance of the bubble $h$ and the curve parameter $\xi$ are initially chosen to model the results found by Tomita et al.

Figure 5.2 shows the experimental results for a bubble with stand-off distance $h = 0.95$ near a rigid boundary with $\xi = 0.19$, below are the corresponding simulated images. As the bubble grows initially it remains spherical with little interaction from the interface. Near maximum radius, at $t = 0.07$, the bottom of the bubble nearest the rigid boundary begins to flatten, similar to the growth of a bubble near a flat surface. The significant differences occur during the collapse at $t = 0.12$. Due to the Bjerknes forces, the bubble is attracted to the rigid boundary. The closer the proximity to the boundary the greater the attraction. The shape of the boundary tapers away from the bubble as the radial distance outward increases, giving a smaller portion of the bubble surface near the rigid boundary compared to the flat interface case. This gives the smallest distance between the bubble surface and the interface at the centre $r = 0$. Therefore during the collapse phase, the bottom of the bubble nearest the boundary remains near the surface. This causes the bubble to become "tear-drop shaped" with its point nearest the interface at $t = 0.16$. A jet forms at this point of highest curvature on the bubble surface away from the rigid boundary during the collapse at $t = 0.1975$, this jet is due to the 'inflow induced along the boundary' [58]. A second jet forms, typical of bubble collapse near a rigid boundary, on

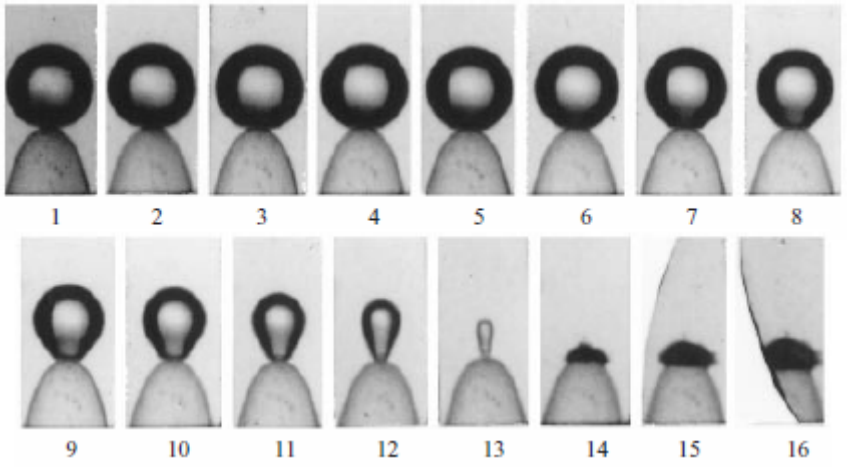


(a)

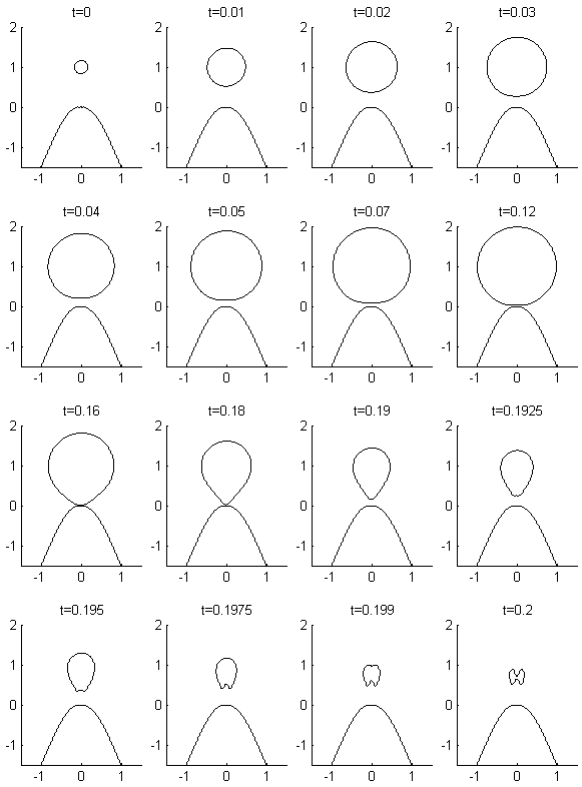


(b)

Figure 5.2: (a) Images of a bubble collapsing near a curved rigid wall with $\xi = 0.19$ and stand-off $h = 0.95$. (b) Plots of a simulated bubble with $\xi = 0.2$ and stand-off $h = 1.0$.

the top of the bubble due to the bubbles attraction to the rigid wall at $t = 0.199$. During the final images of the collapse these two jets come to meet one another with opposing directions in the middle of the bubble.

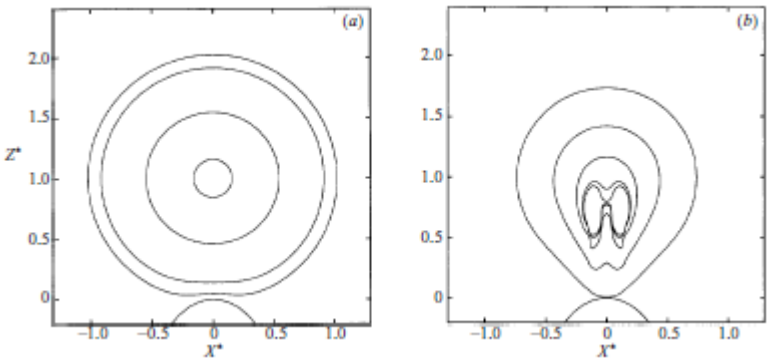


Figure 5.3: Plots simulated using the boundary integral method and image theory by Tomita et al. of a bubble with $\xi = 0.2$ and stand-off $h = 1.0$.

The experimental and the model compare very well for the majority of the bubbles lifetime, with some discrepancies during the very end of the collapse. The model also compares well with the collapse simulated by Tomita et al. using the image of the bubble in the curved interface shown in figure 5.3. The method presented in this paper gives the advantage of introducing the curved interface with a simple change of node placement, as opposed to introducing new terms into the Green's functions to account for the image theory used by Tomita et al, allowing for greater flexibility in the implementation of multiple bubble collapse scenarios, without the need to rewrite sections of the code.

Introducing a concave rigid boundary also affects the bubble collapse. By having the bubble grow within a small divot, more of the bubble surface is closer to the rigid boundary. Therefore the attraction between them causes the bubble to be drawn to a broader area. Tomita et al. found that the bubble motion towards the boundary is "slightly delayed" compared to the flat interface, showing that the attraction is no longer focused at $x = 0$. Figure 5.4 show the experimental and modelled collapse of a bubble near a concave rigid boundary with $\xi = 1.19$ and stand-off $h = 1.7$. The bubble growth remains spherical and the collapse is similar to that of a flat rigid boundary. The model shows good correlation with the experimental results, as well as the results modelled by Tomita et al. To consider

the extent of the effect of a concave boundary has on bubble collapse, the curvature needs to be increased beyond those values considered by Tomita et al.

## 5.2 Curved Rigid Boundary Predictions Beyond Experimental Values

As mentioned previously, simulating a bubble near a concave rigid boundary brings much more of the bubble surface closer to the interface, increasing the bubble surface area affected by the boundary. Therefore considering a curved boundary with a large $\xi$ will show how much a bubble collapse can change when surround by an attractive rigid boundary. Figure 5.5 shows the collapse of a bubble near a curved interface with $\xi = 8$ and a stand-off distance of $h = 1$. This simulates a bubble deep within a narrow depression in a rigid surface. The expansion of the bubble is much slower than that of a bubble near a flat wall. By being beset on half of its surface by a rigid boundary in close proximity, the bubble is less able to push fluid away from its centroid. This causes comparatively faster growth on the top of the bubble, causing the bubble to become taller initially at $t = 0.02$. The easier expansion on the top of the bubble can be seen clearly in the velocity plot shown in figure 5.6(a) at time t=0.1. The fluid moves rapidly from the bubble centroid on the uppermost side of the bubble with non-dimensional velocities around 0.25, while the lower side has much slower expansion with velocities of 0.1. As the bubble approaches maximum volume the attraction to the boundary makes the bubble spherical again, then further attraction produces a wide bubble during the collapse stage at $t = 0.18$. As the collapse continues a jet forms from the top of the bubble towards the bottom of the "hole" at $t = 0.3$. Figure 5.6(b) shows this jet to be much slower and much broader than jets seen by a collapsing bubble near a flat rigid boundary. The attraction from the wall nearer the sides of the bubble widens the jet, and without the focus of the attraction coming from directly beneath the bubble, the jet speed is less. This also lessens the impact on the

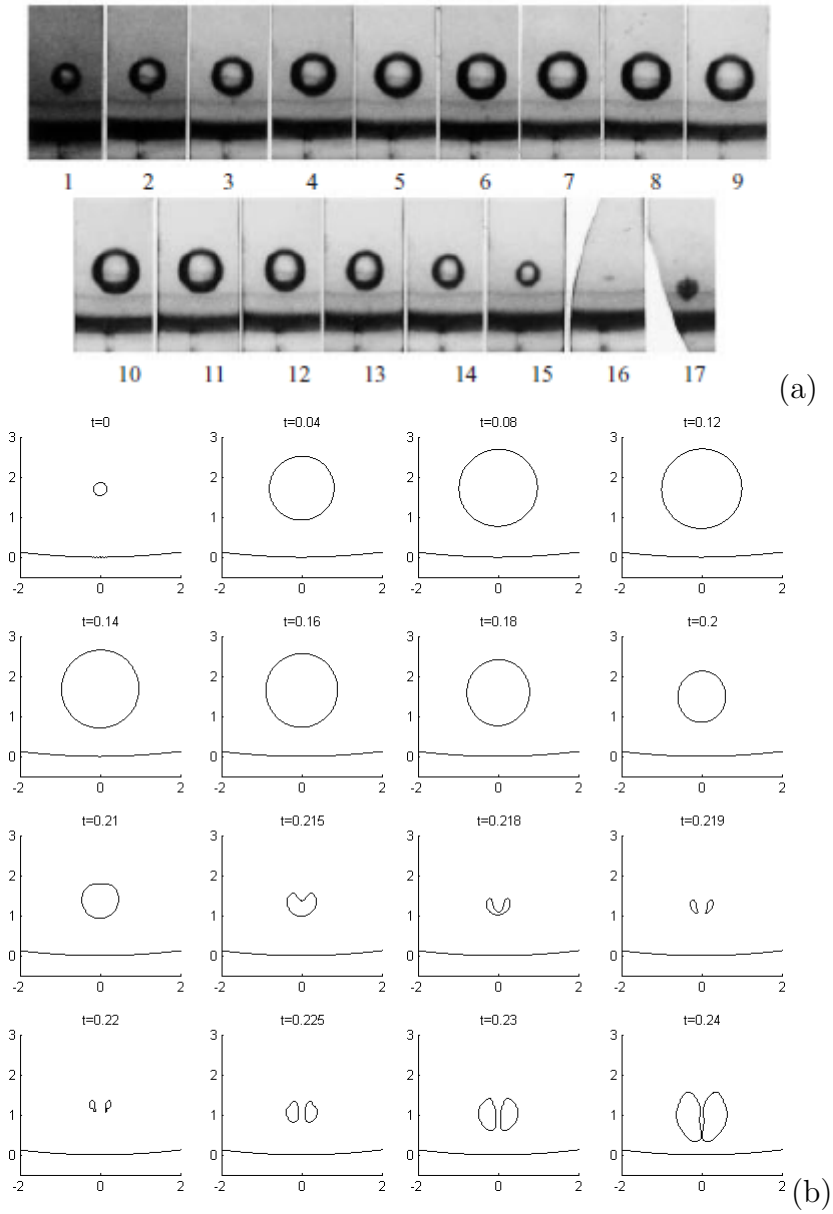


Figure 5.4: (a) Images of a bubble collapsing near a curved rigid wall with $\xi = 1.19$ and stand-off $h = 1.70$. (b) Plots of a simulated bubble with $\xi = 1.19$ and stand-off $h = 1.70$.

boundary once the bubble goes toroidal by spreading it over a larger area, as shown in the velocity and pressure plots in figure 5.6(c). Near the curved rigid boundary the pressures reach around $p = 3$ non-dimensional units, which pales in comparison to the pressures around $p = 25$ seen in figure 3.5 for the flat rigid boundary. Similarly the velocities of the fluid towards the boundary are much less than those observed for the flat case. This shows that changing the curvature of a rigid boundary can lessen the damage caused by a collapsing bubble near a rigid boundary.

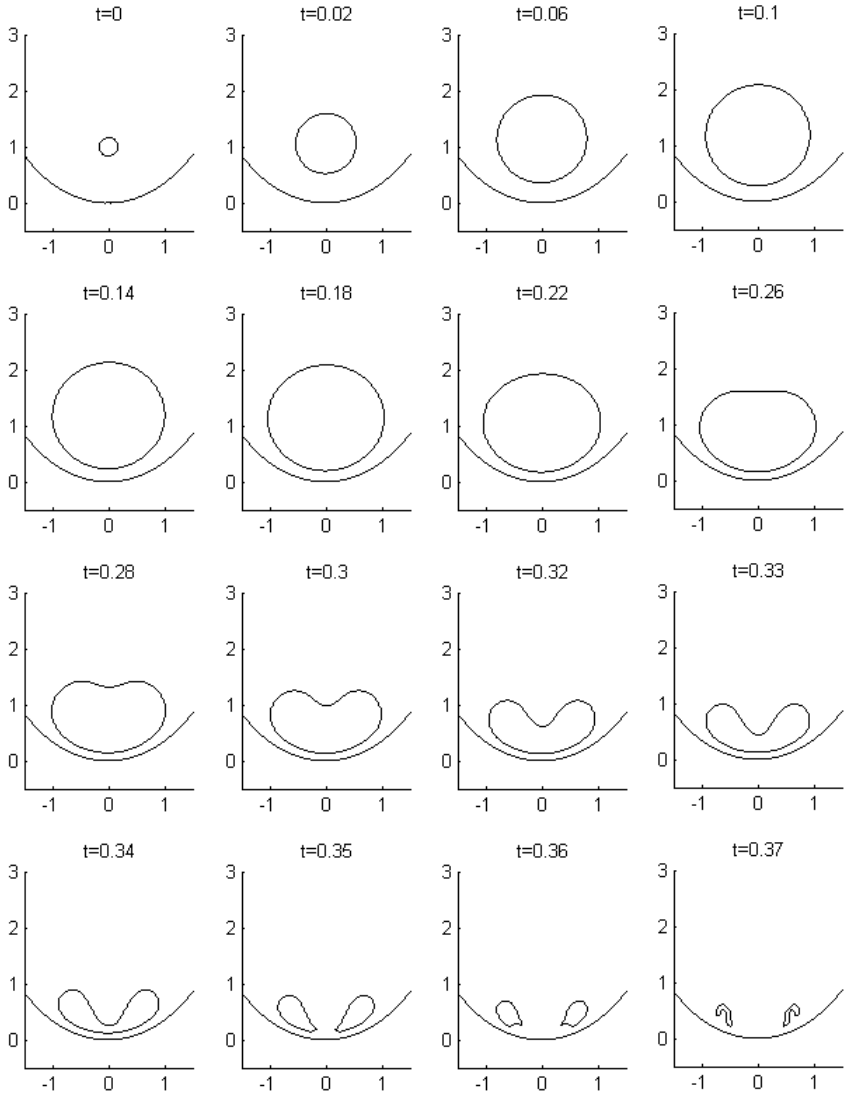


Figure 5.5: Plots of a simulated bubble with $\xi = 8$ and stand-off $h = 1.0$.

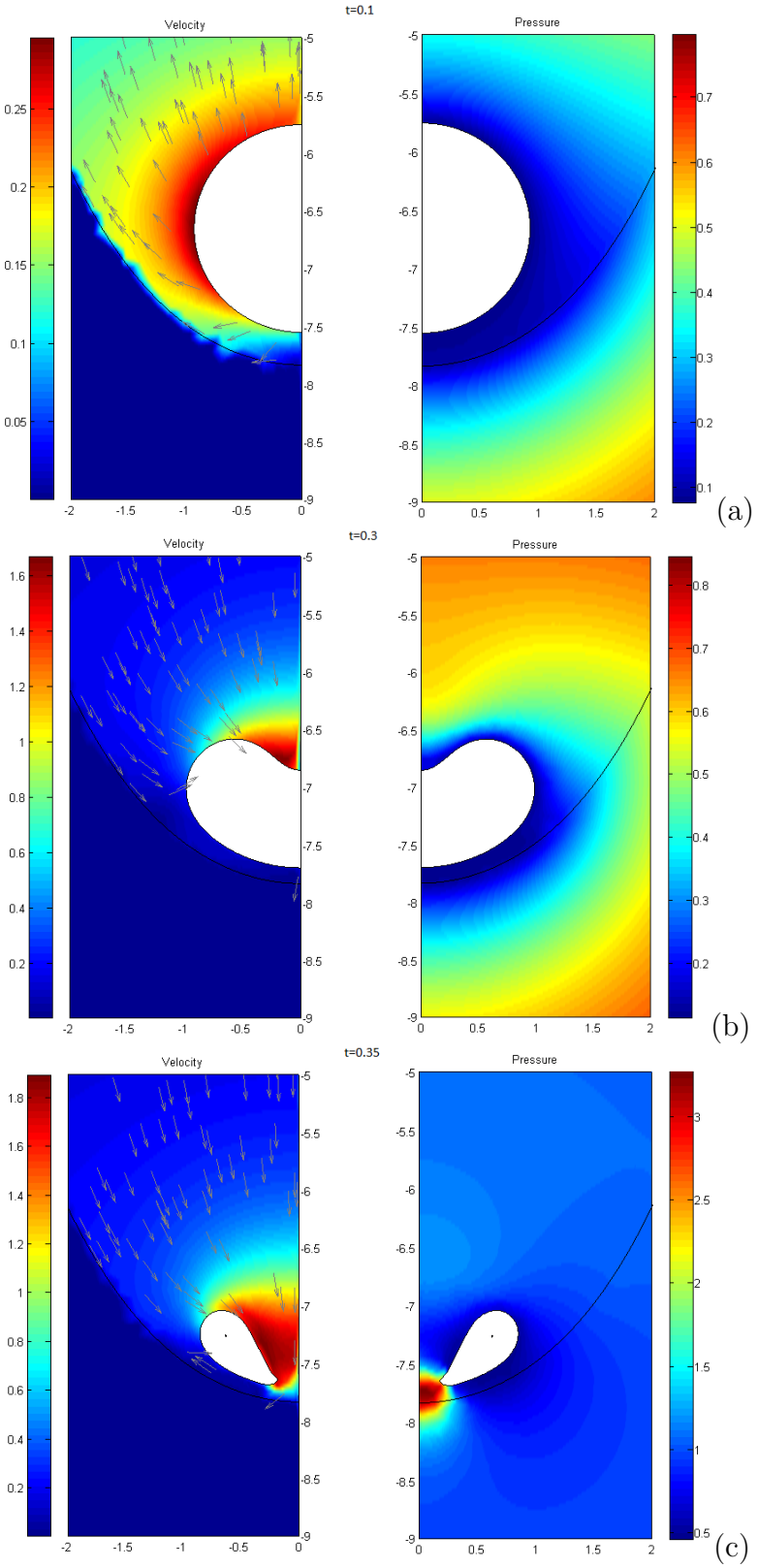


Figure 5.6: Velocity and pressure plots of a simulated bubble with $\xi = 8$ and stand-off $h = 1.0$ at times (a) $t = 0.1$, (b) $t = 0.3$ and (c) $t = 0.35$.

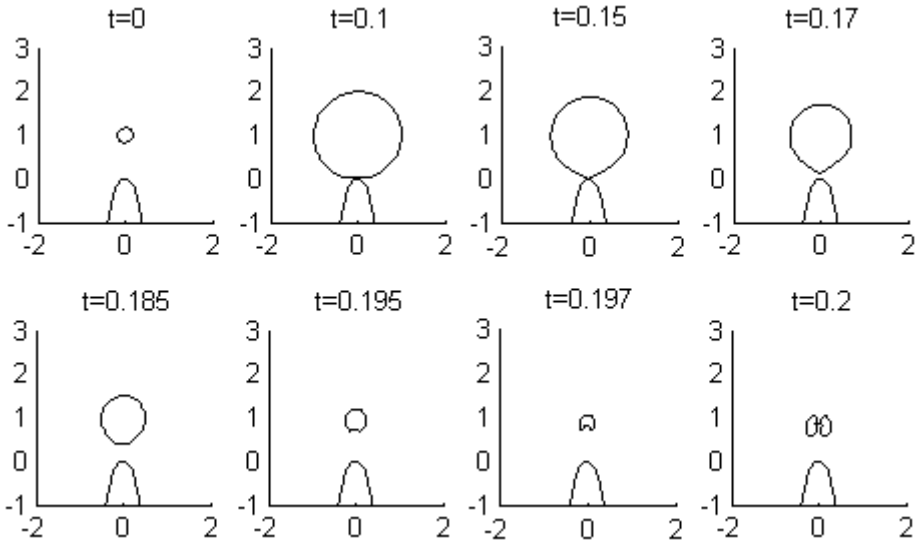


Figure 5.7: Plots of a bubble collapsing near a curved rigid wall with $\xi = 0.1$ and stand-off $h = 1$.

The images obtained in figure 5.5 match well with the understanding of bubble collapse near a concave wall gained from the experiments by Tomita et al. By considering the physics involved with a bubble near a wall of high concave curvature, the simulations for $\xi = 8$ give an accurate representation. Though no experimental results are available for comparison, the model has provided a strong depiction of the collapse that would be observed.

Decreasing the value of $\xi$ below the experimentally observed $\xi = 0.2$, seen in figure 5.2, to $\xi = 0.1$ has little effect on the observed bubble collapse. Figure 5.7 shows the collapse of a bubble with stand-off distance $h = 1.0$ maximum bubble radii near a curved rigid boundary with curve parameter $\xi = 0.1$. The collapse is almost identical to the previously modelled experimental results for $\xi = 0.2$. Decreasing the value of $\xi$ makes the peak sharper, however, there is only a slight decrease in the portion of rigid boundary in close proximity to the bubble surface. As the main influence on the bubble are the interface

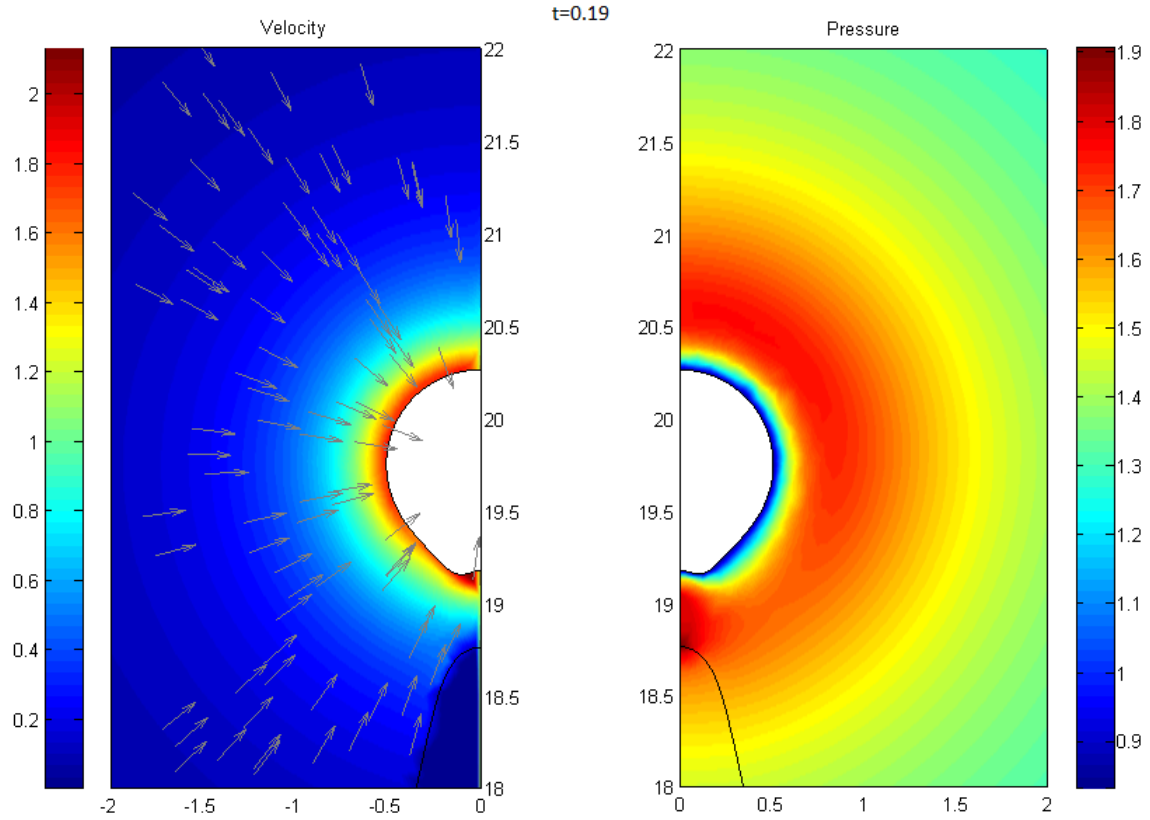


Figure 5.8: Velocity and pressure plots of a bubble collapsing near a curved rigid wall with $\xi = 0.1$ and stand-off $h = 1$.

points nearest its surface, this causes little difference in the observed collapse. Therefore decreasing $\xi$ below this point will yield similar results.

As seen for the concave case of $\xi = 8$, a convex alteration in the shape of the rigid boundary from the flat case can also alleviate some of the pressure caused by a collapsing bubble. Figure 5.8 show the velocity and pressure plots for $\xi = 0.1$. As the bubble jet moves away from the rigid boundary, the highest pressures on the curved wall are observed after the expansion of the bubble. At $t = 0.19$ the maximum pressure observed on the rigid boundary are around $p = 1.9$ non-dimensional pressure units. This is again much lower than the values of $p = 25$ obtained for the flat rigid boundary in figure 3.5.

Therefore the effects of cavitation damage can also be lessened by the introduction of a convex rigid boundary, as well as a concave boundary.

The introduction of the curved rigid boundary into the model is simple and allows for accurate representation of bubble collapse in various situations. The downfall of altering the surface geometry comes when buoyancy also needs to be considered. An important use bubble collapse near curved rigid boundaries is to consider the effects of explosion bubbles on the hull of a ship or submarine. Due to the size of the bubbles to be considered, buoyancy begins to play a large part in the evolution of the bubble. However, buoyancy will also have an effect on the curved interface as well. Buoyancy essentially wants the denser fluid to move down while lighter fluids float upwards, this causes bubbles to rise and denser objects to sink. In the curved rigid boundary problems considered above, the wall is still a fluid and will sink under the effects of buoyancy. Therefore when considering a convex peak, as seen in figure 5.4(b), the introduction of buoyancy should see the interface fall. Figure 5.9 shows the collapse for buoyancy values $\delta = 0.1$, 1.0 and 2.0 for stand-off distance $h = 1.0$ and curvature parameter $\xi = 0.2$. The bubble no longer follows the same collapse as originally seen for $\delta = 0$ in figure 5.4(b), instead the bubble slowly migrates upwards with jetting being direct away from the rigid interface. This is to be expected due to the effects of buoyancy on a bubble as observed by Blake and Gibson [4]. The interface however shows very little movement as time advances, which is contrary to the actions of a dense fluid under the effects of buoyancy. This is due to the extremely fast dynamics of bubble collapse compared to the movement of the falling interface. In the time it takes a bubble evolve through the growth phase and collapse as a toroidal bubble, the interface has only rounded slightly with very little falling. Therefore buoyancy need only be applied to the bubble, as the curved rigid interface will barely be affected. As the interaction between the bubble and the boundary is the main focus of this chapter,

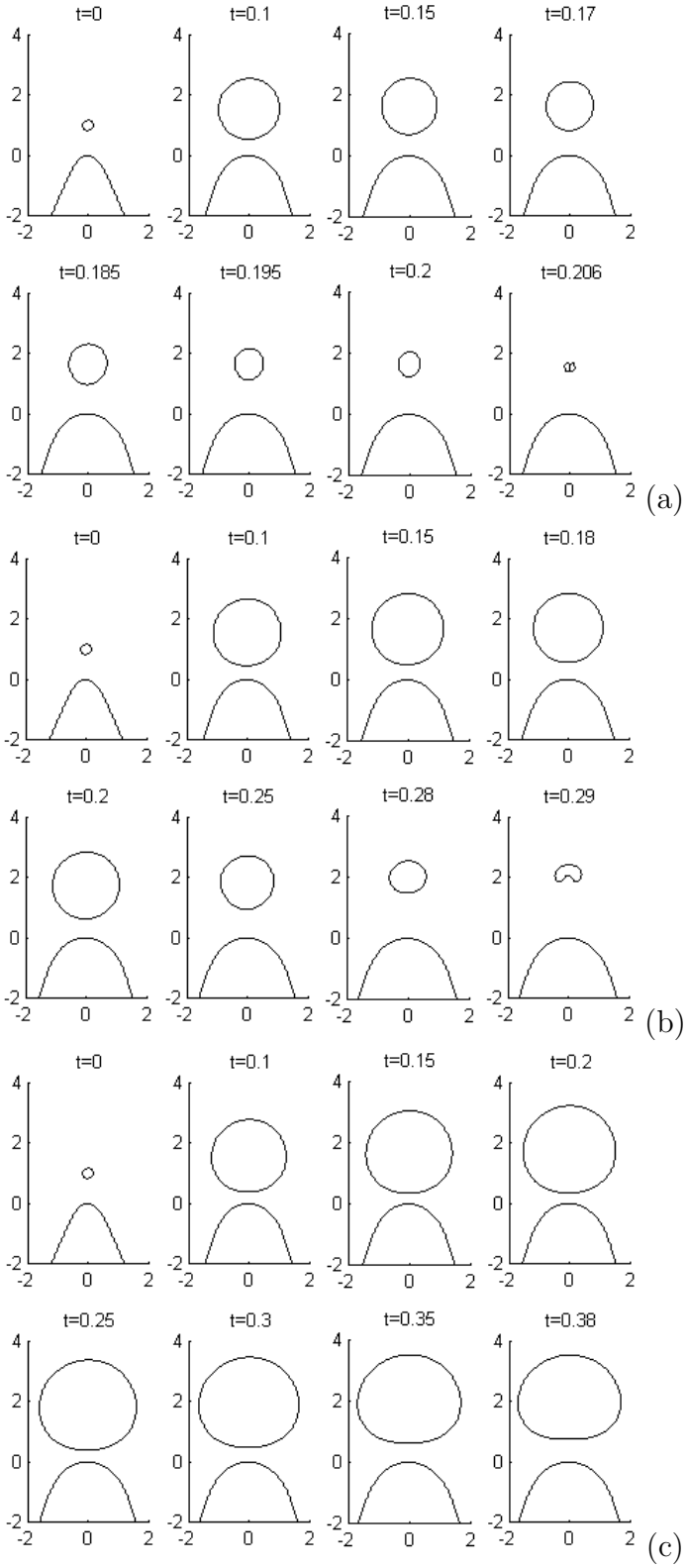


Figure 5.9: Plots of a bubble collapsing near a curved rigid wall with $\xi = 0.2$, stand-off $h = 1$ and buoyancy (a) $\delta = 0.1$, (b) $\delta = 1.0$, (c) $\delta = 2.0$.

buoyancy will be neglected.

## 5.3 Alternative Geometries of a Rigid Boundary

Modelling a curved interface using equation (5.1.1) from Tomita et al. has yielded some interesting results. Unfortunately using image theory limits the number of cases that can be explored. Calculating the image of a single bubble in a non-uniform surface can take time and in some cases be too intricate to compute. In biological processes, surfaces are rarely perfectly flat or easily expressed by a function, making it uncommon to find ideal cavitation scenarios that can be modelled mathematically. Various research and experiments have been carried out to determine the use of bubble collapse on kidney stones [45][12], the idea being to use the collapse of bubbles to breakdown the stone. Kidney stones do not have a smooth surface and often have ridges, valleys, pits and peaks in various assortments across the surface. The introduction of an interface with some of these feature would aid in accurately modelling the bubble collapse. Using the boundary integral method makes inputting alternative interface geometries simpler and only requiring the placement of nodes be continuous across the surface. Figure 5.10 shows the plot of a bubble collapsing near a raised "crater" on a rigid boundary. This can represent some of the unusual features found on the surfaces of biomedical masses that are to be broken down. The crater is modelled using,

$$z = f(x) = \begin{cases} x^2 (x-2)^2 & 0 \leqslant x \leqslant 2 \\ 0 & 2 < x \end{cases}. \tag{5.3.1}$$

This equation ensures that $f'(0) = 0$ and $f(2) = f'(2) = 0$, for the interface to be continuous and differentiable across the line of symmetry and at $x = 2$ respectively. This crater has a radius at its rim equal to 1 bubble radius.

The bubble initially grows spherically from a stand-off distance of $h = 1.5$ from the base

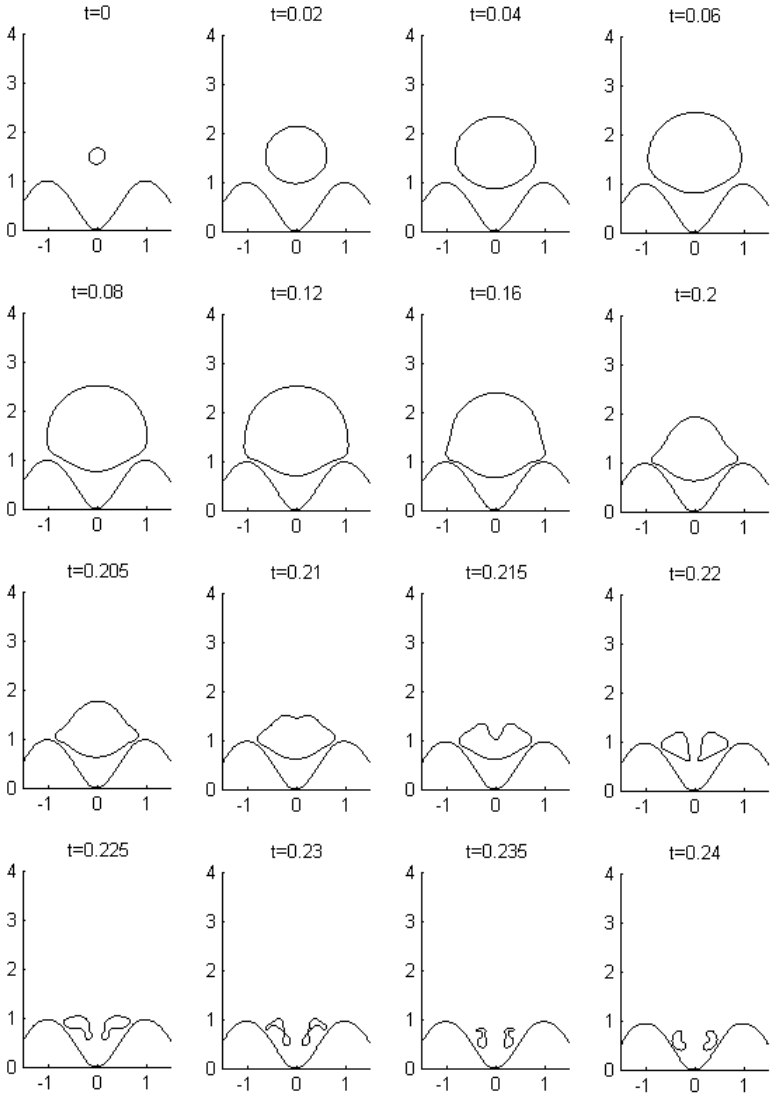


Figure 5.10: Plots of a simulated bubble near a crater with a rim radius of one bubble radius and a stand-off from the bottom of the crater of $h = 1.5$.

of the crater. It meets the rim of the crater at $t = 0.16$, where it flattens at the edges but continues to expand into the crater. During the collapse phase the bottom of the bubble remains in place, as the top collapses downwards to form a "lemon-shape" at $t = 0.205$. Further collapse see a jet form from the top of the bubble, similar to bubble collapse near a flat rigid boundary. Once in the toroidal stage, the bubble continues to migrate towards the bottom of the crater, and the moves towards the crater walls once inside. This collapse agrees with rigid boundary bubble collapse as the bubble is attracted to the closest part of the interface. The Bjerknes forces acting on the bubble cause it to end within the pit of the crater, in a similar manner to the bubble collapse near curved wall with $\xi = 8$. The collapse is slow and produces comparable pressures to those seen in figure 5.6. Therefore, in the interest of damage to the surface, the introduction of the crater on a rigid boundary would drastically lower the possibility of breakdown. This shows the effect a slight change in geometry can have when investigating bubble collapse near a rigid boundary.

To demonstrate the relative ease in changing the surface geometry compared to the change it has on the bubble collapse, the above equation is altered to introduce a much larger crater. Figure 5.11(a) shows an interface represented by the function,

$$z = f(x) = \begin{cases} x^2 (x-4)^2 & 0 \leqslant x \leqslant 4 \\ 0 & 4 < x \end{cases}. \tag{5.3.2}$$

The shape is the same as surface seen in figure 5.10 on a larger scale. The bubble is now situated within the middle of the crater, away from the bottom and the crest. The bubble only feels the effect of the sloped walls near the point of inception, giving the simulation of a bubble within a conical cylinder. This geometry is less likely to be seen in biological procedures, however it may be seen in industrial processes or within hydraulic machin-

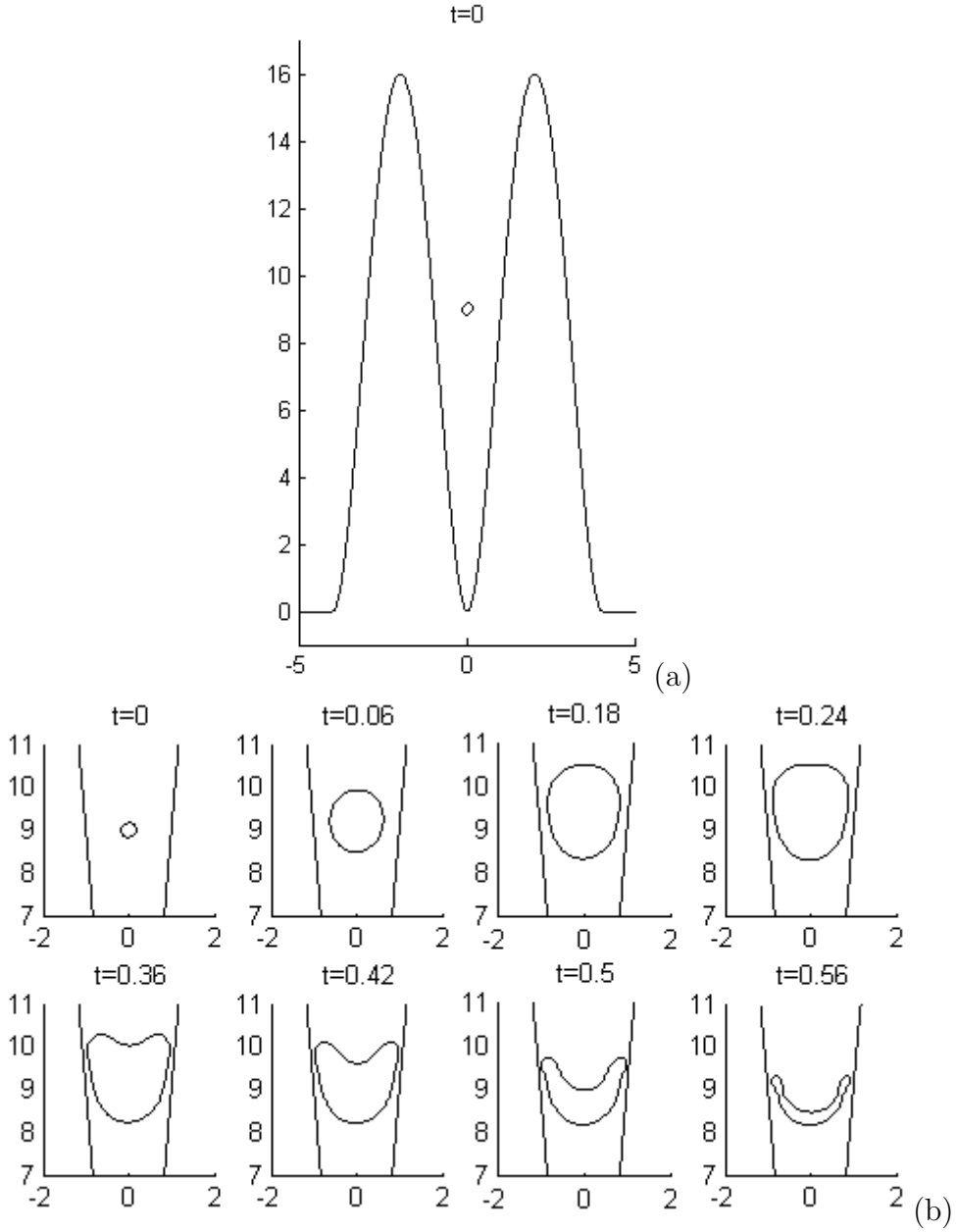


Figure 5.11: (a) Plot of a simulated bubble within a larger crater or conical vessel. (b) Plots of the bubble collapse within the cone.

ery. A change in the formation of the interface as small as changing the crater size can completely change the simulation scenario, while keeping the mathematical code the same.

Figure 5.11(b) shows the collapse of the bubble, with the axis changed to focus on the

bubble. The bubble is initiated in the "cone" where the radius is roughly the same as the maximum bubble radius, $r = 1$. As the bubble grows it is constricted by the walls and elongates at $t = 0.06$. As the bubble reaches maximum radius it takes on the shape of the cone, by becoming wider at the top and narrower at the bottom at $t = 0.18$. The bubble then begins to collapse from the top towards the base, showing that the slight inclination of the wall is enough to direct the jet to where the bubble is nearest the rigid boundary. At time $t = 0.56$ the jet formed is very wide due to the attraction coming from the sides of the bubble, as opposed to the bottom as seen in previous examples. This causes a very slow collapse with the simulation terminating before the bubble becomes toroidal.
These two simulations show very different bubble collapses with very different interface geometries, but with very little change to the formulation of the rigid surface. Thus changing the geometry of the interface can have a profound impact on the range of simulations with very little computational difficulty.

By eliminating the need to use image sources within the computation of bubble collapse near alternative rigid boundaries, the input of geometries can be greatly simplified. Equation 5.1.1 is a complicated way to simulate a concave or convex boundary. Similar curved holes or mounds can be generated using the equation for the arc of a circle. Figure 5.12 shows the collapse of a bubble with stand-off $h = 1.0$ in a "bowl" given by the equation,

$$z = f(x) = \begin{cases} -\sqrt{x^2 - 1.5^2} & 0 \leqslant x \leqslant 1.5 \\ 0 & 1.5 < x \end{cases}. \tag{5.3.3}$$

As you can see the bubble undergoes a similar collapse as seen in figure 5.5, with the bubble being attracted to a larger portion of the interface due to the increase in the amount of rigid boundary near the bubble surface. Equation 5.3.3 is simpler and easier to implement than 5.1.1, without the need of defining a curvature parameter $\xi$. Another

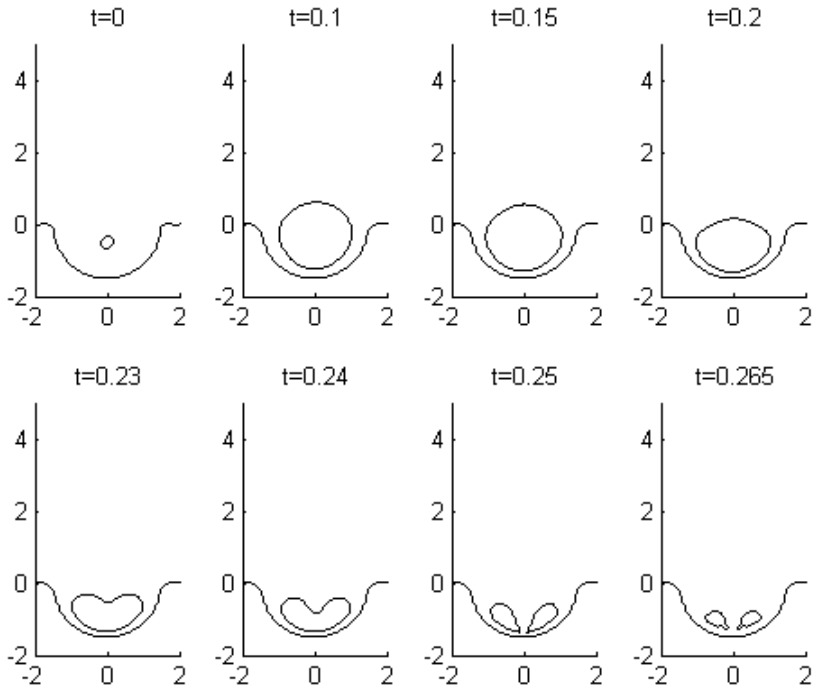


Figure 5.12: Plot of a simulated bubble within a bowl of size 1.5 given by equation 5.3.3 with bubble stand-off $h = 1.0$ and density ratio $\rho_A = 10000$.

drawback of using 5.1.1 is the large differences between the top and the bottom of the curve. As mentioned previously, the curve is only plotted for $x <= 3$, with only the surface near the bubble shown in the plots. For extreme values of $\xi$, the depth or height of the concave or convex interface can reach several bubble radii. Equation 5.3.3 has the advantage of only being as deep or as high as the width of the curve. This allows for both the bubble and the entire curve to be contained near the origin at $z = 0$. Therefore a second interface can be inserted into the simulation to further increase the number of scenarios that can be modelled.

One simulation that can now be observed is the evolution of a bubble within a bowl, as before, with a free surface above. This is similar to the LIFT experiments mentioned in Chapter 3 where a bubble is initiated in a thin film of fluid. Figure 5.13 shows the collapse of a bubble within a bowl as before, with stand-off distance $h = 1$ and the rigid wall

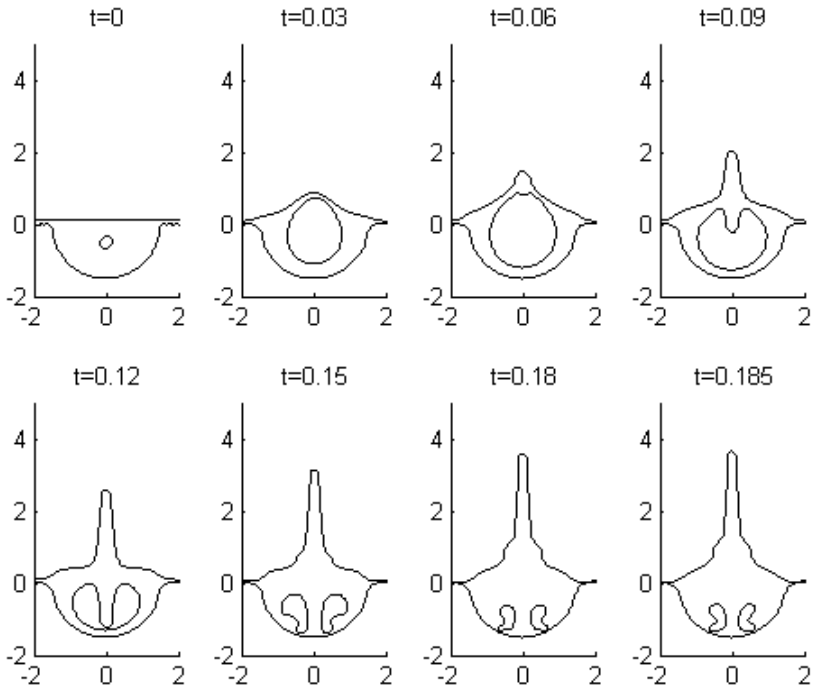


Figure 5.13: Plot of a simulated bubble within a bowl of size 1.5 given by equation 5.3.3 with bubble stand-off $h = 1.0$ and density ratio $\rho_B = 10000$. A free surface is located above at $z = 0.1$ with a density ration of $\rho_A = 0$.

simulated by $\rho_B = 10000$. In addition, a second interface has been inserted just above the bowl at $z = 0.1$, the density ratio across this interface is set to $\rho_A = 0$ to simulate a free surface. Though the second interface extends to the far field, the simulation will resemble that of a bubble in a small bowl that is filled to the brim with water.

The collapse shown in figure 5.13 has comparable elements with both the LIFT numerical results in figure 3.11 and the bowl collapse in figure 5.12. Initially the bubble is free to grow upwards with no resistance from the free surface. The bubble shape at $t = 0.03$ is the same as seen initially in bubble interaction with just a free surface as in figure 3.6, showing that the curved rigid boundary is having little effect on the bubble evolution at this time. As the bubble continues to grow, the top of the bubble begins to form a jet as the free surface protrudes upwards. The collapse is almost identical to the LIFT results upto time $t = 0.12$. Beyond this point the effect of the bowl causes the free surface located

above the bowl to rise. As the fluid being pushed outwards from the bubble cannot escape to the sides, as in figure 3.11, the fluid is forced upwards to the free surface. This causes a second wider free surface jet to emerge at the base of the first. This gives an added rise to the initial jet allowing it to achieve a greater height than the LIFT results.
The introduction of the bowl interface into the LIFT scenario does not make a large impact to the overall intended outcome of allowing the surface jet to imprint onto some substrate. The advantage of initiating the bubble in a bowl allows for removal of the thin liquid film, allowing for printing to be achieved while using less of the fluid to be printed. More experiments would have to be performed to verify the use of fluid in a bowl for this printing technique, though the numerical simulation run here gives a good suggestion that the new approach is possible.

The introduction of new geometries to the rigid boundary has given some interesting results, with many other scenarios to be considered. The overall control of the interfaces given by the numerical method in this thesis allows for new dynamics of bubble collapse to be easily implemented. However in this chapter the curved interfaces used thus far have been limited to a rigid boundary, with the emphasis being on how the bubble reacts to the new interface shape. By considering more malleable density ratios, the evolution of the curved interface near a collapsing bubble can be observed.

## 5.4 Modelling Bubble Collapse near a Cell

The introduction of smaller density ratios across the curved interface will give insight into the affect the bubble has on the fluid-fluid interface evolution. With the addition of surface tension and selecting appropriate geometries for the interface, the collapse of a bubble near a cell wall can be investigated.
Bubble-cell interaction is a relatively new area of research within the biomedical disci-

pline. Many papers have been written on the various ways bubbles can be used to move, influence or even break down cells. Cell lysis is the breaking down of cells due to viruses, enzymes or osmosis. It is a key component in the process of microfluidic DNA extraction. Tan et al. [57] inserted a bubble into a droplet containing multiple cells, the resulting jet from the bubble collapse provides high enough velocities to lyse the cells suspended in the fluid. Thus releasing the contents of the cells into the fluid to be easily analysed. In addition to the insertion of the bubble, ultrasound can be applied to the fluid domain to oscillate the bubble, leading to further cell interaction. This process is known as sonoporation. High doses of ultrasound can cause rapid oscillation of the bubble, which can kill cells through lethal sonoporation. This can be through direct physical lysis or by the initiation of programmed cell death, known as apoptosis [48][19]. This has applications in destroying tumour cells and other unwanted cells. Lower levels of ultrasound can cause cell membranes to become more permeable, allowing for larger substrates to enter or leave a cell which previously could not. This allows for targeted application of medicines or to release cell contents without damaging the viability of the cell [33]. Unfortunately this application of sonoporation affects all surrounding cells, for more precise injection of a substance into a single cell alternative methods must be used.

The physical process of microinjection with a microneedle is a method that will avoid pen-

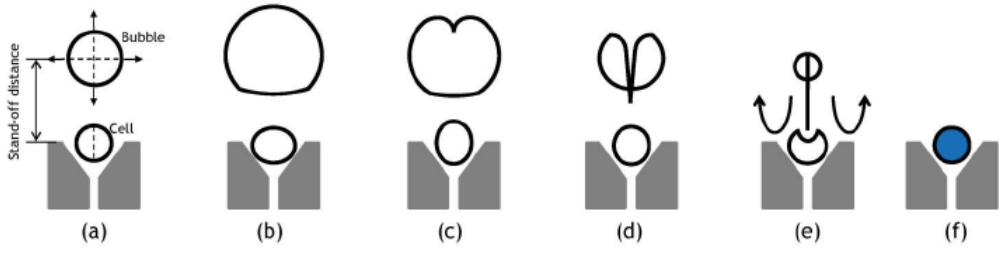


Figure 5.14: Images showing the method used by Li et al. in the poration of a cell membrane. [36]

etrating multiple cells [1], though a similar result can be achieved using bubble-induced microjets. The approach used by Li et al. [36] traps a cell in a gap on a rigid boundary, as seen in figure 5.14. A bubble is introduced above the cell, where the attraction to the rigid boundary causes the bubble to collapse forming a jet towards the cell. The impact of the jet on the cell causes poration of the cell surface allowing for fluid to pass through the cell membrane.

In this section a similar approach will be used to study the effect on bubble collapse near a cell-like surface. The interface will be geometrically deformed to give a similar shape to the surface of a cell. Surface tension and a density ratio will be introduced to mimic the properties of a cell membrane. Beneath the cell a second interface will be used as a flat rigid backing to cause the bubble to collapse toward the cell, as in figure 5.14. A bubble will be introduced above the "cell" and the resulting affects will be noted and applied to poration of cells. The modelling of bubble interaction with a tissue layer has been researched by Curtiss et al. [18]. The addition of the interface geometry will give better understanding of bubble interaction with a single cell.

The aim of this section is show how the numerical model described in Chapter 2 can be applied to model bubble interaction with a cell. As such the values used to model the cell are estimations, where actual values for cell size, density and surface tension will be considered further work.

The shape of the cell will have similar geometry to the bowl from equation 5.3.3, the difference being the boundary will be convex instead of concave. Quintic splines will be used to merge the cell shape with the flat interface to the far field interface position $z = 0$. Therefore the geometry of interface A will be given by,

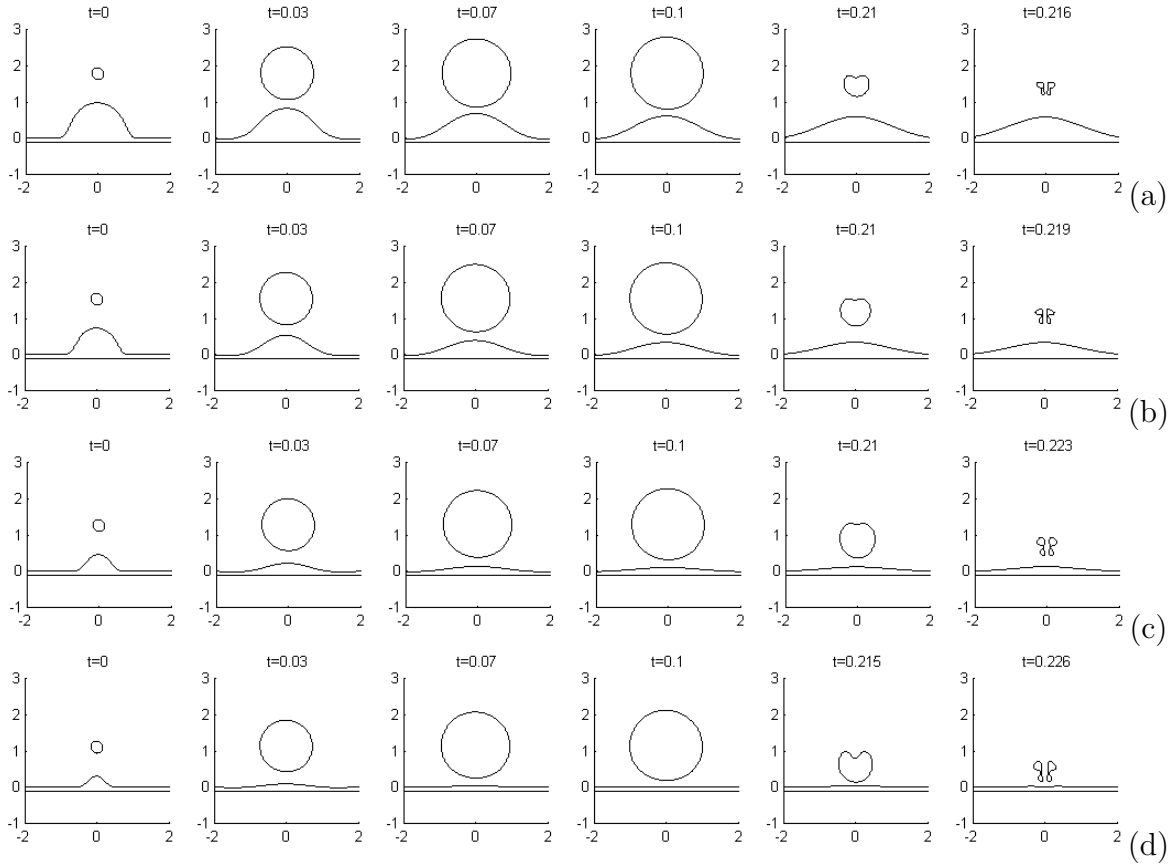


Figure 5.15: Plot of bubble interaction with a cell. The bubble has stand-off $h = 0.8$ from the cell and interface A has density ratio $\rho_A = 1$, while interface B is the rigid boundary with density ratio $\rho_B = 10000$. The cell shapes for each simulation are (a) $C = 0.7$, (b) $C = 0.5$, (c) $C = 0.3$ and (d) $C = 0.2$.

$$z = f(x) = \begin{cases} \sqrt{x^2 - C^2} & 0 \leqslant x < C - 0.1 \\ \text{quintic spline} & C - 0.1 \leqslant x \leqslant C + 0.4\,, \\ 0 & 1.5 < x \end{cases} \tag{5.4.1}$$

where $C$ is a parameter for giving the shape of the cell. To begin with the cell shape is varied to consider the optimal stand-off distance for the bubble to interact with the rigid boundary. The density ratio across the cell wall is $\rho_A = 1$ and the rigid wall has density ratio $\rho_B = 10000$, surface tension is neglected. Figure 5.15 shows the collapse of a bubble with stand-off distance $h = 0.8$ from the cell surface, the cell shapes considered

are $C = 0.7$, 0.5, 0.3 and 0.2 bubble radii. Due to the addition of the quintic spline the crest of the cell stands at $z = 0.97$, 0.73, 0.45 and 0.30 respectively. The cell shape has been chosen to be less than the maximum radius of the bubble to allow the bubble to have a greater impact on the cell wall.

The largest size considered is for $C = 0.7$, as seen in figure 5.15(a). As the bubble grows to maximum radius at $t = 0.1$, the fluid is pushed outwards, as expected. This causes the cell to flatten to have an apex around 0.6 bubble radii, only slightly less than the original $z = 0.97$. The bubble then begins to react to the rigid boundary and collapses in the direction of the cell. Unfortunately, due to the distance from the wall, the collapse is slow forming a rather weak jet. Therefore the collapse of the bubble has little influence on the cell by the end of the simulation. Decreasing the cell shape to $C = 0.5$ reduces the stand-off distance of the bubble from the wall to $h = 1.53$ in figure 5.15(b). This decrease causes the bubble to have a greater attraction to the wall, though not enough to see any significant changes in the collapse. The bubble migrates closer to the wall than seen for $C = 0.7$, but not enough for the jet formed during the collapse to impact the cell. This remains the case for $C = 0.3$ in figure 5.15(c), the bubble migrates even closer due to the increased attraction to the rigid boundary. However, this moves the bubble closer to the cell during the collapse stage. The movement of fluid toward the bubble centre causes the cell to move upwards slightly towards the end of the simulation. The only case to show any impact on the cell from the bubble jet is for cell shape $C = 0.2$ in figure 5.15(d). The bubble grows spherically as before, flattening the cell to an almost flat interface at $t = 0.1$. The collapse again draws the cell wall towards the bubble, as seen for $C = 0.3$. However in the final frame at $t = 0.226$, the jet from the bubble collapse impacts on the cell causing an impression on the cell surface. This is the effect that will most likely cause poration of the cell wall, allowing for the inject of fluid into the cell. Therefore for the following simulations the bubble shape $C = 0.2$ will be used to have the

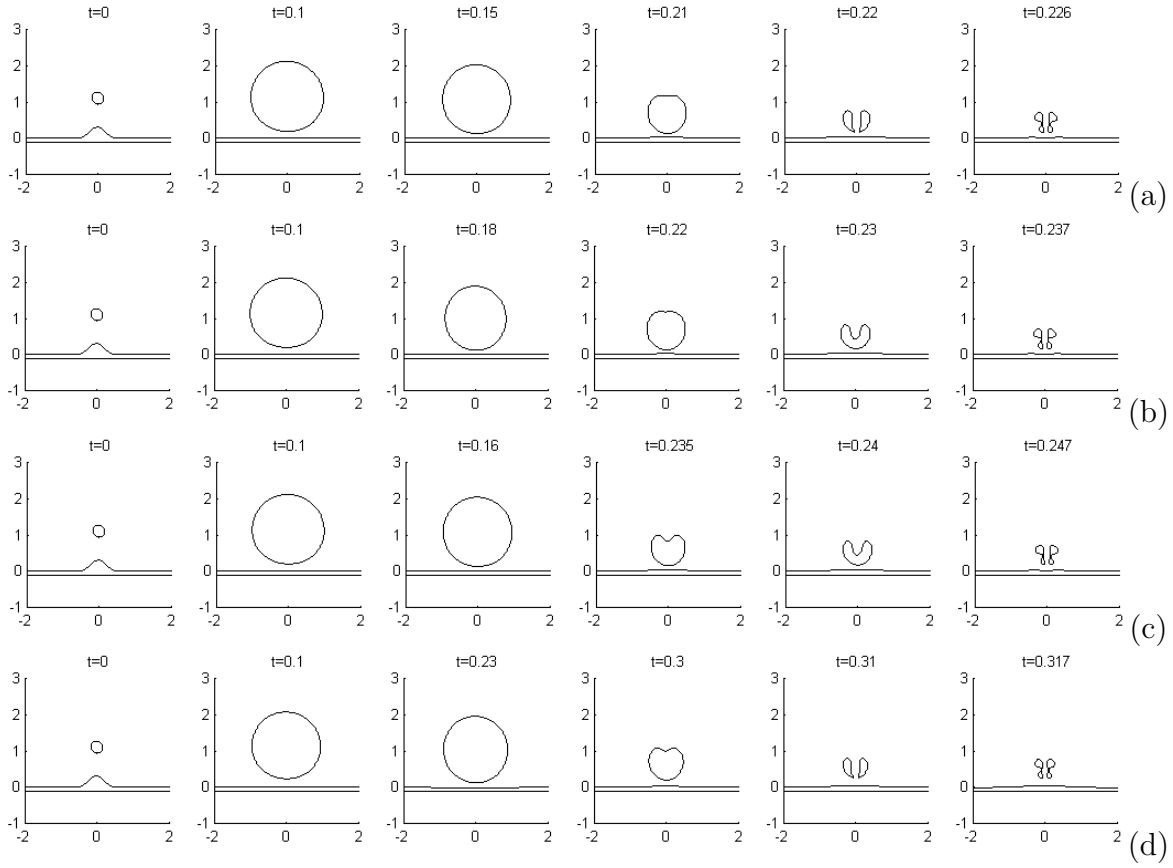


Figure 5.16: Plot of bubble interaction with a cell. The bubble has stand-off $h = 0.8$ from the cell and the cell shape is $C = 0.2$, while interface B is the rigid boundary with density ratio $\rho_B = 10000$. The density ratios across the cell wall in each simulation are (a) $\rho_A = 1.0$, (b) $\rho_A = 1.1$, (c) $\rho_A = 1.2$ and (d) $\rho_A = 2.0$.

greatest interaction between the bubble and the rigid boundary.

Due to the orientation of the simulation, it is necessary to assume the density of the cell is greater than that of the fluid, otherwise any experimental data would show the cell float upwards under the effect of gravity. Though as the cell is still malleable, the density within cannot be very large. Therefore the density ratios compared in figure 5.16 are $\rho_A = 1.0$, 1.1, 1.2 and 2.0. The base case of $\rho_A = 1.0$ is the same as for $C = 0.2$ in figure 5.15. The bubble growth is initially spherical with the collapse stage drawing the cell into the bubble centroid, the jet formed by the bubble then impacts on the surface on the cell

causing an indentation. At first glance, nothing has changed when increasing the density ratio to $\rho_A = 1.1$ in figure 5.16(b). The same growth, collapse and cell surface indentation occurs. The difference comes when the time stamps are observed. The overall evolution of the bubble is extended by the introduction of the new cell density. The growth stage is the same, with the maximum radius being achieved at $t = 0.1$. The collapse however is much slower, with the bubble going toroidal after $t = 0.23$. Whereas the bubble was already toroidal at $t = 0.22$ for $\rho_A = 1.0$. The increase in density causes the cell wall to move slower under the effect of the bubble growth, causing the cell to act as a "buffer" between the bubble and the rigid wall. This is enough to slow the overall bubble evolution, increasing the run time by $t = 0.11$. This becomes more evident when the density ratio is increased to $\rho_A = 1.2$ with a runtime of $t = 0.247$. The overall collapse is the same, with a slight increase in resistance to the bubble jet from the cell wall in the final frame of figure 5.16(c). The impact zone on the cell surface at the axis of symmetry is smaller than the previous cases, showing the increase in density of the cell cause the cell wall to be influenced less by the bubble collapse. To show the total effect of the increase in cell density, the density ratio is raised to $\rho_A = 2.0$. Once again the evolution of the bubble is slower with a much greater runtime. The notable difference is the lack of indentation from the bubble jet on the cell surface. The density is now high enough to resist the impact caused by the jet. Considering any higher density ratios will yield no further indentations. Therefore to maintain the biological model of a cell with greater density than the surrounding fluid, yet still observe indentation on the cell wall, the density ratio should be only slightly greater than the uniform density ratio $\rho_A = 1.0$.

A cell is distinguished from a simple ball of fluid by the cell membrane or wall, this retains the fluid within the cell and is the main feature that causes it to be nonporous. So to simulate a cell wall, surface tension on the interface is introduced. Figure 5.17 shows the

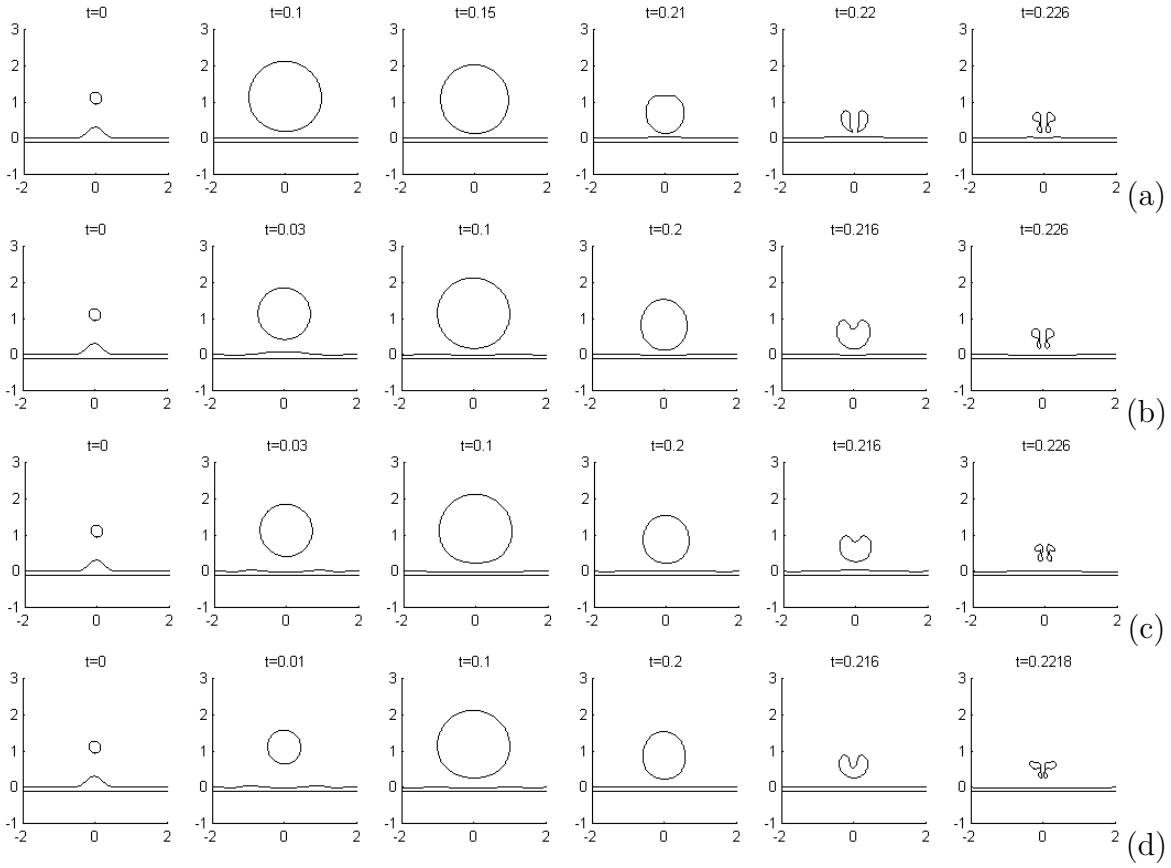


Figure 5.17: Plot of bubble interaction with a cell. The bubble has stand-off $h = 0.8$ from the cell and the cell shape is $C = 0.2$, while interface B is the rigid boundary with density ratio $\rho_B = 10000$. The surface tension across the cell wall in each simulation are (a) $\sigma = 0.0$, (b) $\sigma = 0.01$, (c) $\sigma = 0.1$ and (d) $\sigma = 1.0$.

effect the surface tension of the fluid interface has on the evolution of a bubble for surface tensions $\sigma = 0.0$, 0.01, 0.1 and 1.0. The density ratio is set to $\rho_A = 1.0$ so that only the effect of surface tension is observed.

As before, the base case of $\sigma = 0.0$ shows spherical bubble growth with the jet from the collapse impacting on the surface of the cell. Increasing the surface tension slightly to $\sigma = 0.01$ causes the cell to resist against the growth of the bubble, creating a wave passing along the interface from the position of the cell. This causes the interface to ripple with small amplitude into the collapse stage of the bubble. In the final frame, the tension on the cell surface is enough to spread the impact of the jet across a larger portion of the cell.

When the jet hits the middle of the cell it pushes that portion down, the surface tension resists by moving the surrounding cell wall down as well, shown by the wider dip at time $t = 0.226$. When the surface tension is set to $\sigma = 0.1$ the interface ripples much more than previously. As the surface resists the bubble more, the cell is closer to the bubble during the collapse. This causes the surface to be drawn into the bubble at $t = 0.216$. In the final frame there is no impression on the cell surface due to the jet having to push back the drawn-in portion of the surface. Once again the jet impact in the final frame is spread across a larger portion of the surface by the surface tension, shown by the dip below $z = 0$ out towards $r = 2$.

Finally for $\sigma = 1.0$ the surface tension causes a very fast wave as the cell is flattened much more rapidly, with very small ripples continuing as the bubble reaches maximum radius. The increased surface tension causes the surface to come to rest quickly during the initial bubble collapse. When the bubble has collapsed completely it appears the jet has made no impact, however the surface tension has spread the impact over an area large enough for the entire cell surface to be below $z = 0$ at $t = 0.2218$.

The addition of surface tension into the simulation sees less localised impact of the jet, instead the force is spread out across increasingly larger portions of the surface. This allows for the cell wall to act as more of a restrictive barrier, similar to the physical properties of a cell. Unfortunately it limits the indentation seen on the surface that would indicate poration. To find a balance between physical representation and possible observations of porosity, the surface tension will be set as $\sigma = 0.01$ in the following simulations.

With the cell shape chosen for maximum influence from the bubble, the density low enough to allow for surface indentation and the surface tension set to show the physical effects of a cell wall, simulations can be run to approximately indicate how a bubble will collapse near a cell. Figure 5.18 shows the bubble collapse of bubbles with cell shape $C = 0.2$,

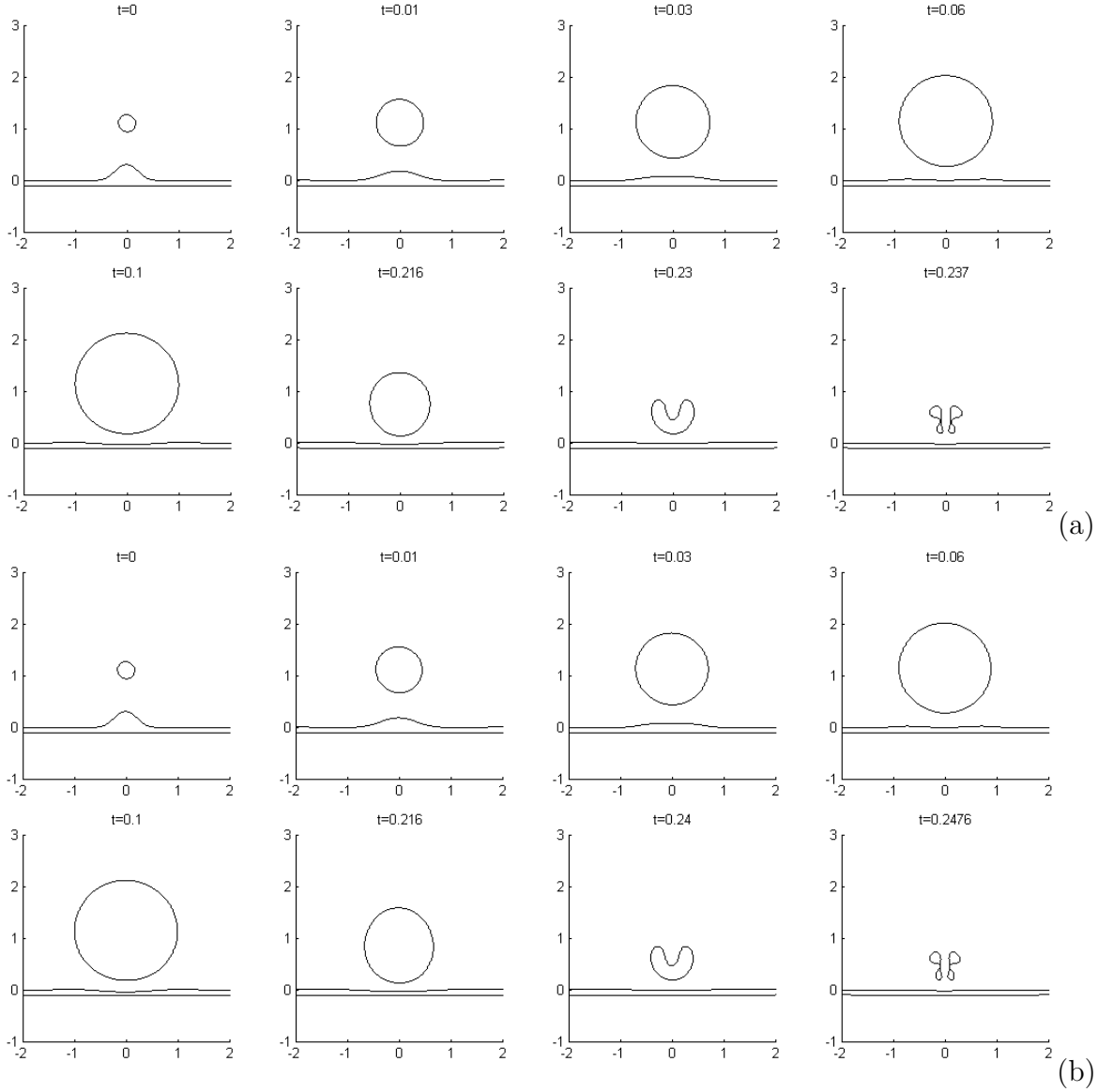


Figure 5.18: Plot of bubble interaction with a cell. The bubble has stand-off $h = 0.8$ from the cell and the cell shape is $C = 0.2$ with surface tension $\sigma = 0.01$, while interface B is the rigid boundary with density ratio $\rho_B = 10000$. The density ratios across the cell wall in each simulation are (a) $\rho_A = 1.1$, (b) $\rho_A = 1.2$.

surface tension $\sigma = 0.01$ and density ratios $\rho_A = 1.1$ and 1.2 respectively. When both surface tension and cell density are non-zero they combine their influence over the bubble and cell shape. When the density ratio is $\rho_A = 1.1$ or 1.2 in figure 5.18, the coupling of the two features causes the cell surface to resist the expansion of the bubble more than

previously seen for these properties individually. The density again acts a buffer for the bubble collapse, extending the time of the evolution compared to the case of only surface tension $\sigma = 0.01$ in figure 5.17(b). While the surface tension continues to distribute the impact from the growth of the bubble reaching maximum radius at $t = 1.0$, compared to the case of only density ratio $\rho_A = 1.1$ in figure 5.16(b). However, despite the two resistive forces included in these simulations, the final frames still show indentation on the cell surface from the impacting jet. Showing that poration of the cell may be a possibility.

Within this section density and surface tension have been added to a curved interface to give a representation of a cell. Though the final model in figure 5.18 is only a theoretical model, it shows that this method of simulating bubble collapse can be used to research cell poration. However, for the simulations to yield any informative results, experimental values for the properties of a cell must be measured.

## 5.5 Chapter Summary

Within this chapter the shape of the interface was altered to see the impact surface geometry can have on the collapse of the bubble. The purpose was to show how easily the numerical method in Chapter 2 can adapt to a change in interface shape, and give an accurate representation of bubble collapse near a curved boundary.

Initially the experiments of Tomita et al. [58] were used for comparison to show the accuracy of the numerical method for bubble collapse near a curved rigid boundary. The results paired well with experimental data for both a convex and a concave boundary. In addition, the simulations made by the boundary integral method were compared with the method of images used by Tomita et al. The collapses were nearly identical showing the validity of the model, though the computation of a curved rigid boundary using the numerical method in this thesis, is much easier to implement than the method of images.

With validation from the experiments conducted by Tomita et al., the model was then used to compute bubble collapse near curved rigid boundaries beyond the scope of the paper. By introducing extreme values for the surface curvature parameter, $\xi$, the effect of curvature on the bubble collapse could be explored. For a concave rigid boundary the bubble collapse was less vigorous, due to the attraction of the bubble to the partly encapsulating wall. Causing low velocities and pressures on the rigid boundary. For a convex boundary the bubble was only attracted to a single point, causing the collapse to form a "tear-drop" shape. The bubble then jets away from the rigid boundary as the bubble collapses, once again causing very low velocities and pressures to impact on the convex rigid wall. This shows that cavitation damage could be lessened by the introduction of curvature to a rigid boundary.

To show the versatility of the curved rigid boundary, alternative interface shapes were introduced. Firstly the interface was shaped to give a crater when rotated around the axis of symmetry. With the radius of the crater being equal to the bubble radius, the bubble grew partially into and around the crest of the crater. During the collapse, the bubble jetted towards the rigid boundary, eventually migrating to the base of the crater. The size of the crater was then increased to simulate the collapse of a bubble in the middle of a "conical cylinder", the bubble only felt attraction from the angled walls around its sides. Initially the bubble formed the shape of the surrounding walls, then collapsed producing a wide jet downwards as the bubble migrated deeper into the crater. With a change in the surface geometry bubble collapse within a bowl was considered. The collapse was similar to that of the concave boundary, though the interface could be modelled within a smaller area of the fluid domain. This allowed for the introduction of a second interface, representing a free surface. The bubble collapse produced a tall surface jet similar to those seen during LIFT experiments, providing an alternative method to the printing technique without the need of a fluid film.

Finally the curved boundary was used to model a biological cell by varying the density ratio and the surface tension of the interface. The results showed that with more research into the properties of a cell, the numerical method in this thesis could be used to simulate the collapse of a bubble near a cell. Thus providing more insight into the use of bubbles in cell membrane poration. Possible ways to improve the model of a cell will be included as further work.

# Chapter 6

# Conclusions and Further Work

The area of cavitation and bubble dynamics has become a large part of applied mathematics over the last few decades. From the oscillations of spherical cavities to the more modern applications in sonochemistry and sonoluminescence, the field is always evolving and new uses are being found for the dynamics of a bubble. This has sparked the interest of many scientists mentioned in this thesis, to explore as many scenarios in which bubbles can be used to aid physical processes. With numerous experiments being conducted, much data has been collected on the impact a bubble can have on the surrounding environment, and vice versa. This data has then been analysed mathematically in the hope to produce as accurate a model as possible, to assist in furthering experimental approaches. Starting with Rayleigh and Plesset deriving an equation that accurately predicted the oscillations of a spherical bubble, mathematicians have refined their models over time to include rigid wall interaction, free surface collapse and pressure fields. Different approaches have been made to simulate the surface of the bubble and nearby interfaces with great success, giving way to a multitude of mathematical codes capable of recreating scenarios with various parameters. Within this thesis the numerical approach of one of these codes has been presented, and analysis of the results produced have been discussed.

The numerical model introduced in Chapter 2 uses the boundary integral method to model the collapse of multiple bubbles in the vicinity of two interfaces. Boundary conditions are applied to all surfaces to incorporate the kinematic and dynamics properties of bubbles and fluid-fluid interfaces within a fluid domain. For bubbles that interact with their environment to collapse into toroidal bubbles, vortex ring calculations are introduced to account for any circulation on the surface lost during the bubble shape transformation. These equations are then discretised and represented in matrix notation to compute the velocity potentials on each surface. To complete the model, quintic splines are used to give a continuous representation of the surfaces on the bubbles and fluid-fluid interfaces. This model was then compared to past literature and experiments on the evolution of bubbles for various scenarios in Chapter 3. Firstly the model was compared with the Rayleigh-Plesset equation for a spherical bubble in an infinite fluid domain. When observing the radius of the bubble from inception for more than two oscillations, the results matched extremely well with little deviation after the second rebound. The representation of the fluid domain from the Rayleigh-Plesset equation also showed great likeness to the numerical method with the two fluid-fluid interfaces separating three fluids of equal density.

To observe the non-spherical collapse of the bubble, a rigid boundary was introduced into the fluid domain. The numerical model was compared with that using the finite difference method and with experimental results for varying stand-off distances. In both cases, the simulations produced compared well with the work from previous papers, showing that the numerical method of Chapter 2 is capable of modelling rigid boundary collapse. Velocity and pressure plots were also produced to show the large pressures that can be exerted on the rigid boundary during bubble collapse, thus showing the cause of cavitation damage in physical processes. Next the density ratio properties of the fluid-fluid interface were altered to mimic a free surface near the bubble. The free surface collapse was compared

with experimental data, showing excellent comparison with the bubble collapse and the characteristic free surface jet produced. Once again the velocities and pressures were plotted to observe the point of high pressure between the bubble and the free surface that causes both the bubble and free surface jets.

With good comparison found between for the spherical bubble, the rigid boundary and free surface evolutions, the density ratios were then adapted to utilise both fluid-fluid interfaces in the model. Firstly the bubble was inserted between two infinite rigid plates to observe the resulting collapse. The numerical method showed good agreement for a bubble evenly positioned between the plates, and when the bubble was offset closer to one plate than the other. In each case the characteristic bubble shapes observed were identical to those seen in the experimental data. Finally the process of laser induced forward transfer was modelled by setting one fluid-fluid interface as a rigid boundary, and the other as a free surface. Though the experimental data did not show the evolution of the bubble, a similar fast, thin fluid surface jet was observed. Therefore it was reasonable to assume the numerical model mimicked the key features that would be seen by the collapsing bubble in a LIFT experiment.

With the numerical model from Chapter 2 compared with experimental data and other numerical models from past papers to a high degree of accuracy, it was now necessary to apply the model to create new results within the area of bubble and cavitation dynamics.

## 6.1 Conclusions

The first application of the numerical model in Chapter 4 was to consider how two fluids separated by an interface can be mixed using the collapse of two bubbles in alternate fluids. The mixing process was quantified by considering how far the fluid interface moved from the initial position into either fluid, and how much volume of fluid was displaced

into the initial domain of the other fluid. The strength and inception time of one of the bubbles were varied to see the effect it had on the mixing process.

Firstly, the strength was considered. The results showed that the attraction of the weaker bubble to the stronger, would form a jet through the weaker bubble in the direction of the stronger. This jet would then push the fluid containing the weaker bubble into the other fluid, thus promoting mixing. As the difference in strength between the bubbles was increased, so would the depth of penetration off the fluid containing the weaker bubble. This trend would end once the strength of the stronger bubble became too large for the bubble surface and fluid-fluid interface to remain separate, thus terminating the simulation early. It was found that the amount of volume displaced during the collapses was not determined by the bubble jet, but by the growth phases of the bubble. Therefore the greater the strength of the stronger bubble the more fluid it would push outwards on expansion, thus moving more of the fluid containing the stronger bubble into the other fluid. Hence, if there is a preference over which fluid is to be inserted into the other; for deepest penetration the weaker bubble should be in the main fluid to be displaced, and for greatest volume displaced the stronger bubble should be in the main fluid to be displaced.

Secondly, the inception times of the bubbles were considered to utilise a feature of two bubble collapse called the catapult effect. By introducing the second bubble into the fluid domain when the first bubble is near maximum radius, the catapult effect increases the maximum interface displacement and the maximum volume transferred to give optimal mixing. This is applicable when inserting the fluid containing the latter bubble into the fluid containing the first.

Next the pressures and volumes of the bubbles were used with a simplified version of the ideal gas law to give insight into the temperature changes that can be observed during the bubble collapses. For certain collapses, in varying either bubble strength or inception

time, it was found that spikes in the bubble temperature occurred which were greater than the initial values found at the inception of the bubble. This gave reason to believe that the process of mixing could be combined with application of heat, for use in chemical and biological reactions that need specific input energies. Alternatively, processes that can be hindered by increases in temperature, could avoid the bubble formations that cause these high temperature spikes during collapse.

A combination of both strength and inception times were used to find how interface displacement of volume transfer could be maximised. The results showed that interface displacement was greatest for when a strong bubble was incepted at the maximum radius of the first bubble, with the amount of displacement tending to a maximum of 1 bubble radii for increasing strength. However, for maximum volume transferred the stronger bubble should be incepted at the maximum radius of the first bubble for lower strength differences. As the difference in strength of the two bubbles increases, the stronger bubble should be introduced earlier in the life time of the first bubble, tending to an inception time of $t = 0.1$. When using the combination of strength and inception time, the stronger latter bubble should be incepted in the fluid that is to be inserted into the other.

Finally the mixing of fluids of different densities was considered, using the same strength and inception time variations as before. When the density ratio was high, the mixing of the fluids was hindered and became more ineffective, as expected. Though to optimise the mixing of fluids with more comparable densities, the stronger bubble should be placed within the denser fluid. While for inception times, the latter bubble should also be placed within the denser fluid for maximum effect in both interface displacement and volume transfer.

In Chapter 5 the geometry of an interface was altered to see the effect it had on the bubble collapse, and vice versa. Initially the collapse of a bubble near a curved rigid boundary

was modelled and compared to experimental and other numerical results. For both a concave and a convex rigid boundary the numerical method from this thesis showed good agreement with the data from the previous paper. To show the versatility and ease of altering the geometry of the interface using this numerical method, the curvature parameter was increased past the values considered in the original paper. The results showed a slower collapse of bubble when near a concave boundary compared to that of a flat boundary. Also the pressures formed on the interface were much lower than those seen for flat rigid boundaries, implying that introducing curvature to rigid surfaces could reduce cavitation damage. Similarly, low pressures were found when a bubble collapse near the peak of a very convex boundary, with the bubble jetting away from the rigid surface. The purpose of this portion of the chapter was to show how the surface geometry can easily be changed without the use of complicated image theory of the bubbles. The boudary integral method used in this thesis allows for a simple change in nodal placement for the simulations to be performed.

To observe the level the interface can be changed, more unusual geometries were introduced. The collapse of a bubble near a crater on the surface saw the bubble take the shape of the lip of the crater, while continuing to expand inside it. During the collapse the bubble migrated into the crated with a slow jet directed towards the boundary. With a simple change in size of the crater, a simulation for a bubble within a conical cylinder was produced. The bubble expanded within the cylinder, forming to the sloped walls. The bubble then collapsed with a wide jet directed downwards, while the bubble migrated deeper into the large crater. The purpose of the crater simulations was to show that a multitude of interface shapes could be considered as long as the interface remained continuous and sufficiently smooth.

Next a simple bowl shape was formed by the interface to show how similar results to the concave boundary can be produced, without the need for the surface shape to extend

outwards to several bubble radii. With the bubble collapsing into the localised bowl comparing well with the concave boundary, a free surface was introduced above the bowl to further show the many bubble collapse scenarios that can be modelled using the numerical method from Chapter 2. The simulation provided a possible alternative to the set-up of LIFT experiments, by eliminating the need of a fluid film.

Finally, the use of the curved interface and the second fluid-fluid interface were combined to model a cell on a rigid surface. By varying the interface density ratio and surface tension, the curved interface was used to give a crude model of a cell. The collapse of a bubble near the surface showed the possibility of poration of the cell.

The simulations shown in Chapter 5 are to show how the numerical model in this thesis can easily be used to consider bubble collapse near curved interfaces. There are almost limitless possibilities for various types of bubble collapse that can be observed by changing the geometry of the interfaces, confined within an axisymmetric coordinate system. With manipulation of the properties of the interfaces the model can be used to show the collapse of a bubble near a concave or convex wall, a crater, a conical cylinder, or even a cell. Thus showing the true versatility of this numerical method.

## 6.2 Further Work

The results in this thesis have provided great insight into many applications of bubble collapse, though additions can always be made. While producing the results for the mixing process in Chapter 4, the simulations would terminate due the close proximity of the bubble surface to the interface. This problem could be overcome by allowing bubbles to transfer over the fluid-fluid interface. For the transition of a bubble form one fluid domain to the other to be physically possible, the density ratio would have to be sufficiently low to avoid a bubble migrating into a rigid wall. Mathematically the fluid domains must remain separate, to avoid errors when computing the Green's function. A

similar transition has been computed by Boulton-Stone and Blake [8] and Georgescu et al. [27], in which a bubble near a free surface "bursts" by removing the point where the bubble surface and interface meet, leaving a cavity in the interface.

When computing the representations for the temperatures in the collapsing bubbles during the mixing process, a simplified form of the ideal gas law was used. To give more accurate representation of the temperatures achieved, specific types of gas can be introduced to give values for the number of moles within the bubble during collapse. If the temperature analysis needs to be more robust, additional properties of mass transfer from the bubble to the fluid could be included in the boundary equations for the bubble.

As mentioned in Chapter 5, the model provided for the cell is a rough estimate of the parameters. To improve the model further, properties of cell density and surface tension of the cell membrane must be measured. With accurate representation of the cell, the bubble collapse and cell interaction simulated will have some bearing on the physical process. If the values obtained for surface tension and cell density are too high for the bubble collapse to show any sign of poration, ultrasound can be added into the model by varying the amplitude and frequency of the far field pressure. This can supply the bubble with more energy during the collapse stage, producing a faster jet with a greater impact on the cell. Additionally the shape of the rigid boundary could be altered to give a concave bowl, therefore simulating a more spherical cell as opposed to hemispherical.

The numerical model used within this thesis is already well equipped to simulate a wide array of bubble collapses in a number of scenarios. The results obtained from the use of this model will greatly further the understanding of bubble collapse in many industrial and biological processes.

# Appendix A
# Rayleigh-Plesset Equation Derivation

Taking the fluid velocity to be given by $\mathbf{u}$, incompressibility is given by $\nabla \cdot \mathbf{u} = 0$. As the bubble is spherically symmetric we know that the bubble only has radial velocity. So in standard spherical coordinates we have $\mathbf{u} = (u_r, u_\theta, u_\phi)$, and for the spherically symmetric case $u_\theta = u_\phi = 0$. Combining this with the assumption that the flow is incompressible, and with conservation of mass we have:

$$\nabla \cdot \mathbf{u} = \frac{1}{r^2}\frac{\partial}{\partial r}[r^2 u_r] + \cancel{\frac{1}{r\sin(\theta)}\frac{\partial}{\partial \theta}[\sin(\theta)u_\theta]} + \cancel{\frac{1}{r\sin(\theta)}\frac{\partial}{\partial \phi}[u_\phi]} = 0$$

$$\frac{1}{r^2}\frac{\partial}{\partial r}[r^2 u_r] = 0.$$

Now multiply through by $r^2$

$$\frac{\partial}{\partial r}[r^2 u_r] = 0.$$

And integrate with respect to $r$

$$r^2 u_r = F$$

$$\text{or} \qquad u_r(r,t) = \frac{F(t)}{r^2}, \tag{A.1}$$

where $F(t)$ is the constant of integration which can depend on time. We want to consider the case where there is zero mass transfer across the bubble surface, this means we have no condensation or evaporation at the bubble surface. For this to occur we need the velocity in the radial direction to be equal to the rate of change of the radius, otherwise we would need to include a term for the change in volume due to the change in mass inside the bubble. So we have $u_r(R,t) = \frac{dR}{dt}$, where $R = R(t)$ is the radius at time t, which gives

$$\begin{aligned} \frac{dR}{dt} &= \frac{F(t)}{R^2} \\ F(t) &= R^2 \frac{dR}{dt}. \end{aligned}$$

Substituting this value for $F(t)$ into (A.1) gives

$$u_r(r,t) = \frac{R^2}{r^2}\frac{dR}{dt} = \frac{R^2\dot{R}}{r^2}, \tag{A.2}$$

here dot denotes differentiation with respect to time, t.
We now substitute this velocity into the Navier-Stokes equations, which are given by

$$\frac{\partial\,\mathbf{u}}{\partial t} + (\mathbf{u}\cdot\nabla)\,\mathbf{u} = \mathbf{f} - \frac{\nabla p}{\rho} + \nu\nabla^2\mathbf{u}.$$

Here we have density $\rho$, pressure $p = p\,(r,\theta,\phi,t)$ (spherical symmetry gives $\frac{\partial p}{\partial\theta} = \frac{\partial p}{\partial\phi} = 0$), viscosity $\mu$, velocity $\mathbf{u}$, and time $t$. For this derivation we assume there are no body forces acting on the fluid, so $\mathbf{f} = 0$. Rearranging the Navier-Stokes equation in spherical coordinates and substituting in our velocity $\mathbf{u} = (u_r, 0, 0)$ we get the relationship between velocity and pressure in the radial direction $r$ as.

$$-\frac{1}{\rho}\frac{\partial p}{\partial r} = \frac{\partial u_r}{\partial t} + u_r\frac{\partial u_r}{\partial r} - \nu\left[\frac{1}{r^2}\frac{\partial}{\partial r}\left(r^2\frac{\partial u_r}{\partial r}\right) - \frac{2u_r}{r^2}\right]. \tag{A.3}$$

So if we substitute (A.2) into (A.3) we get

$$\begin{aligned} -\frac{1}{\rho}\frac{\partial p}{\partial r} =& \frac{\partial}{\partial t}\left[\frac{R^2\dot{R}}{r^2}\right] + \frac{R^2\dot{R}}{r^2}\frac{\partial}{\partial r}\left[\frac{R^2\dot{R}}{r^2}\right] \\ =& \frac{1}{r^2}\left[\dot{R}\frac{d}{dt}\left[R^2\right] + R^2\frac{d}{dt}\left[\dot{R}\right]\right] + \frac{R^2\dot{R}}{r^2}R^2\dot{R}\frac{d}{dr}\left[\frac{1}{r^2}\right] \\ =& \frac{1}{r^2}\left[\dot{R}\cdot 2R\cdot\dot{R} + R^2\ddot{R}\right] + \frac{R^2\dot{R}}{r^2}R^2\dot{R}\left[\frac{-2}{r^3}\right] \\ =& \frac{1}{r^2}\left[2R\left(\dot{R}\right)^2 + R^2\ddot{R}\right] - \frac{2}{r^5}\left(R^2\dot{R}\right)^2. \end{aligned}$$

Note that the viscous terms have disappeared, this is due to the velocity in (A.2) giving $\nabla^2\mathbf{u} = 0$. Now we integrate with respect to $r$

$$-\frac{1}{\rho}p = -\frac{1}{r}\left[2R\left(\dot{R}\right)^2 + R^2\ddot{R}\right] + \frac{1}{2r^4}\left(R^2\dot{R}\right)^2 + C, \tag{A.4}$$

where C is an constant. As $r \longrightarrow \infty$, we get

$$-\frac{1}{\rho}p_\infty = \cancelto{0}{-\frac{1}{r}\left[2R\left(\dot{R}\right)^2 + R^2\ddot{R}\right]} - \cancelto{0}{\frac{1}{2r^4}\left(R^2\dot{R}\right)^2} + C$$

$$C = -\frac{1}{\rho}p_\infty, \tag{A.5}$$

where $p_\infty$ is the far field pressure at infinity. Substituting the value for C from (A.5) back into (A.4)

$$-\frac{1}{\rho}p = -\frac{1}{r}\left[2R\left(\dot{R}\right)^2 + R^2\ddot{R}\right] - \frac{1}{2r^4}\left(R^2\dot{R}\right)^2 - \frac{1}{\rho}p_\infty.$$

Then rearrange to get

$$\frac{p - p_\infty}{\rho} = \frac{1}{r}\left[2R\left(\dot{R}\right)^2 + R^2\ddot{R}\right] - \frac{1}{2r^4}\left(R^2\dot{R}\right)^2.$$

On the boundary of the bubble, when $r = R$, we have

$$\begin{aligned}\frac{p(R) - p_\infty}{\rho} =& \frac{1}{R}\left[2R\left(\dot{R}\right)^2 + R^2\ddot{R}\right] - \frac{1}{2R^4}\left(R^2\dot{R}\right)^2 \\ \frac{p(R) - p_\infty}{\rho} =& 2\left(\dot{R}\right)^2 + R\ddot{R} - \frac{1}{2}\left(\dot{R}\right)^2.\end{aligned} \tag{A.6}$$

To find an expression for the pressure at the boundary we must first look at the forces acting here. The force per unit area at the surface $\frac{\partial F}{\partial A}$, is created from the internal pressure of the bubble $p_{bubble}$, the surface tension $\sigma$, and the liquid pressure $p_{liquid}$. For a viscous fluid, the pressure on the surface of the bubble in the $-r$-direction is equal to the stress of the fluid in the opposite direction. So we can write the outer pressure as $p_{liquid} = -S_{rr}$, where $S_{rr}$ is the stress of the liquid. So we obtain

$$\frac{\partial F}{\partial A} = (S_{rr})_{r=R} + p_{bubble} - \frac{2\sigma}{R}.$$

This equation can be found from the Young-Laplace equation, which relates pressure differences across a lamina to the surface tension on the lamina. For zero mass transfer to occur at the boundary, we require that the force per unit area of the surface, $\frac{\partial F}{\partial A}$, to be equal to zero, giving

$$(S_{rr})_{r=R} + p_{bubble} - \frac{2\sigma}{R} = 0.$$

As we are using an incompressible Newtonian fluid, we get an expression for the stress of the liquid as

$$
\begin{aligned}
S_{rr} &= -p(r) + 2\mu \frac{\partial u_r}{\partial r} \\
&= -p(r) + 2\mu \frac{\partial}{\partial r}\left(\frac{R^2\dot{R}}{r^2}\right) \\
&= -p(r) - 4\mu \frac{R^2\dot{R}}{r^3} \\
(S_{rr})_{r=R} &= -p(R) - 4\mu \frac{\dot{R}}{R}.
\end{aligned}
$$

Substituting this expression for stress into the surface forces equation, we rearrange to get

$$p(R) = p_{bubble} - \frac{2\sigma}{R} - \frac{4\mu}{R}\dot{R}, \tag{A.7}$$

where $\mu$ is the viscosity of the liquid. Introducing the adiabatic pressure term,

$$p_{bubble} = p_v + p_0\left(\frac{V_0}{V}\right)^{\gamma}$$

and equation (A.7) into equation (A.6) and rearranging gives the Rayleigh-Plesset Equation,

$$R\ddot{R} + \frac{3}{2}\left(\dot{R}\right)^2 = \frac{1}{\rho}\left[p_v - p_\infty + p_0\left(\frac{V_0}{V}\right)^{\gamma} - \frac{2\sigma}{R} - \frac{4\mu}{R}\dot{R}\right].$$

This can now be non-dimensionalised with respect to the maximum bubble radius $R_{max}$ and pressure difference $\Delta_p = p_\infty - p_v$ to give $\overline{R} = RR_{max}^{-1}$ and $\bar{t} = rR_{max}^{-1}\sqrt{\rho^{-1}\Delta_p}$. Hence,

$$\overline{R}\ddot{\overline{R}} + \frac{3}{2}\left(\dot{\overline{R}}\right)^2 = \varepsilon\left(\frac{\overline{R}_0}{\overline{R}}\right)^{3\gamma} - 1 - \frac{2\overline{\sigma}}{\overline{R}} \tag{A.8}$$

where viscosity has been neglected and the dimensionless parameters are given by

$$\varepsilon = \frac{p_0}{\Delta_p} \text{ and } \overline{\sigma} = \frac{\sigma}{\Delta_p R_{max}}.$$

# List of References


[1] Andrea Adamo and Klavs F. Jensen. Microfluidic based single cell microinjection. *The Royal Society of Chemistry*, 8:1258–1261, 2008.

[2] T.B. Benjamin and A.T. Ellis. The collapse of cavitation bubbles and the pressures thereby produced against solid boundaries. *Philosophical Transactions of the Royal Society of London*, 260:221–240, 1966.

[3] J.P. Best. The formation of toroidal bubbles upon the collapse of transient cavities. *Journal of Fluid Mechanics*, 251:79–107, 1993.

[4] J.R Blake and D.C. Gibson. Growth and collapse of a vapour cavity near a free surface. *Journal of Fluid Mechanics*, 111:123–140, 1981.

[5] J.R. Blake and D.C. Gibson. Cavitation bubbles near boundaries. *Annual Review of Fluid Mechanics*, 19:99–123, 1987.

[6] J.R. Blake, B.B. Taib, and G. Doherty. Transient cavities near boundaries. part 1. rigid boundaries. *Journal of Fluid Mechanics*, 170:479–497, 1986.

[7] J.R. Blake, B.B. Taib, and G. Doherty. Transient cavities near boundaries. part 2. free surfaces. *Journal of Fluid Mechanics*, 181:197–212, 1987.

[8] J.M Boulton-Stone and J.R. Blake. Gas bubbles bursting at a free surface. *Journal of Fluid Mechanics*, 254:437–466, 1993.

[9] C. Brennen. *Cavitation and Bubble Dynamics*. Oxford University Press, 1995.

[10] E.A. Brujan, G.S. Keen, A. Vogel, and J.R. Blake. The final stage of the collapse of a caviation bubble close to a rigid boundary. *Physics of Fluids*, 14(1):85–92, 2002.

[11] M.A. Burns, B.N. Johnson, S.N. Brahmasandra, et al. An integrated nanoliter dna analysis device. *American Association for the Advancement of Science*, 282(5388):484–487, 1998.

[12] M.L. Calvisi, J.I. Iloreta, and A.J. Szeri. Dynamics of bubbles near a rigid surface subjected to a lithotripter shock wave. part 2. reflected shock intensifies non-spherical collapse. *Journal of Fluid Mechanics*, 616:63–97, 2008.

[13] M.L. Calvisi, O. Lindau, J.R. Blake, and A.J. Szeri. Shape stability and violent collapse of microbubbles in acoustic travelling waves. *Physics of Fluids*, 19, 2007.

[14] B.C. Carlson. Elliptic integrals. *NIST Handbook of Mathematical Functions*, 2010.

[15] CAV2001: Fourth International Symposium on Cavitation. *Cavitation bubble behaviour near solid boundaries*, California Institute of Technology, Pasadena, CA, USA, 2001.

[16] J.K. Choi and G.L. Chahine. Noise due to extreme bubble deformation near inception of tip vortex cavitation. *Physics of Fluids*, 16(7):2411–2418, 2004.

[17] G.A. Curtiss. *Non-linear, non-spherical bubble dynamics near a two fluid interface.* PhD thesis, The University of Birmingham, 2009.

[18] G.A. Curtiss, D.M. Leppinen, Q.X. Wang, and J.R. Blake. Ultrasonic cavitation near a tissue layer. *Journal of Fluid Mechanics*, 730:245–272, 2013.

[19] Rory Dijkini, Severine Le Gac, Erwin Nijhuis, et al. Controlled cavitation-cell intercation: trans-membrane transport and viability studies. *Physics in Medicine and Biology*, 53:375–390, 2008.

[20] M. Duocastella, J.M. Fernández-Pradas, J.L. Morenza, and P. Serr. Time-resolved imaging of the laser forward transfer of liquids. *Journal of Applied Physics*, 106, 2009.

[21] M. Duocastella, A. Patrascioiu, J.M. Fernández-Pradas, J.L. Morenza, and P. Serr. Film-free laser forward printing of transparent and weakly absorbing liquids. *Optics Express*, 18, 2010.

[22] M.D. Esson. The osillcatory nature of bubbles. Master's thesis, The University of Birmingham, 2010.

[23] S.W. Fong, D. Adhikari, E. Klaseboer, and B.C. Khoo. Intercations of multiple spark-generated bubbles with phase differences. *Experiments in Fluids*, 46(4):705–724, 2009.

[24] D.F. Gaitan, L.A. Crum, C.C. Church, and R.A. Roy. Sonoluminescence and bubble dynamics for a single, stable, cavitation bubble. *Journal of the Acoustical Society of America*, 91:3166–3183, 1992.

[25] P. Garstecki, M.A. Fischbach, and G.M. Whitesides. Design for mixing using bubbles in branched microfluidic channels. *Applied Physics Letters*, 86(244108), 2005.

[26] P. Garstecki, M.J. Fuerstman, M.A. Fischbach, et al. Mixing with bubbles: a practical technology for use with portable microfluidic devices. *Lab on a Chip*, 6:207–212, 2006.

[27] S.C. Georgescu, J.L. Achard, and E. Canot. Jet drops ejection in bursting gas bubble processes. *European Journal of Mechanics B*, pages 265–280, 2002.

[28] S. Gonzalez-Avila, C. Song, and C.D. Ohl. Fast transient microjets induced by hemispherical cavitation bubbles. *Journal of Fluid Mechanics*, 2013.

[29] A.N. Hellman, K.R. Rau, H.H. Yoon, S. Bae, et al. Laser-induced mixing in microfluidic channels. *Analytical Chemistry*, 79:4484–4492, 2007.

[30] A. Kucera and J.R. Blake. Approximate methods for modelling cavitation bubbles near boundaries. *Bulletin of the Australian Mathematical Society*, 41:1–44, 1990.

[31] H. Lamb. *Hydrodynamics*. Dover, New York, 1932.

[32] W. Lauterborn and H. Bolle. Experimental investigations of cavitation-bubble collapse in the neighbourhood of a solid boundary. *Journal of Fluid Mechanics*, 72:391–399, 1975.

[33] Severine Le Gac, Ed Zwaan, Albert van der Berg, and Claus-Dieter Ohl. Sonoporation of suspension cells with a single cavitation bubble in a microfluidic confinement. *The Royal Society of Chemistry*, 7:1666–1672, 2007.

[34] M. Lee, E. Klaseboer, and B.C. Khoo. On the boundary integral method for the rebounding bubble. *Journal of Fluid Mechanics*, 570:407–429, 2007.

[35] T.G. Leighton. The inertial terms in equations of motion for bubbles in tubular vessels or between plates. *Journal of the Acoustic Society of America*, 130(5):3333–3338, November 2011.

[36] Z.G. Li, A.Q. Liu, E. Klaseboer, et al. Single cell membrane poration by bubble-induced microjets in a microfluidic chip. *The Royal Society of Chemistry*, 13:115–1150, 2013.

[37] R.H. Liu, J. Yang, M.Z. Pindera, M Athavale, and P. Grodzinski. Bubble-induced acoustic micromixing. *Lab on a Chip*, 2:151–157, 2002.

[38] R. Löfstedt, K. Weniger, S. Putterman, and B.P. Barber. Sonoluminescing bubbles and mass difusion. *Physical Review E*, 51(5):4400–4410, 1995.

[39] T.S. Lundgren and N.N. Mansour. Vortex ring bubbles. *Journal of Fluid Mechanics*, 224:177–196, 1991.

[40] J.M. Ottino and S. Wiggins. Introduction: mixing in microfluidics. *Philosophical Transactions: Mathematical, Physical and Engineering Sciences*, 362:923–935, 2004.

[41] J.D. Oxley, T. Prozorov, and K.S. Suslick. Sonochemistry and sonoluminescence of room-temperature ionic liquids. *Journal of the American Chemical Society*, 125:11138–11139, 2002.

[42] A. Pearson, J.R. Blake, and S.R. Otto. Jets in bubbles. *Journal of Engineering Mathematics*, 48:391–412, 2004.

[43] T.J. Pedley. The toroidal bubble. *Journal of Fluid Mechanics*, 32:97–112, 1968.

[44] A. Philipp and W. Lauterborn. Cavitation erosion by single laser-produced bubbles. *Journal of Fluid Mechanics*, 361:75–116, 1998.

[45] Y.A. Pishchalnikov, O.A. Sapozhnikov, M.R. Bailey, et al. Cavitation bubble cluster activity in the breakage of kidney stones by lithotripter shockwaves. *Journal of Endourology*, 17(7):435–446, September 2003.

[46] M.S. Plesset and A. Prosperetti. Bubble dynamics and cavitation. *Annual Review of Fluid Mechanics*, 9:145–185, 1977.

[47] M.S. Plesset and Chapman R.B. Collapse of an initially spherical vapour cavity in neighbourhood of a solid boundary. *Journal of Fluid Mechanics*, 47:283–290, May 1971.

[48] P.A. Prentice, D. McLean, A. Cuschieri, et al. Spatially controlled sonoporation of prostate cancer cells via ultrasound activated microbubble cavitation. International IEEE EMBS Special Topic, May 2005.

[49] P.A. Quinto-Su, M. Suzuki, and Ohl C.D. Fast temperature measurement following single laser-induced cavitation inside a microfluidic gap. *Scientific Reports*, 4(5445), 2014.

[50] Lord Rayleigh. On the pressure developed in liquid during the collapse of a spherical void. *Philosophical Magazine*, 34:94–98, 1917.

[51] Brian D. Storey and Andrew J. Szeri. Water vapour, sonoluminescence and sonochemistry. *Proceedings of The Royal Society A*, 456:1685–1709, 2000.

[52] Brian D. Storey and Andrew J. Szeri. A reduced model of cavitation physics for use in sonochemistry. *Proceedings of The Royal Society A*, 457:1685–1700, 2001.

[53] K.S. Suslick. Sonoluminescence and sonochemistry. pages 523–532. IEEE Ultrasonics Symposium, October 1997.

[54] K.S. Suslick and D.J. Flannigan. Inside a collapsing bubble: Sonoluminescence and the conditions during cavitation. *Annual Review of Physical Chemistry*, 59:659–683, 2008.

[55] A.J. Szeri, B.D. Storey, A. Pearson, and J.R. Blacke. Heat and mass transfer during the violent collapse of nonspherical bubbles. *Physics of Fluids*, 15(9):2576–2586, 2003.

[56] B.B. Taib. *Boundary integral method applied to cavitation bubble dynamics*. PhD thesis, The University of Wollongong, 1985.

[57] Jue Nee Tan, Charles Ma, Ninnuja Sivanantha, and Adrian Neild. Bubble inducing cell lysis in a sessile drop. *Applied Physics Letters*, 104, 2014.

[58] Y. Tomita, P.B. Robinson, R.P. Tong, and J.R. Blake. Growth and collapse of cavitation bubbles near a curved rigid boundary. *Journal of Fluid Mechanics*, 466:259–283, 2002.

[59] Q.X. Wang, K.S. Yeo, B.C. Khoo, and K.Y. Lam. Vortex ring modelling of toroidal bubbles. *Theoretical and Computational Fluid Dynamics*, 19(5):303–317, 2005.

[60] S. Wiggins and J.M. Ottino. Foundation of chaotic mixing. *Philosophical Transactions: Mathematical, Physical and Engineering Sciences*, 362:937–970, 2004.

[61] H. Yuan and A. Prosperetti. Gas-liquid heat transfer in abubble collapsing near a wall. *Physics of Fluids*, 9:127–142, 1997.

[62] Y.L. Zhang, K.S. Yeo, B.C. Khoo, and C. Wang. 3d jet impact and toroidal bubbles. *Journal of Computational Physics*, 2001.